Single-station inversion of seismic data for the InSight mission to Mars

Rakshit Joshi

München 2022

Cover: 'Planetary Aantomy' by Chris Bickel/Science, Data: InSight Mars SEIS Data Service (2019). Reprinted with permission from AAAS. Background image and cover designed by Rakshit Joshi.

Single-station inversion of seismic data for the InSight mission to Mars

Rakshit Joshi

Dissertation
an der Fakultät für Geowissenschaften
der Ludwig–Maximilian–Universität
München

vorgelegt von
Rakshit Joshi
aus Nainital

München, den 18.07.2022

Erstgutachter: Prof. Dr. Heiner Igel
Zweitgutachter: Prof. Dr. Ulrich Christensen
Tag der mündlichen Prüfung: 8.12.2022

Contents

List of Figures

List of Tables

Zusammenfassung

Terrestrische Planeten, wie zum Beispiel Erde und Mars, besitzen eine Kruste, die sich während der Akkretion bildet und Informationen über grundlegenden Prozesse konserviert, die an deren Entstehung und Entwicklung beteiligt sind. Im Unterschied zur Erde, bei der ein Großteil der alten Kruste recycelt wurde, ist die Marskruste aufgrund fehlender Plattentektonik erhalten geblieben. Die Untersuchung von dessen Dicke und Struktur kann dazu beitragen, die frühe Entwicklung und Bildung des Planeten einzugrenzen. Bisherige Schätzungen der Dicke der Marskruste basieren, aus Ermangelung verfügbarer seismographischer Daten, hauptsächlich auf orbitalen Topographie- und Schwerkraftdaten. Die Ergebnisse waren sehr unsicher, da diese Methoden nur relative Variationen statt absoluter Daten liefern können. Im November 2018 hat die InSight-Mission erfolgreich ein Dreikomponenten-Breitband-Seismometer auf der Marsoberfläche in Betrieb genommen. Nach kontinuierlicher seismischer Überwachung des Planeten für mehr als drei Erdjahre, geben die Daten von InSight nun zum allerersten Mal die Möglichkeit zur Insitu-Untersuchung der Marskruste. Diese Dissertation zielt darauf ab, eine Methode für eine einzelne seismische Station zu entwickeln und anzuwenden, mit der die Kruste des Mars abgebildet und seine Dicke und Struktur basierend auf aufgezeichneten Marsbeben unterhalb des InSight-Landeplatzes evaluiert werden kann. Eine solche Messung dient auch als Referenzpunkt, der zusammen mit Gravitations- und Topographiedaten genutzt werden kann, um Schwankungen der globalen Krustendicke einzugrenzen. Es wird eine Technik präsentiert, die auf dem Receiver Function (RF)-Verfahren basiert. Unter Verwendung von Phasenumwandlungen zwischen Kompressionswellen (P) und Scherwellen (S), können RFs planeteninterne Grenzflächen abbilden, während seismische Wellen durch diese propagieren. Um die Mehrdeutigkeit der Inversionen zu reduzieren, wurde eine einfache Relation genutzt, die die scheinbare S-WellenGeschwindigkeit als eine Funktion von beobachteten Einfallswinkeln scheinbarer P-Wellen beschreibt, was wiederum den Parameterraum einschränkt. Diese Einfallswinkel werden, zusammen mit der Bewertung der Parameterunsicherheiten und den RFs gemeinsam invertiert. Terrestrische Daten mit verschiedenen zu Grunde liegenden geologischen Gegebenheiten veranschaulichen die Methode. Die erhaltenen Werte zu Krustendicke, Geschwindigkeiten und Anzahl der Schichten innerhalb der Marskruste stimmen mit den Ergebnissen früherer Studien überein. Diese Dissertation präsentiert die erste RF-Analyse seismischer Marsdaten unter Verwendung mehrerer Marsbeben. RF-Berechnungen und Inversionen nach verschiedenen Ansätzen zeigen durchgängig drei klare Phasenankünfte innerhalb der ersten 8 Sekunden. Diese wer-

den als Konvertierungen von entweder einer zweischichtiger Kruste mit einer Dicke von 20 km oder einer dreischichtige Kruste mit einer Dicke von 39 km interpretiert. Extrapolation dieser Punktmessungen auf den gesamten Planeten unter Verwendung von Schwerkraft- und Topographiedaten schätzen die durchschnittliche Dicke der Marskruste auf zwischen 24 und 72 km. Um die Mehrdeutigkeit des Modells aufzulösen, ist ein Ansatz zur Identifizierung von mehrfach konvertierten Phasen in RF-Wellenformen unter Verwendung der Zufallsmatrixtheorie umrissen. Ein Spike-Kovarianzmodell für die Daten voraussetzend, approximiert und extrahiert das Verfahren zufällige Rauschkontamination aus den RF-Wellenformen und erlaubt dadurch die Beobachtung kohärenter Phasenankünfte. Neue mehrfach reflektierte Phasenankünfte werden mit dieser Methode in den InSight-Daten identifiziert. Die Ergebnisse zeigen ein dreischichtiges Krustenmodell mit einer Krustendicke von 43 km, konsistent mit dem dreischichtigen Modell der früheren Studie.

Summary

Terrestrial planets, such as Earth and Mars, possess a crust that forms during the accretion phase, preserving impressions of the fundamental processes involved in their formation and evolution. Unlike Earth, where most of the ancient crust has been recycled, Mars retains most of it as it does not possess plate-tectonics. Investigation of its crustal thickness and structure can thus help constrain its early evolution and formation. Previous estimates of Martian crustal thickness have been primarily based on orbital topography and gravity data due to a lack of seismic data. The results were highly uncertain as these can only constrain relative variations and not absolute values.

In November 2018, the InSight mission successfully deployed a three-component, very broad-band seismometer on the surface of Mars. With continuous seismic monitoring of Mars for over three Earth years, the seismic data from InSight now presents us with an opportunity for in-situ investigation of the Martian crust for the very first time. This thesis aims to develop and apply a single-station seismic method to image the crust of Mars and evaluate its crustal thickness and structure below the InSight landing site using the recorded marsquakes. Such a measurement also serves as a "tie-point" that can be used with the gravity and topography data to provide constraints on the global crustal thickness variations of the Martian crust.

A technique based on the Receiver Function (RF) method has been introduced. RFs can image subsurface interfaces by utilizing the mode conversion between the compressional (P) and shear (S) waves as seismic waves propagate through them. To reduce the non-uniqueness of their inversions, a simple relation which defines apparent S-wave velocity as a function of observed apparent P-wave incidence angle has been used to constrain the parameter space. This is then used with RFs simultaneously in a joint inversion scheme along with the evaluation of parameter uncertainties. Terrestrial data from various geological settings illustrate the method. The obtained crustal thickness values, velocities and inter-crustal layerings are consistent with results obtained in previous studies.

This thesis presents the first RF analysis of Martian seismic data using several marsquakes. RF computation and inversions using different approaches consistently show three clear phase arrivals within the first 8 seconds. These are interpreted as conversions from either a two-layer crust with a thickness of 20 km or a three-layer crust with a thickness of 39 km. Extrapolation of these point measurements to the whole planet using gravity and topography data estimates the average thickness of the martian crust to lie between 24 and 72 km. To help resolve the model ambiguity, an approach to identify multiply con-

verted phases in the RF waveforms using the random matrix theory is outlined. Assuming a spiked covariance model for the data, the method approximates and extracts random noise contamination from the RF waveforms and emphasizes coherent phase arrivals. New multiply reflected phase arrivals are identified in the InSight data using this method. Inversion results indicate a three-layer crustal model with a crustal thickness of 43 km below the InSight landing site, consistent with the three-layer model and global thickness values of the earlier study.

Chapter 1

Introduction

Along with Earth, Venus, and Mercury, Mars is one of the four terrestrial planets in our Solar System. With striking similarities and differences to our world, it has been a focus of planetary exploration since the beginning of the space age. Questions about its past, present and future continue to spark curiosity and fantasy. Early telescopic observations of Mars showed numerous dark linear canals on its surface, interpreted as evidence of intelligent civilizations inhabiting the planet (Lowell, 1906). It was not until the first Mars flyby missions broadcasted clear pictures of its surface in the late 1960s that these interpretations were finally debunked. Our understanding of the planet has increased enormously over these last 60 years, with crewed missions and habitats planned for the next decades. With over a dozen successful missions to Mars, evidence strongly suggests that Mars was once much more Earth-like with a warmer, wetter climate.

The crust of Mars presents more such conundrums. A sharp contrast exists between the elevation and crustal thickness of the Northern plains and the Southern highlands. Moreover, the density of impact craters is much higher in Southern highlands than in the smoother, younger terrain of the North. This dramatic difference between the two hemispheres is known as the Martian crustal dichotomy and is one of the planet's most prominent and ancient features. Sitting on the edge of this dichotomy is Tharsis, an enormous elevated volcanic plateau. The evolution of this dichotomy remains unclear, with competing explanations of both endogenic and exogenic origins. It is also naively reminiscent of the oceanic-continental crustal diversity on Earth, with the bizarre confinement of continents to just one hemisphere. But, contrary to the Earth's granitic continental crust, the composition of the Martian crust is basaltic and resembles the Earth's oceanic crust. Mars also does not seem to have active plate-tectonics and is presumed to be surrounded by one single rigid plate that forms an outer shell of the planet.

The thickness of the crust has profound implications for a planet's present physical state and past evolution. It influences the rate at which heat is released to the surface and sets conditions for the rigour of mantle convection. A planet with plate tectonics dissipates internal heat by transporting it to the surface and radiating it through a thin lithosphere. A single lid planet, on the other hand, will cool down by lithosphere growth resulting in a thicker crust. Thus, a precise estimate of the Martian crustal thickness has fundamental

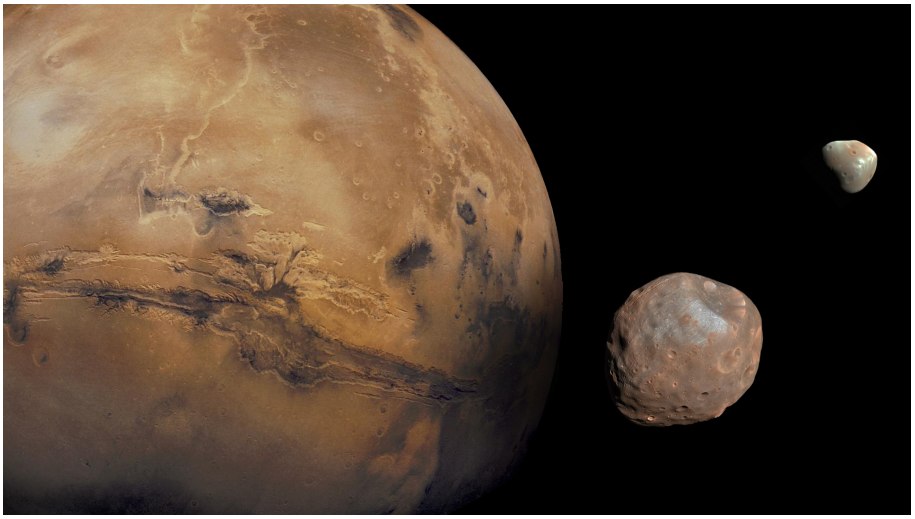

Figure 1.1: Mars and its two moons, Phobos and Deimos. Courtesy of NASA/JPL-Caltech

importance as it can help put better constraints on the planet's evolution, present and past plate-tectonic processes, and the origins of its hemispheric dichotomy. Previous estimates using gravity and topography data have high uncertainty as these could only constrain relative values. The estimated range of the crustal thickness lies between 30 and 115 km, with a mean thickness of 65 km. With in-situ surface observations now available through the seismometer on board the InSight mission, this thesis aims to develop and apply single-station seismic methods to measure the crust's thickness below the lander to within a few kilometres and reveal any possible crustal stratification.

1.1 Mars

The contents of this section have been compiled from Taylor (2009), Taylor and McLennan (2009), and Barlow (2014) unless otherwise indicated.

Mars is a complex, vast world with a long history of formation. Like other terrestrial planets, it is postulated to have been born in the inner half of a slowly rotating cloud of gas and dust, known as a proto-planetary disc, surrounding the early Sun. The extremely high temperatures within the disc cause all volatile elements like water to exist only in a gaseous state. With increasing solar activity, these elements migrate outwards to regions with lower temperatures. Only non-volatile elements such as metals and oxides of silicon and magnesium remain suspended in solid form in the inner regions. These slowly agglomerate by repeated collisions to form kilometre-sized objects called planetesimals, which are the building blocks of planets. With enough mass and gravity to attract more material, planetesimals undergo an accretion process that rapidly leads them to grow into planetary embryos. A final stage of planetary formation, the late accretion stage, consists of planetary embryos either increasing or decreasing in size due to impacts, similar to the events

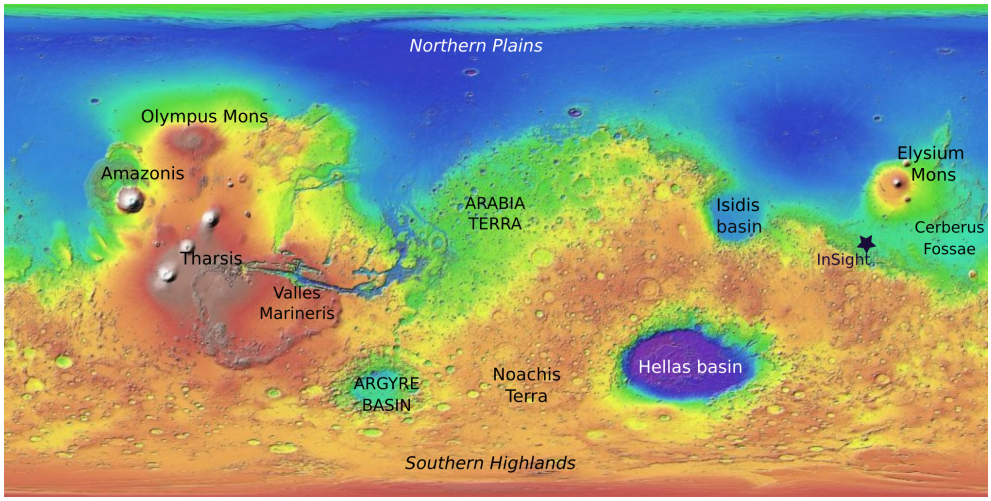

Figure 1.2: Topography map of Mars constructed from MOLA data indicating the hemispheric dichotomy and other relevant features. Lowest elevation is shaded in blue while highest elevation is shaded in white. Courtesy of NASA/JPL-Caltech

that lead to the formation of the Earth-Moon system. This last stage is mainly responsible for the planet's final characteristics like mass, size, and rotation rate. Current theories suggest that such a collision also led to the formation of the two martian moons, Phobos and Deimos. Figure 1.1 shows an image of Mars along with its moons.

With an average distance of 2.279×10^8 km from the Sun, Mars is the fourth planet in the Solar System, lying between Venus and Earth. It has an equatorial radius of 3397 km and is about half the size of Earth. A solar day on Mars, referred to as a Sol, is 24 h 39 m 35 s and is slightly longer than the Earth's, defined to be exactly 24 h. Like Earth, its rotation axis is tilted with respect to its orbital plane at an angle of 25.1°, and undergoes precession due to the gravitational perturbations from the Sun and other planets. This precession rate for Mars is rather unstable, and is presently -7576 ± 35 milli-arcseconds per year (Folkner et al., 1997), as calculated by Mars Viking and Pathfinder missions. The orbit of Mars around the Sun is also inclined at an angle of about 1.851° to the ecliptic plane, and its orbit is one of the most eccentric in the Solar System. This results in a significant difference in its perihelion and aphelion distances. Mars and Earth are aligned on the same side of the Sun and are the nearest to each other approximately every 779 Earth days. This serves as a cost-effective launch window for Mars expeditions.

The atmosphere is thin and made up of 95% carbon dioxide, 3% nitrogen, and 1.6% argon gases, along with trace amounts of oxygen, carbon monoxide, water, methane, and other noble gases. With a density of ~ 0.020 kg/m^3, its surface pressure is only about 1% of that of the Earth's and prohibits the existence of liquid water on the surface. It is debated whether the atmosphere was much thicker in the past, allowing liquid water to accumulate. The density of the atmosphere varies throughout the year, decreasing by about 25% during winters when the carbon dioxide partially freezes and settles into the polar caps. The daily

temperature range in the lower atmosphere varies considerably from $-75°$ to $0°$ near the surface. The upper atmosphere temperatures are also significantly lower than on the Earth as there is no stratospheric ozone layer on Mars. Massive convective vortexes often form on the surface due to heating and load vast volumes of dust particles into the air. These often form dust devils with diameters of tens of meters, extending to several kilometres in height. In addition, there are regular local and regional dust storms that cover the atmosphere and sometimes can even be seen on telescopic observations.

Martian topography has been determined by the Mars Orbiter Laser Altimeter (MOLA) with a vertical accuracy of ~ 1 m (Smith et al., 2001). As mentioned before, the most prominent feature of the Martian surface is the hemispheric dichotomy in crustal thickness topography and crater density between the young plains in the northern hemisphere and the older, elevated southern terrain. The northern lowlands comprise about one-third of the surface of Mars, with the southern highlands accounting for the other two-thirds. The separating boundary is complex and consists of three geologically-distinct regions: the Tharsis Province, fretted terrain and the chaotic terrain (Robinson, 1995). The Tharsis province consists of a volcanic plateau located at the western edge of the dichotomy boundary. Here we find the largest volcano in the Solar System - Olympus Mons (21.287 km in height), along with three enormous shield volcanoes. To the east of the Tharsis lies a canyon system stretching for about a quarter of the planet's circumference - Valles Marineris. Fretted terrain is characterized by abrupt and highly irregular escarpments, while the chaotic terrain comprises areas of deep fractured depressions that consist of polygonal blocks (Robinson, 1995; Pedersen, 2014). The origin of the crustal dichotomy is still debated, with main theories proposing either a low-angle giant impact or a degree-one mantle convection.

1.2 Interior

The accretion process leads to the formation of a homogeneous hot planet that gradually cools down over time. The two main contributions to this heat energy come from the accretion heating and compaction, and small quantities of radioactive elements contained within the planet that generate heat as they decay with time. This heat energy is sometimes enough to melt the planet entirely. At this point, the semi-fluid state of the planet allows high-density, iron-rich material to sink down towards the centre while the lower low-density material starts to rise to the surface. This allows materials to segregate into distinct layers in a process called differentiation. The primary reason for this is the density difference of materials and their chemical affinities. Thus, iron and siderophile elements like nickel (Ni), cobalt (Co), platinum (Pt), and iridium (Ir) settle at the centre to form the core. In contrast, lighter oxygen-affine lithophile elements like potassium (K), sodium (Na), calcium (Ca), and silicon (Si) rise to the surface to form the crust. This gives rise to a differentiated interior with a high-density core, intermediate-density mantle, and a low-density buoyant crust (Elkins-Tanton et al., 2003).

Early indications of Mars having such a differentiated interior predominantly came from geodetic data and the results of geochemical analysis of several meteorites believed

to have come from Mars. Geodetic data on the gravity field, shape, and rotation of a planet is usually derived from various landers and spacecrafts orbiting it. Radio science data from Doppler tracking of spacecrafts in orbit around Mars, such as Mars Global Surveyor (MGS), Mars Odyssey (ODY), Mars Reconnaissance Orbiter (MRO), and Mars Express (MEX), have been the primary source of this information. The gravity field depends on the three-dimensional distribution of mass within the planet and thus provides information on how density varies laterally and with depth. It is generally expressed in terms of spherical harmonic functions with lower degree terms describing the deep interior. With the estimates of mass, radius and precession rate or ellipsoidal flattening from these observations, the mean density and the mean moment of inertia of the planet can be calculated, which can further constrain the composition and density variations within the planet. The impact of tidal forces on a planet can also provide crucial information on the interior mass distribution, for example, the k2 Love number that describes the change in the second spherical harmonic coefficient of tidal potential on the body due to the gravitational influence of another.

For Mars, the gravity field has been accurately determined up to harmonic degree 120, corresponding to a horizontal surface resolution of about 215 km (Konopliv et al., 2016; Genova et al., 2016). Using precise orientation parameters including precession, pole location, and rotation rate from data spanning several decades (Le Maistre, 2013; Konopliv et al., 2011), a mean moment of inertia and k2 Love number have been calculated (Konopliv et al., 2016). Value for the principal moment of inertia has been previously estimated using the zonal harmonics of the radio Doppler tracking data along with measurement of the precession of the rotation axis (Folkner et al., 1997; Kaula, 1979). The SNC meteorites (short for shergottites, nakhlites, and chassignites), believed to be of Martian origin, are achondritic meteorites that derive from a basaltic crust (shergottites and nakhlites) and an olivine upper mantle (chassignites). Several techniques have been developed to extract a chemical composition of Mars using elemental correlations in the meteorites (e.g., Dreibus and Wänke (1984); Wänke and Dreibus (1994); Taylor et al. (2006)) and isotopic mass balance methods (e.g., Lodders and Fegley Jr (1997); Sanloup et al. (1999)). These provide important constraints on the timeline of the early evolution and differentiation (Lee and Halliday, 1997; Kleine et al., 2002) and have allowed calculations of mineralogy and areotherms of the Martian interior using analytical and experimental techniques (Bertka and Fei, 1997, 1998a; Fei et al., 2000). All these studies suggest Mars is a differentiated planet with a distinct crust, mantle and core. However, there is little consensus on the exact extent of these.

In the absence of seismic data, the gravity and topographic data analysis has been the primary source of information for the thickness of the crust and the lithosphere of Mars. The inversion of the gravity field alone is inherently a non-unique problem, hence it is only possible to infer properties of the crust and the lithosphere using some reasonable assumptions and the surface topography of the planet (Smith et al., 2001). Several approaches have been developed to this end. One method predicts a relationship between the average crustal thickness, the crustal density and the ratio of the geoid and topography (Wieczorek and Phillips, 1997), assuming an interior differentiated into a crust, mantle and core

with the thick southern crust being isostatically compensated by Airy mechanism. Based on the petrological properties of the SNC meteorites, Wieczorek and Zuber (2004) used conservative values for the density of the crust and mantle in the ranges 2700-3100 kgm^{-3} and 3400 –3550 kgm^{-3} and estimated the best-fitting average thickness of the highlands crust to lie between 53 and 68 km. Considering 1σ uncertainties, they concluded that the mean crustal thickness of Mars is 57 ± 24 km.

The ratio of the geoid and topography is generally known as admittance. Spectral studies of localized regions can result in a wavelength-dependent admittance function. These studies have also been employed previously to infer crustal properties like density and elastic thickness (e.g., Nimmo (2002); McGovern et al. (2002, 2004)). Here it is assumed that the planet's lithosphere acts as an elastic layer and responds to loads on the surface with compensatory deflections. For a given lithosphere thickness, models that match the observed surface topography can be constructed. From the line-of-sight observations of spacecraft acceleration over the southern hemisphere, McKenzie et al. (2002) constrained an effective compensation depth of less than 10 km and an associated elastic thickness of 14.5 km. A similar method employed by Nimmo (2002) constrained the crustal and elastic thicknesses of the dichotomy boundary to values within the range 1–79 km and 37–89 km, respectively. They further concluded an elastic plate model comprising two distinct crustal layers. McGovern et al. (2002) obtained values of 50 ± 12 km for Noachis Terra using spherical harmonic gravity field studies to calculate local admittance values. Turcotte et al. (2002) used a spatial approach and obtained a mean crustal thickness of 90 ± 10 km around the Hellas basin.

Another approach assumes that the observed gravitational field is exclusively the result of surface topography and relief along the crust-mantle interface. Using constant values for the density of the crust and mantle, and a mean crustal thickness, one can invert for the relief along the Moho (e.g., Wieczorek and Phillips (1998); Neumann et al. (2004)). This results in a global crustal thickness map without any assumptions on isostasy. Since the mean thickness itself is unknown, the thickness of the crust can be anchored to a specific value. In practice, the minimum estimate of the crustal thickness is usually set to an arbitrary value greater than 0. With gravity data from the Viking mission, Bills and Ferrari (1978) first used this technique and postulated the Hellas impact basin to be such a minimum-thickness region, and inferred a minimum globally averaged crustal thickness of 23–32 km. Zuber et al. (2000) used the MGS data, improved the crustal thickness maps to spherical-harmonic degree 60 and showed that the Isidis basin, and not Hellas, was the region of minimum crustal thickness. By setting the minimum crustal thickness to 3 km and assuming crust and mantle densities of 2900 and 3500 kgm^{-3} respectively, they deduced a mean crustal thickness of 50 km for Mars. Using a crustal density of 2900 kgm^{-3} with a contrast of 600 kgm^{-3} at the mantle, Neumann et al. (2004) reported a bimodal result with average crustal thicknesses of 32 km and 58 km for the northern and the southern hemispheres, respectively, and a mean global crustal thickness > 45 km.

The major uncertainties in these estimates result from the assumed densities of the crust and the mantle. For example, Goossens et al. (2017) constrained the average crustal density to be as low as 2582 ± 209 kgm^{-3} while McGovern et al. (2004) places the upper-

bound at 3100 kgm^{-3}. These differ significantly from the 2660 − 2760 kgm^{-3} range assumed by Khan et al. (2018). Pauer and Breuer (2008) provide a maximum density value of 3020 kgm^{-3} and argue that the mean crustal thickness can be as high as 110 km. Furthermore, it is also possible that the density of the crust has lateral variations, which introduces more uncertainty in the constraints given by gravity and topography measurements (e.g., Spohn et al. (2001); Plesa et al. (2016)). Other lose constraints on the Martian crustal thickness have been provided by the moment of inertia studies in conjunction with mineralogical constraints (e.g., Sohl and Spohn (1997); Bertka and Fei (1998a,b)). With such a large uncertainty in its value, it is, therefore, crucial to obtain an in-situ measurement of the crustal thickness of Mars. Such a measurement will also serve as an "anchor" point that can be used in conjunction with the existing gravity and topographic data to extract the global crustal thickness of the planet.

1.3 InSight mission

InSight, short for Interior Exploration using Seismic Investigations, Geodesy and Heat Transport, is a Mars lander designed for geophysical exploration of Mars (Banerdt et al., 2013). It successfully landed at the Elysium Planitia region of Mars on 26 November 2018 and has been in operation since then. The mission's main objective is to place a seismometer on the surface of Mars that would allow the investigation of its internal structure, which will further aid in understanding the formation and evolution of terrestrial planets. Apart from the moon, where the Apollo program in the 1960s previously deployed seismometers, InSight is the first successful seismic mission to another planet. Previous attempts of establishing a seismic network on Mars have been unsuccessful due to mission failures or instrument deployment problems. For example, the Mars 96 mission had two seismometers on board but failed to launch. In contrast, the Viking mission could not unlock the first seismometer and the second one provided no convincing event detection after 19 months of operation (e.g., Anderson et al. (1977); Surkov and Kremnev (1998)).

The three main instruments onboard the InSight lander are the Seismic Experiment for Interior Structure (SEIS) (Lognonné et al., 2019, 2020), the Heat Flow and Physical Properties Package (HP^3) (Spohn et al., 2018), and the Rotation and Interior Structure Experiment (RISE) (Folkner et al., 2018). SEIS monitors the planet's seismic activity and records the ground motion caused by seismic waves travelling through its interior. Using the lander's low gain X-band antennas to precisely track its location, RISE measures the rotation rate of Mars and its precession and nutation. These measurements will further enable tight constraints on the Martian core size, its density and state (liquid or solid). The HP^3 is now inactive but was designed to burrow 5 m into the subsurface and measure the thermal conductivity to constrain the heat flow out of the planet's interior. On 14 January 2021, the efforts to drill into the martian surface using the device were finally terminated due to friction between the soil and the probe being too low for the mole to hammer itself deeper than 40 cm (Spohn et al., 2022). In addition, the lander is equipped with a temperature sensor, pressure sensor, wind sensor (TWINS), and a magnetometer to

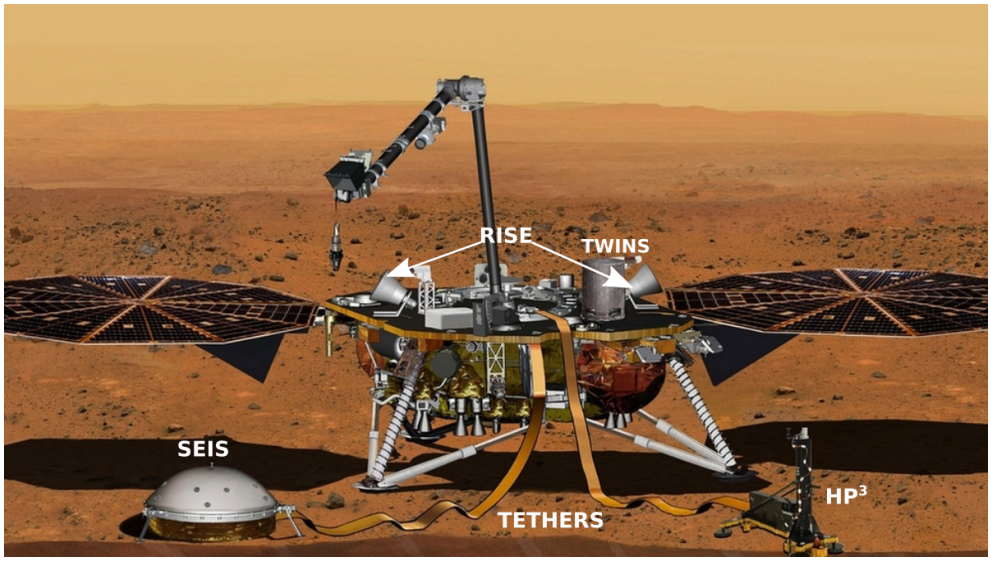

Figure 1.3: Artist's view of the InSight lander on Mars showing the SEIS, HP^3, RISE and TWINS instruments. Courtesy of NASA/JPL-Caltech

help decorrelate the seismic signals from atmospheric disturbances and measure magnetic potentials on the surface (Banfield et al., 2019). Figure 1.3 shows an artist's view of the InSight lander on Mars and the onboard instruments. HP^3 and SEIS were deployed on the surface by the robotic arm (Trebi-Ollennu et al., 2018) while the RISE is located on the lander.

With this set of instrumentation, the InSight mission aims to accomplish six primary science objectives (Banerdt et al. 2013):

- Determine the size, composition, and physical state of the core
- Determine the thickness and structure of the crust
- Determine the composition and structure of the mantle
- Determine the thermal state of the interior
- Measure the rate and distribution of internal seismic activity
- Measure the rate of impacts on the surface

This work aims to contribute to the fulfilment of the second scientific objective - to determine the thickness and structure of the crust. For this, the data from the seismic experiment suite SEIS has been used here. It consists of a three-component ultra-sensitive broad-band seismometer (VBB) and a co-located miniature three-component short-period seismometer (SP). Both of these are based on the principle of an inertial mass in suspension, which is excited into vibration by external forces. The VBB sensors are sensitive to

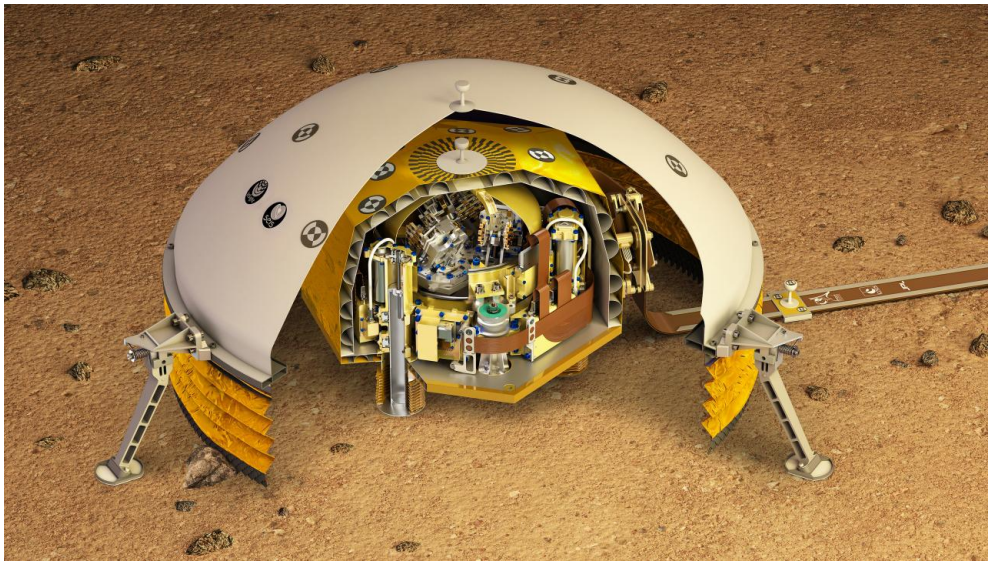

Figure 1.4: Cross-section image of the complete SEIS assembly. Courtesy of IPGP/D. Ducros

frequencies between 0.01 Hz and 10 Hz, and three SP sensors are sensitive to frequencies between 0.1 Hz and 50 Hz (Lognonné et al., 2019, 2020). This broad frequency range makes the VBB more suitable to detect distant marsquakes, while the SP is better capable of detailed analysis of regional events and lander-induced signals (Teanby, 2015). The VBB sensors are placed in a tetrahedron configuration inside a vacuum sphere, serving as a thermal protection layer. The SP sensors are placed around this sphere. This assembly rests on a motor-driven, three-legged, conical levelling system (LVL), specially designed to sink into the Martian regolith to form a solid mechanical coupling. These together comprise the sensor assembly (SA), which is further covered by a Wind and Thermal Shield (WTS), and connected to the electronic box inside the lander by a semi-rigid umbilical teether (Mimoun et al., 2017). SEIS is also equipped with internal heaters that can be activated when inside temperatures for any component drops below $-65°$ C. A schematic figure of the SEIS assembly can be seen in Figure 1.4

The six axes of SEIS have been continuously recording the seismic data since the deployment was completed. The VBB has a sample acquisition frequency of 20 samples per second (sps) while the SP records data at 100 sps. This data is stored in a flash memory inside the lander's electronic box before they are decimated and transmitted to SISMOC (SEIS on Mars Operations Center) at rates from 2 to 20 sps for continuous records and 100 sps for event records. After an initial inspection and basic technical processing (e.g. time stamp corrections and file format conversions) in near real-time, it is transmitted to mission support groups such as the Marsquake Service (MQS) (Ceylan et al., 2021). The MQS is an official service within the InSight community responsible for routine data monitoring for detecting seismic events, locating them, and curating a seismicity catalogue for Mars during the mission's lifetime (Clinton et al., 2018). With a specially developed suite

of single-station approaches and a prioiri interior models (e.g., Panning et al. (2015); Khan et al. (2016); Böse et al. (2017)), the MQS verifies a suspected event signal and calculates magnitude, distance, and location of the event, whenever possible. This information is then catalogued and communicated to the InSight team for further analysis.

1.4 SEIS continuous data

The VBB sensors have an oblique, non-Galperin configuration, recording ground motion in the U, V, and W coordinate system, while the SPs are aligned orthogonally in one vertical and two horizontal components. With data from different instrument packages, instrument sub-types, and gain, sampling rates and operating modes, InSight uses an extended version of the SEED (Standard for the Exchange of Earthquake Data) data format with a unique channel/location code combination for different data streams (Ceylan et al., 2021). Table 1.4 shows an example of the inventory code used to fetch VBB data. The main features of the continuous SEIS data have been documented in detail in Lognonné et al. (2020) and Ceylan et al. (2021). Due to very low self-noise, the SEIS VBB sensors have been able to record the lowest noise on the surface of a terrestrial body at periods between 5 and 20 seconds (Lognonné et al., 2020). Unlike Earth, where the seismic noise spectrum is dominated by ocean wave activity (e.g., Hasselmann (1963); Rhie and Romanowicz (2006); Tanimoto et al. (1998)), the seismic noise on Mars is $\sim$ 500 times lower than on Earth, reaching -200 dB in acceleration at night (Stutzmann et al., 2021). A typical Sol of seismic data on Mars shows three primary distinct noise regimes. From early morning until sunrise relatively weak laminar winds dominate the noise spectrum, followed by thermally-driven strong turbulent winds that last throughout the day until sunset. This noisy daytime eventually turns into extremely quiet evenings as the wind fluctuations settle until early morning (Banfield et al., 2020; Lognonné et al., 2020). Most marqaukes have been identified in this quiet period of the Sol. This picture can most clearly be expressed by Figure 1.5 where the stacked spectrograms from Sol 72 to Sol 478 show the evolving broadband background noise recorded by vertical component of the VBB along with the identified events. The event quality and family is further discussed in Section 1.5. The correlations of the seismic data with the wind and pressure sensors of the APSS package confirm that the martian atmosphere is the principal contributor to the noise spectrum.

Besides noise signals, several other sustained and transient signals of aseismic origin are observed in the continuous SEIS data. Figure 1.6 displays some of these as seen in the spectrogram of Sol 99 data. Here the most prominent of such features have been summarized. For a detailed description, the reader is referred to Scholz et al. (2020) and Kim et al. (2021).

- **Lander modes**: The spectrogram of the seismic data shows certain bands at various frequencies like 3.3 Hz, 4.1 Hz, 6.8 Hz, and 8.6 Hz. These are resonances of the InSight lander which have been consistent throughout the mission. Their frequency can vary with wind and temperature (Clinton et al., 2021; Dahmen et al., 2021b).

Instrument	Loc./Channel	Samp. rate	Details
VBB	02.MH [UVW]	2	VEL high gain SCI mode
	07.ML [UVW]	2	VEL low gain SCI mode
	17.ML [UVW]	2	VEL low gain ENG mode
	72.MH [UVW]	2	VEL high gain SCI mode
	03.BH [UVW]	2	VEL high gain SCI mode
	02.BH [UVW]	20	VEL high gain SCI mode
	00.HH [UVW]	100	ERP, high gain SCI mode

Table 1.1: Location and channel code used for VBB data. U, V and W denotes the three non-orthogonal components of of VBB. VEL: velocity, SCI: science, ENG: engineering, ERP: event request proposal

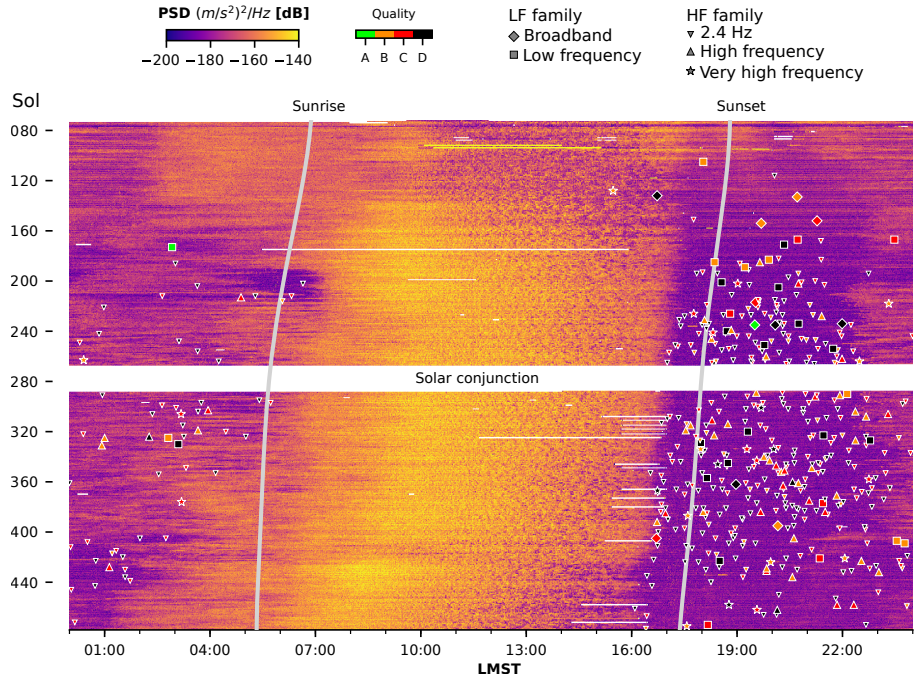

Figure 1.5: Stacked spectrograms showing evolving broadband background noise recorded by vertical component of VBB along with identified events. Event types are indicated by geometrical symbols and event quality by the colour. Sunrise and sunset times are indicated by grey lines and data gaps are displayed as white and yellow bars. The long data gap around Sol 280 is the conjunction period when SEIS was not operating. High noise levels are observed between sunrise and sunset. Quiet period is seen from sunset to early mornings. LMST stands for for Local Mars Solar Time. Figure adapted from Clinton et al. (2021)

- **Ticks**: Sustained artefacts at 1 Hz and their harmonics existing upto 6 Hz produced by the electrical cross-talk of various instrument components.

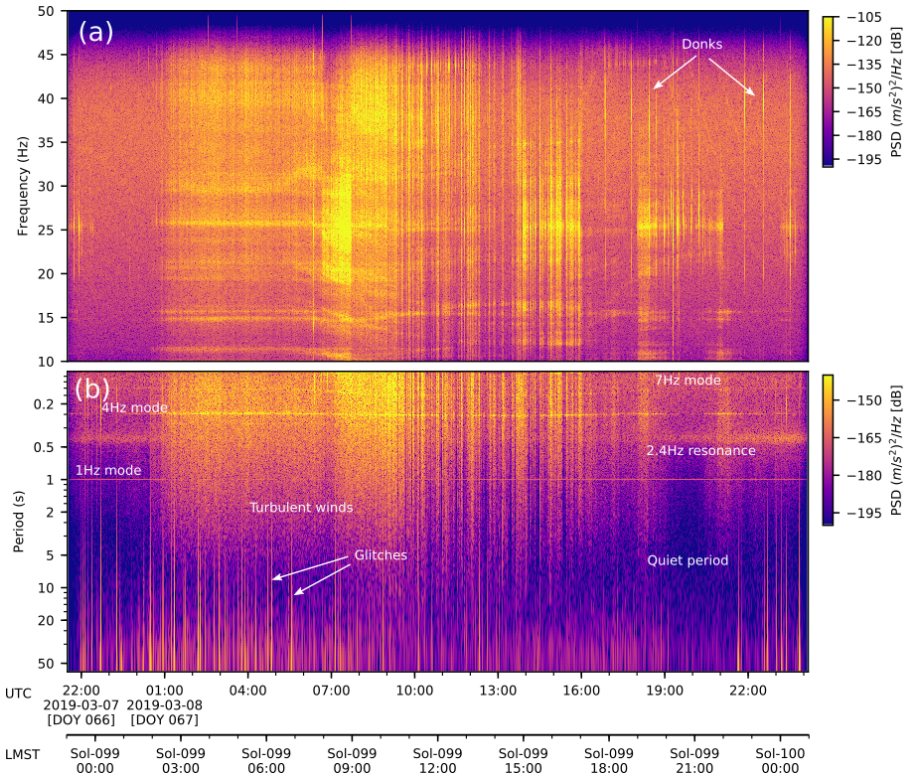

Figure 1.6: Vertical VBB acceleration spectrograms and average power spectral density (PSD) for Sol 99 showing various signals of aseismic origin that can be seen in data. (a) for frequencies between 10–50 Hz in a linear scale (b) for longer periods between 0.1 and 50 s in log scale. Figure adapted from (Ceylan et al., 2021)

- **2.4 Hz resonance**: A sustained broad resonance band around 2.4 Hz that is unaffected by wind speed and temperature variations. The exact origin of this is not yet clearly understood but appears to be related to the subsurface structure (Hobiger et al., 2021). It is systematically excited by seismic waves and amplifies the observed seismic signals (van Driel et al., 2021).

- **Glitches**: Transient instrumental self-noise appearing as a high-amplitude, one-sided pulse. The time duration of these is related to the instrument's transfer function and has been modelled as a step function in acceleration convolved with instrument response (Scholz et al., 2020; Ceylan et al., 2021). Glitches are the most common types of anomaly seen on the VBB data.

- **Donks**: High frequency ($\sim$ 12 Hz) pulses of energy burst that excite all the lander modes and can be observed simultaneously on all the components of SEIS. They have a duration of a few seconds and resemble a waveform pattern of micro quakes.

In addition, there are disturbances injected by the turbulent martian environment, despite the additional deployment of the WTS to isolate exterior effects from seismic signals.

For example, there are regular transient drops in the pressure sensor due to dust devils whose signatures appear as tilt effects on the seismic data. Evening rumbles also appear in the frequency-domain data and can mimic low events with low-frequency content and long duration, often 2-3 hours. These artefacts and injections must be isolated and taken care of before any analysis for sub-surface structure is performed using the SEIS data. The InSight science team has endeavoured to present pitfalls and corresponding methodologies associated with these features. For example, Kim et al. (2021) attempt to provide some basic guidance to make robust interpretations from the data by taking into account these idiosyncrasies which manifest in waveforms and noise correlograms. Similarly, Scholz et al. (2020) present various methods and algorithms to detect and remove the glitches that contaminate the SEIS data.

1.5 Martian seismicity

Mars does not currently possess active plate tectonics and is considered a stagnant lid planet. However, theoretical studies have suggested some level of active seismicity on Mars resulting from surface faulting (e.g., Golombek et al. (1992); Knapmeyer et al. (2006)) and lithospheric thermo-elastic cooling (Phillips and Grimm, 1991). These studies predict the seismicity level of Mars to lie somewhere between that of the intraplate activity of Earth and the shallow quake seismicity of the moon. There have been past indications of ongoing seismic activity in the Cerberus Fossae region based on the bolder trails assumed to be originating from marsquakes (Knapmeyer et al., 2006; Roberts et al., 2012). Meteorite impacts have been another expected source of seismicity on Mars. They could provide further constraints if their location could be identified using orbital imaging, making them an essential part of the analysis.

With a highly sensitive broadband seismometer currently active on Mars, InSight is now providing us with unprecedented information about its true seismicity levels. As of 1st June 2022, the MQS has identified and catalogued 1244 marsquakes since the beginning of its operation (InSight Marsquake Service, 2022). Most events are generally low in amplitude and were identified in the quiet early evening hours up to midnight. Each quake is named after the solar day it was observed, followed by a letter (a, b, c, etc.) in case there were multiple events on that particular day. Marsquakes are further categorised into different families, depending on their type and quality. The event type reflects the signal's frequency content, the primary types being low-frequency and high-frequency. They are distinguished based on the 2.4 Hz resonance mode. The low-frequency family consists of low-frequency (LF) and broadband (BB) events. The energy content of LF events is predominantly below 1 Hz, while BB events have energy content up to 2.4 Hz. These events are similar to those observed on Earth and occur at teleseismic distances (Brinkman et al., 2021). The high-frequency family consist of high frequency (HF), very high frequency (VF), and 2.4 Hz events which have energy predominately around 2.4 Hz and above. These events have highly scattered waveforms, making their analysis more complex than their low-frequency counterparts. The propagation of HF events is believed to be restricted to the crust that

Event Type	Details
Low Frequency (LF)	Energy in all three components below 2.4 Hz
Broadband (BB)	Energy in all three components predominantly below 2.4 Hz but excite the 2.4 Hz resonance
2.4 Hz	Energy in all three components centered around the 2.4 Hz resonance
High Frequency (HF)	Energy in all three components predominantly at and above 2.4 Hz
Very High Frequency	Special case of VF events with horizontal energy significantly larger than vertical energy at higher frequencies
Super High-Frequency (SF)	Very short duration high frequency events with energy in range 5-10 Hz

Table 1.2: Characteristics of the different types of events as defined by the MQS. The Low Frequency and High Frequency families are separated to show their respective sub-families.

acts as a waveguide (Giardini et al., 2020; van Driel et al., 2021) for the energy. More than 90% of the total events fall into this category. In addition, a separate independent family is defined for events of unusual characteristics with very high energy content in the range of 5-10 Hz and short duration ($\sim 20s$), called Super High Frequency (SF) events. With their origin linked to the local thermal cracking of the crust (Dahmen et al., 2021a), there are more events in this family than in LF and HF families combined, totalling 1291 events. A summary of all event families is provided in Table 1.2.

Further, an event quality is assigned to each event based on the strength of the signal and the ability to identify and interpret various phase arrivals (Giardini et al., 2020). The event quality classifies the seismic events into four categories: Quality A for events with a high signal-to-noise ratio (SNR) with multiple clear and identifiable phase arrivals and clear polarisation. This indicates that a location for the event can be determined. Quality B is for events with medium SNR with multiple clear phase arrivals but no clear polarisation. These events cannot be located with a single station. Quality C is for events for low SNR events with either no phase arrival or a single-phase arrival identified. Quality D is maintained for signals that are almost indistinguishable from noise. Only a handful of events (10) have been assigned Quality A, and their locations are well constrained. Most of these originate in the general Cerberus Fossae region at 30° distance from InSight (Giardini et al., 2020; Clinton et al., 2021) which is believed to have had recent volcanic activity (Vaucher et al., 2009). Owing to their highly scattered waveform, none of the events belonging to the high-frequency family has yet been located (van Driel et al., 2021).

The magnitudes of Quality A events range between 1 and 4, with an uncertainty of ± 0.4 (Clinton et al., 2021). A detailed description of the method of calculating moment magnitudes for marsquakes is available in Böse et al. (2018). One peculiar feature of marsquakes is that they generally do not contain surface wave arrivals. Few exceptions have been observed so far, most of which have been associated with a meteorite impact. However, orbital techniques have not imaged an impact crater for all these events. Based

on the identified locations of the LF events, marsquakes seem to be predominantly related to tectonically induced stresses and thermo-elastic cooling. It should be noted that the observed seismic activity on Mars till now is comparable to that estimated previously by Golombek et al. (1992) and Knapmeyer et al. (2006). Like earthquakes, many marsquakes show evidence of aftershocks with characteristics similar to those of the mainshock (Giardini et al., 2020). However, unlike earthquakes that closely follow the Gutenberg-Richter magnitude law and have random time distribution, the HF events on Mars also show some evidence of seasonality which associates them with variations in solar illumination, the CO_2 ice cycle and solar tides (Knapmeyer et al., 2021; Dahmen et al., 2021a).

1.6 Methods

1.6.1 Receiver Function Analysis

Analyzing the Martian interior structure using the data from the InSight mission requires special methods that utilize only a single sensor. These so-called "single-station techniques" are well-established and have previously been used to infer properties of the Earth, although new array-based methods involving numerous broadband sensors have recently become more common with the increase in terrestrial coverage of seismic networks. One widely used single-station technique is the Receiver Function (RF) analysis (Langston, 1979). The RF technique uses teleseismic body waveforms to image the crustal structures directly beneath seismic stations or receivers. The seismic wavefield inside an isotropic, layered media consists of one compressional P-wave component and two shear (SV and SH) wave components, all of which differ in particle motion. The principle behind the RF technique is that apart from reflection and refraction, the P-waves give rise to converted S-waves and vice-versa when they interact with a velocity discontinuity. For horizontally-layered structures, all converted P-wave energy results only in SV phases that can be observed on the radial component of the seismic data. For anisotropic and dipping structures, P-to-SH conversions are commonly observed along with the SV conversions (Levin and Park, 1998).

These parent and converted phases differ in their velocity. They, therefore, arrive at the station with a time-lag that depends on the depth to the seismic discontinuity, velocity of the layer above, and the distance of the teleseimic event from the station (i.e., ray parameter). If the velocity of the above layer is known, this time-lag can lead to an estimate of the depth to the discontinuity that produced the converted phases. In addition to the converted wave, we also commonly observe their multiples which can further help constrain the interface depth as both the depth and the velocity of the above layer are usually unknown. Figure 1.7 illustrates this in the case of a layer over a half-space with an incident P-wave giving rise to converted S-waves. Mathematically, for a P-to-S conversion, the time separation between the direct and the converted wave, t_{Ps}, is provided by:

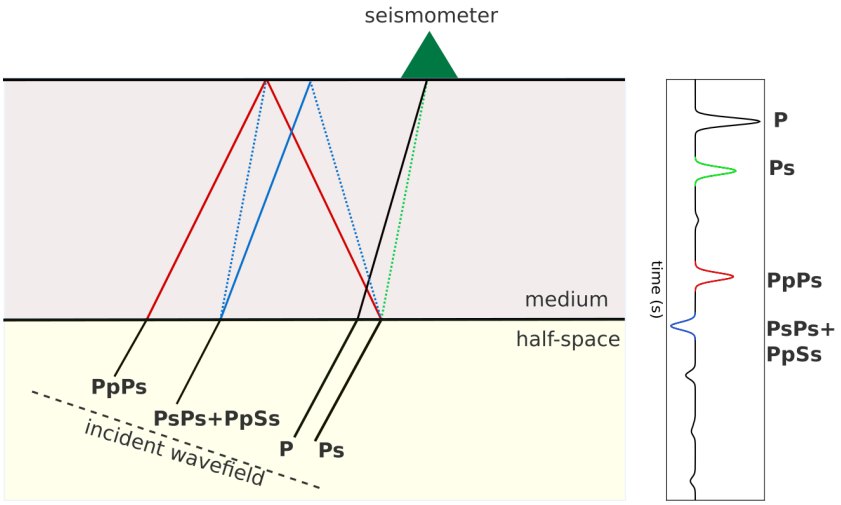

Figure 1.7: Theoretical ray paths and RF waveform for a layer-over half-space model. Note that Ps is a direct conversion, while PpPs, PpSs, and PsPs are generated by multiple reflections

$$t_{Ps} = H\left(\sqrt{\frac{1}{V_s^2} - p^2} - \sqrt{\frac{1}{V_p^2} - p^2}\right) \tag{1.1}$$

Similarly, for the multiply converted phases, PpPs,PpSs and PsPs, the time separation can be expressed as:

$$t_{PpPs} = H\left(\sqrt{\frac{1}{V_s^2} - p^2} + \sqrt{\frac{1}{V_p^2} - p^2})\right) \tag{1.2}$$

$$t_{PpSs+PsPs} = 2H\left(\sqrt{\frac{1}{V_s^2} - p^2}\right) \tag{1.3}$$

Here, H, V_s, V_p, and p denote the layer thickness, S-wave velocity, P-wave velocity and the ray parameter, respectively. A similar set of equations describe the Sp arrival and its multiply reflected reverberations relative to the parent S-wave arrival.

Figure 1.7 shows the synthetic case with only direct and converted phases in the signal. However, there is a lot more complexity in a real seismogram generated by a complex earth structure, making it challenging to identify these low-amplitude converted phases. To isolate the impulse response of the crust and the upper-mantle near the receiver location, other unwanted contaminations such as distant structural variations, path effects, etc. should be removed from the raw data (e.g., Vinnik (1977)). Assuming a convolutional

model, different components of the seismic record can be effectively used to cancel these common features. This convolutional model describes the recorded wavefield as the convolution of the source-signal of the event with different operators that affect this signal from the origin-time to its arrival at the seismic station. Receiver functions are then described as the time series obtained from three-component seismic data by removing source and path effects to isolate the vertically-varying velocity structure beneath the receiver. The components that contribute the most to the convolutional representation are:

- **Near Source Effects (N_s)**: Seismic waves emanating from the source first interact with the local structure in the vicinity of the hypoceneter. These effects include surface reflections, their reverberations and internal reflections produced by strong seismic interfaces.

- **Path Effects (P)**: Teleseismic events sample the planet along specific ray-paths and are affected by lateral variations in seismic velocity, multi-path effects, small scale heterogeneity, geometrical spreading, and frequency dependent anelasticity. During their propagation, these effects are picked up by the waves causing distortion in phase, amplitude, and energy content.

- **Near Receiver Effects (N_r)**: The structure in the vicinity of the seismic station has the most dominant effect on the recorded signal. These effects primarily include reflections from the seismic discontinuities below, their multiples, sedimentary reverberations. This is the component of the signal we are interested in.

- **Instrument response (I_p)**: Recording seismic signals involves the conversion of a mechanical and electrical response to a unit of displacement or velocity. This response varies for different sensors and should be taken into account during the analysis of seismic data.

The linear system theory is often used to describe an observed seismic signal produced by a source using the principle of superposition (Lay and Wallace, 1995). Here, the response at any point in space can be represented by a set of cascaded linear systems acting on the source-time function S(t). The three components of ground motion can then be written as a convolution operation:

$$u_V(t) = S(t) * N_s * P(t) * N_{r_V} * I_p(t) \tag{1.4}$$

$$u_R(t) = S(t) * N_s * P(t) * N_{r_R} * I_p(t) \tag{1.5}$$

$$u_T(t) = S(t) * N_s * P(t) * N_{r_T} * I_p(t) \tag{1.6}$$

Here u_V indicates the vertical, u_R the radial component on the great circle between the source and the receiver, u_T the tangential component in the horizontal plane and t

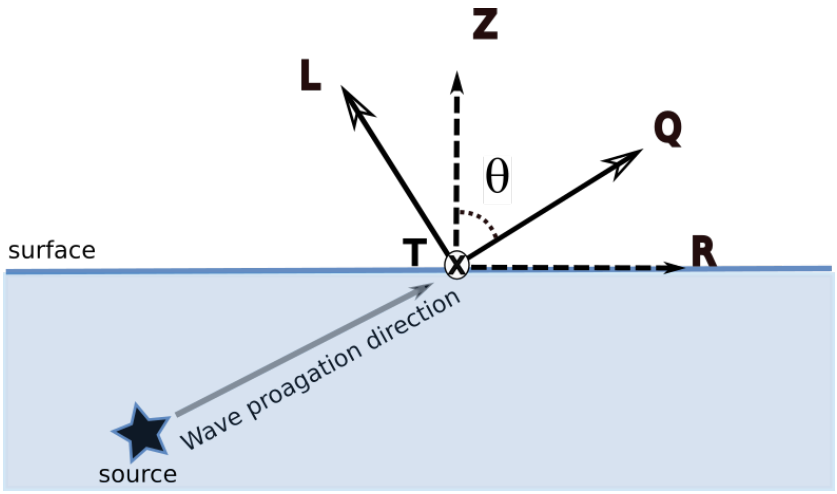

Figure 1.8: Rotation of the ZRT into LQT coordinate system through the angle of incidence θ

represents the time. This can be written in the frequency-domain using the multiplicative property of Fourier Transforms:

$$u_V(\omega) = S(\omega) \times N_s \times P(\omega) \times N_{r_V} \times I_p(\omega) \tag{1.7}$$

$$u_R(\omega) = S(\omega) \times N_s \times P(\omega) \times N_{r_R} \times I_p(\omega) \tag{1.8}$$

$$u_T(\omega) = S(\omega) \times N_s \times P(\omega) \times N_{r_T} \times I_p(\omega) \tag{1.9}$$

with ω representing the angular frequency. The various components of ground motion recording can also be expressed in the ray-coordinate system (LQT or P-SV-SH system). This is achieved by rotating the Z and R components into L and Q using the polarization angle of the incident P-wave, as shown in Figure 1.8. The L-component indicates the direction of the incoming P-wave and contains mainly P-wave energy, while the Q and T components include the SV and SH energy, respectively. This work has adopted the ZRT coordinate system.

A deconvolution operation of various components with each other can now eliminate the common terms. This operation is called "source-equalization" as termed by Langston (1979). To emphasize the converted S-waves, the radial component is usually deconvolved with the vertical component resulting in the radial P-receiver function. This leads to the emergence of N_{r_R} term among all the other contributions. Similarly, the deconvolution of the transverse component from the vertical leads to the emergence of the N_{r_T} term, giving the transverse component of the P-receiver function. The vertical component of the receiver function is ideally a spike located at the incident P-wave arrival time, usually re-scaled to 0 time ($t = 0$) to define a relative time-scale between the direct and various

converted phases.

$$RF_R = \frac{u_R(\omega)}{u_V(\omega)} = \frac{N_{r_R}}{N_{r_V}} \tag{1.10}$$

$$RF_T = \frac{u_T(\omega)}{u_V(\omega)} = \frac{N_{r_T}}{N_{r_V}} \tag{1.11}$$

Various methods have been proposed for the implementation of the deconvolution operation (e.g., Phinney (1964); Langston (1979); Owens et al. (1987); Kind et al. (1995); Menke (1984)). For details and comparison of various methods, the reader is referred to Pesce (2010). In this work, the time-domain deconvolution technique based on Wiener Filtering (Kind et al., 1995) has been utilized. A time-domain Wiener filter is computed using the P-wave signal on the vertical component, such that it transforms the complex P-wave signal into a band-limited spike. The R and T components are then folded with this filter to obtain the vertical and transverse RFs. The Wiener filter is estimated using the built-in function "spiking" of the Seismic Handler package (Stammler, 1993).

Phinney (1964) was one of the first to use the RF technique using teleseismic P-waves to analyze the crustal structure beneath stations at Albuquerque and Bermuda using the ratio of the vertical and horizontal component spectrum. (Langston, 1979) later modified the processing technique and used time-domain deconvolution to study the structure beneath stations at Mount Rainier in Washington. Owens et al. (1987) introduced a linearized time-domain inversion technique of RF waveforms to estimate the crustal structure using data from broadband sensors. Ammon (1991) added correction by introducing a method to estimate absolute RF amplitudes and showed a decrease in the amplitude of converted phases with epicentral distance. Since then the RF method has been extensively used in various settings to the study the crust (e.g., Kind et al. (1995); Park and Levin (2000); Sheehan et al. (1995); Grad et al. (2009); Geissler et al. (2010)) and the upper mantle (e.g., Farra and Vinnik (2000); Levin et al. (2002); Lawrence and Shearer (2006); Andrews and Deuss (2008); Ozacar et al. (2008)). S-wave RFs have been widely used to study the Moho depth and the lithosphere-aesthenosphere boundary of the earth (e.g., Yuan et al. (2006); Savage and Silver (2008); Geissler et al. (2010); Kind et al. (2012); Knapmeyer-Endrun et al. (2017)). Various strategies have also been proposed for inferring seismic anisotropy of the crust and upper-mantle using the RF waveforms (e.g., Levin and Park (1997); Savage (1998); Bianchi et al. (2010); Schulte-Pelkum and Mahan (2014)). In the context of extra-terrestrial seismology, the use of RFs has been limited to the Moon due to a lack of successful seismic missions to other planetary bodies (e.g., Vinnik et al. (2001); Lognonné et al. (2003); Gagnepain-Beyneix et al. (2006)). In this study, we show the application of receiver function analysis to the InSight seismic data for inferring the properties of the Martian crust.

1.6.2 Apparent S-wave velocity

For a P-wave arriving at a station, an apparent incidence angle can be defined by analysing the particle motion of the three-component seismic data. This particle motion recorded at

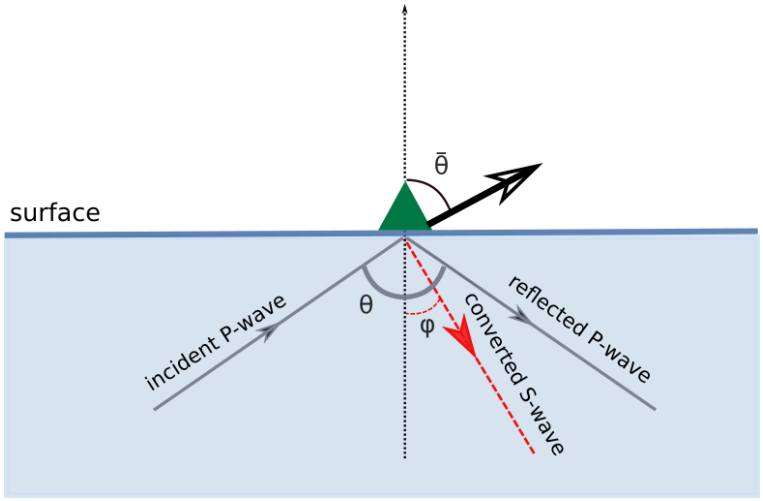

Figure 1.9: Schematic representation of the relationship between the true incidence angle θ and the apparent incidence angle $\bar{\theta}$

the surface results from the superposition of the incoming P-wave and two outgoing waves - the P-wave reflected off the free surface and the converted Ps wave. As a result, the apparent incidence angle at the sensor is different from the true P-wave incidence angle. Figure 1.9 shows this schematically. To quantify this, consider a P-wave travelling in the x-y plane, arriving at an incidence angle θ to the vertical. Assuming ϕ as the S-wave angle to the vertical, and α and β as the P and S-wave velocities of the medium, the total displacement u^P can be written as:

$$u^P(x,y,t) = U^P(\sin\theta\hat{\mathbf{x}} - \cos\theta\hat{\mathbf{y}})\exp\left[i\omega\left(\frac{\sin\theta}{\alpha}x - \frac{\cos\theta}{\alpha}y - t\right)\right] \tag{1.12}$$

$$+U^P(\sin\theta\hat{\mathbf{x}} + \cos\theta\hat{\mathbf{y}})\acute{P}\grave{P}\exp\left[i\omega\left(\frac{\sin\theta}{\alpha}x + \frac{\cos\theta}{\alpha}y - t\right)\right]$$

$$-U^P(\cos\phi\hat{\mathbf{x}} - \sin\theta\hat{\mathbf{y}})\acute{P}\grave{S}\exp\left[i\omega\left(\frac{\sin\phi}{\beta}x + \frac{\cos\phi}{\beta}y - t\right)\right]$$

Here U_P is the amplitude of the incident P-wave, ω is the angular velocity and $\acute{P}\grave{P}$ and $\acute{P}\grave{S}$ are the P-to-P and P-to-S reflection coefficients. $\hat{\mathbf{x}}$ and $\hat{\mathbf{y}}$ denote the unit vectors along the x and y directions. For a sensor placed at the free-surface, $y = 0$. In this case, the equation reduces to:

$$u^P(x,0,t) = U_P\left\{\left[(1+\acute{P}\grave{P})\sin\theta + \acute{P}\grave{S}\cos\phi\right]\hat{\mathbf{x}} + \left[(-1+\acute{P}\grave{P})\cos\theta - \acute{P}\grave{S}\sin\phi\right]\hat{\mathbf{y}}\right\}\exp[i\omega(px-t)]$$

Here p denotes the ray parameter given by the Snell's law: $p = \frac{\sin\theta}{\alpha} = \frac{\sin\phi}{\beta}$

$$\tan\bar{\theta} = \frac{(1 + \acute{P}\grave{P})\sin\theta + \acute{P}\grave{S}\cos\phi}{(1 - \acute{P}\grave{P})\cos\theta + \acute{P}\grave{S}\sin\phi} \tag{1.13}$$

Aki and Richards (2002) derive the forms of $\acute{P}\grave{P}$ and $\acute{P}\grave{S}$ using the free-surface boundary condition

$$\acute{P}\grave{P} = \frac{-A + B}{A + B}$$

and

$$\acute{P}\grave{S} = \frac{C}{A + B}$$

where $A = \left(\frac{1}{\beta^2} - 2p^2\right)^2$, $B = 4p^2\frac{\cos\theta}{\alpha}\frac{\cos\phi}{\beta}$ and $C = 4p\frac{\cos\theta}{\beta}\left(\frac{1}{\beta^2} - 2p^2\right)$
Substituting for these in equation 1.13, we get

$$\tan\bar{\theta} = \tan 2\phi \tag{1.14}$$

which leads to the result,

$$\bar{\theta} = 2\phi \tag{1.15}$$

Further, using the Snell's law, its straight forward to derive the relation:

$$\bar{\theta} = 2\arcsin(\beta p) \tag{1.16}$$

This shows that the apparent P-wave incidence angle measured at the sensor does not depend on the P-wave velocity of the medium (v_P), but solely on the S-wave velocity v_S. This result was first derived by Wiechert and Zoeppritz (1907). Here, the derivation from Park and Ishii (2018) has been adapted. Equation 1.17 can be rearranged to express v_S as a function of the apparent P-wave incidence angle. v_S is relabelled as $v_{S,app}$ to emphasize its dependence on the apparent P-wave incidence angle rather than the true angle of incidence.

$$v_{S,app} = \frac{\sin(0.5 i_p)}{p} \tag{1.17}$$

The polarization angle of body waves has traditionally been calculated by measuring the particle motion on the vertical (Z) and radial (R) component of three-component seismic data using specific time windows around their arrival time. Svenningsen and Jacobsen (2007) proposed a method to directly estimate the apparent incidence angle using RFs instead of the raw waveform data to minimize the contamination from the P-wave complexity. Here they estimate the apparent P-wave incidence angle from the amplitudes of vertical (ZRF) and radial receiver functions (RRF) at time t=0 using the relation:

$$\tan\bar{i_p} = \frac{RRF(t=0)}{ZRF(t=0)} \tag{1.18}$$

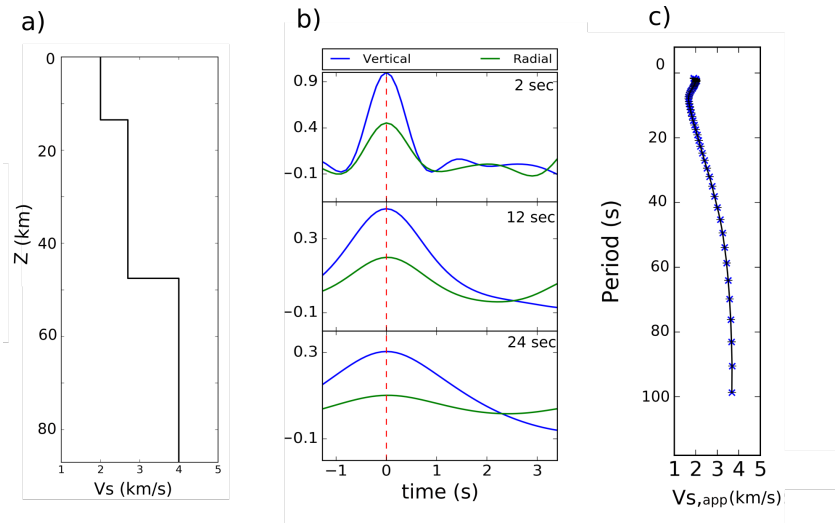

Figure 1.10: (a) An example crustal model showing V_s profile (b) Vertical and Radial RFs at different filter periods. The red, dashed-line represents the P-wave arrival. (c) $v_{S,app}$ curve derived from the ratio of Vertical and Radial RFs at filter periods up to 100 s

By successive filtering at increasingly longer periods (T), the variations of the apparent incidence angle as a function of the filter period (T) can be estimated. Then, using equation 1.17, this can be transformed into a frequency-dependent apparent S-wave velocity profile $v_{S,app(T)}$. Larger T implies that more multiples at later times influence the values of the filtered receiver functions at t=0, sampling increasingly deeper subsurface velocities. For this, Svenningsen and Jacobsen (2007) proposed the use of low-pass cosine filters with increasing, logarithmically distributed corner frequencies to emphasize the $v_{S,app}$ variations. Following Hannemann et al. (2016), a set of second-order zero-phase Butterworth low-pass filters was used to estimate the variation of $v_{S,app}$ with period. The corner periods of the filters are selected to be logarithmically distributed, and periods smaller than the dominant period of the spike on the ZRF are discarded to avoid measurements at periods shorter than the corner period of the event's source spectrum. Figure 1.10 graphically displays the procedure of estimating $v_{S,app}$ for an example crustal model with Moho depth of 50 km. The suitability of the application of $v_{S,app}$ curves to Mars along with depth-sensitivity profiles has been studied in detail by Knapmeyer-Endrun et al. (2018). They successfully apply the method to Martian synthetic and terrestrial data from various geological settings using a grid-search procedure on the parameter-space. This thesis closely follows their work and uses $v_{S,app}$ in conjunction with RF data and Monte-Carlo sampling schemes.

1.6.3 Inverse Problem

For a physical system, the 'forward' problem involves using a physical theory to predict an outcome of a series of possible experiments. For example, in seismology, given some parameters for an interior mode (v_S, depth, v_p/v_S ratio, attenuation, etc.) and a source, the

forward problem will use the theory of seismology to calculate the observed seismograms at different places on the surface of a planet. This is mathematically represented as:

$$\mathbf{d}_{obs} = G(\mathbf{m}) \tag{1.19}$$

The observed data, $\mathbf{d}_{obs}$, can be regarded as a projection of the model through a function G. The 'inverse problem', on the other hand, consists of estimating a suitable model for the planet's interior, given a set of seismic observations or seismograms. Thus, the problem involves finding a model, $\mathbf{m}$ that corresponds to some observed data $\mathbf{d}_{obs}$

$$\mathbf{m} = G^{-1}(\mathbf{d}_{obs}) \tag{1.20}$$

Often G^{-1} is highly non-linear and not available in an analytical form. In this case, G can represent the result of an algorithm that allows the calculation of data based on given model parameters. The RF inverse problem also falls into this category. Various methods have been proposed in the literature to estimate a solution to this problem.

One way is to linearize the problem around some reference model using a Taylor expansion and seek a damped least-square solution using a gradient-based, iterative approach (e.g., Owens et al. (1987); Ammon et al. (1990); Wilde-Piorko et al. (2002); Mangino et al. (1993)). The solution may or may not converge or converge to a local minimum and shows a strong dependence on the starting model. Kosarev et al. (1987) and Kind et al. (1995) proposed the use of Tikhonov and Arsenin (1979) approach of tying the solution to an a priori model for stability. For simple models, a brute-force grid-search approach was introduced by (Zhu and Kanamori, 2000). This, however, proves inadequate for crustal models comprising dipping interfaces and several layers. Techniques utilizing global search algorithms such as simulated annealing and its variants based on physical annealing process (e.g., Zhao et al. (1996); Vergne et al. (2002); Vinnik et al. (2004)), and genetic algorithm based on analogy with biological evolution (Shibutani et al. (1996); Levin and Park (1997)) were later introduced to infer subsurface structure from the RF waveforms. Both of these techniques belong to a wider class of algorithms known as Monte-Carlo methods and provide a possible methodology for RF inversions to avoid solutions trapped in local minima of the objective function. However, a full analysis of the model parameter uncertainties in the inversion results is difficult and remains limited to only a few cases.

The inversion of RFs is also inherently a non-unique problem. Non-uniqueness arises because of the higher sensitivity of RFs to S-wave velocity contrasts than to the absolute values. This is usually referred to as a velocity-depth trade-off that makes shallower low-velocity models and the deeper, high-velocity models fit the data equally well (e.g., Ammon et al. (1990); Julià et al. (1998); Frederiksen et al. (2003); Jacobsen and Svenningsen (2008)). One solution to reduce this non-uniqueness is the simultaneous inversion of RF data with other independent datasets with different sensitivities like gravity (e.g., Lawrence et al. (2006); England and Ebbing (2012); Chai et al. (2015)), surface-wave dispersion (e.g., Özalaybey et al. (1997); Du and Foulger (1999); Julia et al. (2000); Chang et al. (2004)) and Rayleigh wave ellipticity (Chong et al., 2016). Successful implementation of these techniques is encouraging and usually reduces non-uniqueness and improves model

resolution. To deal with the RF non-uniqueness, the joint inversion of the RF data with frequency-dependent S-wave velocity curves is proposed here. Previous studies have been limited to terrestrial data, and only a few implement a joint inversion of receiver functions and P-wave polarisation (e.g., Kieling et al. (2011); Schiffer et al. (2016, 2019, 2022)). Such a joint inversion approach is applied here to data from the InSight mission using two Monte-Carlo-based global sampling methods - (i) The Neighbourhood Algorithm, (ii) Transdimensional reversible-jump Markov-chain Monte Carlo (rj-McMC) Method

To estimate full uncertainties of the model parameters, a Bayesian approach to the inverse problem has been adopted (e.g., Tarantola and Valette (1982); Mosegaard and Tarantola (1995)). The basic idea is to represent all information in a probabilistic formulation. Given some prior information about the system expressed as a probability distribution, $p(\mathbf{m})$, the aim is to quantify the posterior distribution of the model parameters, $\mathbf{m}$, given some observed data, $\mathbf{d}$. This posterior distribution is then expressed as a joint probability density, $p(\mathbf{m}|\mathbf{d}_{obs})$, over the full range of the parameter space. The Bayes' rule (Bayes, 1763) is then used to combine the likelihood of observing the data with the prior distribution to define a joint posterior probability density function of the model parameters:

$$p(\mathbf{m}|\mathbf{d}_{obs}) \propto p(\mathbf{d}_{obs}|\mathbf{m})p(\mathbf{m}) \tag{1.21}$$

The term $p(\mathbf{d}_{obs}|\mathbf{m})$ is called the likelihood function and describes the goodness of fit of a model to the observed data. Its exact form depends on the definition of the misfit function and hence, the assumed distribution of the data noise. In the following, the essence of the sampling algorithms that have been used in this study are briefly described. For full details, the reader is referred to Sambridge (1999), Mosegaard and Tarantola (1995) and Bodin et al. (2012)

The Neighbourhood Algorithm

A fully nonlinear, derivative-free, direct-search algorithm referred to as 'The Neighbourhood Algorithm' (NA) was proposed in Sambridge (1999). It uses nearest-neighbour regions called Voronoi cells to tessellate the parameter space and model the misfit function. The misfit within each cell is assumed to be constant, and with each iteration, the sampling gets concentrated in cells where the computed misfit value is lower than the rest. Thus the random generation of samples is guided by the previous computations toward more promising regions. The algorithm has only two tuning parameters: N_s, the number of tessellations produced in each iteration and N_r, the number of low-misfit cells selected for further sampling. The algorithm comprises four basic steps:

- Uniformly generate N_s samples in the parameter space with their Voronoi cells
- Calculate the misfit between the observed and predicted data from the generated models and select N_r models with lowest misfit

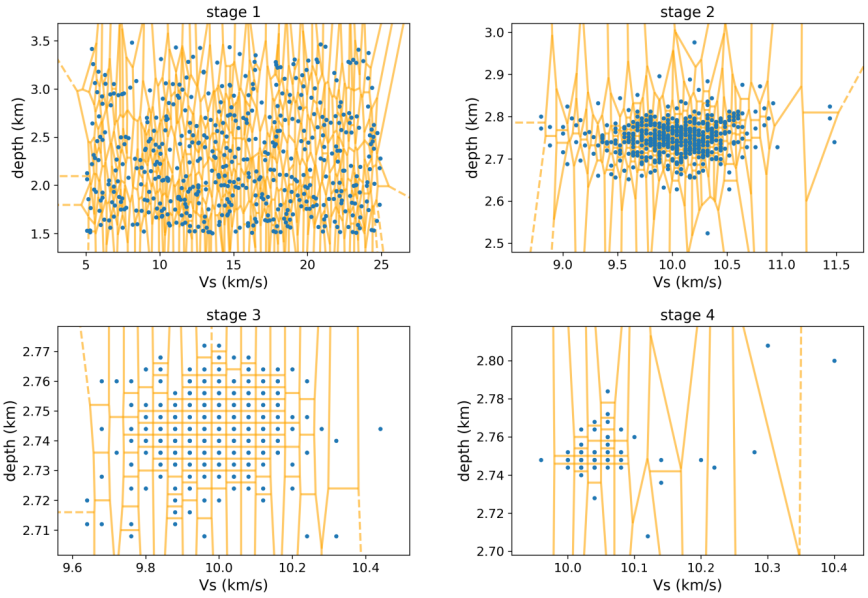

Figure 1.11: Various search stages of the NA shown in a 2 parameter (velocity and depth) space. The algorithm starts with a random coarse sampling of the whole parameter space, and with each iteration, the sampling concentrates into low misfit regions

- Generate new N_s models inside the Voronoi cells of these Nr lowest misfit models by uniform random walk
- Reiterate step 2

In addition, the total number of iterations is supplied by the user. Fig 1.11 shows various stages of the inversion process as the algorithm proceeds. As the number of iterations grow, the sampling gets increasingly concentrated in regions of lower misfit values. The ratio N_s/N_r controls whether the algorithm behaves exploratively or exploitatively, i.e., if it quickly convergence to a minimum of the misfit function or slowly investigates all the potential regions in the misfit landscape. With comprehensive sampling of the parameter space, rather than taking a single 'best fit' model as the solution, an alternative is to use the entire ensemble of generated models to draw inferences about the observed data. To employ the Bayesian approach, we use the complete ensemble of generated models and characterise them according to their misfits. The L2 norm is used to define the misfit, $\Phi(m)$, between the observed d_{obs} and the predicted data for the model $g(\mathbf{m})$

$$\Phi(m) = \left\| \frac{g(\mathbf{m}) - d_{obs}}{\sigma_d} \right\|^2 \tag{1.22}$$

σ denotes the uncertainty of the observed data. The likelihood function then takes the form:

$$p(\mathbf{d}_{obs}|\mathbf{m}) \propto exp\left(\frac{-\Phi(m)}{2}\right) \tag{1.23}$$

A minimal prior knowledge is imposed on all the model parameters using a uniform distribution over the full range of values. Thus, the prior for each parameter takes a constant value over its defined interval. For example, if the range of values assumed by the parameter x_i lie between X_{min} and X_{max},

$$p(x_i) = \begin{cases} \frac{1}{\Delta X}, & \text{if } X_{min} \leq x_i \leq X_{max} \\ 0, & \text{otherwise} \end{cases} \tag{1.24}$$

where,

$$\Delta X = X_{max} - X_{min}$$

Transdimensional rj-McMC Inversion

Like most other inversion schemes, the NA adopts fixed dimension model parameters that need to be specified. In the transdimensional rj-McMC formulation, the number of model parameters itself becomes an unknown quantity that needs to be estimated along with the other model parameter and, therefore, the posterior density is defined across the whole range of available dimensions. This way, the method lets the data themselves infer the complexity of the model rather than the user having to specify the model parametrization a priori individually. Since the misfit decreases with an increase in the number of model parameters, it is often difficult to determine the level of model complexity needed to estimate the solution of an inverse problem. The transdimensional approach avoids this problem as it is inherently designed to find a parsimonious solution (Malinverno, 2002), i.e., models with a higher level of complexity are naturally discouraged, and the least complex models are preferred to avoid the over-fitting of data.

Each model is parameterized by velocity, depth, v_P/v_S ratio, layers, and the noise parameters of the observed data which include two the noise correlation r and the noise amplitude σ. The initial model parameters are randomly drawn according to the prior distribution. A new model is generated at each following iteration by perturbing the previous model according to some specified proposal distribution. The proposed model is evaluated in comparison to the current model according to its acceptance probability α and is either accepted or rejected based on that. α is computed as:

$$\alpha = \text{prior ratio} \times \text{likelihood ratio} \times \text{proposal ratio} \times \text{Jacobian}_{\mathbf{m}\rightarrow\mathbf{m}'} \tag{1.25}$$

$$\alpha(\mathbf{m}'|\mathbf{m}) = min\left[1, \frac{p(\mathbf{m}')}{p(\mathbf{m})} \times \frac{p(\mathbf{d}_{obs}|\mathbf{m}')}{p(\mathbf{d}_{obs}|\mathbf{m})} \times \frac{q(\mathbf{m}|\mathbf{m}')}{q(\mathbf{m}'|\mathbf{m})} \times |\mathbf{J}|\right] \tag{1.26}$$

Similar to the NA case, the prior distributions for the model parameters are again taken as uniform random. The various terms of the above equation can be simplified and assume specific forms depending on the type of perturbation imposed. Details can be found in Bodin et al. (2012).

The likelihood term $p(\mathbf{d}_{obs}|\mathbf{m})$ for each proposed model is defined as:

$$p(\mathbf{d}_{obs}|\mathbf{m}) = \frac{1}{\sqrt{(2\pi)^n |C_e|}} \times exp\left\{-\frac{\Phi(\mathbf{m})}{2}\right\} \tag{1.27}$$

where $\Phi(\mathbf{m})$ is the Mahalanobis distance (Mahalanobis, 1936) between the observed and predicted data vectors, and is given by

$$\Phi(\mathbf{m}) = (g(\mathbf{m}) - d_{obs})^T C_e^{-1} (g(\mathbf{m}) - d_{obs}) \tag{1.28}$$

C_e in equations 1.27 and 1.28 is the data covariance matrix and its form depends on the assumptions imposed on data noise. A Gaussian correlation law $c_i = r^{(i^2)}$ has been assumed here. In this case C_e^{-1} and $|Ce|$ do not have any analytical form and need to be estimated which is costly for each iteration. Since

$$C_e^{-1} = (\sigma^2 R)^{-1} \text{ and } |C_e| = \sigma^{2n}|R| \tag{1.29}$$

it is possible to fix a value of r and invert for σ at each iteration. C_e can then be obtained by equation 1.29.

1.6.4 Random Matrix Theory

A random matrix is a matrix that has random numbers generated from some joint probability distribution (here, Gaussian) as its elements. The eigenvalues and eigenvectors of such matrices are also random. The main objective of this subject is to understand the behaviour of the properties of random matrices, which show remarkable deterministic properties. Two particular kind of well-studied random matrices are Wigner and Wishart Matrices. A Wigner matrix is a random Hermitian matrix defined by:

$$X_N(ij) = X_N(ji) = \begin{cases} \frac{Z_{i,j}}{\sqrt{N}}, & \text{if } i < j \\ \frac{Y_i}{\sqrt{N}}, & \text{if } i = j \end{cases} \tag{1.30}$$

where $Z_{i,j}$ and Y_i can be complex or real numbers and N is the dimension of the square matrix. The distribution of the eigenvalues for such matrices almost surely convergence to a semi-circular form as the size of the matrix grows. This is called Wigner's semi-circular law and is as universal as the central limit theorem in statistics. Figure 1.12 shows the distribution of the eigenvalues of such a random matrix with size 500x500. As $n \to \infty$, the shape of the distribution reaches a perfect semi-circle.

Similarly, for a non-symmetric matrix Z with i.i.d entries, a Wishart matrix is defined as:

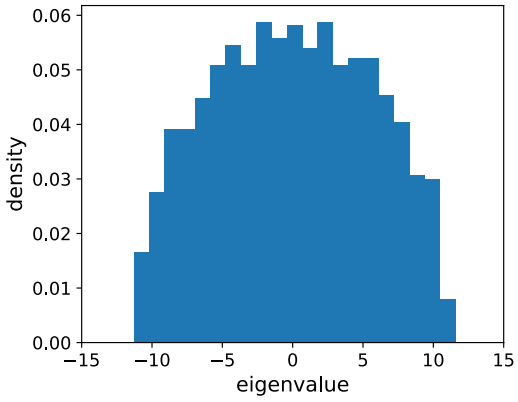

Figure 1.12: Distribution of eigenvalues of a 500 × 500 Wigner random matrix

$$X_{n\times n} = \frac{Z^{\star}_{n\times m} Z_{n\times m}}{\sqrt{n}} \tag{1.31}$$

In analogy with Wigner's semi-circular Law, the limiting eigenvalue distribution of such a Wishart matrix is given by the Marchenko-Pastur (MP) Law. Suppose X denotes a $m \times n$ random matrix which has i.i.d. entries with mean 0 and variance σ^2, and $\lambda_1, \lambda_2, \lambda_3, ...$ are the eigenvalues of X, the MP Law can be written as:

$$p(\lambda|\sigma,\gamma) = \begin{cases} \frac{\sqrt{(\lambda_+ - \lambda)(\lambda - \lambda_-)}}{2\pi\lambda\gamma\sigma}, & \text{if } \lambda_- \leq \lambda \leq \lambda_+ \\ 0, & \text{otherwise} \end{cases} \tag{1.32}$$

with $\lambda_\pm = \sigma^2(1 \pm \sqrt{\gamma})^2$

λ_-, λ_+, σ, and γ denote the smallest eigenvalue, largest eigenvalue, noise level, and matrix aspect ratio n/m, respectively. The shape of the MP distribution depends on γ. Figure 1.13 (a) shows the distribution for $\gamma = 1/3$. The MP law can equivalently be expressed in terms of the singular values of non-symmetric matrix $Z_{n\times m}$ rather than the eigenvalues of the Hermitian matrix $X_{n\times n}$. In the case of $\gamma = 1$, this then reduces to the quarter-circle law (Figure 1.13(b)).

This self-arranging behaviour of the eigenvalues of Wishart matrices into a "bulk" is a universal phenomenon and was interpreted by Dyson as the particles of a Coulomb gas confined to a quadratic potential (Dyson, 1962). The positions of the gas particles can be identified as the eigenvalues of the random matrix arranged on a line. The largest and the smallest eigenvalues ($\lambda_\pm$) of this bulk fluctuate on the small scale $n^{-2/3}$ according to the Tracy-Widom distribution (Tracy and Widom, 1996). In the presence of a non-random coherency (e.g. a signal) superimposed with the random matrix, a phase transition phenomenon (Baik et al., 2005) is observed. If this signal is above a certain signal threshold,

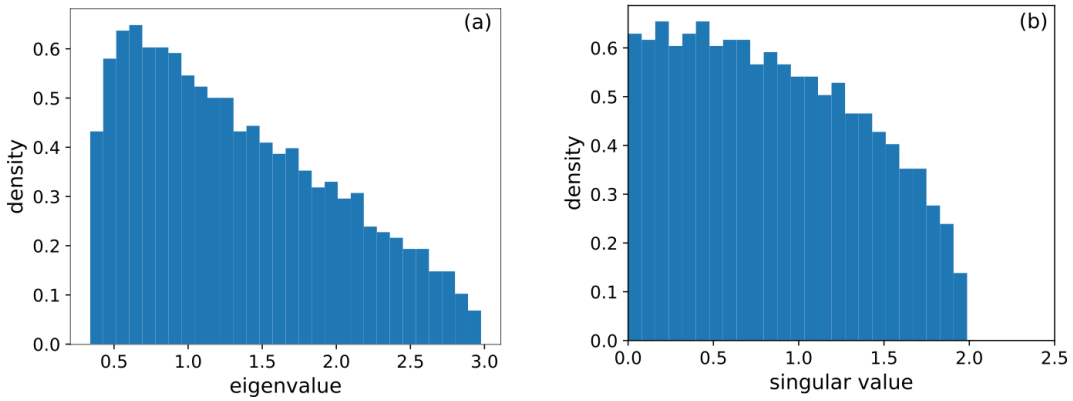

Figure 1.13: (a) Distribution of eigenvalues of a Wishart matrix with $\gamma_Z = 1/3$ (b) Distribution of singular values of a random matrix Z with $\gamma_Z = 1$

the signal eigenvalues separate away from the "bulk" eigenvalues of the random matrix and converge asymptotically to a different distribution. The corresponding eigenvectors also show such a transition behaviour. Within the bulk, they are orthogonal to the signal vectors but become strongly correlated and show a non-zero dot product past the largest eigenvalue. The same follows for the singular values which scale as the square-root of eigenvalues (Benaych-Georges and Nadakuditi, 2012) and the corresponding singular vectors. This phase transition is known as the BBP phase transition (Baik–Ben Arous–Péché), named on its founders.

These properties of the Wishart Matrix and the MP Law can be well applied to multivariate statistics where random noise contamination is of concern. Given a set of n independent random m-vectors X_i, i = 1, 2, . . . , n, that are drawn from the same underlying distribution, one can estimate a covariance matrix Σ for these. One way to think about this is as a set of measurements obtained from a physical system. The data covariance matrix Σ has the form:

$$\Sigma = \sum_{i=1}^{N} (X_i - \bar{X})^T (X_i - \bar{X}) \tag{1.33}$$

$$= X^T X, \text{ for } \bar{X} = 0 \tag{1.34}$$

Here, $\bar{X}$ denotes the mean vector. This is equivalent to equation 1.31 when $X_{ij} \in \mathbb{R}$. In fact, the covariance matrix of a set of random m-vectors belongs to the Wishart distribution. In absence of an underlying coherent signal in the data, the eigenvalue spectrum of the covariance matrices should follow the MP Law. However, if coherent signals are present, the BBP phase phenomenon is observed above a certain signal threshold, and the eigenvalues of these signals separate out.

Figure 1.14 illustrates this using a simple toy problem. 100 time-series with 500 samples each were produced by adding high amplitude random noise to a sine wave. Subplot (a)

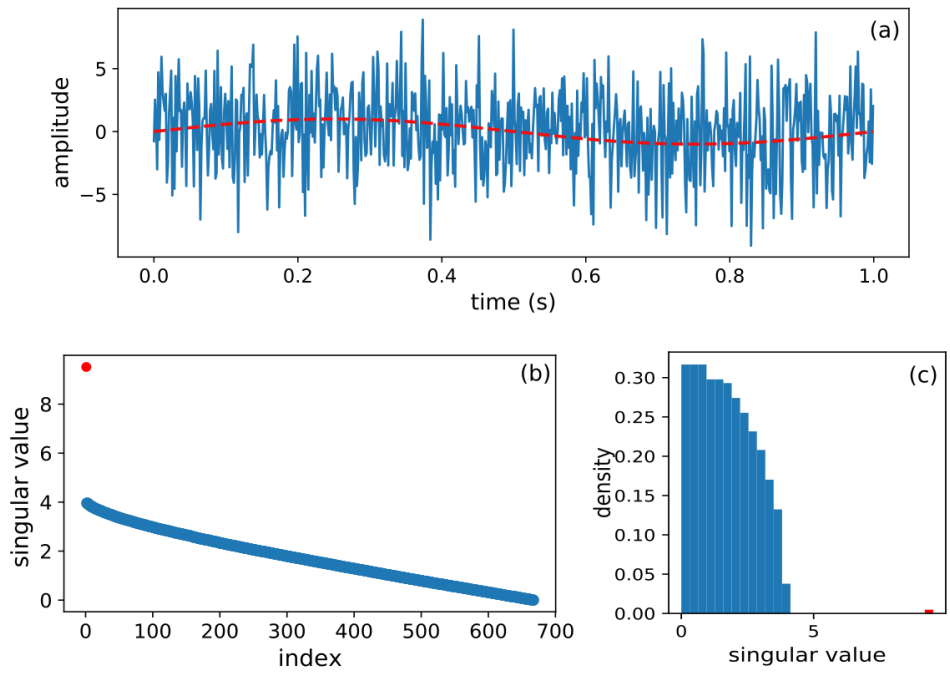

Figure 1.14: (a) Sine wave with added high amplitude random noise (b) Singular value spectrum of the dataset (c) Histograms of the singular values showing bulk separation

shows one of these series. The singular value spectrum of the data matrix was analysed. In subplot (b) the singular value spectrum is presented. The first singular value, marked in red, represents the sine wave signal present within the random noise. The singular values of the random noise decay down slowly. Subplot (c) shows a histogram plot for these. The noise singular values all bunch together to form the bulk while the value for coherent sine wave signal separates out. λ_+ gives an estimate for the edge of the bulk. The distance between the bulk and the signal singular value depends on the strength of the signal. If the signal showed more attributes, e.g., translation of the sine wave with time, more singular values would separate out to accommodate for this.

Chapter 4 outlines a procedure to estimate a threshold that separates the noise singular values from the signal singular values. The example in Figure 1.14 uses a simple random noise model for the purpose of illustration. This results in a clean and uncomplicated singular value spectrum. However, the spectrum could get much more complicated in real data where simple heuristics and scree plots often lead to overestimation or underestimation of noise. The application of random matrices originated with its use in nuclear physics by Eugene Wigner who first modelled the complex atomic spectra using an ensemble of random matrices. Since then random matrices have been used to model many dynamical systems. However, its use in seismology has been limited. Wave coherency based techniques like Karhunen-Loève transform (e.g., Jones (1985); Jones and Levy (1987); Al-Yahya (1991)),

singular value decomposition, and PCA have been widely used in exploration seismology to enhance and identify signals from subsurface reflectors, and separate ground roll, diffracted and guided waves from reflected phases (e.g., Freire and Ulrych (1988); Jackson et al. (1991); Bekara and Van der Baan (2007); Liu (1999)). However, an objective criterion to select the required number of components has not been well established. This work shows how these methods can work in conjunction with random matrix theory to identify an objective threshold and extract various coherent phase arrivals in RF data. Once identified, the secondary phase arrivals together with the primary conversions from crustal interfaces can be used to invert for the structure.

Chapter 2

Joint inversion of receiver functions and apparent incidence angles

This chapter was published in Earth and Space Science, Volume 8, Issue 10, in September 2021 under the title "Joint Inversion of Receiver Functions and Apparent Incidence Angles for Sparse Seismic Data" by Joshi et al. Conceptualization, data analysis, creation of figures, and writing the draft was carried out by me, under the supervision of Dr. B. Knapmeyer-Endrun, Prof. Dr. Heiner Igel and Prof. Dr. Ulrich Christensen.

The supporting information for this chapter can be found in Appendix A. At the request of the publishing journal, the following text has been included without any changes in presentation or the contents of the copyright information.

Earth and Space Science

RESEARCH ARTICLE
10.1029/2021EA001733

Joint Inversion of Receiver Functions and Apparent Incidence Angles for Sparse Seismic Data

Rakshit Joshi[1,4], Brigitte Knapmeyer-Endrun[2], Klaus Mosegaard[3], Heiner Igel[4], and Ulrich R. Christensen[1]

[1]Max-Planck-Institute for Solar System Research, Göttingen, Germany, [2]Bensberg Observatory, University of Cologne, Cologne, Germany, [3]University of Copenhagen, Niels Bohr Institute, Copenhagen, Denmark, [4]Ludwig-Maximilians-Universität, Munich, Germany

Key Points:

- We propose the joint inversion of receiver functions and apparent S-wave velocity curves to estimate crustal thickness
- Using the Neighborhood Algorithm, we show how a full uncertainty estimate can be computed from an ensemble solution
- The method is applied to Martian synthetics and terrestrial data sets comprising single and multiple events

Supporting Information:

Supporting Information may be found in the online version of this article.

Correspondence to:

R. Joshi,
joshir@mps.mpg.de

Citation:

Joshi, R., Knapmeyer-Endrun, B., Mosegaard, K., Igel, H., & Christensen, U. R. (2021). Joint inversion of receiver functions and apparent incidence angles for sparse seismic data. *Earth and Space Science*, *8*, e2021EA001733. https://doi.org/10.1029/2021EA001733

Received 8 MAR 2021
Accepted 8 SEP 2021

Abstract The estimation of crustal structure and thickness is essential in understanding the formation and evolution of terrestrial planets. Initial planetary missions with seismic instrumentation on board face the additional challenge of dealing with seismic activity levels that are only poorly constrained a priori. For example, the lack of plate tectonics on Mars leads to low seismicity, which could, in turn, hinder the application of many terrestrial data analysis techniques. Here we propose using a joint inversion of receiver functions and apparent incidence angles, which contain information on absolute S-wave velocities of the subsurface. Since receiver function inversions suffer from a velocity depth trade-off, we in addition exploit a simple relation that defines apparent S-wave velocity as a function of observed apparent P-wave incidence angles to constrain the parameter space. We then use the Neighborhood Algorithm for the inversion of a suitable joint objective function. The resulting ensemble of models is then used to derive uncertainty estimates for each model parameter. In preparation for the analysis of data from the InSight mission, we show the application of our proposed method on Mars synthetics and sparse terrestrial data sets from different geological settings using both single and multiple events. We use information-theoretic statistical tests as model selection criteria and discuss their relevance and implications in a seismological framework.

1. Introduction

Receiver function (RF) analysis is a powerful technique to gain information about the discontinuities in the crust and upper mantle beneath a single three-component seismic station. RFs are essentially time series that are sensitive to the structure near the receiver. The basic principle behind this method is that when a seismic wave is incident upon a discontinuity, mode conversion between the compressional (P) and shear (S) waves will take place in addition to the generation of reflected and transmitted waves. The resulting converted wave (Ps or Sp) will have a time offset with respect to its parent wave, and this time offset is directly proportional to the depth of the discontinuity and the velocity of the layers above. In addition to the direct converted waves, the multiples resulting from reflections and conversions between the discontinuity and the free surface can provide further constraints on the layer thickness and help to resolve the depth-velocity trade-off. The RF can be obtained by deconvolving the vertical component from the radial component of a teleseismic event recorded on a three-component seismometer (Ammon, 1991; Langston, 1979; Owens et al., 1987). Since only a small percentage of the incident energy is converted at a discontinuity, it is difficult to observe these conversions in a single seismogram. A number of RFs can instead be used to measure the crustal thickness and average v_P/v_S ratios by H-k (crustal thickness—average v_P/v_S) stacking for individual stations (Helffrich & Thompson, 2010; Zhu & Kanamori, 2000) or for imaging by common conversion point (CCP) stacking of data from many stations (Dueker & Sheehan, 1997). This, however, requires assumptions on the velocity structure.

One method to obtain a detailed velocity structure is to directly invert the calculated RFs using linearized iterative procedures, but Ammon et al. (1990) showed that such inversions of RF contain an inherent trade-off between the depth to a discontinuity and the velocity above. The primary sensitivity of the RF inversion is to velocity contrasts and relative travel time, not to absolute velocity. This lack of sensitivity to absolute velocity results from the relative S-P travel time constraints along with the limited range of horizontal slowness contained in the data (Ammon et al., 1990). Thus RF data sets are generally inverted jointly with

other independent data sets that provide additional constraints on absolute shear wave velocities like surface wave dispersion curves (e.g., Du & Foulger, 1999; Julia et al., 2000), or Rayleigh wave ellipticity (Chong et al., 2016). One such relation, which has not been heavily exploited is between apparent S-wave velocities and P-wave polarization. The polarization of body waves has been traditionally used in seismology to study the anisotropy of crustal and upper-mantle structures (Fontaine et al., 2009; Schulte-Pelkum et al., 2001). But the P-wave polarization can also be used to constrain the near-surface shear wave speed. Svenningsen and Jacobsen (2007) showed that the amplitudes of the vertical (Z) and radial (R) components of the P-receiver function at zero time is directly related to the polarization of P-waves. Deconvolution removes the complex waveform of the incoming P-waves, which dominate the Z component. Hence the Z RF is an approximate zero-phase spike with arrival instant at exactly $t = 0$, where the time is measured relative to the P-wave arrival. This can be used to estimate the apparent P-wave incidence without influences from the P-wave coda. Further, filtering at successively long periods, a frequency-dependent apparent shear wave velocity profile can be obtained (Knapmeyer-Endrun et al., 2018; Svenningsen & Jacobsen, 2007) which can be used as an effective independent data set to be jointly inverted with the RFs.

Svenningsen and Jacobsen (2007) used a linearized inversion of apparent S-wave velocity curves and demonstrated its independence of the starting model. Hannemann et al. (2016) applied the method to an ocean-bottom data set and used a grid search method concluding that the method is usable for single station estimates of the local S-wave velocity structure beneath the ocean bottom. Schiffer et al. (2016) used an iterative least squares method to jointly invert apparent velocity curves and RFs utilizing a minimum number of layers (6–8). Knapmeyer-Endrun et al. (2018) used a grid search over parameter space to invert the S-wave velocity curve for crustal structure at several Earth stations with varying geology and synthetic Mars data. It has also been shown that a priori S-wave velocity information deduced from P-wave polarizations can be useful when inverting RF waveforms (Peng et al., 2012). Park and Ishii (2018) further showed that the S-wave polarization is sensitive to both the compressional and shear wave speeds, and successfully combined P- and S-wave polarization directions measured by principal component analysis to derive the distribution of near-surface P- and S-wave speeds in Japan.

In this study, we use a modified version of the Neighborhood Algorithm (Sambridge, 1999a; Wathelet, 2008) for the joint inversion of receiver functions and apparent S-wave velocity profile. The Neighborhood Algorithm (NA) is a derivative-free optimization method that uses a pseudo-random trajectory in exploring the parameter space. Rather than making inferences on model parameters using only the lowest-misfit model, it provides the option of using the suite of all generated models for this purpose. With a well-sampled parameter space, an ensemble algorithm also benefits from the possibility of a probabilistic solution with full uncertainty estimates. In contrast with earlier studies on this topic, which are predominantly based on large amounts of available data, we show how this method can be used with limited data sets comprising only a few events. This becomes crucial in the context of planetary seismology where the amount of data may be limited. For example, it can be used to study the crustal structure of Mars using data from the InSight mission (Lognonné et al., 2019). Another problem associated with determining the crustal structure is the number of inter-crustal layers to be inverted for. We address this problem using a two-fold approach: we start by inverting for a model of low complexity and gradually increase it till no significant velocity contrast along with misfit reduction is observed, with major discontinuities being adequately represented by the model. We then use Akaike weights derived from Akaike Information Criterion (AIC) values (Akaike et al., 1973) for all of these models as selection criteria. We apply this joint inversion scheme on synthetic seismograms for Mars and selected terrestrial data.

2. Data Sets

2.1. Mars Synthetics

In order to demonstrate and verify our proposed method, we first use synthetic seismograms for Mars that are generated using Green's Function (GF) databases prepared for a suite of a priori one-dimensional (1D) velocity models with varying crustal thicknesses, seismic wave speeds, densities, mantle compositions, and aerotherms. These a priori models are obtained by the inversion of bulk chemistry, mineralogy, and geotherm, following the approach described in Khan and Connolly (2008), Connolly (2009), and Khan et al. (2016). The GF databases are computed using a 2.5D axis-symmetrical spectral element code, AxiSEM

Table 1
Event Information for Stations BFO and SUW

Date	Origin time (UTC)	Station	Ray p (s/deg)	Location		Distance		
				Latitude	Longitude	M_w	(°)	$2\sigma_{RF}$
Sep 3, 2007	16:14:53	BFO	5.35	45.836°N	150.060°E	6.2	79	0.036
Jul 6, 2008	09:08:21	BFO	5.31	45.387°N	150.965°E	5.7	82	0.052
Jun 6, 2009	20:33:28	BFO	7.66	23.864°N	46.105°W	6.0	51	0.056
Nov 24, 2008	09:02:58	BFO	5.68	54.203°N	154.322°E	5.3	70	0.048
Oct 29, 2009	17:44:31	BFO	7.78	36.391°N	70.722°E	6.2	45	0.078
Feb 8, 2008	09:38:14	SUW	6.38	10.671°N	41.899°W	6.8	72	0.082
Sep 30, 2009	10:16:09	SUW	5.17	0.720°S	99.867°E	6.9	82	0.063
Oct 7, 2009	21:41:13	SUW	5.57	4.079°N	122.371°E	6.8	77	0.056
Mar 30, 2010	01:02:53	SUW	6.26	43.308°N	138.379°E	5.7	68	0.162
Sep 10, 2008	13:08:14	SUW	6.35	8.093°N	38.705°W	5.2	64	0.052
Oct 2, 2007	18:00:06	SUW	6.01	54.511°N	161.708°W	5.8	60	0.073

(Nissen-Meyer et al., 2014), and are publicly available within the Marsquake Service (MQS) at ETH Zurich (Ceylan et al., 2017, http://instaseis.ethz.ch/marssynthetics/). Synthetic broadband seismograms can be calculated from these GF databases for arbitrary moment tensors and source-receiver combinations using the Instaseis package (van Driel, Krischer, et al., 2015). These simulations are based on full numerical solutions of the visco-elastic wave equation and include the effects of attenuation, are accurate down to a period of 1 s, and allow for a total simulation duration of 30 min.

Since a large variation in crustal thickness is expected across Mars, a thin (30 km) and thick (80 km) crust is employed to create the initial models, both with a 10 km thick upper crustal layer. Further details of these models can be found in Ceylan et al. (2017). The thin and thick crusts with different velocity contrasts at the Moho represent 1-D global end-member models, rather than what is expected beneath the InSight landing site. In this study, we have used two thin crust models (C30VH_AKSNL, C30VL_AKSNL) and one thick crust model (C80VL_AKSNL) for the purpose of demonstrating the method. For all of these models, we calculated synthetic seismograms and receiver functions at epicentral distances between 15° and 180° in 1° increments. Assuming normal faulting, a dip-slip source at an angle of 45° and at a depth of 5 km north of the seismometer was used to generate the synthetic waveforms. Since the synthetics do not have any added noise, we assume a reasonable 25% standard deviation on mean absolute values of RFs and $V_{S,app}$ whenever appropriate for likelihood calculations. We demonstrate the results of applying our method first on a single event and then multiple events together.

2.2. Terrestrial Data

To verify how the algorithm works in a real setting, we analyzed data from two stations in Central Europe—BFO in Germany (Federal Institute for Geosciences and Natural Resources, 1976) and SUW in Poland (GEOFON Data Centre, 1993). Details of the events used are listed in Table 1. Reference values of crustal thickness for these stations were taken from the Moho depth map of the European plate (Grad et al., 2009) and Knapmeyer-Endrun et al. (2014). Because these sites have known differences in crustal structure, this gives us the opportunity to test how the method works in a range of possible scenarios and in the presence of noise. Station BFO is located on the thinned crust of the Upper Rhine Graben, which is a part of the European Cenozoic Rift system (Ziegler, 1992). In contrast to this, station SUW is situated on the relatively thick East European Craton, which is the core of the Baltica proto-plate and occupies the northeastern half of Europe. It is characterized by a thick three-layer crust with an additional fast lower crustal layer (Grad et al., 2003). The East European Craton is of Precambrian origin and overlain by a young thin sedimentary cover (Bogdanova et al., 2006) which leads to strong reverberations in the P-receiver function for SUW (Wilde-Piórko et al., 2017)

3. Method

3.1. Calculation of Receiver Functions

The teleseismic P-wave receiver function represents the structural response near a recording station to the incoming teleseismic P-wave. It can be obtained by removing the source wavelet, propagation effects and the instrument response from the vertical, radial and transverse waveforms. This is generally done by deconvolving the vertical component from the radial and transverse components in a process called source equalization (Phinney, 1964; Vinnik, 1977). Several methods have been described in the literature for this deconvolution process (e.g., see Kind et al., 1995; Langston, 1979; Owens et al., 1987; Phinney, 1964; Vinnik, 1977). We use a time-domain Wiener filter for deconvolution as described by Hannemann et al. (2017). The receiver function datasets used here are a subset of those used in Knapmeyer-Endrun et al. (2014) and Knapmeyer-Endrun et al. (2018). The synthetic seismograms do not require the removal of any instrument response, but they are filtered between 1 Hz and 50 s, 1 Hz being the upper-frequency limit of the synthetics. Additionally, due to the alignment of source and receiver, these data are already in the ZRT system. For the terrestrial data, we first remove the instrument response from all components and then filter the seismograms between 5 Hz and 50 s. The ZNE coordinate system is then rotated into ZRT using back-azimuths determined by polarization analysis (Jurkevics, 1988) to obtain radial and transverse components. The Wiener filter is determined such that it transforms the P-wave signal on the vertical component into a band-limited spike. This filter is then applied to all components of the signal to finally obtain the RF with the spike positioned at the centroid of the signal.

3.2. Apparent S-Wave Velocity

Following the relationship between true and apparent incidence angles (Wiechert, 1907), it can be shown that the apparent incidence angle is sensitive to absolute shear wave velocity

$$v_{S,app} = \sin(0.5\overline{i_p})/p \tag{1}$$

where $\overline{i_p}$ denotes the apparent P-wave incidence angle and p denotes ray parameter. Svenningsen and Jacobsen (2007) proposed a method to directly estimate the apparent incidence angle using RFs instead of the raw waveform data, which in turn emphasized the true S-wave velocity information contained in them. We follow a similar procedure and estimate the apparent P-wave incidence angle from the amplitudes of vertical and radial receiver functions at time $t = 0$ using the relation

$$\tan\overline{i_p} = \frac{RRF(t\ =\ 0)}{ZRF(t\ =\ 0)} \tag{2}$$

Now estimating $\overline{i_p}$ as a function of low pass Butterworth filter period (T) results in a $v_S(T)$ curve which emphasizes the absolute S-wave velocity variation with depth. Larger T implies more smoothing and thus more multiples at later times influence the values of the filtered receiver functions at $t = 0$. In contrast with the squared cosine filters used by Svenningsen and Jacobsen (2007), we use a Butterworth filter which has twice the corner period as a cosine filter. For each trace we measure the dominant period of the spike in the ZRF and discard the values of filter periods smaller than that. We show cases with both single and multiple events. When multiple events are used at varying epicentral distances, we calculate the median of the apparent S-wave velocity curve at each sample period. For a numerical approximation of sensitivity kernels, showing the change in $v_{S,app}(T)$ curves in response to changes in S-wave velocity in the background model IASP91 (Kennett et al., 1995), see Knapmeyer-Endrun et al. (2018).

3.3. Inversion

For the purpose of this study, we have employed a modified version of the Neighborhood Algorithm (NA) (Wathelet, 2008) for the joint inversions of RF and apparent S-wave velocity curves. Being a derivative-free optimization algorithm and taking into account the low dimensionality of our problem, NA seems to be a good choice because of its simplicity (two tuning parameter scheme) and lack of dependence on starting models (Sambridge, 1999a). Moreover, an ensemble of models rather than a single model can be used to make robust statistical inferences about the model parameters. The modifications by Wathelet (2008) further implement dynamic scaling of model parameters and allows to define irregular limits to the searchable

parameter space. The idea behind the NA is to start with an initial coarse sampling of the parameter space, then select the regions with lowest misfits and continue to resample these regions such that the heaviest sampled regions correspond to the models which best fit the data. In each iteration, the NA uses nearest-neighbor regions defined by Voronoi cells to partition and search the parameter space. The misfit is assumed to be constant within each of these Voronoi cells, and with each iteration, sampling is concentrated on the cells with lower misfit relative to the rest of the cells. The algorithm relies on only two control parameters: Ns - number of new samples to generate at each iteration and Nr—number of promising models to select for further sampling. The ratio Ns/Nr controls whether the algorithm behaves exploratively or exploitatively (Sambridge, 1999a, 1999b).

We use the L2 norm in order to measure how well a given model with a particular set of parameters can reproduce the given data quantitatively

$$\Phi(m) = \left\| \frac{\mathrm{g}(\mathbf{m}) - d_{obs}}{\sigma_d} \right\|^2 \tag{3}$$

where $g(\mathbf{m})$ is the estimated data and σ_d^2 is the estimated variance of the data noise. In this study, the noise has been assumed uncorrelated for simplicity and thus a simple Euclidean distance can be used. For a joint inversion of receiver function and apparent S-wave velocity, the objective function is defined by the linear combination of misfits of the weighted receiver functions Φ_{RF} and the apparent velocity curve $\Phi_{V_{app}}$, using the L2 norm, thus takes the form

$$\Phi(m) = \alpha\Phi_{RF} + \Phi_{V_{app}} \tag{4}$$

The weighting constant α is tuned manually by sample forward runs prior to the inversion process such that both the individual misfits are of the same order of magnitude. Here we have used $\alpha = 8$ for synthetic data and $\alpha = 10$ for terrestrial data. As mentioned before, the two parameters that control the NA need to be tuned depending on the problem and the style of sampling needed. For a more explorative search that is robust against local minima, we perform 1200 iterations in each inversion run with 300 models produced at each iteration (n_s) and 100 cells re-sampled at each iteration (n_r), resulting in an ensemble of ~360,000 models per run. Each inversion was repeated several times to test the stability of the results. High n_s/n_r ratio ensures faster convergence while a high number of initial models ($n_{s_0} = 3000$) ensures highly explorative behavior.

Knapmeyer-Endrun et al. (2018) compared several algorithms used in literature for the computation of receiver functions before choosing the forward calculation implemented by Shibutani et al. (1996). The algorithm calculates the impulse response of a layer stack in the P-SV system. We then convolved the resulting synthetic Z- and RRFs with the observed ZRFs to account for the observed complexity and waveform widths. Once the RFs are obtained, we can straight away calculate the apparent S wave velocities using the procedure described in the last section. Density was not considered to be a parameter to be inverted for and was calculated using Birch's law (Birch, 1961), while the S-wave velocity and the v_P/v_S ratio of each layer were allowed to vary. Furthermore, the S-wave velocity was constrained to increase with increasing depth. The fact that a single forward calculation can be performed in a matter of seconds and the waveform complexity matches that of real data makes this algorithm suitable for the purpose of this study.

3.4. Bayesian Formulation

The Bayesian formulation allows to account for prior knowledge of the parameters of our model, provided that this information can be expressed as a probability distribution $\rho(\mathbf{m})$. The prior corresponds to the knowledge that we have about our system, for example from previous studies. As new data is available, often in the form of likelihoods, this prior information can then be updated using Bayes' rule. This results in what is known as the posterior distribution for these unknowns—A distribution over the full range of these parameters.

3.4.1. Computing Average Likelihoods

The likelihood $\rho(\mathbf{d_{obs}}|\mathbf{m})$ is a function of the model parameters that describes the goodness of fit of a model to the observed data. Assuming a Gaussian error distribution for a given misfit measure, $\mathbf{\Phi}(\mathbf{m})$, the likelihood function is defined as:

$$\boldsymbol{\rho}(\mathbf{d_{obs}}|\mathbf{m}) \propto exp\left(\frac{-\Phi(m)}{2}\right) \tag{5}$$

As mentioned before, the NA initially starts with a coarse sampling of the parameter space, and eventually, the algorithm guides the sampling such that the best fitting regions of the parameter space are also the most heavily sampled regions. This, therefore, introduces a bias in the sampling of the parameter space which otherwise could be used to compute the full uncertainty from the ensemble of acceptable solutions. Sambridge (1999b) demonstrates that this could be achieved by a Gibbs re-sampling of the output ensemble which essentially concentrates on the low misfit regions and approximates the true posterior density by an approximate one. Here we show a simple alternative method to compute marginal histograms from the biased samples based on binning model parameters. In essence, each model in the ensemble has a pair-wise distance to every other model, which can be calculated using multi-dimensional scaling. Binning model parameters within a small distance and computing average likelihoods then approximates the true posterior density as a histogram.

Consider N sample models $\mathbf{m}^{(1)},\ldots,\mathbf{m}^{(\mathbf{N})}$ in a K-dimensional space, distributed according to an (everywhere positive) unknown distribution $\boldsymbol{\nu}(\mathbf{m})$. Assume that $\boldsymbol{\nu}(\mathbf{m})$ is close to the distribution, $f(\mathbf{m})$, and that we wish to compute the marginal histograms $f_k(m_k)$ from the samples.

The height $h_{[a,b]}$ of the histogram column for an interval [a,b] must (for $N \to \infty$) be proportional to the marginal probability $P_k(a < m_k < b)$. Hence,

$$h_{[a,b]} \approx \int_a^b f_k(m_k)dm_k \tag{6}$$

except for a normalization factor. This can be re-written as a mean value (expectation) of the ratio $\frac{f_k(m_k)}{\nu(m_k)}$ over the interval $[a,b]$ with respect to $\nu(m_k)$:

$$h_{[a,b]} \approx \int_a^b \frac{f_k(m_k)}{\nu(m_k)}\nu(m_k)dm_k \tag{7}$$

and since the sample models $\mathbf{m}^{(1)},\ldots,\mathbf{m}^{(\mathbf{N})}$ are distributed according to $\boldsymbol{\nu}(\mathbf{m})$, we have the approximation:

$$h_{[a,b]} \approx \frac{1}{N}\sum_{\{i|a<m_k^{(i)}<b\}}\frac{f_k(\mathbf{m}^{(i)})}{\boldsymbol{\nu}(\mathbf{m}^{(\mathbf{i})})} \tag{8}$$

This expression can be used when f_k can be evaluated in the sample points, and when we can evaluate $\boldsymbol{\nu}(\mathbf{m}^{(\mathbf{i})})$ from the density of sample points. The density at $\mathbf{m}^{(i)}$ can, for example, be evaluated over a cube C with edge length Δm, centered at $\mathbf{m}^{(i)}$:

$$\boldsymbol{\nu}(\mathbf{m}^{(\mathbf{i})}) = \frac{1}{(\Delta m)^K}N_c \tag{9}$$

where N_C is the number of sample points in C

3.4.2. Priors

We impose a minimal prior knowledge on all the parameters by using the uniform distribution as our choice of priors. The prior for each parameter takes a constant value over a defined interval. For example, if X is a model parameter which can take values over the interval $\Delta X = (X_{max} - X_{min})$, we define the prior probability density as:

$$\rho(x_i) = \begin{cases} \frac{1}{\Delta X}, & \text{if } X_{min} \le x_i \le X_{max} \\ 0, & \text{otherwise} \end{cases} \tag{10}$$

We can now apply Bayes' rule (Bayes, 1763) to combine the likelihood of observing the data with the prior distribution and to give the posterior probability density function:

$$\boldsymbol{\rho}(\mathbf{m}|\mathbf{d_{obs}}) \propto \boldsymbol{\rho}(\mathbf{d_{obs}}|\mathbf{m})\boldsymbol{\rho}(\mathbf{m}) \tag{11}$$

Note that the denominator in the Bayes' rule, $\boldsymbol{\rho}(\mathbf{d_{obs}})$, which is a sum over all possible models has been treated as a constant in this work, leading to a proportionality sign in the equation.

3.5. Model Selection

We use AIC (Akaike et al., 1973) as a model selection criterion, which essentially gives the Kullback-Leibler divergence between a candidate model and the true model as

$$AIC = 2k - 2ln(L) \tag{12}$$

where k and L denote the number of model parameters and the value of maximum likelihood of the model, assuming Gaussian errors. The first term in this equation is a measure of fit between the synthetic model and the true model representing the reality; the second term penalizes the order of complexity of this synthetic model. While raw AIC values themselves have no meaning, the quantity $exp\left(\frac{AIC_{min} - AIC_i}{2}\right)$ is an estimate of the relative likelihood of the th model. These model likelihoods can then be normalized to obtain Akaike weights w_i(AIC) (Burnham & Anderson, 2002; Wagenmakers & Farrell, 2004),

$$w_i(AIC) = \frac{exp\{-0.5\Delta_i(AIC)\}}{\sum_{k=1}^{K} exp\{-0.5\Delta_k(AIC)\}} \tag{13}$$

which can be interpreted as the probability that the th model is the best (i.e., it minimizes the estimated information loss Anderson & Burnham, 2004). The strength of evidence in favor of one model over the other can then also be obtained by dividing their respective Akaike weights. When the number of samples is small, a correction factor is added to the above equation giving the corrected AIC (AICc) values

$$AICc = 2k - 2ln(L) + \frac{2kn}{n - k - 1} \tag{14}$$

Here k denoted the number of model parameters and n the number of independent samples. Since the samples of a seismogram are generally correlated, with the correlation length being proportional to sampling frequency, we instead use the product of the Nyquist rate and the signal length as a measure of the number of independent samples (van Driel, Wassermann, et al., 2015). For a band-limited signal, the Nyquist rate is given by $2 * (f_{high} - f_{low})$ which gives 1.96 and 9.96 Hz for synthetics and terrestrial data, respectively (f_{high} and f_{low} denote the upper and lower frequency limits). Anderson and Burnham (2004) suggest using AICc when the ratio between the sample size n and the number of model parameters k is low (< 40). We will therefore use AICc when dealing with synthetic data and AIC for terrestrial data.

4. Results

4.1. Mars Synthetics

Figures 1 and 2 show the result of applying the method on single events for a priori Martian velocity models with a thin fast (C30VH_AKSNL) and a thick slow (C80VL_AKSNL) crust, respectively. Since noise is not a limiting factor here, in both cases, the residual includes the misfit for the complete waveform up to 30 s and apparent S wave velocity to 117 s. Each inversion was repeated three times to test the stability and the results were concatenated. The plots include all models within a maximum misfit value, ranked and color-coded according to misfit with black models being the best fitting solutions. This maximum misfit value is derived such that it encompasses the best 25% of all the models in the ensemble.

Adding a third layer to the model parameterization did not produce any considerable changes to the result. For C30VH_AKSNL the additional third layer produced a velocity contrast of around 0.8% against the layer adjacent to it with an insignificant misfit drop, while C30VH_AKSNL produced a similar low velocity contrast of around 0.45%. This shows that an additional layer is not warranted by the data. This is also confirmed numerically by our model selection criteria. Figures 3a and 3b show the respective probabilities obtained from AICc values for 1, 2, 3, and 4 layer models with constant velocity over a half-space for C30VH_AKSNL and C80VL_AKSNL respectively. For C30VH_AKSNL, there is a higher probability (~ 16%) of explaining the data with just a single layer than for C80VL_AKSNL. This is consistent with a weak Moho signal produced by the small velocity contrast. Since the two layer model has the highest probability (and thus minimum AIC), we conclude that it is the optimum model that explains this data set. This is also in agreement with the true models indicated by the blue dashed lines in Figures 1 and 2. The a priori range for each parameter in both cases are identical to the ranges shown for the 1D marginals and can be retrieved from Figures 4 and 5.

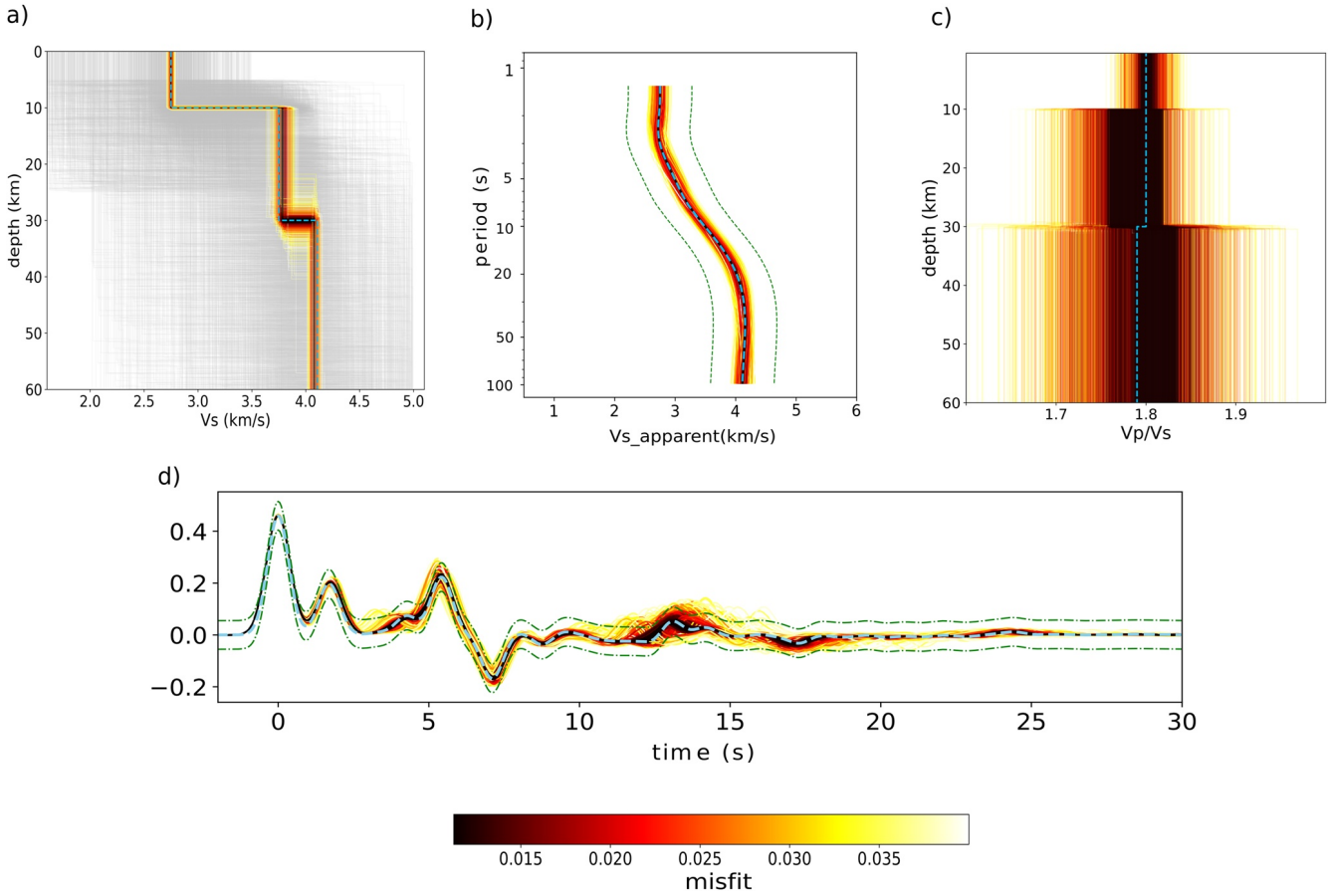

Figure 1. Result for thin crust model C30VH_AKSNL and event distance 70° (a) 1-D velocity profile. The light gray lines represent traversed models outside the maximum misfit range. The blue dashed line represents the true model. (b) Fit to $v_{S,app}$, (c) v_P/v_S ratio as a function of depth and (d) Fit to receiver function waveforms. The blue dashed lines denote the observed data and the green dash-dotted lines represent the uncertainty in observations.

The top layer crustal *S*-wave velocity and transition depth is well resolved for both the representative end-member models. For C30VH_AKSNL, there is high uncertainty in the Moho depth which in turn escalates the uncertainty in the *S*-wave velocity in the lower crust. This might be explained as the direct converted phase (1.8 s) and the multiples (5.5 and 7.2 s) produced by the intra-crustal discontinuity at 10 km depth are clearly visible in the data while the Moho conversion (4.1 s) for the thin crust model is not readily recognizable. This is in contrast to C80VL_AKSNL where the direct converted phase (14.7 s) produced at the Moho is clearly visible. The mantle S-wave velocities on the other hand are better constrained for C30VH_AKSNL than for C80VL_AKSNL. This is explained by the $v_{S,app}$ curves for the models. The $v_{S,app}$ curve for C80VL_AKSNL does not contain any information on the upper mantle velocity within its period range whereas in the $v_{S,app}$ curve for C30VH_AKSNL, the velocities converge to the upper mantle velocity of 4.1 km/s for periods longer than ~ 50 s. This demonstrates the advantage of inverting receiver functions along with frequency-dependent apparent S-wave velocities.

In both cases, the v_P/v_S ratio is also fairly well constrained for the top two layers by the method, as can be seen in the sub-figures (d). This is in agreement with Sambridge (1999a), where it was shown that the v_P/v_S ratio from the NA inversion is better resolved in the top layers than for the deeper ones. The thickness of the layers and their corresponding S-velocities are also better constrained than the v_P/v_S ratio. For C80VL_AKSNL, the v_P/v_S ratio of the half-space is not well resolved and varies across the whole model range investigated, whereas for C30VH_AKSNL, it is adequately resolved for all the layers even though the variance increases with depth.

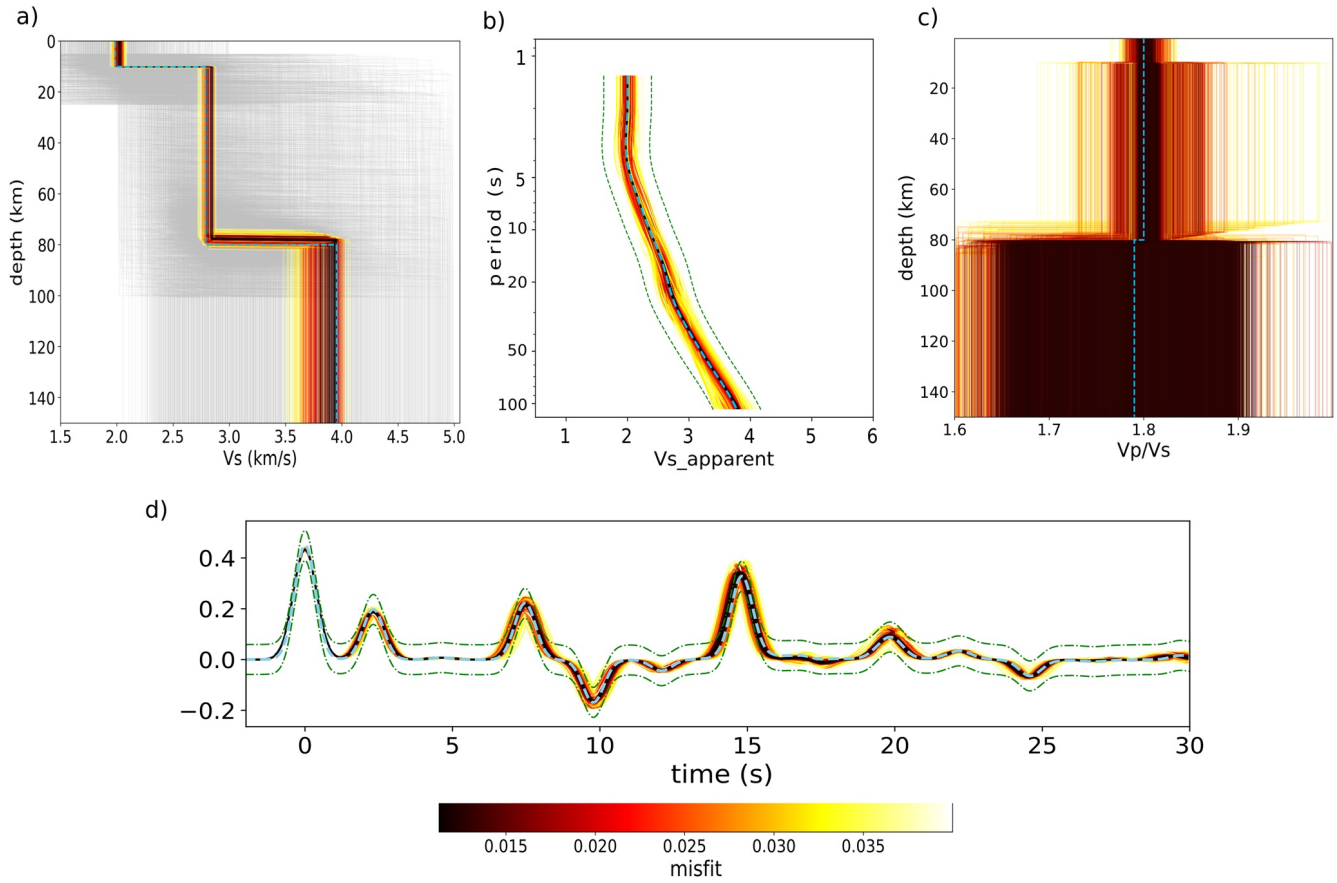

Figure 2. Same as Figure 1 for C80VL_AKSNL. Event distance is 40°.

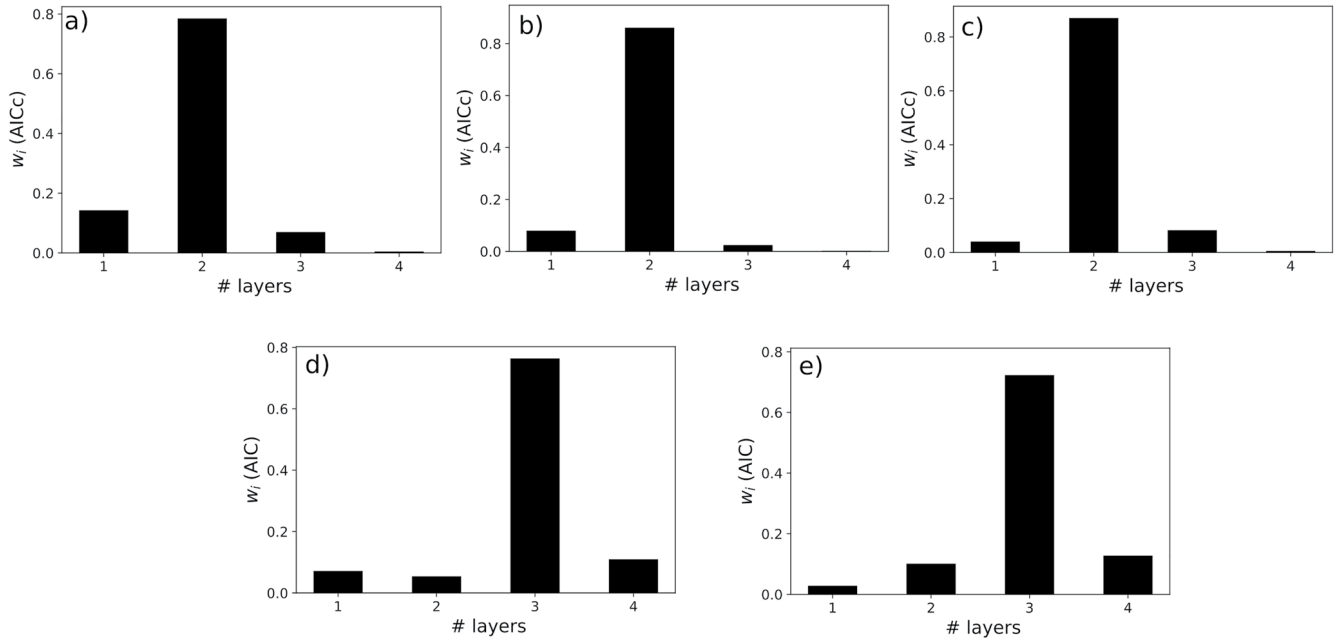

Figure 3. Model probabilities based on Akaike Information Criterion (AICc) values for (a) C30VH_AKSNL (b) C80VL_AKSNL (c) C30VL_AKSNL and AICc values for (d) BFO (e) SUW.

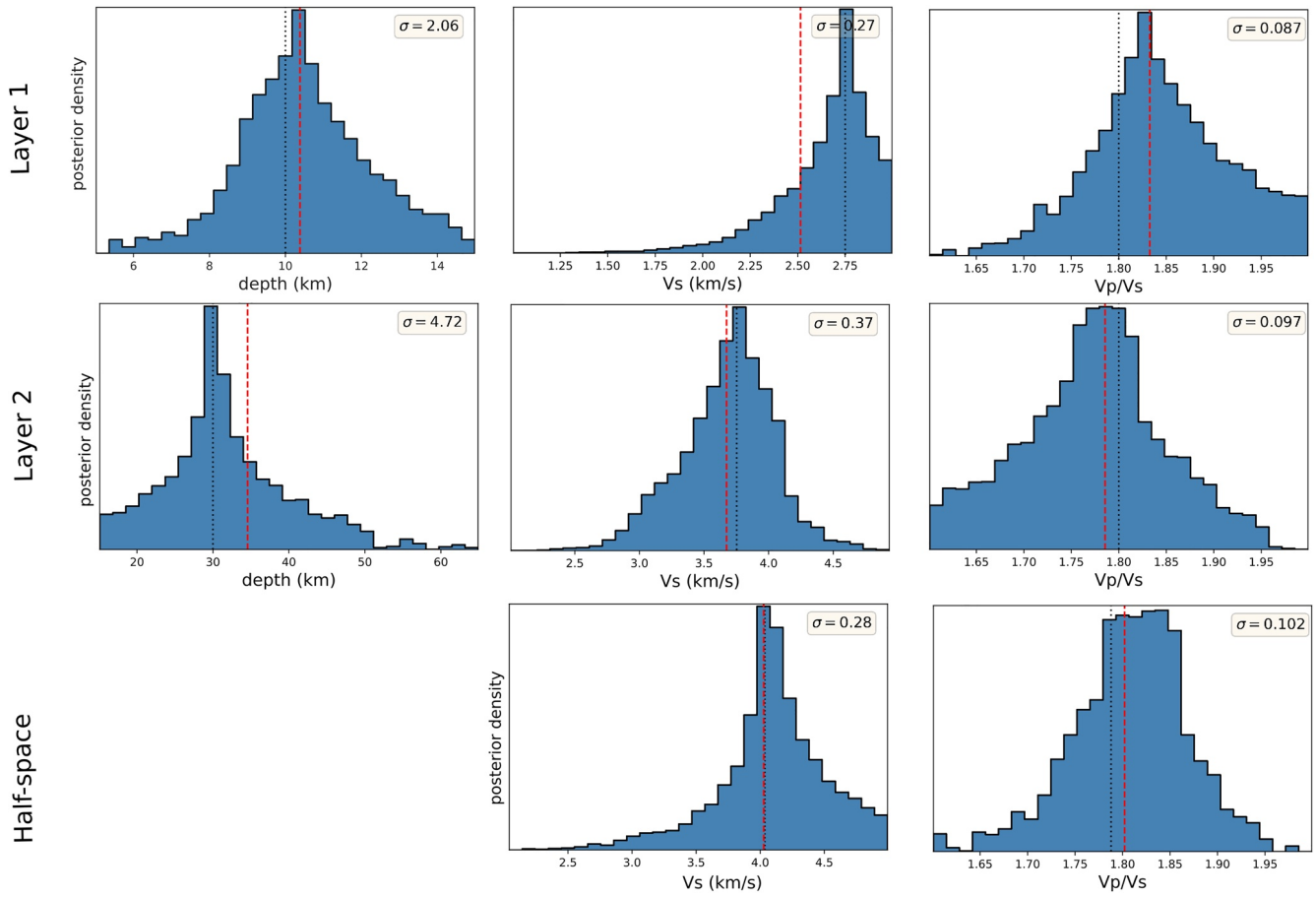

Figure 4. C30VH_AKSNL: 1D marginal posterior densities of depth, velocity and v_P/v_S ratio for each layer. The half-space has no depth parameter. The red dashed line denotes the mean value and the black dotted line represents the true parameter value.

To test how the method performs when multiple events are available, a median $v_{S,app}$ curve was calculated for model C30VL_AKSNL from the RFs between 40° to 90° where the $v_{S,app}$ curves are similar for each distance (Knapmeyer-Endrun et al., 2018). This median $v_{S,app}$ curve was then jointly inverted with 6 receiver functions selected at epicentral distances of 90°, 80°, 70°, 60°, 50° and 40°. The resulting profile along with the waveform fit for each RF and $v_{S,app}$ curve is shown in Figure 6. The velocity profile lies well within the range of the uncertainty and the receiver function at each distance is also well modeled. The variance in velocity again increases with depth and is maximum for the mantle. The median $v_{S,app}$ curves are also close to the observed curve, even though the kinks between 2–3 s and 7 s appear to be slightly sharper than in the observed curve. Unlike C30VH_AKSNL, C30VL_AKSNL has a shorter $v_{S,app}$ curve extending to 82 s (Figure 7). This restricts the retrieval of S-wave velocity information from longer periods and has the effect of an increased variance in the upper mantle velocity. The Moho on the other hand is well resolved due to a high impedance contrast which results in a direct phase at around 6 s for RFs at 40° and 50°, and a clear multiple at around 19 and 24 s for RFs at 90°, 80°, and 70°. Looking at the probability densities we see that using more data has the effect of an overall decrease in uncertainty levels. From Figure 3c, we see that the data is best explained by a 2 layer model which has the highest value for w_j (AICc). To check how a joint inversion performs against separate inversions of $v_{S,app}$ and RF, we further compared their density plots for depth and the velocity of the second layer using the data generated from model C30VL_AKSNL. Here we used the best 25% models of the respective ensembles. In the case of RF inversion alone (Figure 8a), we see a strong trade-off between the Moho depth and velocity above, as RFs as a relative travel-time method are sensitive to the depth-velocity quotient and not absolute velocity. When $v_{S,app}$ data are inverted alone (Figure 8b), the velocity is well recovered but the Moho depth is not very well constrained. Joint inversion of both datasets (Figure 8c) shows a considerable improvement in resolving both the depth and velocity of

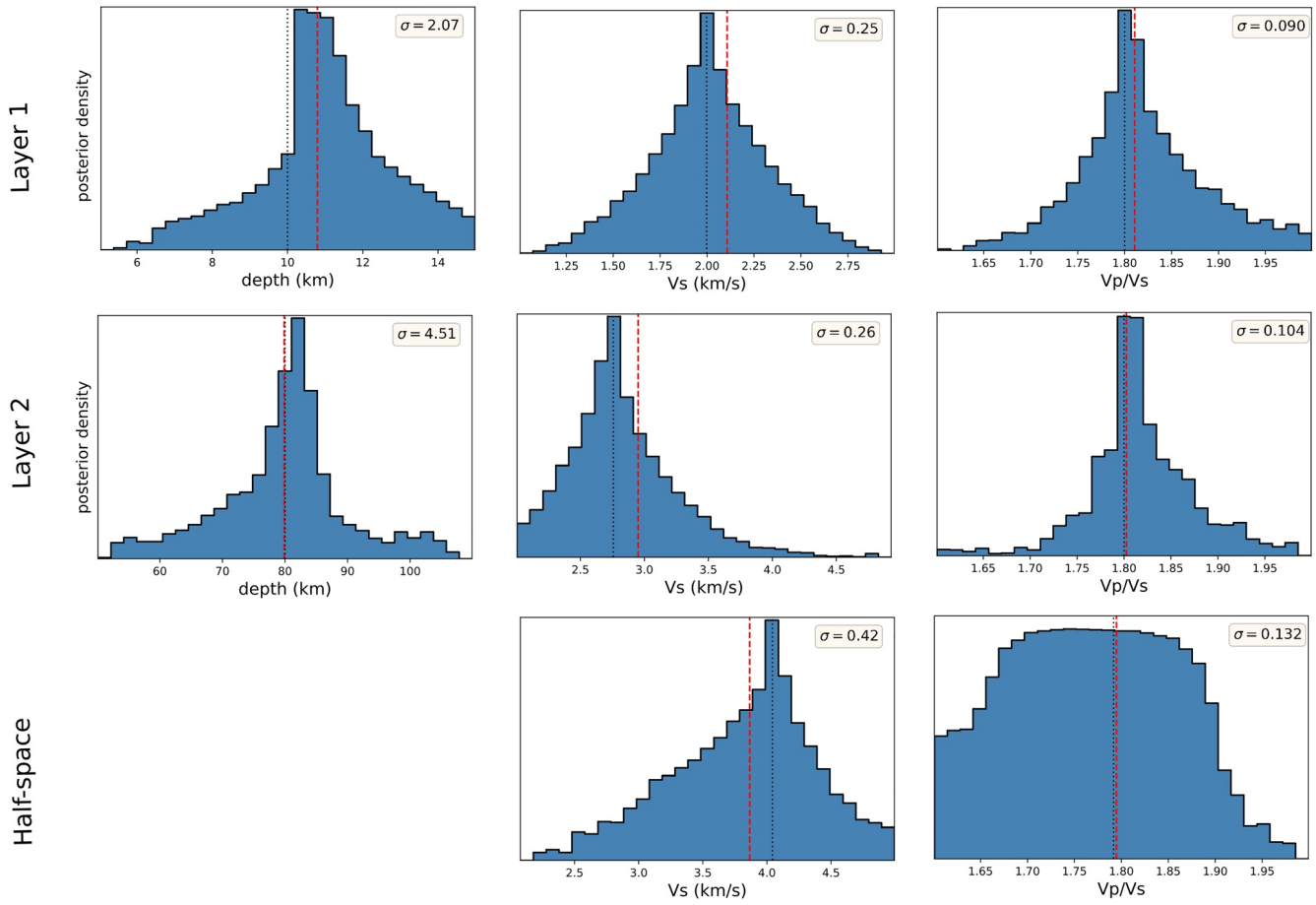

Figure 5. Same as Figure 4 for C80VL_AKSNL.

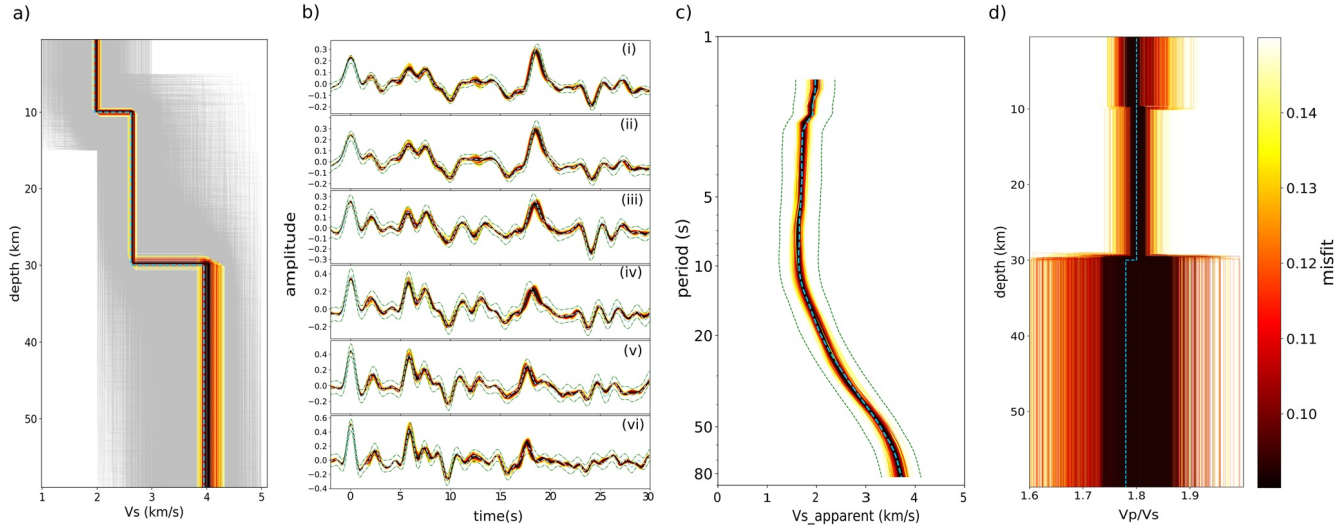

Figure 6. Example of multiple inversions for C30VL_AKSNL (a) 1-D velocity profiles. The light gray lines represent traversed models outside the maximum misfit range. (b) Fit to receiver function waveforms at epicentral distance of (i)90° (ii) 80° (iii) 70° (iv) 60° (v) 50° and (vi) 40° (c) Fit to the median $v_{S,app}$ (d) v_P/v_S ratio as a function of depth. The blue dashed curves denote the observed data and the green dash-dotted lines represent the data uncertainty.

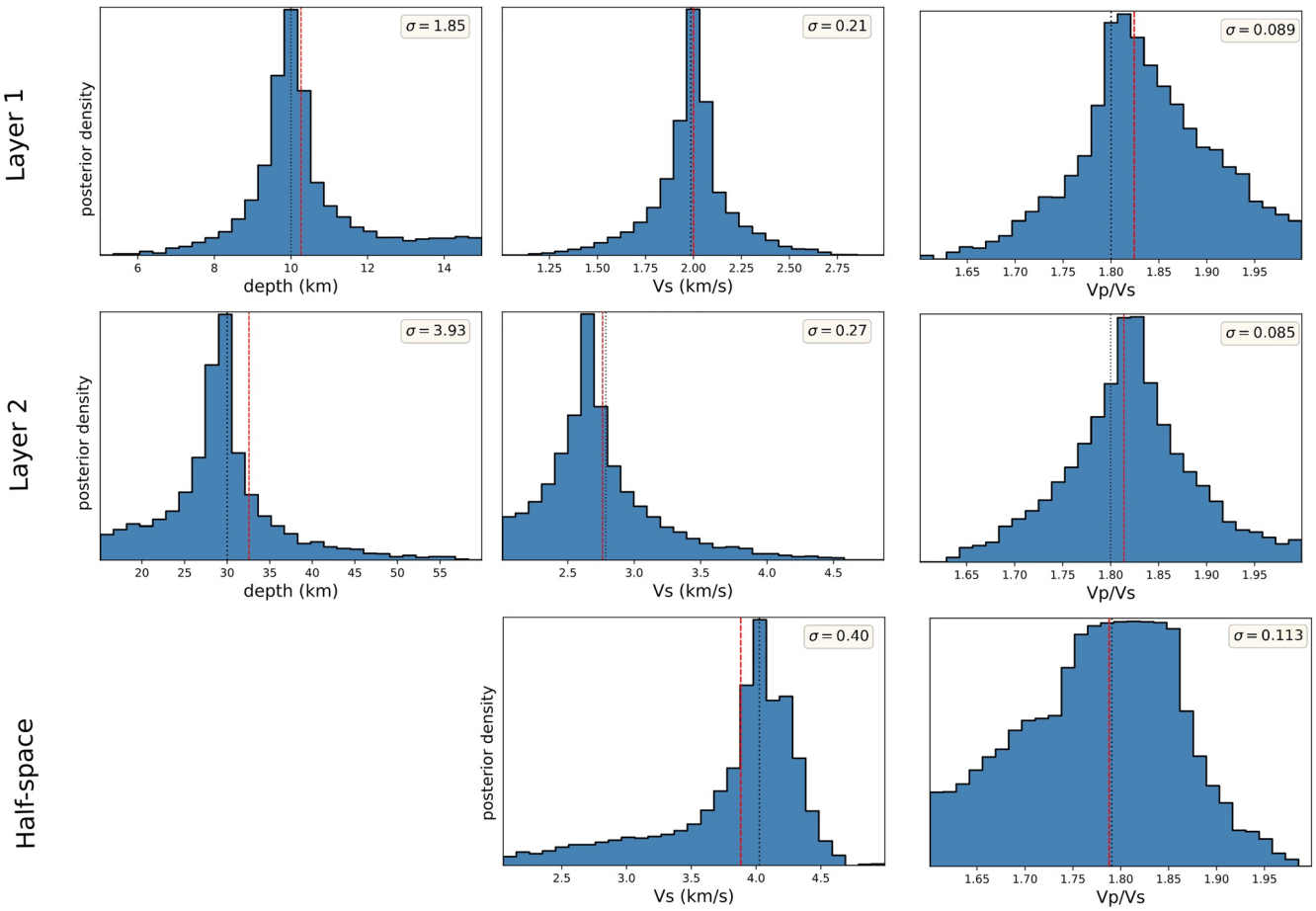

Figure 7. Same as Figure 4 for C30VL_AKSNL.

the second layer and, therefore, the two data types are complementary. For an application of the method to synthetic data with added noise see Drilleau et al. (2020).

4.2. Terrestrial Data

The examples above from synthetic data show that in principle the joint inversion of apparent S-wave velocity with receiver functions serves as a useful complement. This section presents inversion results for

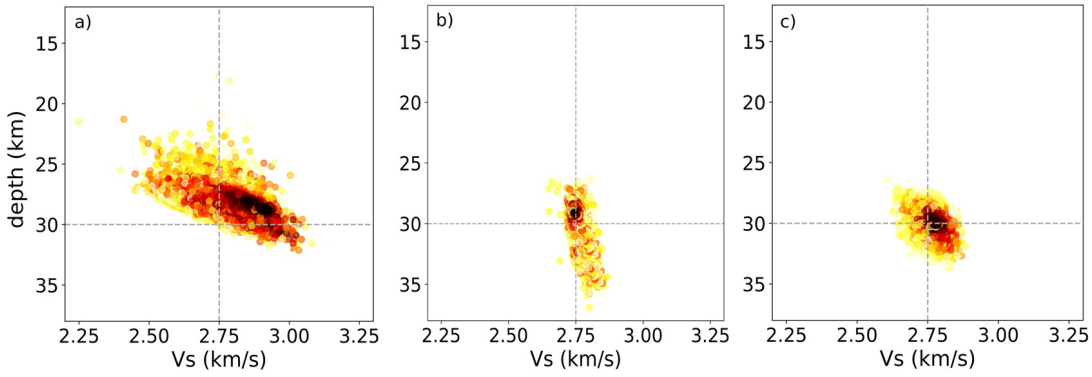

Figure 8. Comparison of depth-velocity trade-off for (a) receiver function (RF) inversion (b) $v_{S,app}$ inversion (c) Joint inversion of RF with $v_{S,app}$. The gray dashed lines denote the true values of depth and velocity of second layer.

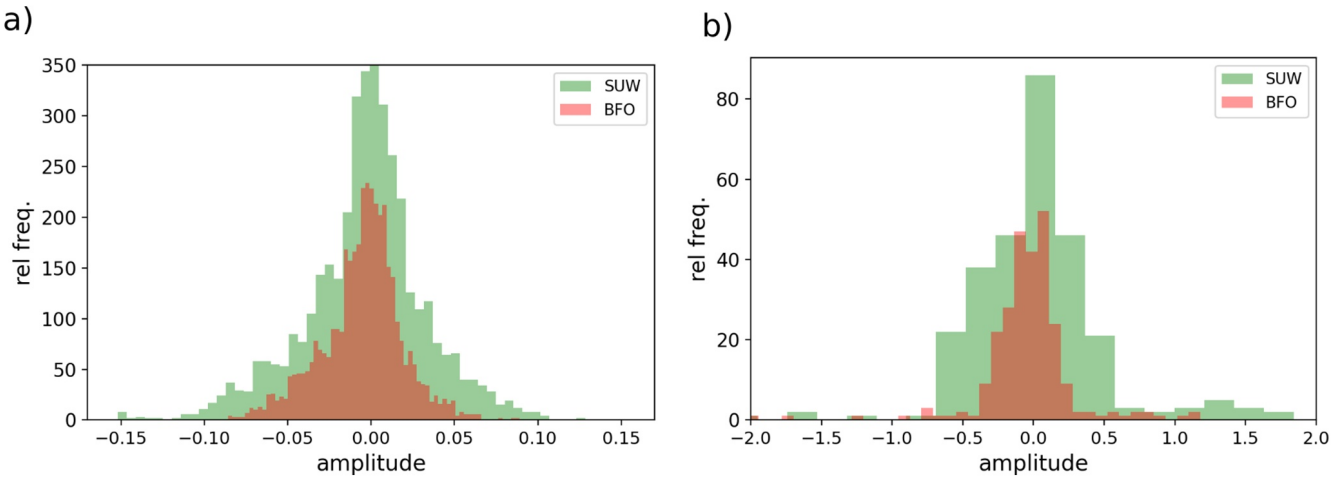

Figure 9. Noise characteristics of (a) Receiver function (RF) shown as a frequency distribution of amplitude calculated from radial component of receiver functions for different stations (b) $v_{S,app}$ calculated as a frequency distribution of error from the median curve.

terrestrial data where the inherent data noise becomes an important consideration and has a strong influence on the resulting model parameters and their associated uncertainties. The RF uncertainty is calculated using the pre-event noise of the radial component of the receiver function since it should ideally be independent and non-correlated. It is defined as twice the standard deviation of the amplitude of the pre-event radial receiver function between −30 and −10 s, relative to the direct P-wave arrival. The uncertainty value for each RF is listed in Table 1. Similarly, the uncertainty in the $v_{S,app}$ is defined as twice the standard deviation of the residuals from the median curve. Figure 9a shows the noise levels computed for stations BFO (green) and SUW (blue)—for each station we calculate the mean of the pre-event noise of the radial component of each receiver function from all the events considered here for multiple inversions and bin them according to amplitude, creating a distribution from which noise parameters can be estimated. The variance in noise level was found to be the higher for SUW with each roughly following a Gaussian distribution. Similarly, Figure 9b shows the noise characteristics for the $v_{S,app}$ curve for both the stations calculated by binning of residuals from the median curve.

Selection of the model complexity that best describes the data is again done using the procedure described in the previous section. Starting at a low degree, we gradually increase the complexity until the parameterization produces no significant deviation in profile and misfit reduction. We then compare the corresponding relative likelihood values and choose the maximum.

The results for seismic station BFO are summarized in Figure 10. From the velocity profile (subplot a) we can see that the data can be sufficiently described by a minimum parameterization comprising 3 layers with constant velocity over a half-space—A low velocity top layer of sediments, an upper crustal layer extending from the base of the sediments to a depth of ~ 7 km and a thick lower crust that extends from 7 to 8 km to the Moho at ~ 25 km depth. Various studies found the Moho depth between 23.8 and 27 km for station BFO (Geissler et al., 2008; Grad et al., 2009; Knapmeyer-Endrun et al., 2014). The mantle velocities are also adequately constrained by the data showing a maximum probability for mantle v_S velocity of 4.6 km/s. The results for the S-wave velocity model also show close agreement with Svenningsen and Jacobsen (2007) (shown in blue dashed lines) and Knapmeyer-Endrun et al. (2018) (shown in green dashed lines). Since Svenningsen and Jacobsen (2007) used the apparent velocity curve up to 0.2 s in contrast to 1.3 s allowed by our data set, the top sediment layer could be better resolved to thickness values below 1 km. Subplots (b) and (c) show the corresponding fits to the receiver function for each event and a median $v_{S,app}$ curve. Except for the RF waveform in event (i) where the phase at ~ 10 s is over-pronounced, the models fit the data from other events adequately well. The modeled $v_{S,app}$ curve also follows the data closely at all periods, including the sharp kink around ~ 2 s. At longer periods after ~ 50 s, the velocities seem to converge to ~ 4.8 km/s providing a tight constraint on the upper mantle which explains the low uncertainty seen in the half-space v_S.

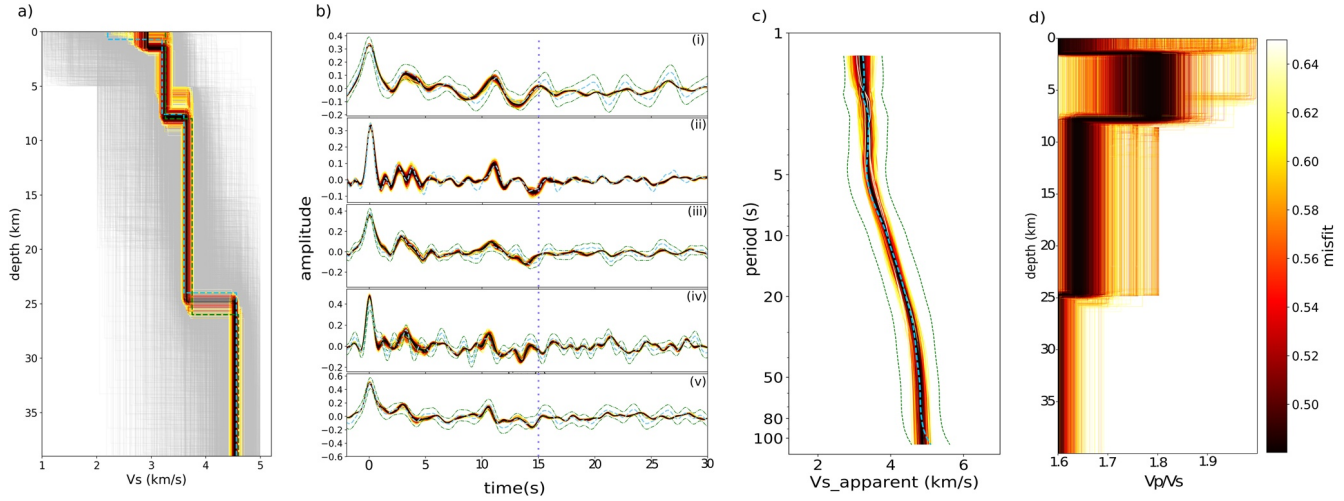

Figure 10. Example of joint inversions for terrestrial data from station BFO (a) 1-D velocity profiles. The blue and green dashed line represents the results from Svenningsen and Jacobsen (2007) and Knapmeyer-Endrun et al. (2018). The light gray lines represent traversed models outside the maximum misfit range. (b) Fit to receiver function waveforms at epicentral distance of (i) 82° (ii) 79° (iii) 70° (iv) 51° (v) 45°. The blue dashed curve denotes the observed radial receiver function and green dashed lines represent the standard error. The dark blue dotted line at 15s shows the end of the misfit window. (c) Fit to the median $v_{S,app}$ (d) v_P/v_S ratio as a function of depth.

Station SUW is located on the East European craton and sits on a relatively thicker crust than BFO. Using a similar parameterization as before with 3 layers including a top sedimentary layer results in a subsurface velocity profile shown in Figure 11a. The model predicts the Moho to be located at a depth of ~ 45 km with the highest probability density and an intra-crustal discontinuity at 15 km. Previous studies have estimated the Moho depth to lie between 41 and 46.8 km for station SUW (Geissler et al., 2008; Grad et al., 2009; Knapmeyer-Endrun et al., 2014). The thickness and v_S of the sedimentary layer, however, are not well constrained with the uncertainty for v_S being the highest amongst all layers. This is also evident from the modeled $v_{S,app}$ curves (subplot c) which show a slight deviation from the observed curve at short periods. Such a deviation could indicate that the sedimentary layer is more complex than our parameterization, which models it simply as a layer with constant velocity. An increase in the model complexity (e.g., modeling the sedimentary layer with a velocity gradient) could lead to a better fit here as suggested by Knapmeyer-Endrun et al. (2018). Further, the missing v_S information at long periods in the observation leads to an increase

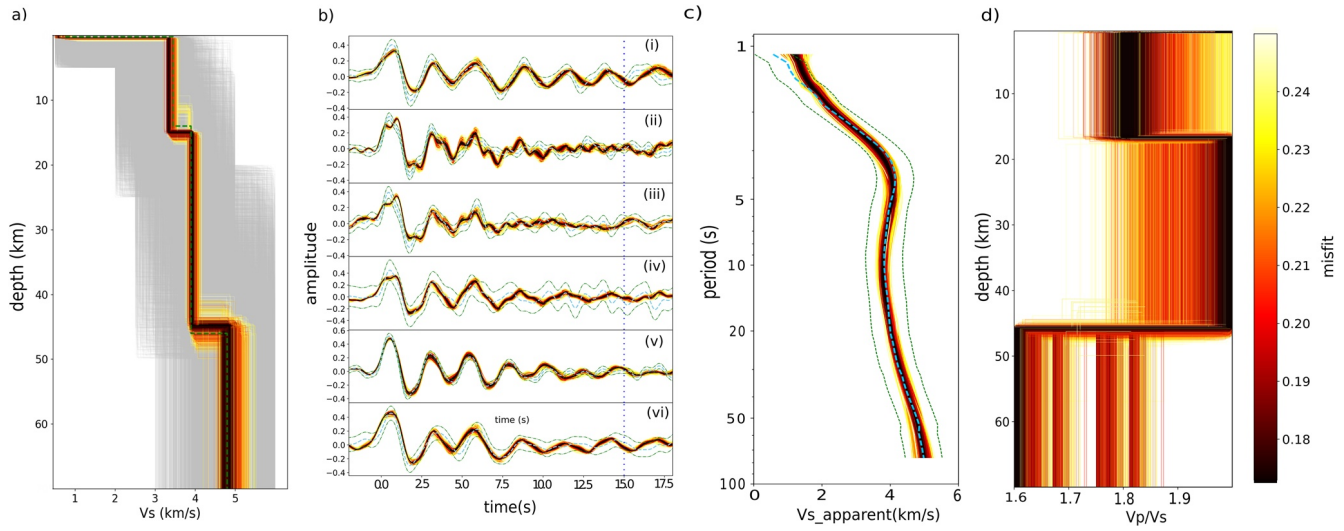

Figure 11. Same as Figure 10 for station SUW (b) shows the fit to receiver function waveforms at epicentral distances of (i) 82° (ii) 77° (iii) 72° (iv) 68° (v) 64° (vi) 60°.

in uncertainty in the upper mantle velocity which shows the highest probability density at a value of ~ 4.9 km/s. The modeled RFs shown in Figure 11b clearly show the ringing effect with gradual decrease in amplitude with time caused by the thin sediment layer. These strong reverberations produce high amplitude oscillations in the early part of the signal and completely masks the direct Moho conversion at ~ 6*s*. This example in particular shows that caution is needed to interpret receiver functions with a sedimentary layer in terms of subsurface structures.

Figures 3d and 3e show the respective model probabilities obtained from AIC values. We see that both the data can be best explained by three layer models with constant velocity over a half-space. However, there is still ~ 9% probability for a 4 layer model in both cases. The resulting values for v_P/v_S for each layer are also shown in subplots (d) in Figures 10 and 11. The a priori ranges for these were selected such they contain and considerably extend around the results from previous studies. Here we used Knapmeyer-Endrun et al. (2014) and Geissler et al. (2008) for information on crustal v_P/v_S values and Artemieva (2007) for the upper mantle. Unlike the case for synthetics, a high variation is observed here between the layers. In all the examples, the top sediment cover shows the highest uncertainty. The first and second layers are better resolved. For the half-space, the resulting values for BFO were observed to be rather variable dependent on the a priori range which indicates that one should be cautious in interpreting the result and that this parameter is not well constrained. The average crustal v_P/v_S values estimated from RF analysis in previous studies are between 1.69 and 1.75 for BFO (Geissler et al., 2008; Knapmeyer-Endrun et al., 2014) and between 1.81 and 1.84 for SUW. We find that the mean values from our results are broadly similar with values of 1.67 and 1.82, respectively. Figures 12 and 13 show the respective 1D marginal posterior densities and a priori ranges used for stations BFO and SUW.

5. Implications for InSight

Some aspects in applying this method to InSight data do warrant attention. As the primary aim here is to obtain a first-order 1D subsurface structure, we have neglected the effects induced by azimuthal anisotropy from our analysis. Although this could potentially lead to amplitude errors in the observed RF waveforms, with only sparse data available, we can consider these to be of second-order. The effect of location uncertainties will also considerably affect the calculation of $v_{S,app}$. Knapmeyer-Endrun et al. (2018) showed that the biggest effect in $v_{S,app}$ can be caused by uncertainty in distance and back azimuth. A ± 25% uncertainty in distance could yield an uncertainty of ± 1 s/deg of the ray parameter for the P phase, while an erroneous back azimuth will lead to a decrease in estimated v_S values at shorter periods. The thickness and velocity of a thin regolith layer can also be quite difficult to resolve if there is missing or erroneous information at short periods, as was the case in our study of terrestrial data. Another factor that limits the information that can be obtained from $v_{S,app}$ on Mars is long-period noise and effects of glitches (Scholz et al., 2020). Knapmeyer-Endrun et al. (2018) suggests that long period noise will affect longer periods while it has been observed that glitches can contaminate any part of the signal. Unlike the synthetics and terrestrial data used in this study, the $v_{S,app}$ curve obtained from actual Mars data could be limited to much shorter periods. This would then increase the uncertainty in the retrieved v_S values at larger depths. A similar situation was encountered in Drilleau et al. (2020). In our previous study, Lognonné et al. (2020), we have been able to constrain the S-wave velocity and depth for the first inter-crustal layer of Mars between 1.7–2.1 km/s and 8–11 km, respectively, using such a limited $v_{S,app}$ curve while further work involving the entire crust is in preparation. It is therefore important that all these factors are correctly accounted for.

6. Summary and Conclusion

In the context of the InSight mission, receiver function analysis has been envisioned as a likely method to study the crustal structure of Mars (Panning et al., 2017). In order to diminish the depth-velocity trade-off inherent in travel time methods, we propose to use the information provided by apparent P-wave incidence angles derived from P-receiver functions as an additional constraint (Knapmeyer-Endrun et al., 2018). In this study, we present a method for joint inversion of receiver functions and frequency-dependent apparent S-wave velocity curves using the Neighborhood Algorithm. This results in an ensemble of model solutions

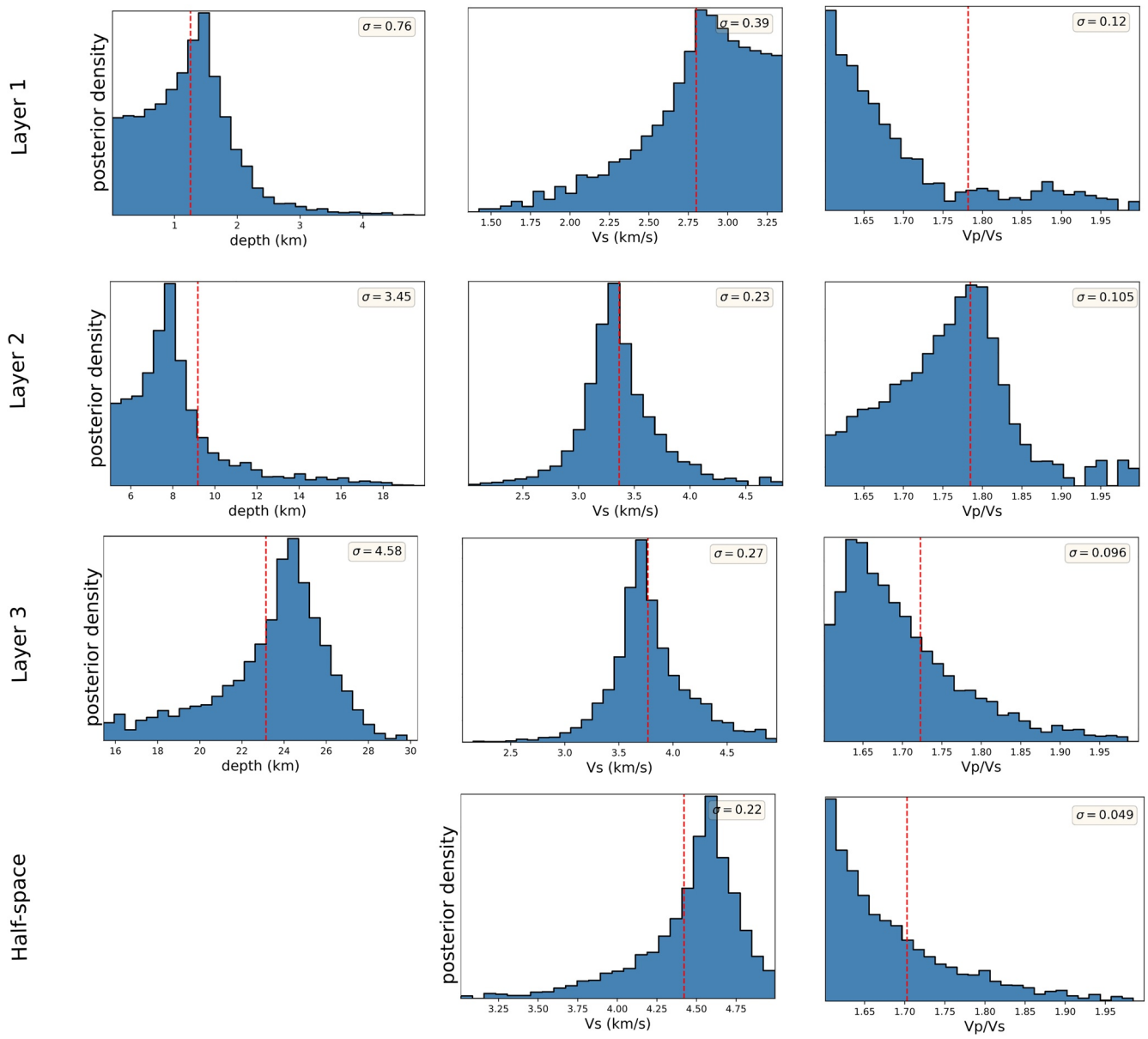

Figure 12. Same as Figure 4 for the inversion of data from station BFO.

along with their respective misfit values which can, in turn, be used to compute the full uncertainty of the model parameters. We then develop such a probabilistic solution using the resultant ensemble and apply this method to various data sets. Further, determining the sufficient number of layers for an optimal model presents another challenge in waveform inversion. We tackle this by gradually increasing the number of layers till adding yet another produces no significant change, and then using AIC as a statistical inference test on all possible model families. The method is successfully applied to synthetic seismograms generated for three a priori Mars subsurface models. Here we used both single and multiple events, and the uncertainty in the retrieved model parameters decreases with an increase in the size of the data set. We then applied the method on terrestrial data from three different seismic stations located in different geological settings. The resulting subsurface models were in good agreement with the results obtained in previous studies using diverse approaches, which corroborated the efficacy of the method.

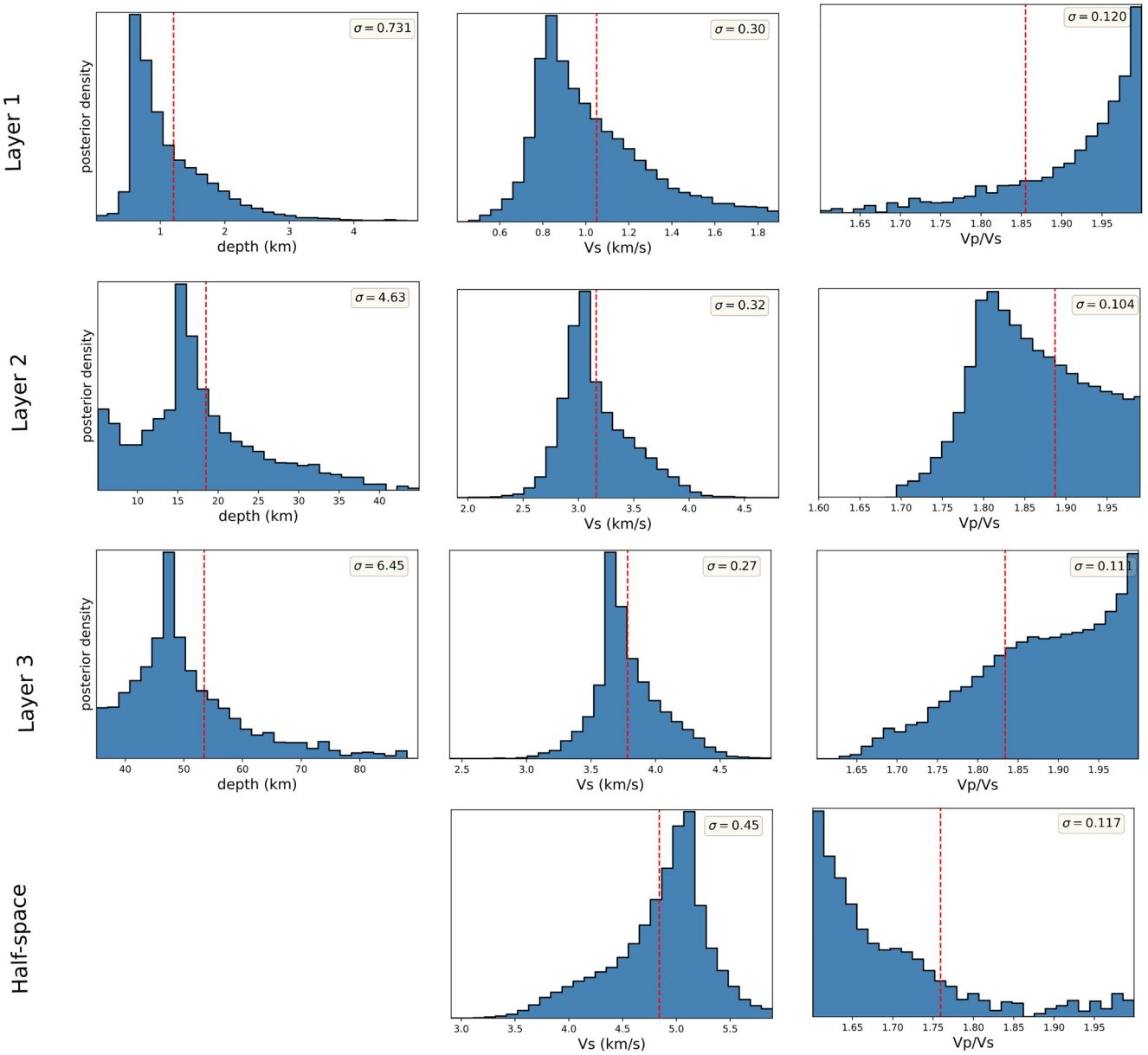

Figure 13. Same as Figure 4 for the inversion of data from station SUW.

Data Availability Statement

Seismic data for station BFO and SUW were obtained from the Federal Institute for Geosciences and Natural Resources and GEOFON data centre of the GFZ German Research Centre for Geosciences, respectively. The data are publicly available and can be obtained from EIDA (http://www.orfeus-eu.org/data/eida/) using the event details listed in Table 1. The GF databases for Martian synthetics are publicly available within the Marsquake Service (MQS) at ETH Zurich (http://instaseis.ethz.ch/marssynthetics/). Details of the seismic station used to retrieve the terrestrial data can be found in the supplement. The authors are thankful to the two anonymous reviewers for their feedback, which helped to improve the manuscript. This study is InSight Contribution Number 216.

Acknowledgments
R. Joshi acknowledges the funding provided by the IMPRS and the Emeritus group. The MPS MPG SEIS team acknowledges funding for development of the SEIS leveling system by the DLR German Space Agency. Open access funding enabled and organized by Projekt DEAL.

References

Akaike, H., Petrov, B. N., & Csaki, F. (1973). *Second international symposium on information theory*. Akademiai Kiado.

Ammon, C. J. (1991). The isolation of receiver effects from teleseismic P waveforms. *Bulletin of the Seismological Society of America*, *81*, 2504–2510. https://doi.org/10.1785/bssa0810062504

Ammon, C. J., Randall, G. E., & Zandt, G. (1990). On the nonuniqueness of receiver function inversions. *Journal of Geophysical Research*, *95*(B10), 15303–15318. https://doi.org/10.1029/jb095ib10p15303

Anderson, D., & Burnham, K. (2004). *Model selection and multi-model inference*. Springer-Verlag.

Artemieva, I. M. (2007). Dynamic topography of the east European craton: Shedding light upon lithospheric structure, composition and mantle dynamics. *Global and Planetary Change*, *58*(1–4), 411–434. https://doi.org/10.1016/j.gloplacha.2007.02.013

Bayes, T. (1763). LII. An essay towards solving a problem in the doctrine of chances. By the late Rev. Mr. Bayes, FRS communicated by Mr. Price, in a letter to John Canton, AMFRS. *Philosophical Transactions of the Royal Society of London*, *53*, 370–418. https://doi.org/10.1098/rstl.1763.0053

Birch, F. (1961). The velocities of compressional waves in rocks to 10 kilobars, Part 2. *Journal of Geophysical Research*, *66*, 2199–2224. https://doi.org/10.1029/jz066i007p02199

Bogdanova, S., Gorbatschev, R., Grad, M., Janik, T., Guterch, A., Kozlovskaya, E., et al. (2006). Eurobridge: New insight into the geodynamic evolution of the East European Craton. *Geological Society, London, Memoirs*, *32*(1), 599–625. https://doi.org/10.1144/gsl.mem.2006.032.01.36

Burnham, K. P., & Anderson, D. R. (2002). *Model selection and multimodel inference*. Springer.

Ceylan, S., van Driel, M., Euchner, F., Khan, A., Clinton, J., Krischer, L., & Giardini, D. (2017). From initial models of seismicity, structure and noise to synthetic seismograms for Mars. *Space Science Reviews*, *211*(1–4), 595–610. https://doi.org/10.1007/s11214-017-0380-6

Chong, J., Ni, S., Chu, R., & Somerville, P. (2016). Joint inversion of body-wave receiver function and Rayleigh-wave ellipticity. *Bulletin of the Seismological Society of America*, *106*(2), 537–551. https://doi.org/10.1785/0120150075

Connolly, J. A. D. (2009). The geodynamic equation of state: What and how. *Geochemistry, Geophysics, Geosystems*, *10*(10). https://doi.org/10.1029/2009gc002540

Drilleau, M., Beucler, E., Lognonn, P., Panning, M. P., Knapmeyer-Endrun, B., Banerdt, W. B., et al. (2020). MSS/1: Single-station and single-event marsquake inversion. *Earth and Space Science*, *7*(12), e2020EA001118. https://doi.org/10.1029/2020EA001118

Du, Z., & Foulger, G. (1999). The crustal structure beneath the northwest fjords, Iceland, from receiver functions and surface waves. *Geophysical Journal International*, *139*(2), 419–432. https://doi.org/10.1046/j.1365-246x.1999.00945.x

Dueker, K. G., & Sheehan, A. F. (1997). Mantle discontinuity structure from midpoint stacks of converted P to S waves across the Yellowstone hotspot track. *Journal of Geophysical Research*, *102*(B4), 8313–8327. https://doi.org/10.1029/96jb03857

Federal Institute for Geosciences and Natural Resources. (1976). *German Regional Seismic Network (GRSN)*. Bundesanstalt für Geowissenschaften und Rohstoffe. Retrieved from https://www.seismologie.bgr.de/doi/grsn/

Fontaine, F. R., Barruol, G., Kennett, B. L., Bokelmann, G. H., & Reymond, D. (2009). Upper mantle anisotropy beneath Australia and Tahiti from P-wave polarization: Implications for real-time earthquake location. *Journal of Geophysical Research*, *114*(B3). https://doi.org/10.1029/2008jb005709

Geissler, W. H., Kind, R., & Yuan, X. (2008). Upper mantle and lithospheric heterogeneities in central and Eastern Europe as observed by teleseismic receiver functions. *Geophysical Journal International*, *174*(1), 351–376. https://doi.org/10.1111/j.1365-246x.2008.03767.x

GEOFON Data Centre. (1993). *Geofon seismic network*. Deutsches GeoForschungsZentrum GFZ. Retrieved from http://geofon.gfz-potsdam.de/doi/network/GE

Grad, M., Jensen, S. L., Keller, G. R., Guterch, A., Thybo, H., Janik, T., et al. (2003). Crustal structure of the Trans-European suture zone region along POLONAISE'97 seismic profile P4. *Journal of Geophysical Research*, *108*(B11). https://doi.org/10.1029/2003jb002426

Grad, M., Tiira, T., & Group, E. W. (2009). The Moho depth map of the European Plate. *Geophysical Journal International*, *176*(1), 279–292. https://doi.org/10.1111/j.1365-246x.2008.03919.x

Hannemann, K., Krüger, F., Dahm, T., & Lange, D. (2016). Oceanic lithospheric S wave velocities from the analysis of P wave polarization at the ocean floor. *Geophysical Journal International*, *207*, 1796–1817. https://doi.org/10.1093/gji/ggw342

Hannemann, K., Krüger, F., Dahm, T., & Lange, D. (2017). Structure of the oceanic lithosphere and upper mantle north of the Gloria fault in the eastern mid-Atlantic by receiver function analysis. *Journal of Geophysical Research*, *122*, 7927–7950. https://doi.org/10.1002/2016JB013582

Helffrich, G., & Thompson, D. (2010). A stacking approach to estimate Vp/Vs from receiver functions. *Geophysical Journal International*, *182*(2), 899–902. https://doi.org/10.1111/j.1365-246x.2010.04628.x

Julia, J., Ammon, C. J., Herrmann, R., & Correig, A. M. (2000). Joint inversion of receiver function and surface wave dispersion observations. *Geophysical Journal International*, *143*(1), 99–112. https://doi.org/10.1046/j.1365-246x.2000.00217.x

Jurkevics, A. (1988). Polarization analysis of three-component array data. *Bulletin of the Seismological Society of America*, *78*(5), 1725–1743.

Kennett, B. L. N., Engdahl, E. R., & Buland, R. (1995). Constraints on seismic velocities in the Earth from traveltimes. *Geophysical Journal International*, *122*(1), 108–124. https://doi.org/10.1111/j.1365-246X.1995.tb03540.x

Khan, A., & Connolly, J. (2008). Constraining the composition and thermal state of Mars from inversion of geophysical data. *Journal of Geophysical Research: Planets*, *113*(E7). https://doi.org/10.1029/2007je002996

Khan, A., van Driel, M., Böse, M., Giardini, D., Ceylan, S., Yan, J., et al. (2016). Single-station and single-event marsquake location and inversion for structure using synthetic Martian waveforms. *Physics of the Earth and Planetary Interiors*, *258*, 28–42. https://doi.org/10.1016/j.pepi.2016.05.017

Kind, R., Kosarev, G., & Petersen, N. (1995). Receiver functions at the stations of the German Regional Seismic Network (GRSN). *Geophysical Journal International*, *121*, 191–202. https://doi.org/10.1111/j.1365-246x.1995.tb03520.x

Knapmeyer-Endrun, B., Ceylan, S., & van Driel, M. (2018). Crustal S-wave velocity from apparent incidence angles: A case study in preparation for insight. *Space Science Reviews*, *214*(5), 83. https://doi.org/10.1007/s11214-018-0510-9

Knapmeyer-Endrun, B., Krüger, F., & Group, t. P. W. (2014). Moho depth across the Trans-European Suture zone from P- and S-receiver functions. *Geophysical Journal International*, *197*(2), 1048–1075. https://doi.org/10.1093/gji/ggu035

Langston, C. A. (1979). Structure under Mount Rainier, Washington, inferred from teleseismic body waves. *Journal of Geophysical Research*, *84*(B9), 4749–4762. https://doi.org/10.1029/jb084ib09p04749

Lognonné, P., Banerdt, W. B., Giardini, D., Pike, W., Christensen, U., Laudet, P., et al. (2019). SEIS: Insight's seismic experiment for internal structure of Mars. *Space Science Reviews*, *215*(1), 12.

Lognonné, P., Banerdt, W. B., Pike, W., Giardini, D., Christensen, U., Garcia, R. F., et al. (2020). Constraints on the shallow elastic and anelastic structure of mars from insight seismic data. *Nature Geoscience*, *13*(3), 213–220.
Nissen-Meyer, T., van Driel, M., Stahler, S. C., Hosseini, K., Hempel, S., Auer, L., et al. (2014). AxiSEM: Broadband 3-D seismic wavefields in axisymmetric media. *Solid Earth*, *5*, 425–445. https://doi.org/10.5194/se-5-425-2014
Owens, T. J., Taylor, S. R., & Zandt, G. (1987). Crustal structure at regional seismic test network stations determined from inversion of broadband teleseismic P waveforms. *Bulletin of the Seismological Society of America*, *77*(2), 631–662.
Panning, M. P., Lognonné, P., Bruce Banerdt, W., Garcia, R., Golombek, M., Kedar, S., et al. (2017). Planned products of the Mars structure service for the insight mission to Mars. *Space Science Reviews*, *211*(1), 611–650. https://doi.org/10.1007/s11214-016-0317-5
Park, S., & Ishii, M. (2018). Near-surface compressional and shear wave speeds constrained by body-wave polarization analysis. *Geophysical Journal International*, *213*(3), 1559–1571. https://doi.org/10.1093/gji/ggy072
Peng, H.-C., Hu, J.-F., Yang, H.-Y., & Wen, L.-M. (2012). An effective technique 628 to constrain the non-uniqueness of receiver function inversion. *Chinese Journal of Geophysics*, *55*(2), 194–205.
Phinney, R. A. (1964). Structure of the Earth's crust from spectral behavior of long-period body waves. *Journal of Geophysical Research*, *69*(14), 2997–3017. https://doi.org/10.1029/jz069i014p02997
Sambridge, M. (1999a). Geophysical inversion with a neighbourhood algorithm—I. Searching a parameter space. *Geophysical Journal International*, *138*, 479–494. https://doi.org/10.1046/j.1365-246X.1999.00876.x
Sambridge, M. (1999b). Geophysical inversion with a neighbourhood algorithm—II. Appraising the ensemble. *Geophysical Journal International*, *138*(3), 727–746. https://doi.org/10.1046/j.1365-246x.1999.00900.x
Schiffer, C., Stephenson, R., Oakey, G. N., & Jacobsen, B. H. (2016). The crustal structure of Ellesmere Island, Arctic Canada—Teleseismic mapping across a remote intraplate orogenic belt. *Geophysical Journal International*, *204*(3), 1579–1600. https://doi.org/10.1093/gji/ggv539
Scholz, J.-R., Widmer-Schnidrig, R., Davis, P., Lognonné, P., Pinot, B., Garcia, R. F., et al. (2020). Detection, analysis, and removal of glitches from insight's seismic data from mars. *Earth and Space Science*, *7*(11). https://doi.org/10.1029/2020ea001317
Schulte-Pelkum, V., Masters, G., & Shearer, P. M. (2001). Upper mantle anisotropy from long-period P-wave polarization. *Journal of Geophysical Research*, *106*(B10), 21917–21934. https://doi.org/10.1029/2001jb000346
Shibutani, T., Sambridge, M., & Kennett, B. (1996). Genetic algorithm inversion for receiver functions with application to crust and uppermost mantle structure beneath eastern Australia. *Geophysical Research Letters*, *23*(14), 1829–1832. https://doi.org/10.1029/96gl01671
Svenningsen, L., & Jacobsen, B. (2007). Absolute S-velocity estimation from receiver functions. *Geophysical Journal International*, *170*(3), 1089–1094. https://doi.org/10.1111/j.1365-246x.2006.03505.x
van Driel, M., Krischer, L., Stähler, S. C., Hosseini, K., & Nissen-Meyer, T. (2015). Instaseis: Instant global seismograms based on a broadband waveform database. *Solid Earth*, *6*(2), 701–717. https://doi.org/10.5194/se-6-701-2015
van Driel, M., Wassermann, J., Pelties, C., Schiemenz, A., & Igel, H. (2015). Tilt effects on moment tensor inversion in the near field of active volcanoes. *Geophysical Journal International*, *202*(3), 1711–1721. https://doi.org/10.1093/gji/ggv209
Vinnik, L. (1977). Detection of waves converted from P to SV in the mantle. *Physics of the Earth and Planetary Interiors*, *15*(1), 39–45. https://doi.org/10.1016/0031-9201(77)90008-5
Wagenmakers, E.-J., & Farrell, S. (2004). AIC model selection using Akaike weights. *Psychonomic Bulletin & Review*, *11*(1), 192–196. https://doi.org/10.3758/bf03206482
Wathelet, M. (2008). An improved neighborhood algorithm: Parameter conditions and dynamic scaling. *Geophysical Research Letters*, *35*, L09301. https://doi.org/10.1029/2008GL033256
Wiechert, E. (1907). *Über Erdbebenwellen. I. Theoretisches über die Ausbreitung der Erdbebenwellen. Nachrichten von der Gesellschaft der Wissenschaften zu Göttingen*. Mathematisch-Physikalische Klasse.
Wilde-Piórko, M., Grycuk, M., Polkowski, M., & Grad, M. (2017). On the rotation of teleseismic seismograms based on the receiver function technique. *Journal of Seismology*, *21*(4), 857–868. https://doi.org/10.1007/s10950-017-9640-x
Zhu, L., & Kanamori, H. (2000). Moho Depth variations in southern California from teleseismic receiver functions. *Journal of Geophysical Research*, *105*(B2), 2969–2980. https://doi.org/10.1029/1999jb900322
Ziegler, P. A. (1992). European Cenozoic rift system. *Geodynamics of Rifting*, *1*, 91–111. https://doi.org/10.1016/b978-0-444-89912-5.50009-0

Chapter 3

Thickness and structure of the martian crust from InSight seismic data

This chapter was published in Science, Vol 373, Issue 6553 in July 2021 under the title "Thickness and structure of the martian crust from InSight seismic data" by Knapymeyer-Endrun et al. Conceptualization, data analysis, creation of figures, and contribution to the supplement were carried out by me under the supervision of Dr. B. Knapmeyer-Endrun.

The supporting information for this chapter can be found in Appendix B. At the request of the publishing journal, the following text has been included in the accepted version of the manuscript without any changes.

Thickness and structure of the Martian crust from InSight seismic data

Brigitte Knapmeyer-Endrun[1]*, Mark P. Panning[2], Felix Bissig[3], Rakshit Joshi[4], Amir Khan[3,5], Doyeon Kim[6], Vedran Lekić[6], Benoit Tauzin[7,8], Saikiran Tharimena[2,9], Matthieu Plasman[10], Nicolas Compaire[11], Raphael F. Garcia[11], Ludovic Margerin[12], Martin Schimmel[13], Éléonore Stutzmann[10], Nicholas Schmerr[6,] E. Bozdağ[14], Ana-Catalina Plesa[15], Mark A. Wieczorek[16], Adrien Broquet[17,16], Daniele Antonangeli[18], Scott M. McLennan[19], Henri Samuel[10], Chloé Michaut[7,20], Lu Pan[21],Suzanne E. Smrekar[2], Catherine L. Johnson[22,23], Nienke Brinkman[3], Anna Mittelholz[3], Attilio Rivoldini[24], Paul M. Davis[25], Philippe Lognonné[10,20], Baptiste Pinot[11], John-Robert Scholz[4], Simon Stähler[3], Martin Knapmeyer[15], Martin van Driel[3], Domenico Giardini[3], W. Bruce Banerdt[2]

[1] Bensberg Observatory, University of Cologne, Vinzenz-Pallotti-Str. 26, 51429 Bergisch Gladbach, Germany.

[2] Jet Propulsion Laboratory, California Institute of Technology; 4800 Oak Grove Dr., M/S 183-301, Pasadena, CA 91109, USA.

[3] Institute of Geophysics, ETH Zurich, Sonneggstr. 5, 8092 Zürich, Switzerland.

[4] Max Planck Institute for Solar System Research, Justus-von-Liebig-Weg 3, 37077 Göttingen, Germany.

[5] Physik-Institut, University of Zurich, Zurich, Switzerland.

[6] University of Maryland, College Park, Department of Geology, 8000 Regents Dr., College Park, MD, 20782-4211, USA.

[7] Université de Lyon, Ecole Normale Supérieure de Lyon, Université Claude Bernard Lyon 1, CNRS, Laboratoire de Géologie de Lyon : Terre, Planètes, Environnement, 69622 Villeurbanne, France.

[8] Research School of Earth Sciences, The Australian National University, Canberra, Australian Capital Territory 0200, Australia.

[9] now at University of Vienna, Althanstrasse 14, 1090 Vienna, Austria.

[10]Université de Paris, Institut de Physique du Globe de Paris, CNRS, F-75005 Paris, France.

[11] Institut Supérieur de l'Aéronautique et de l'Espace SUPAERO, 10 Avenue Edouard Belin, 31400 Toulouse, France.

[12] Institut de Recherche en Astrophysique et Planétologie, Université Toulouse III Paul Sabatier, CNRS, CNES, 14 Av. E. Belin, 31400, Toulouse, France.

[13] Geosciences Barcelona - CSIC, Barcelona, Spain.

[14] Colorado School of Mines, Department of Geophysics, 1500 Illinois Street, Golden, CO 80401, USA.

[15] Institute of Planetary Research, German Aerospace Center (DLR), 12489 Berlin, Germany.

[16] Université Côte d'Azur, Observatoire de la Côte d'Azur, CNRS, Laboratoire Lagrange, France.

[17] Lunar and Planetary Laboratory, University of Arizona, Tucson, AZ 85721, USA.

[18] Sorbonne Université, Muséum National d'Histoire Naturelle, UMR CNRS 7590, Institut de Minéralogie, de Physique des Matériaux et de Cosmochimie, IMPMC, 75005 Paris, France.

[19] Department of Geosciences, Stony Brook University, Stony Brook, NY, 11794-2100, USA.

[20] Institut Universitaire de France.

[21] University of Copenhagen, GLOBE Institute, Center for Star and Planet Formation, Copenhagen, Denmark.

[22] Department of Earth, Ocean and Atmospheric Sciences, University of British Columbia, Vancouver, BC, V6T 1Z4, Canada.

[23] Planetary Science Institute, Tucson, 1700 East Fort Lowell, Suite 106, Tucson, AZ 85719-2395, USA.

[24] Royal Observatory of Belgium, Brussels, Belgium.

[25] Department of Earth, Planetary, and Space Sciences, University of California Los Angeles, CA90095, USA.

*Correspondence to: bknapmey@uni-koeln.de.

A planet's crust bears witness to the history of planetary formation and evolution, but for Mars, no absolute measurement of crustal thickness was available. Here, we determine the structure of the crust beneath the InSight landing site on Mars using both marsquake recordings and the ambient wavefield. Analyzing seismic phases that are reflected and converted at subsurface interfaces, we find that the observations are consistent with models with at least two, and possibly three interfaces. If the second interface is the boundary of the crust, the thickness is 20±5 km, while if the third interface is the boundary, the thickness is 39±8 km. Global maps of gravity and topography allow extrapolation of this point measurement to the whole planet, showing that the average thickness of the Martian crust lies between 24 and 72 km. Independent bulk composition and geodynamic constraints show that the thicker model is consistent with the abundances of crustal heat-producing elements observed for the shallow surface, whereas the thinner model requires greater concentration at depth.

One Sentence Summary:
Based on multiple approaches, direct seismic measurements constrain global crustal thickness, geochemistry and geodynamic processes.

Planetary crusts form as a result of mantle differentiation and subsequent magmatic processes, including partial melting of mantle reservoirs that may continue to the present day *(1)*. For Mars, the cratering record shows that much of its crust formed early in the planet's history and was accompanied by substantial volcanism *(2,3)*. During both the initial crystallization of a putative magma ocean as well as later-stage partial melting, incompatible components, including heat-producing elements (HPE) and volatiles, concentrated in the melt and were largely sequestered into the crust. The thickness of the crust of Mars thus provides fundamental constraints on how the planet differentiated, how incompatible elements were partitioned among the major silicate reservoirs, and how the planet evolved thermally and magmatically over geologic time *(4-6)*.

Previous estimates of the crustal thickness of Mars and its spatial variations were made by modeling the relationship between gravity and topography. By assuming Airy isostasy and using a restrictive range of crustal densities of 2700-3100 kg m^{-3}, the average crustal thickness of the planet was reported to be 57±24 km *(7)*. More recent analyses, however, have used elemental abundances of the surface *(8)* along with major element chemistry of Martian meteorites to argue that the crust could be considerably denser, with values close to ~3300 kg m^{-3}. If these higher densities were representative of the underlying crust, the gravity data would allow average crustal thicknesses up to 110 km *(9)*. In contrast, bulk crustal densities lower than previously assumed (~2600 kg m^{-3}) have been inferred from gravity analyses and would allow a thinner average crustal thickness *(10)*. Low densities were confirmed locally for the near-surface sediments in Gale crater *(11)* as well as the pyroclastic deposit of the Medusa Fossae Formation *(12)*. Low bulk crustal densities could result from either substantial porosity or the presence of buried silica- and feldspar-rich rocks *(13)*. Silica-rich magmatic rocks are potentially consistent with ancient evolved lithologies identified in Martian meteorite breccias *(14)*.

We used data from the Seismic Experiment for Interior Structure (SEIS) on NASA's InSight mission *(15)* to provide an absolute measurement of Mars' crustal thickness and layering. Our assessment of the crustal structure at the landing site is based on a combination of methods using both converted and reflected seismic phases, in order to resolve trade-offs between the depth of a layer and its seismic velocity *(16)*. By calculating receiver functions *(17,18)*, we extracted P-to-S conversions from the P-wave coda of three seismic events with the clearest P-wave onsets and polarizations. In addition, we applied seismic interferometric techniques by calculating autocorrelations of both ambient noise and event coda using the vertical component. Under the assumption of a diffuse wavefield, as expected in the case of noise from homogeneously distributed, uncorrelated sources as well as in the coda of high-frequency events, the correlations can be interpreted as zero-offset vertical reflection responses *(19)*. By focusing on the reflected wavefield, the autocorrelations provide independent and complementary information to the receiver function conversion-based methods that make use of the transmitted wavefield *(20)*.

In a previous study *(18)*, we already considered P-to-S receiver functions for two of the same events, but only inverted for the properties of the interface at the base of the shallowest layer (interpreted there as a transition from fractured to unfractured basalt within the crust), causing the first converted arrival at 2.4 s. Including an additional event and applying extensive re-analysis to the data *(16)*, the P-to-S receiver functions for 9 different processing methods *(16)* show three consistent positive arrivals within the first 8 s, but no clear and consistent negative arrivals or later phases (Fig. 1A). As all three events are located at epicentral distances between 25° and 59° *(21,22)*, no strong move-out of either direct arrivals or multiple reflections is expected, which impedes the unambiguous identification of multiples. The third positive arrival at 7.2-7.5 s could be either simply a PpPs multiple of the first arrival at 2.4 s (ray path 3 in Fig. 2B), or contain additional energy from a direct conversion from a third, deeper discontinuity (ray path 3 in Fig. 2D). We applied two inversion approaches to the P-to-S receiver functions *(16)*, and both can match the three clear peaks with either two (Fig. 2A-B) or three interfaces (Fig. 2C-D). In both inversion approaches, our models showed robust and consistent depths of the two shallowest interfaces. The first layer with a thickness of 6-11 km and an S-wave velocity between 1.2 and 2.1 km/s is consistent with the previous results for the shallow crust *(18)*, whereas a second interface is found at 15-25 km depth independent of the model parameterization. The third interface, the existence of which is supported but not absolutely required by the data, showed greater variability in depth between different inversion choices and generally required a smaller velocity contrast at the base of this layer than for the shallower second interface (Figs. S18, S19). Based on the ensemble of models from the two inversion approaches, our results are consistent with either a local crustal thickness at the InSight landing site of 15-25 km, when the base of layer 2 is the Moho (thin crust models), or 27-47 km, when the base of layer 3 is the Moho (thick crust models; Figs. 2, S18, S19). S-to-P receiver functions can also be calculated for 2 events (S0173a and S0235b; Figs. S4, S6, S7) and both show a signal consistent with conversion at the first interface, while S0235b also shows possible arrivals consistent with deeper conversions *(16)*. Further support for the P-to-S receiver function-derived models is provided by waveform fits in inversions for source mechanisms *(16)*, where a strong interface around 24 km depth is required to match S-precursors.

Vertical component autocorrelations based on different data sets and processing algorithms *(16,23)* show consistent energy maxima in the 5 to 6 s, 10 to 11 s, and 20 to 21.5 s time ranges (Fig. 3). Comparison with predicted arrival times from representative models produced by the receiver function inversion shows that these energy maxima can be explained by P-wave reflections in those models interacting with the first two interfaces, without any clear observations requiring the third interface. Previously published autocorrelations *(24)* contain an arrival near 10 s that is consistent with our results, and which can be explained as a P-wave reflection from the bottom of the second layer at around 22 km depth. A second arrival reported by *(24)* near 20 s, that is also present in many of the autocorrelation functions calculated here, is consistent with a multiple reflection from that layer (Fig. 3). These arrivals were interpreted by Deng and Levander *(24)* as P and S reflections, respectively, from a crust-mantle discontinuity at a depth

of 35 km. However, we do not expect a strong S reflection in a vertical autocorrelation as vertically propagating S waves are horizontally polarized. Interpreting the second arrival as a multiple P reflection instead is consistent with our receiver function-derived results and more likely to be observed in a vertical component autocorrelation. The previously published crustal thickness estimate of 35 km based on autocorrelations *(24)* is consistent with the possible range of the thick crust models, but the specific arrivals identified in that study are more consistent with a reflection and multiple from the shallower second interface around 20 km depth.

We inverted for the thickness of the crust at global scale using the seismically-estimated thickness at the InSight landing site and observed gravity field as constraints *(16)*. Our models consider the gravity of hydrostatic relief along density interfaces beneath the lithosphere, surface relief, variations in thickness of a constant density crust, and the low-density polar cap deposits *(25)*. We employed several different interior pre-landing models *(26)* that specify the density profile of the mantle and core, and for each, we constructed crustal thickness models for all permissible crustal densities. For a given seismic thickness, the mean thickness of the crust depends almost exclusively on the density contrast across the crust-mantle interface (Fig. S22). To ensure that the thickness of the crust is positive within the major impact basins, each reference model has a maximum permissible crustal density. If the thin crust seismic model is used as a constraint, the global mean crustal thickness is predicted to lie between 24 and 38 km and the maximum permissible density of the crust is 2850 kg m^{-3} (Figs. 4, S22, S23). For the thick crust seismic model, the average crustal thickness lies between 39 and 72 km and the maximum permissible crustal density is 3100 kg m^{-3} (Figs. 4, S22, S23). For both seismic constraints, the crustal density is substantially less than would be expected based on the composition of surface materials *(9)*, which is close to 3300 kg m^{-3}. The lower bulk densities are signatures of highly altered layers and can be accounted for by the presence of more than 5% porosity in the crust on average, the presence of fluids or low-density cements filling fractures and pore space, the existence of abundant petrologically evolved felsic rocks beneath the surface layer, or a combination thereof.

The seismic observations argue for a relatively thin crust, or at least thinner than some earlier predictions *(9)*, providing constraints on crustal heat production and the degree of planetary silicate differentiation (Fig. 4). As the present-day crustal thickness is the outcome of the planet's differentiation history *(27,28)*, geodynamic and geologic modeling can place constraints on the composition of the crust and of the mantle, and on the cooling rate of the planet *(16)*. Our results indicate that average crustal thickness models that are consistent with the thick crust seismic model are compatible with currently accepted bulk *(29,30)* and crustal *(8,31)* heat producing element contents, and the occurrence of present-day melting only in an ascending plume below the thickened crust of the Tharsis province (Fig. S27). Such a scenario implies a crust that is about 13 times more enriched in heat producing elements than the primitive mantle (Fig. S24), consistent with 55-70% of the Martian heat producing elements being sequestered into the crust. In contrast, the thin crust seismic model requires a crust that is about 21 times more enriched than a relatively cold primitive mantle (Fig. S25). This is more than two times larger than estimates from gamma-ray spectroscopy data which constrains the surface layer of the crust (Table S6) and would point towards an enrichment in heat-producing elements beneath the surface layer *(16)*. Furthermore, this would call for an efficient process of incompatible element extraction from the mantle, possibly by upward segregation during the solidification of a magma ocean, or by a secondary differentiation mechanism, as for the continental crust of Earth. In both crustal models, assuming a Wänke and Dreibus *(29)* bulk composition, the present-day heat flux is predicted to lie between 20 and 25 mW m^{-2} (Fig. 4). The depth to the crust-mantle boundary, as well as layering in the crust can further constrain crustal magnetization amplitudes, depending on whether the magnetization is carried in upper or lower crustal layers, or both *(16)*. We can also investigate whether crustal thickness and density models are consistent with moment-of-inertia measurements and constraints on the properties of Mars core from the k_2 tidal Love number *(16)*. Generally, these constraints are easier to match for most mantle composition models with the thick crust seismic models, although some models also allow for the thin crust model. Overall,

when considering geodynamic, geochemical, and geodetic constraints, the thin crust models place tighter constraints on the density and enrichment of heat producing elements within the crust, as well as on the mantle composition, than the thick crust models, but neither of the two can be excluded.

References and Notes:

1. L. T. Elkins-Tanton, Magma oceans in the inner solar system. *Annu. Rev. Earth. Planet. Sci.* **40**, 113-139 (2012).
2. M. Grott et al., Long-term evolution of the Martian crust-mantle system. *Space Sci. Rev.* **174**, 49-111 (2013).
3. F. Nimmo, K. Tanaka, Early crustal evolution of Mars. *Annu. Rev. Earth Planet. Sci.* **33**, 133-161 (2005).
4. D. Breuer, W.B. Moore, "10.08—Dynamics and thermal history of the terrestrial planets, the Moon, and Io", in *Treatise on Geophysics*, G. Schubert Ed. (Elsevier, Oxford, ed. 2, 2015), pp. 255–305.
5. S. A. Hauck II, R. J. Philips, Thermal and crustal evolution of Mars. *J. Geophys. Res.* **107**, 5052 (2002).
6. A.-C. Plesa et al., The thermal state and interior structure of Mars. *Geophys. Res. Lett.* **45**, 12198-12209 (2018).
7. M. A. Wieczorek, M. T. Zuber, Thickness of the Martian crust: Improved constraints from geoid-to-topography ratios. *J. Geophys. Res.* **109**, E01009 (2004).
8. B. C. Hahn, S. M. McLennan, E. C. Klein, Martian surface heat production and crustal heat flow from Mars Odyssey Gamma-Ray spectrometry. *Geophys. Res. Lett.* **38**, L14203 (2011).
9. D. Baratoux et al., Petrological constraints on the density of the Martian crust. *J. Geophys. Res.* **119**, 1707– 1727 (2014).
10. S. Goossens et al., Evidence for a low bulk crustal density for Mars from gravity and topography. *Geophys. Res. Lett.* **44**, 7686– 7694 (2017).
11. K. W. Lewis et al., A surface gravity traverse on Mars indicates low bedrock density at Gale crater. *Science* **363**, 535-537 (2019).
12. L. Ojha, K. Lewis, The density of the Medusae Fossae Formation: Implications for its composition, origin, and importance in Martian history. *J. Geophys. Res.* **123**, 1368– 1379 (2018).
13. V. Sautter et al., In situ evidence for continental crust on early Mars. *Nature Geoscience* **8**, 605-609 (2015).
14. M. Humayun et al., Origin and age of the earliest Martian crust from meteorite NWA7533. *Nature* **503**, 513-516 (2013).
15. P. Lognonné et al., SEIS: Insight's Seismic Experiment for Internal Structure of Mars. *Space. Sci. Rev.* **215**, 12 (2019).
16. Methods and additional materials are available as supplementary materials on Science Online.
17. C. A. Langston, Structure under Mount Rainier, Washington, inferred from teleseismic body waves. *J. Geophys. Res.* **84**, 4749-4762 (1979).
18. P. Lognonné et al., Constraints on the shallow elastic and anelastic structure of Mars from InSight seismic data. *Nature Geoscience* **13**, 213-220 (2020).
19. K. Wapenaar, D. Draganov, R. Snieder, X. Campman, A. Verdel, Tutorial on seismic interferometry: Part 1—Basic principles and applications. *Geophysics* **75**, 75A195-75A209 (2010).
20. D. Kim, V. Lekić, Groundwater variations from autocorrelations and receiver functions. *Geophys. Res. Lett.* **46**, 13722-13729 (2019).
21. D. Giardini et al., The seismicity of Mars. *Nature Geoscience* **13**, 205- 212 (2020).
22. A. Khan et al., Imaging the upper mantle structure of Mars with InSight seismic data. *Science*, submitted (2021).

23. N. Compaire et al., Autocorrelation of the ground vibrations recorded by the SEIS InSight seismometer on Mars. *J. Geophys. Res*. **126**, e2020JE006498, doi:10.1029/2020JE006498 (2021).
24. S. Deng, A. Levander, Autocorrelation Reflectivity of Mars, *Geophys. Res. Lett.* **47**, e2020GL089630 (2020).
25. M. A. Wieczorek, M. Beuthe, A. Rivoldini, T. Van Hoolst. Hydrostatic interfaces in bodies with nonhydrostatic lithospheres, *J. Geophys. Res. Planets* **124**, doi:10.1029/2018JE005909 (2019).
26. S. E. Smrekar et al., Pre-mission InSights on the Interior of Mars. *Space Sci Rev* **215**, 3, doi:10.1007/s11214-018-0563-9 (2019).
27. H. Samuel, P. Lognonné, M. Panning, V. Lainey, The rheology and thermal history of Mars revealed by the orbital evolution of Phobos, *Nature* **569**, 523–527 (2019).
28. M. Thiriet, C. Michaut, D. Breuer, A. C. Plesa, Hemispheric dichotomy in lithosphere thickness on Mars caused by differences in crustal structure and composition, *J. Geophys. Res. Planets* **123**, 823–848 (2018).
29. H. Wänke, G. Dreibus, Chemistry and accretion history of Mars, *Philos. Trans. R. Soc. London. Ser. A Phys. Eng. Sci.* **349**, 285–293 (1994).
30. G. J. Taylor, The bulk composition of Mars, *Geochemistry* **73**, 401-420 (2013).
31. S. R Taylor, S. M McLennan, Planetary Crusts: Their composition, origin and evolution (Cambridge Univ. Press, Cambridge, 2009).
32. InSight Mars SEIS Data Service, SEIS raw data, InSight Mission, IPGP, JPL, CNES, ETHZ, ICL, MPS, ISAE-Supaero, LPG, MFSC, https://doi.org/10.18715/SEIS.INSIGHT.XB_2016 (2019).
33. D. L. Abt, K. M. Fischer, S. W. French, H. A. Ford, H. Yuan, B. Romanowicz, North American lithospheric discontinuity structure imaged by Ps and Sp receiver functions. *J. Geophys. Res.* **115**, B09301 (2010).
34. B. Knapmeyer-Endrun, F. Krüger, the PASSEQ Working Group, Moho depth across the Trans-European Suture Zone from P- and S-receiver functions. *Geophys. J. Int.* **197**, 1048–1075 (2014).
35. J. F. Lawrence, P. M. Shearer, A global study of transition zone thickness using receiver functions. *J. Geophys. Res.*, **111**, B0630 (2006).
36. L. Vinnik, H. Chenet, J. Gagnepain-Beyneix, P. Lognonné, First seismic receiver functions on the Moon. *Geophys. Res. Lett.* **28**, 3031–3034 (2001).
37. P. Lognonné, J. Gagnepain-Beyneix, H. Chenet. A new seismic model of the Moon: implication in terms of structure, formation and evolution. *Earth Planet. Sci. Lett.* **112**, 27–44 (2003).
38. J.-R. Scholz et al., Detection, analysis and removal of glitches from InSight's seismic data from Mars. *Earth and Space Science* **7**, e2020EA001317-T, doi:10.1029/2020EA001317 (2020).
39. J. M. Kolb, V. Lekic, Receiver function deconvolution using transdimensional hierarchical Bayesian inference. *Geophys. J. Int*. **193**, 1791-1735 (2014).
40. B. L. N. Kennett, The removal of free surface interactions from three-component seismograms. *Geophys. J. Int.*, **104**, 153-163 (1991).
41. R. W. Clayton, R. A. Wiggins, Source shape estimation and deconvolution of teleseismic bodywaves, *Geophys. J. Int*. **47**, 151-177, doi:10.1111/j.1365-246X.1976.tb01267.x (1976).
42. J. P. Ligorria, C. J. Ammon, Iterative deconvolution and receiver-function estimation. *Bull. Seism. Soc. Am.* **89**, 1395-1400 (1999).
43. R. Kind, G. L. Kosarev, N. V. Petersen, Receiver functions at the stations of the German Regional Seismic Network (GRSN). *Geophys. J. Int* **121**, 191-202 (1995).
44. K. Hannemann, F. Krüger, T. Dahm, D. Lange, Structure of the oceanic lithosphere and upper mantle north of the Gloria Fault in the eastern mid-Atlantic by receiver function analysis. *J. Geophys. Res.* **122**, 7927-7950 (2017).

45. G. Helffrich, Extended-time multitaper frequency domain cross-correlation receiver function estimation. *Bull. Seism. Soc. Am.* **96**, 344-347 (2006).
46. T. Shibutani, T. Ueno, K. Hirahara, Improvement in the extended-time multitaper receiver function estimation technique. *Bull. Seis. Soc. Am.* **98**, 812-816 (2008).
47. Eagar, K.C., M.J. Fouch, FuncLab: A MATLAB interactive toolbox for handling receiver function datasets, *Seis. Res. Lett.* **83**, doi:10.1785/gssrl.83.3.596 (2012).
48. G. D. Bensen et al., Processing seismic ambient noise data to obtain reliable broad-band surface wave dispersion measurements. *Geophys. J. Int.* **169**, 1239–1260 (2007).
49. R. S. M. De Plaen, T. Lecocq, C. Caudron, V. Ferrazzini, O. Francis, Single-station monitoring of volcanoes using seismic ambient noise. *Geophys. Res. Lett.* **43**, 8511–8518 (2016).
50. Y. Ito, K. Shiomi, Seismic scatterers within subducting slab revealed from ambient noise autocorrelation. *Geophys. Res. Lett.* **39**, L19303 (2012).
51. F. J. Sánchez-Sesma, M. Campillo, Retrieval of the Green's function from cross correlation: the canonical elastic problem. *Bull. Seism. Soc. Am.* **96**, 1182-1191 (2006).
52. R. Snieder, Extracting the Green's function from the correlation of coda waves: A derivation based on stationary phase. *Phys. Rev. E* **69**, 046610 (2004).
53. W. Sun, B. L. N. Kennett, Receiver structure from teleseisms: Autocorrelation and cross correlation. *Geophys. Res. Lett.* **43**, 6234–6242 (2016).
54. InSight Marsquake Service, Mars Seismic Catalogue, InSight Mission; V1 2/1/2020. ETHZ, IPGP, JPL, ICL, ISAE-Supaero, MPS, Univ. Bristol. doi:10.12686/a6 (2020).
55. D. Clarke, L. Zaccarelli, N. M. Shapiro, F. Brenguier. Assessment of resolution and accuracy of the Moving Window Cross Spectral technique for monitoring crustal temporal variations using ambient seismic noise. *Geophys. J. Int.* **186**, 867–882 (2011).
56. M. Schimmel et al., Seismic Noise Autocorrelations on Mars. *Earth and Space Science Open Archive*, doi:10.1002/essoar.10506669.1 (2021).
57. S. Ceylan et al., Companion guide to the marsquake catalog from InSight, Sols 0–478: Data content and non-seismic events. *Physics Earth Planet. Int.* **310**, 106597, doi:10.1016/j.pepi.2020.106597 (2021).
58. M. Schimmel, Phase cross-correlations: design, comparisons and applications. *Bull. Seismol. Soc. Am.* **89**, 1366-1378 (1999).
59. G. Taylor, S. Rost, G. Houseman, Crustal imaging across the North Anatolian Fault Zone from the autocorrelation of ambient seismic noise. *Geophys. Res. Lett.* **43**, 2502–2509, doi:10.1002/2016GL067715 (2016).
60. P. Romero, M. Schimmel, Mapping the basement of the Ebro Basin in Spain with seismic ambient noise autocorrelations. *J. Geophys. Res.* **123**, 5052-5067, doi:10.1029/2018JB015498 (2018).
61. M. Schimmel, E. Stutzmann, S. Ventosa, Low-frequency ambient noise autocorrelations: Waveforms and normal modes. *Seism. Res. Lett.* **89** (4), 1488-1496, doi:10.1785/0220180027 (2018).
62. C. Buffoni, M. Schimmel, N.C. Sabbione, M.L. Rosa, G. Connon, Crustal structure beneath Tierra del Fuego, Argentina, inferred from seismic P-wave receiver functions and ambient noise autocorrelations. *Tectonophysics* **751**, 41-53, doi:10.1016/j.tecto.2018.12.013 (2019).
63. S. Ventosa, M. Schimmel, E. Stutzmann, Towards the processing of large data volumes with phase cross-correlation. *Seism. Res. Lett.* **90**(4), 1663-1669, doi:10.1785/0220190022 (2019).
64. M. Schimmel, J. Gallart, Frequency-dependent phase coherence for noise suppression in seismic array data. *J. Geophys. Res.* **112**, B04303, doi:10.1029/2006JB004680 (2007).
65. M. Schimmel, E. Stutzmann, J. Gallart, Using instantaneous phase coherence for signal extraction from ambient noise data at a local to a global scale. *Geophys. J. Int.* **184**, 494-506, doi:10.1111/j.1365-246X.2010.04861.x (2011).
66. T. S. Pham, H. Tkalčić, On the feasibility and use of teleseismic P wave coda autocorrelation for mapping shallow seismic discontinuities. *J. Geophys. Res.* **122**, 3776-3791 (2017).

67. J. C. VanDecar, R. S. Crosson, Determination of teleseismic relative phase arrival times using multi-channel cross-correlation and least squares. *Bull. Seism. Soc. Am.* **80**, 150-169 (1990).
68. F. Bissig et al., Multifrequency Inversion of Ps and Sp Receiver Functions: Methodology and Application to USArray Data. *J. Geophys. Res.* **126**, e2020JB020350, doi: 10.1029/2020JB020350 (2021).
69. A. Khan et al., A geophysical perspective on the bulk composition of Mars. *J. Geophys. Res.* **123**, 1-37, doi: 10.1002/2017JE005371 (2018).
70. K. Fuchs, G. Müller, Computation of synthetic seismograms with the reflectivity method and comparison with observations. *Geophys. J. Int.* **23**, 417-433, doi:10.1111/j.1365-246X.1971.tb01834.x (1971).
71. H. P. Crotwell, T. J. Owens, J. Ritsema, The TauP Toolkit: Flexible seismic travel-time and ray-path utilities. *Seismol. Res. Lett.* **70**, 154-160, doi:10.1785/gssrl.70.2.154 (1999).
72. K. Mosegaard, A. Tarantola, Monte Carlo sampling of solutions to inverse problems. *J. Geophys. Res.* **100**, 12431-12447, doi:10.1029/94JB03097 (1995).
73. A. Tarantola, Inverse problem theory and methods for model parameter estimation. Society of Industrial and Applied Mathematics (2005).
74. K. Mosegaard, A. Tarantola, Probabilistic Approach to Inverse Problems. In: International Handbook of Earthquake and Engineering Seismology, 237-265. Academic Press (2002).
75. M. Wathelet, An improved neighborhood algorithm: Parameter conditions and dynamic scaling. *Geophys. Res.Lett.* **35**, L09301 (2008).
76. M. Sambridge, Geophysical inversion with a neighbourhood algorithm–I. Searching a parameter space. *Geophys. J. Int.* **138**, 479–494 (1999).
77. R. Joshi, B. Knapmeyer-Endrun, K. Mosegaard, H. Igel, U. Christensen, Joint inversion of receiver functions and apparent incidence angles for sparse seismic data. *Earth and Space Science Open Archive*, doi:10.1002/essoar.10506471.1 (2021).
78. T. Shibutani, M. Sambridge, B. Kennett, Genetic algorithm in-version for receiver functions with application to crust and uppermost mantle structure beneath eastern Australia. *Geophys. Res. Lett.* **23**, 1829–1832 (1996).
79. T. Nissen-Meyer et al., AxiSEM: Broadband 3-D seismic wavefields in axisymmetric media. *Solid Earth* **5**, 425–445 (2014).
80. B. Knapmeyer-Endrun, S. Ceylan, S., M. van Driel, Crustal S-wave velocity from apparent incidence angles: a case study in preparation for InSight. *Space Sci. Rev.* **214**, 83 (2018).
81. F. Birch, The velocities of compressional waves in rocks to 10 kilobars, Part 2. *J. Geophys. Res.* **66**, 2199–2224 (1961).
82. N. Brinkman et al., First focal mechanisms of marsquakes. *J. Geophys. Res.* **126**, e2020JE006546 (2021).
83. M. A. Wieczoreket al., The crust of the Moon as seen by GRAIL. *Science* **339**, 671-675 (2013).
84. T. Yoshizaki, W. F. McDonough, The composition of Mars. *Geochim. Cosmochim. Acta* **273**, 137-162 (2020).
85. M. A. Wieczorek and R. J. Phillips, Potential anomalies on a sphere: Applications to the thickness of the lunar crust, *J. Geophys. Res*. **103**(E1), 1715-1724 (1998).
86. A. Broquet et al., Flexure of the lithosphere beneath the North Polar Cap of Mars: Implications for ice composition and heat flow. *Geophys. Res. Lett*. **47**, e2019GL086746 (2020).
87. M. A. Wieczorek, Gravity and Topography of the Terrestrial Planets. *Treatise on Geophysics*, 2nd edition, Oxford, 153-193 (2015).
88. A. Genova et al., Seasonal and static gravity field of Mars from MGS, Mars Odyssey and MRO radio science, *Icarus* **272**, 228-245 (2016).
89. T. Ruedas, D. Breuer, On the relative importance of thermal and chemical buoyancy in regular and impact-induced melting in a Mars-like planet, *J. Geophys. Res. Planets* **122**, 1554–1579 (2017).

90. E. Takahashi, Speculations on the Archean mantle: missing link between komatiite and depleted garnet peridotite, *J. Geophys. Res.* **95**, 15941–15954 (1990).
91. M. Duncan, N. Schmerr, C. M. Bertka, Y. Fei, Extending the solidus for a model iron-rich Martian mantle composition to 25 GPa. *Geophys. Res. Lett.* **45**, 10,211– 10,220, doi:10.1029/2018GL078182 (2018).
92. A. C. Plesa, N. Tosi, M. Grott, D. Breuer, Thermal evolution and Urey ratio of Mars. *J. Geophys. Res. Planets* **120**, 995–1010 (2015).
93. N. Tosi, M. Grott, A.C. Plesa, D. Breuer, Thermochemical evolution of Mercury's interior. *J. Geophys. Res. E Planets* **118**, 2474–2487 (2013).
94. A. Plesa et al., How large are present-day heat flux variations across the surface of Mars? *J. Geophys. Res.* **121**, 2386–2403 (2016).
95. W. K. Hartmann, Evidence for recent volcanism on Mars from crater counts. *Nature* **397**, 586–589 (1999).
96. G. Neukum, Recent and episodic volcanic and glacial activity on Mars revealed by the High Resolution Stereo Camera, *Nature* **432**, 971–979 (2004).
97. M. Thiriet, D. Breuer, C. Michaut, A.-C. Plesa, Scaling laws of convection for cooling planets in a stagnant lid regime. *Phys. Earth Planet. Inter.* **286**, 138–153 (2019).
98. W. V. Boynton et al., Concentration of H, Si, Cl, K, Fe, and Th in the low- and mid-latitude regions of Mars. *J. Geophys. Res.* **112**, E12S99, doi:10.1029/2007JE002887 (2007).
99. H. E. Newsom et al., Geochemistry of Martian soil and bedrock in mantled and less mantled terrains with gamma ray data from Mars Odyssey. *J. Geophys. Res.* **112**, E03S12, doi:10.1029/2006JE002680 (2007).
100. H. Y. McSween Jr, S. M. McLennan, Mars. In: H. D. Holland and K. Turekian, eds., Treatise on Geochemistry, 2nd Ed.; Vol. 2, A. M. Davis, ed., Planets, Asteroids, Comets and The Solar System (Elsevier, Amsterdam) pp. 251-300 (2014).
101. C. B. Agee et al. Unique meteorite from early Amazonian Mars: Water-rich basaltic breccia Northwest Africa 7034. *Science* **339**, 780-785, doi:10.1126/science.1228858 (2013).
102. B. C.Hahn, B. C. et al., Mars Odyssey gamma-ray spectrometer elemental abundances and apparent relative surface age: Implications for martian crustal evolution. *J. Geophys. Res.* **112**, E03S11, doi:10.1029/2006JE002821 (2007).
103. S. Karunatillake et al., Chemically striking regions on Mars and Stealth revisited. *J. Geophys. Res.* **114**, E12001, doi:10.1029/2008JE03303 (2009).
104. G. J. Taylor et al., Mapping Mars geochemically. *Geology* **38**, 183-186, doi:10.1130/G30470 (2010).
105. P. L. King, S. M. McLennan, Sulfur on Mars. *Elements* **6**, 107-112 (2010).
106. C. L. Johnson et al., Crustal and time-varying magnetic fields at the InSight landing site on Mars. *Nature Geoscience* **13**, 199-204 (2020).
107. B. Langlais et al. A new model of the crustal magnetic field of Mars using MGS and MAVEN. *J. Geophy. Res.* **124**, 1542-1569 (2019).
108. A. Mittelholz, C. L. Johnson, A. Morschhauser. A new magnetic field activity proxy for Mars from MAVEN data. *Geophys. Res. Lett.* **45**, 5899-5907 (2018).
109. R. L. Parker, Ideal bodies for Mars magnetics. *J. Geophys. Res*. **108**, 5006 (2003).
110. A. Mittelholz, C. L. Johnson, J. M. Feinberg, B. Langlais, R. J. Phillips, Timing of the martian dynamo: New constraints for a core field 4.5 and 3.7 Ga ago. *Science Advance*s **6** (2020).
111. A. S. Konopliv et al. Detection of the Chandler wobble of Mars from orbiting spacecraft. *Geophys. Res. Lett.* **47**, e2020GL090568, doi:10.1029/2020GL090568 (2020).
112. D. Kahan et al., Mars precession rate determined from radiometric tracking of the InSight lander. *Planet. Space Sci.* **199**, 105208, doi:10.1016/j.pss.2021.105208 (2021).
113. M. P. Panning et al., Planned products of the Mars structure service for the InSight mission to Mars. *Space Sci. Rev.* **211**, 611–650 (2017).

114. A. Rivoldini, T. Van Hoolst, O. Verhoeven, A. Mocquet, V. Dehant, Geodesy constraints on the interior structure and composition of Mars. *Icarus* **213**, 451-472, doi:10.1016/j.icarus.2011.03.024 (2011).
115. J. A. D. Connolly, Computation of phase equilibria by linear programming: A tool for geodynamic modeling and its application to subduction zone decarbonation. *Earth Planet. Sci. Lett.* **236**, 524-541, doi:10.1016/j.epsl.2005.04.033 (2005).
116. L. Stixrude, C. Lithgow-Bertelloni, Thermodynamics of mantle minerals - II. Phase equilibria. *Geophys. J. Int.* **184**, 1180–1213, doi:10.1111/j.1365-246X.2010.04890.x (2011).
117. G. J. Taylor et al., Variations in K/Th on Mars. *J. Geophys. Res.* **111**, E03S06, doi:10.1029/2006JE002676 (2007).

Acknowledgments: This is Insight Contribution Number (ICN) 187. We acknowledge NASA, CNES, their partner agencies and institutions (UKSA, SSO, DLR, JPL, IPGP-CNRS, ETHZ, IC, MPS-MPG) and the flight operations team at JPL, SISMOC, MSDS, IRIS-DMC and PDS for providing SEED SEIS data. **Funding:** MPP, ST, EB, SES, and WBB were supported by the NASA InSight mission and funds from the Jet Propulsion Laboratory, California Institute of Technology, under a contract with the National Aeronautics and Space Administration. FB was supported by research grant ETH-05 17-1. AK, DG, MVD and SS acknowledge funding by the Swiss National Science Foundation, the Swiss State Secretariat for Education, Research and Innovation, and support from ETHZ through the ETH+ funding scheme (ETH+02 19-1). VL and DK acknowledge funding from Packard Foundation Fellowship to VL. BT is supported by the European Union's Horizon 2020 research and innovation program under the Marie Sklodowska-Curie grant agreement 793824. French co-authors acknowledge the support of CNES and ANR (MAGIS, ANR-19-CE31-0008-08). NS was supported by NASA Grant 80NSSC18K1628. EB was funded through NASA Participating Scientist Program Grant 80NSSC18K1680. ACP gratefully acknowledges the financial support and endorsement from the DLR Management Board Young Research Group Leader Program and the Executive Board Member for Space Research and Technology. Geodynamical models used in this work were performed on the supercomputer ForHLR funded by the Ministry of Science, Research and the Arts Baden-Württemberg and by the Federal Ministry of Education and Research. SMM was funded through NASA InSight Participating Scientist Program Award No. 80NSSC18K1622. CM acknowledges the support of the Institut Universitaire de France (IUF). CLJ and AM acknowledge support from the InSight Mission, the Canadian Space Agency and ETH Zurich (ETH fellowship 19-2 FEL-34). NB is supported by research grant ETH-06 17-02. The work of AR was financially supported by the Belgian PRODEX program managed by the European Space Agency in collaboration with the Belgian Federal Science Policy Office. **Author contributions:** BKE, MPP, FB, RJ, AK, DK, VL, BT, ST, MP, NC, RFG, LM, MS, ES, NS, ACP, MW, DA, SMM, HS, CM, LP, SES, CLJ, PL, MK, DG and WBB contributed to the conceptualization of this study. The applied methodologies were developed by BKE, FB, RJ, AK, DK, VL, BT, ST, MP, NC, RFG, LM, MS, ES, ACP, MW, HS, CM, LP, PMD, PL, BP and JRS. BKE, FB, RJ, AK, DK, NC, MS, ES, ACP, MW, HS, CM, PMD, PL, BP and JRS developed, implemented and tested used software. BKE, MPP, NS, NB and MVD provided validation. Formal analyses were conducted by BKE, RB, RJ, AK, DK, VL, BT, ST, MP, NC, MS, ES, ACP, MW, AB, HS, CM, CLJ, NB, AM, AR, PMD, PL, BP, JRS and SS. BKE, FB, RJ, AK, DK, VL, ST, MP, NC, MS, ES, ACP, MW, SMM, HS, CM, CLJ, NB, AM, AR, PMD, PL, BP, JRS and SS provided investigations. Data curation activities were done by PL, SS, MVD and DG. BKE, MPP, FB, RJ, AK, DK, VL, BT, ST, NC, RFG, LM, MS, ES, ACP, MW, SMM, HS, CM, CLJ, NB, AM, AR and PMD contributed to the writing of the original draft. Review and editing were performed by BKE, MPP, NS, EB, AB, DA, SES, CLJ and MK. BKE, MPP, FB, RJ, AK, DK, VL, BT, NC, MS, ES, NS, ACP, MW, HS, CM, AM, AR and PMD worked on visualizing the results. BKE, MPP, AK, RFG, LM, NS, CLJ, PL and DG supervised junior scientists involved in the project. The project was administrated by SES, PL, DG and WBB, who also acquired funding. **Competing interests:** Authors declare no competing interests. **Data and materials availability:** All InSight SEIS data *(32)* used in this paper are available from the IPGP Data Center, IRIS-DMC and NASA PDS.

Supplementary Materials:

Materials and Methods

Figures S1-S29

Tables S1-S6

References (33-117)

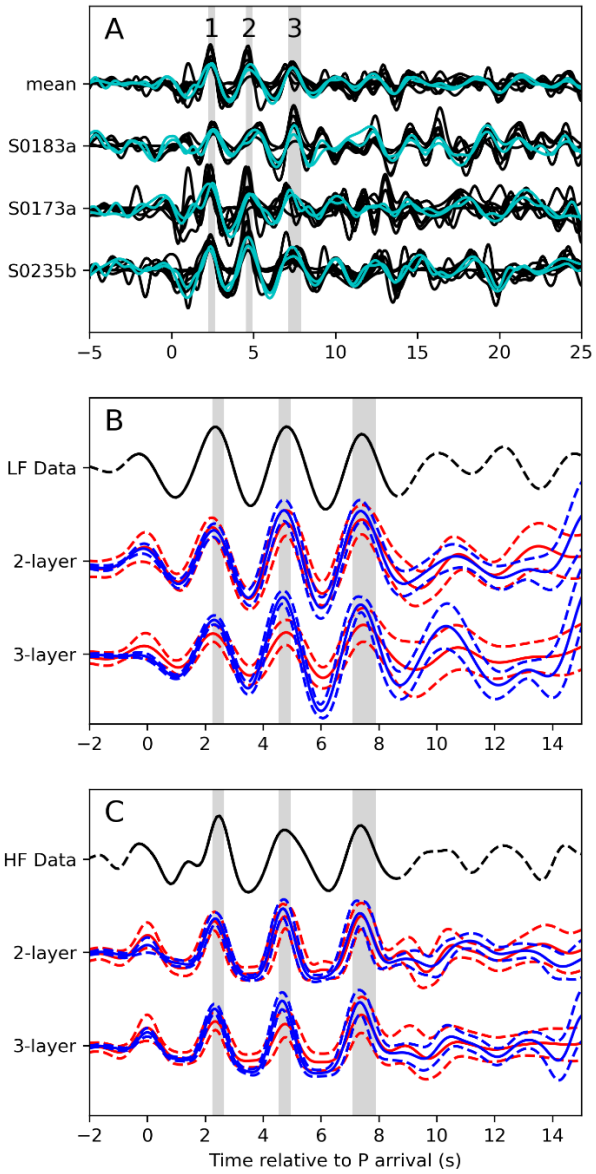

Fig. 1. Measured and modeled converted phases that constrain the crustal structure at the InSight landing site. (**A**) P-to-S receiver functions for the three events considered, and the summed trace. Different traces for each event correspond to different processing methods as described in the Supplementary Materials. Gray shading highlights the three clear positive phases within the first 8 s. Numbered labels correspond to predicted ray paths shown in Fig. 2B,D. The two datasets used for model inversions shown in Fig. 2 are highlighted in cyan. (**B**) Comparison between the low-frequency representative receiver function sum trace and synthetic summed P-to-S receiver functions for the 2- and 3-layer models. Data is shown in black on top, with the time window used in the inversion drawn solid. Solid and dashed red lines show the synthetics computed by the range of models produced by inversion method A *(16)*, while solid and dashed blue lines show the mean receiver functions with standard deviations based on the 5000 best fitting receiver functions derived from inversion method B *(16)*. Gray shaded regions are the same as in **(A)**. **(C)** Same as panel **(B)**, but for the high-frequency receiver functions.

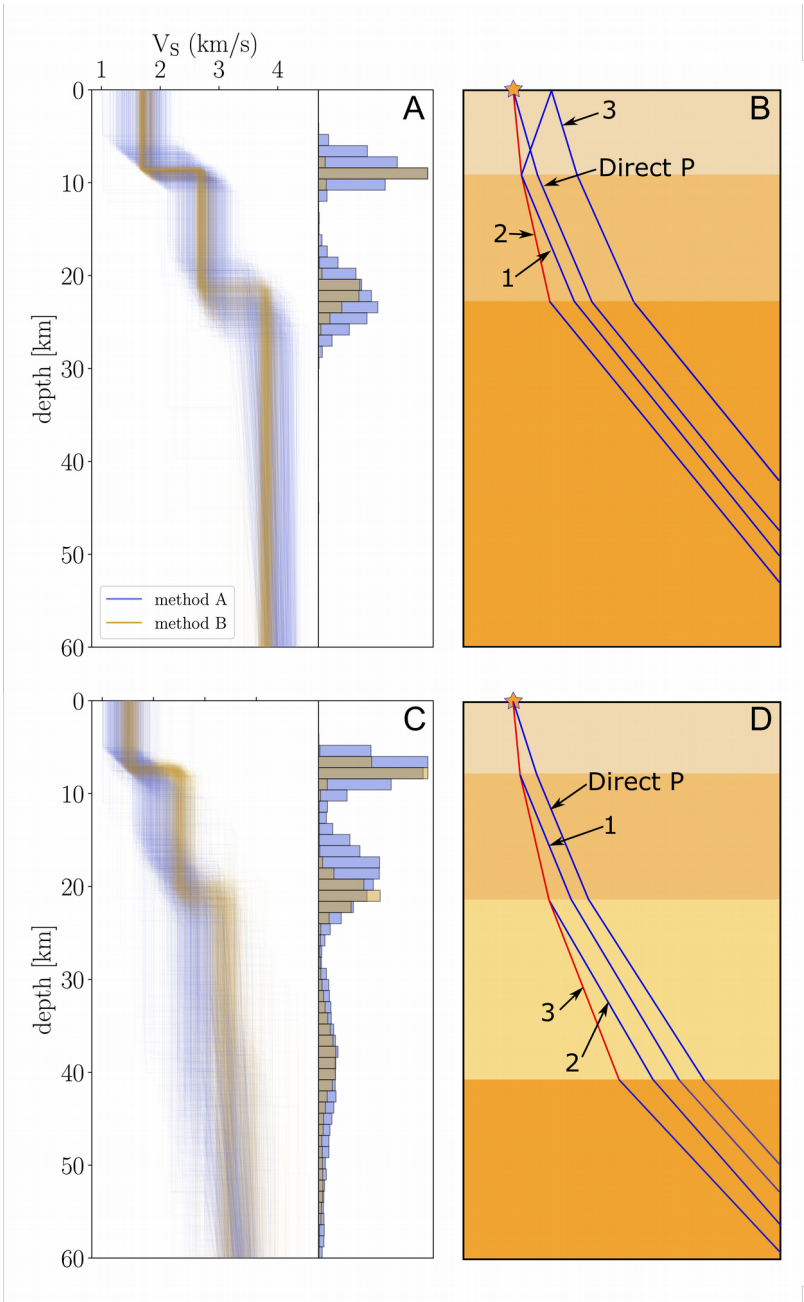

Fig. 2. Synopsis of the crustal structure of Mars at the InSight landing site from receiver function analyses. **(A)** Inversion results for all three events using inversion method A (in blue lines) and method B (in brown) using a two-layer parameterization. **(B)** Cartoon showing the ray paths of the main direct and converted phases present in the data. Blue lines show P phase paths, while the red lines show conversions to S phases at the interfaces below the lander. Direct conversions and one P multiple are shown and numbered labels correspond to arrivals identified in Fig. 1A. **(C-D)** Same as **(A-B)**, except for assuming a three-layer model and excluding the multiple arrival.

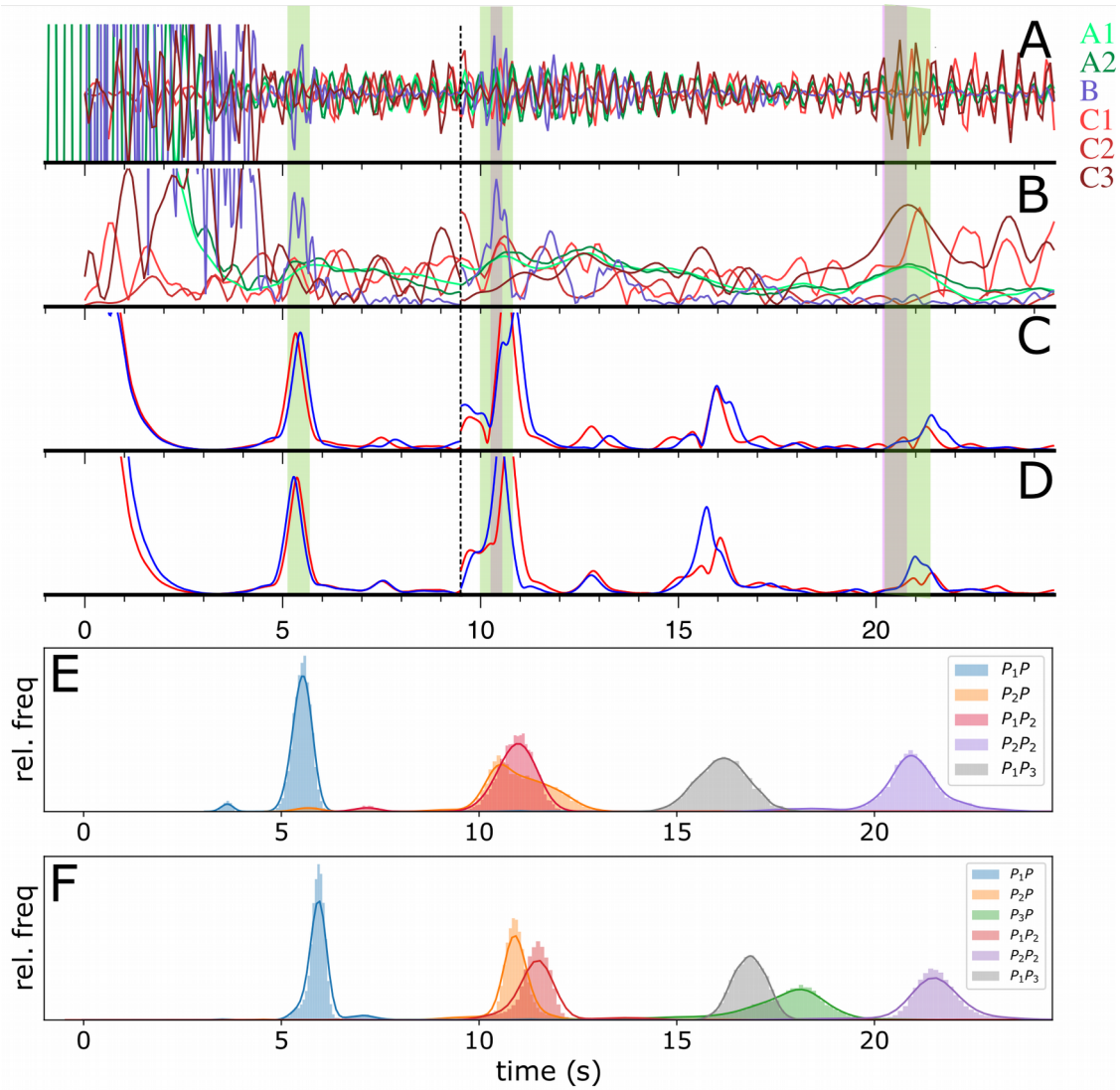

Fig. 3. Autocorrelation functions for different data sets, components, and processing methods. **(A)** Overlaid traces are from the three analysis methods discussed in the supplementary material. The dashed bar at 9.5 s corresponds to a change in normalization in order to see smaller amplitude arrivals later in the trace. Green bars highlight areas where all methods are nearly in-phase and show potential arrivals, whereas purple bars highlight arrivals indicated from an independent study *(24)*. **(B)** Envelopes of the ACFs displayed in **(A)**. **(C)** Envelopes of synthetic zero-offset Green's functions for a representative model from the family of two-layer models in Fig. 2A for method A in blue and method B in red. **(D)** Same as **(C)**, but for the three-layer models from Fig. 2C. **(E)** Histograms of predicted arrivals from the family of two-layer models as shown in Fig. 2A. The first subscript of the arrival in the legend refers to the interface of reflection, and the second subscript (if present) represents a second or third bounce between the free surface and that interface. **(F)** Same as **(E)**, but for the three-layer models in Fig. 2C.

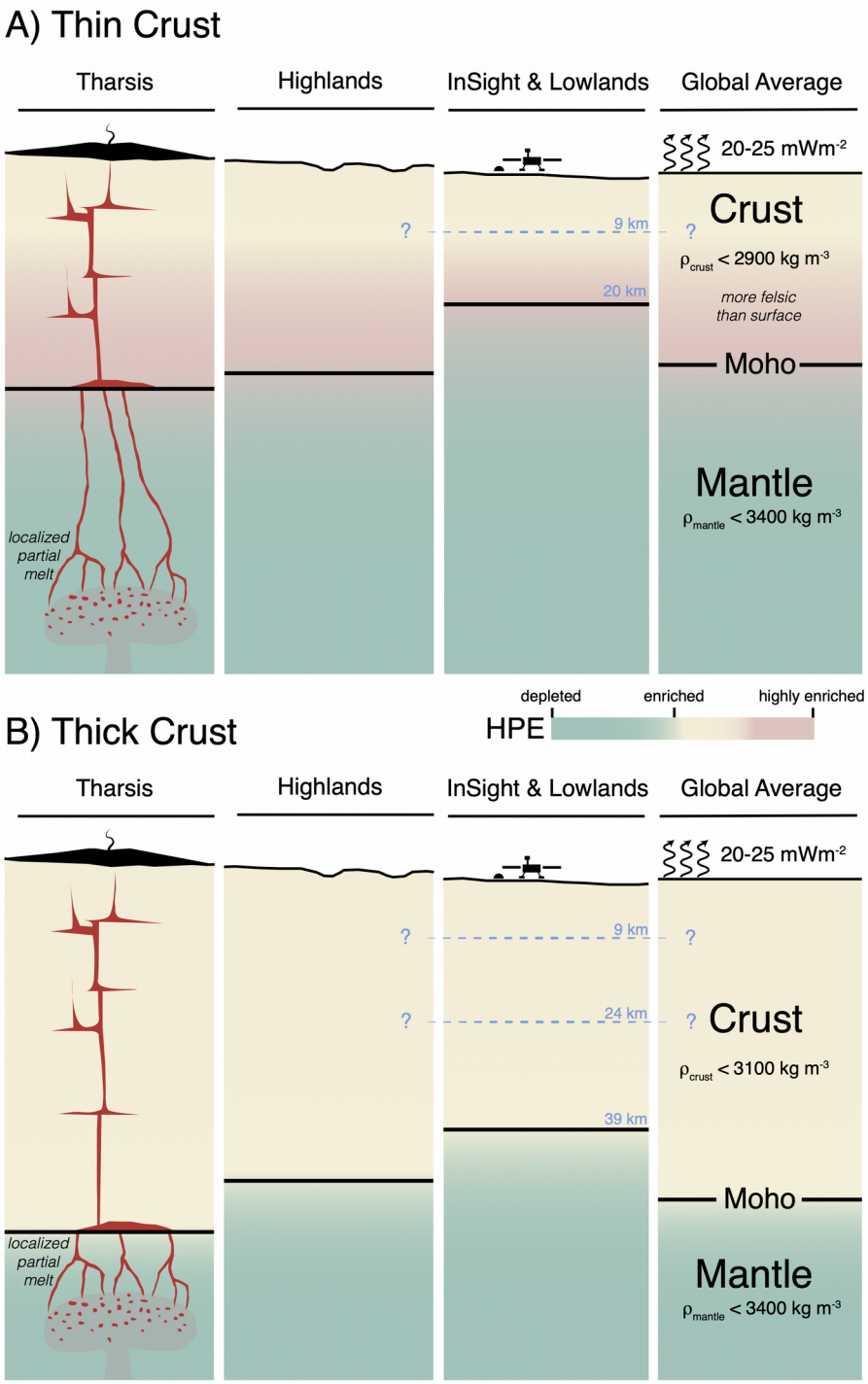

Fig. 4. Schematic interpretations of the geochemical and geodynamical implications for the thin and thick crust models (**A** and **B**, respectively). In order to match geodynamic constraints, an enrichment of heat producing elements, shown in color, and lower density than observed from the surface are required in the thin crust model, whereas the thick crust model is consistent with surface observations.

Chapter 4

Receiver Function analysis of the martian crust

This chapter was published in Geophysical Research Letters, Volume 50, Issue 3, in January 2023 under the title "Joint inversion of receiver functions and in apparent incidence angles to determine the crustal structure of Mars" by Joshi et al. Conceptualization, data analysis, creation of figures and writing of the draft were carried out by me under the supervision of Dr. B. Knapmeyer-Endrun, Prof. Dr. Heiner Igel and Prof. Dr. Ulrich Christensen.

The supporting information for this chapter can be found in Appendix C.

Geophysical Research Letters

RESEARCH LETTER
10.1029/2022GL100469

Joint Inversion of Receiver Functions and Apparent Incidence Angles to Determine the Crustal Structure of Mars

Rakshit Joshi[1,2], Brigitte Knapmeyer-Endrun[3], Klaus Mosegaard[4], M. A. Wieczorek[5], Heiner Igel[2], Ulrich R. Christensen[1], and Philippe Lognonné[6]

[1]Max Planck Institute for Solar System Research, Göttingen, Germany, [2]Ludwig Maximilian University of Munich, Munich, Germany, [3]Bensberg Observatory, University of Cologne, Cologne, Germany, [4]Niels Bohr Institute, University of Copenhagen, Copenhagen, Denmark, [5]Laboratoire Lagrange, Observatoire de la Côte d'Azur, CNRS, Université Côte d'Azur, Nice, France, [6]CNRS, Institut de Physique du Globe de Paris, Université de Paris, Paris, France

Abstract Recent estimates of the crustal thickness of Mars show a bimodal result of either ~20 or ~40 km beneath the InSight lander. We propose an approach based on random matrix theory applied to receiver functions (RFs) to further constrain the subsurface structure. Assuming a spiked covariance model for our data, we first use the phase transition properties of the singular value spectrum of random matrices to detect coherent arrivals in the waveforms. Examples from terrestrial data show how the method works in different scenarios. We identify three previously undetected converted arrivals in the InSight data, including the first multiple from a deeper third interface. We then use this information to jointly invert RFs with the absolute S-wave velocity information in the polarization of body waves. Results show a crustal thickness of 43 ± 5 km beneath the lander with two mid-crustal interfaces at depths of 8 ± 1 and 21 ± 3 km.

Plain Language Summary Recent analysis of seismic data from InSight shows that the crustal thickness beneath the InSight lander can be either 20 or 40 km. To resolve this ambiguity, we apply results from random matrix theory to receiver function (RF) analysis. The distribution of singular values of a random matrix shows well-behaved deterministic properties that can be used to separate them from those of an underlying coherent signal if present. We use examples from terrestrial data to show how the method works. When applied to RFs computed from InSight seismic data, we identify three new energy arrivals, including one that supports the existence of a deeper third layer. Using this information, we simultaneously inverted the RF data along with the measured incidence angle of body waves. Results show a crustal thickness of 43 ± 5 km beneath the lander with two mid-crustal interfaces at depths of 8 ± 1 and 21 ± 3 km.

Key Points:

- We apply recent results from random matrix theory to identify crustal phases in noisy receiver functions for Mars from InSight data
- Once identified, we jointly invert these phases with frequency-dependent apparent S-wave velocity curves
- Results show a crustal thickness of 43 km with two inter-crustal discontinuities at 8 and 21 km beneath the lander

Supporting Information:

Supporting Information may be found in the online version of this article.

Correspondence to:

R. Joshi,
joshir@mps.mpg.de

Citation:

Joshi, R., Knapmeyer-Endrun, B., Mosegaard, K., Wieczorek, M. A., Igel, H., Christensen, U. R., & Lognonné, P. (2023). Joint inversion of receiver functions and apparent incidence angles to determine the crustal structure of Mars. *Geophysical Research Letters*, *50*, e2022GL100469. https://doi.org/10.1029/2022GL100469

Received 8 AUG 2022
Accepted 24 JAN 2023

1. Introduction

The InSight mission landed in the Elysium Planitia plain of Mars on 26 November 2018 (Banerdt et al., 2020) and deployed a three component very broadband seismometer (SEIS; Lognonné et al., 2019, 2020) on the surface. Along with measuring the seismicity and the present thermal state of its interior, a primary goal of the mission is to constrain the interior structure of Mars. In comparison with the Earth, Mars has a low seismicity rate with quakes of smaller magnitude (2–5 M_w) (Giardini et al., 2020). Receiver function (RF) analysis is a robust single station technique that can be used in this case to constrain the crustal structure. Primary body waves (*P* and *S*) give rise to converted secondary phases (Ps and Sp) when they impinge upon a seismic discontinuity from beneath. RFs exploit these converted phases to gain information about the discontinuities in the crust and upper mantle. They have previously been used to investigate the thickness of the lunar crust using seismic data from the Apollo missions (Gagnepain-Beyneix et al., 2006; Lognonné et al., 2003; Vinnik et al., 2001). Using the data from the InSight mission, Lognonné et al. (2020) computed RFs from two marsquakes and showed evidence of subsurface layering with low seismic velocities in the first upper 8–11 km. Recently, Knapmeyer-Endrun et al. (2021) used RFs from three marsquakes and showed the observations to be consistent with either a two-layer model with the Moho at 20 ± 5 km or a three-layer model with the Moho at 39 ± 8 km depth below the lander. Although the thicker model is more compatible with geodynamical constraints, this ambiguity could not be resolved from the data due to a lack of phase move-out information and excessive noise in the later part (>10 s) of the waveforms which inhibited the identification of multiple arrivals. Compaire et al. (2021) and Schimmel et al. (2021) analyzed ambient field autocorrelations and identified reflection signals consistent with the first two interfaces. Li et al. (2022a) confirmed the first interface at ~8 km depth and the anisotropic nature of the layer

above based on SH-wave reflections. Durán et al. (2022) and Kim et al. (2021) later used updated RF data sets with more events to provide additional constraints and connoted a preference for the three-layer crustal model. Drilleau et al. (2022) and Khan et al. (2021) arrived at similar results using body wave travel-times. In this paper, we build upon the previous work of Knapmeyer-Endrun et al. (2021) to infer further constraints on the crustal structure of Mars using new techniques and additional data from the InSight mission.

We first focus on the problem of detection of multiple phases in our selected RF data set. For this, we propose a method that utilizes recent results from the random matrix theory to extract coherent signals in the RF waveforms. Assuming the observed signal to be a superposition of random noise and an underlying low-rank signal, the eigenvalues of the data covariance matrix follow a well behaved and deterministic limiting spectral distribution dictated by the generalized Marchencko-Pastur law. This information can be effectively used to decouple and identify coherent signal eigenvalues reflecting primary subsurface features from a bulk spectrum formed by incoherent scattering, random noise, and small-scale heterogeneity with distinct eigenvector rotation properties. Once identified, the secondary phase arrivals together with the primary conversions from crustal interfaces can be used to invert the structure. We then address the problem of non-uniqueness of RF inversions. Being primarily sensitive to shear velocity contrasts of interfaces and relative travel-time of converted waves, inversions of RF data alone can be affected by depth velocity trade-off (Ammon, 1991). They are therefore usually inverted jointly with other independent data sets that provide additional constraints on absolute shear wave velocities like surface-wave dispersion (e.g., Bodin et al., 2012; Du & Foulger, 1999; Julia et al., 2000). Svenningsen and Jacobsen (2007) showed that *P* wave polarization can also be used to constrain the *S* wave velocity structure of the subsurface using a simple relation between the observed apparent incidence angle and half-space *S* wave velocity (Wiechert, 1907). Following this, we previously showed how a joint inversion of apparent velocity curves and RF data can lead to a well constrained velocity structure for limited data sets comprising only a few events (Joshi et al., 2021). We adopt a similar methodology here to jointly invert an RF data set with a mean apparent velocity curve using a transdimensional approach.

2. Data and Method

2.1. RF Processing

InSight has identified 1,244 marsquakes (InSight Marsquake Service, 2022) since its operations started in 2018. Each quake is assigned a type and quality depending on its energy content and uncertainty in location estimate (Giardini et al., 2020). Only a few of these marsquakes generate waves that propagate through the mantle like teleseismic earthquakes, most of which do not have a precise location. Our database for Mars thus consists of 8 LF and BB seismic events (InSight Mars SEIS Data Service, 2019) with high SNR and event quality A-B (Clinton et al., 2021). Most of these events have similar distances and back azimuths as they all originate in the Cerberus Fosse region which is a young tectonic structure located to the east of the lander. S0183a is located farther away but we nevertheless use it as its inclusion does not have a significant effect on the results. For the terrestrial example, we use data from seismic station VSU in Vasula, Estonia. We select events with a similar back azimuth and distance range to mimic the InSight data. Details of the events used in this study are provided in the Supporting Information (Tables S1, S3, and S4 in Supporting Information S1).

To calculate RFs, we apply a time-domain Wiener filter for deconvolution as described by Hannemann et al. (2017). We first remove the transfer functions from the individual components of the data, rotate to ZNE coordinates as VBB uses the U, V, and W component system, and filter the seismograms between the corner frequencies (Table S1 in Supporting Information S1) using a zero-phase Butterworth filter. Subsequently, the ZNE coordinate system is rotated into ZRT to obtain radial and transverse components using the back azimuth estimates provided by the Marsquake Service (Clinton et al., 2018). For S0784, a back azimuth of 100° was determined by comparing RFs across different azimuths. A Wiener filter is determined such that it transforms the *P* wave signal on the vertical component into a band-limited spike. All the components of the data are then folded with this filter to obtain the RFs. The terrestrial data was processed similarly but was filtered between 5 Hz and 50 s.

2.2. Phase Identification

In RF data, the travel-times of the converted phases relative to the direct *P* arrival depend on the epicentral distance. This is generally seen as phase move-out which is different for direct and multiple phases, and helps to

distinguish between these. For complex structures with dipping interfaces and seismic anisotropy, the travel-times and amplitudes of conversions also vary with back azimuth. Although events generated from similar epicentral distance and back azimuths should theoretically have coherent conversions and multiples, interference with the scattered wavefield, small-scale heterogeneity, and random noise generates variations which can be seen as perturbations superimposed on the response of the primary sub-surface feature. The observed RF data matrix, $Y_{n\times m} = X_{n\times m} + \sigma Z_{n\times m}$, can now be modeled as a fixed rank perturbation (rank$[X] = r \leq n$) of the random noise matrix $Z \sim \mathcal{N}(0, 1)$. This is known as the spiked covariance model (Johnstone, 2001). To extract an approximation of the uncontaminated response $\hat{X}(Y)_{n\times m} \approx X_{n\times m}$, we exploit the fact that the asymptotic eigenvalue distribution of the covariance of a random matrix follows the Marchenko-Pastur (MP) law (Marchenko & Pastur, 1967) which has a compact support Ω with bounds $\lambda_{\pm}$.

$$\Phi(\lambda|\sigma,\gamma) = \begin{cases} \dfrac{\sqrt{(\lambda_+ - \lambda)(\lambda - \lambda_-)}}{2\pi\lambda\gamma\sigma}, & \lambda_- \leq \lambda \leq \lambda_+ \\ 0, & \text{otherwise} \end{cases}, \text{ with } \lambda_\pm = \sigma^2(1 \pm \sqrt{\gamma})^2 \tag{1}$$

Φ denotes the probability density of eigenvalues. λ_-, λ_+, σ, and γ denote the smallest eigenvalue, largest eigenvalue, noise level, and matrix aspect ratio n/m, respectively. $\lambda_\pm$ fluctuate on the small scale $n^{-2/3}$ according to the Tracy-Widom distribution (Tracy & Widom, 1996). Qualitatively, the empirical distribution of the eigenvalues of Z forms a deformed quarter circle bulk with bulk edges given by $\lambda_\pm$ and bulk width $4\sqrt{\gamma}\sigma^2$, and all eigenvalues lie strictly within these bounds. The eigenvalues show a sort of self-arranging behavior which, in presence of a non-random sample coherency (i.e., $X \neq 0$), have a repulsion effect on the signal eigenvalue if present. Thus we see a phase transition phenomenon (Baik et al., 2005) where, above a certain signal threshold, the signal eigenvalues separate away from the bulk "noise" eigenvalues and converge asymptotically to a different distribution. The same follows for the singular values which scale as the square root of the eigenvalues (Benaych-Georges & Nadakuditi, 2012). Setting $X_n = \sum_{i=1}^{m} a_{n,i} x_i b_{n,i}^T$ and $Y_n = \sum_{i=1}^{m} u_{n,i} y_i v_{n,i}^T$, the BBP (Baik-Ben Arous-Péché) phase transition results in a mapping of singular values y_i of the observed matrix Y to x_i of the uncontaminated low rank signal X:

$$y_i \xrightarrow{\text{a.s.}} \begin{cases} \sigma(1+\sqrt{\gamma}) & x_i \leq \sigma\gamma^{\frac{1}{4}} \\ \sqrt{\left(x_i + \dfrac{\sigma}{x_i}\right)\left(x_i + \gamma\dfrac{\sigma}{x_i}\right)}, & x_i > \sigma\gamma^{\frac{1}{4}} \end{cases} \tag{2}$$

Similarly, the left and right singular vectors pairs (u_i, a_i) and (v_i, b_i) are orthogonal within the bulk but become strongly correlated and show a non-zero dot product past the critical point:

$$|\langle a_{n,i}, u_{n,j}\rangle|^2 \xrightarrow{\text{a.s.}} \begin{cases} \dfrac{x_i^4 - \gamma}{x_i^4 + \gamma x_i^2}, & x_i = x_j \\ 0, & x_i \neq x_j \end{cases} \tag{3}$$

$$|\langle b_{n,i}, v_{n,j}\rangle|^2 \xrightarrow{\text{a.s.}} \begin{cases} \dfrac{x_i^4 - \gamma}{x_i^4 + x_i^2}, & x_i = x_j \\ 0, & x_i \neq x_j \end{cases} \tag{4}$$

Using these transition equations, Gavish and Donoho (2014) derive an analytical expression for the optimal rank-r approximation of the data matrix $\hat{X}(Y)$ by minimizing the asymptotic mean squared error of their misfit $\|X - \hat{X}(Y)\|_F^2$ over all singular values $u_i > \sigma\sqrt{1+\gamma}$ and $0 < \gamma \leq 1$. For the complete derivation, see Gavish and Donoho (2014). This results in an expression for a threshold value τ:

$$\tau = \lambda_\star(\gamma) \cdot \sqrt{n}\sigma \tag{5}$$

where

$$\lambda_\star = \sqrt{(2\gamma+1) + \frac{8\gamma}{(\gamma+1) + \sqrt{(\gamma^2 + 14\gamma + 1)}}} \tag{6}$$

This threshold marks the unique transition point of the signal singular values from those of random noise matrix Z for a given spectral distribution of Y with noise σ, taking into account the support fluctuations. The median of a standard MP distribution ($\sigma = 1$) is given by:

$$\mu_{MP} = \frac{1}{2\pi t} \int_{\lambda_-}^{x} \sqrt{(\lambda_+ - t)(t - \lambda_-)} dt \tag{7}$$

The noise σ can be estimated by matching the median of the standard MP distribution to that of the bulk singular values. This results in a robust noise estimator that estimates noise by comparing the perturbed singular values with the MP distribution.

$$\hat{\sigma}(Y) := \frac{\lambda_{med}}{\sqrt{n\mu_{MP}}} \tag{8}$$

Using $\hat{\sigma}(Y)$ for σ in Equation 5, we get

$$\hat{\tau_\star} = \omega(\gamma) \cdot \lambda_{med} \tag{9}$$

where

$$\omega(\gamma) \approx 0.56\gamma^3 - 0.95\gamma^2 + 1.82\gamma + 1.43 \tag{10}$$

In the final step, the singular value matrix y_i is replaced by $\hat{y}_i$ where the values below the threshold limit given by Equation 5 are padded and the approximate uncontaminated signal matrix $\hat{X}(Y)$ is reconstructed from the observations Y using $\hat{X}(Y) = \sum_{i=1}^{m} u_{n,i} \hat{y}_i v_{n,i}^T$. A sample algorithm is provided in the Supporting Information. In essence, the outlined procedure provides objective criteria to select the number of principal components that describe the variance of the structural signal by modeling noise as an additive independent and identically distributed (i.i.d.) random matrix.

2.3. Apparent Velocity Curves

In order to reduce non-uniqueness in the inversion of RFs, we use the absolute S wave velocity information contained within the P wave polarization as a complementary constraint. A consequence of Snell's law, the relation between the apparent P wave incidence angle $\left(\bar{i_p}\right)$ and the subsurface S wave velocity was derived by Wiechert (1907) and is given by Equation 10. Here p denotes the ray parameter. This apparent P wave incidence angle can be calculated directly from the amplitudes of vertical and radial RFs at time $t = 0$, as described in Svenningsen and Jacobsen (2007).

$$v_{S_{,app}} = \sin\left(0.5\overline{i_p}\right)/p \tag{11}$$

$$\tan \overline{i_p} = \frac{RRF(t=0)}{ZRF(t=0)} \tag{12}$$

Following a similar procedure as Knapmeyer-Endrun et al. (2018) and estimating i_p as a function of low pass Butterworth filter period (T), we calculate a frequency-dependent S wave velocity curve $v_S(T)$ which emphasizes the absolute S wave velocity variation with depth. A mean RF is calculated from all the raw RF waveforms in the data set. This is then used to compute a $v_{S_{,app}}$ curve which is jointly inverted together with the mean RF. We measure the dominant period of the spike in the mean ZRF and discard the values of filter periods smaller than that.

2.4. Inversion

A Markov-chain Monte Carlo (McMC) transdimensional Bayesian inversion method based on Bodin et al. (2012) (Dreiling & Tilmann, 2019) was used for the joint inversion of the mean RF and $v_{S_{,app}}$ curve. In this formulation, the number of layers itself becomes an unknown and is also inverted for along with the other model parameters. The solution is an ensemble of models that are distributed according to a posterior probability density function given by Bayes's rule. Each layer is parameterized by depth, V_s and the v_P/v_S ratio. Density is not inverted but is calculated using Birch's law (Birch, 1961). We use flat model priors and their ranges for depth, V_s and v_P/v_S

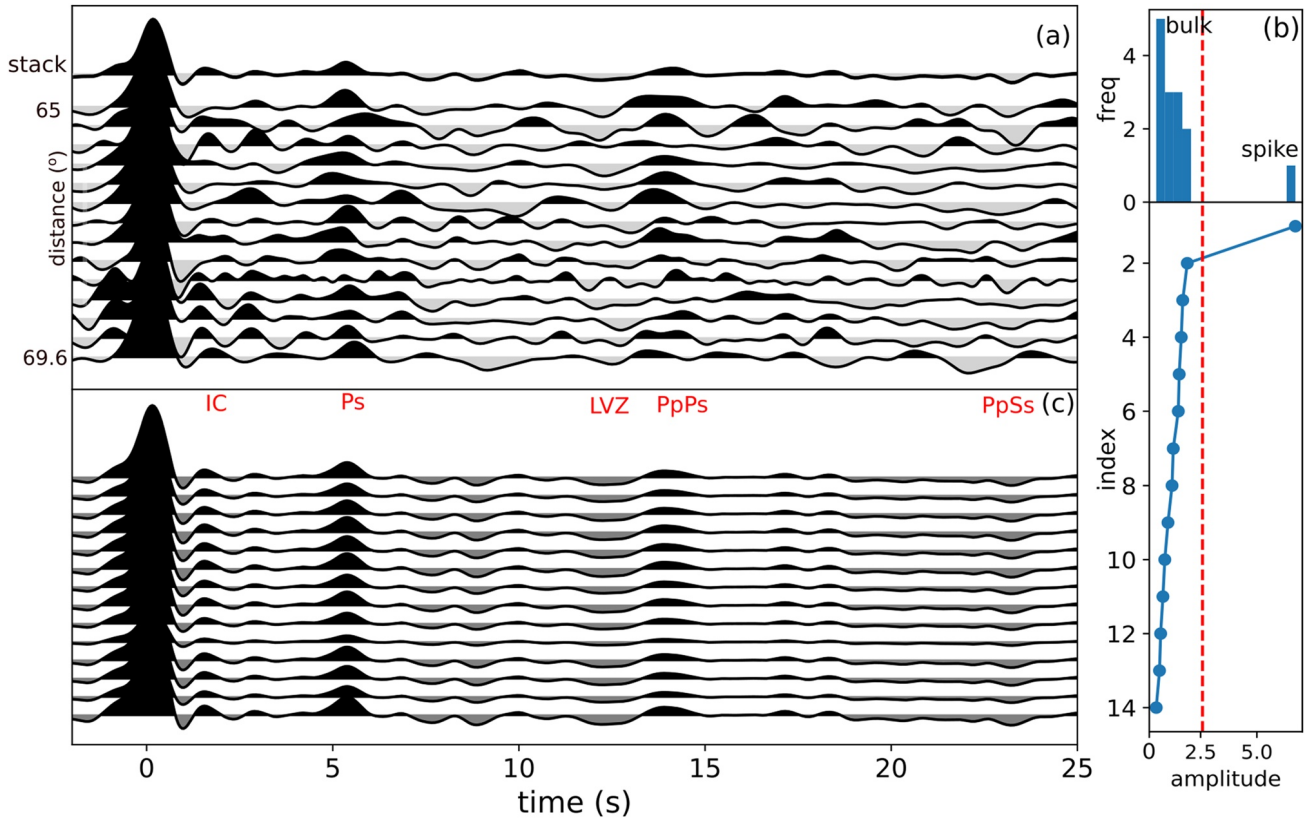

Figure 1. (a) Raw receiver functions (RFs) from terrestrial station VSU in epicentral distance range 65°–69° and back azimuth 10°–40° (b) distribution of the singular spectrum (top) and the singular values arranged in decreasing amplitude (below). The red dashed line denoted the noise threshold. (c) RFs reconstructed using singular values above the noise threshold. The marked phases represent the Ps phases of an intracrustal discontinuity (IC), the Moho (Ps) and a low-velocity zone (LVZ), and the Moho PpPs and PsPs + PpSs phases, respectively.

ratio were set to 0–100 km, 1–5 km/s, and 1.4–2.2, respectively. A maximum of 20 layers was imposed and the range for the noise amplitude was set to 0.01–0.5 with correlation values of RF and $\upsilon_{S,app}$ data fixed to 0.96 and 0, respectively. For calculating synthetic RFs, we use the forward calculation module implemented by Shibutani et al. (1996). The algorithm calculates the impulse response of a layer stack in the P-SV system. The resulting synthetic Z- and RRFs are convolved with the observed ZRF in order to account for the observed waveform complexity (Knapmeyer-Endrun et al., 2018). A $\upsilon_{S,app}$ profile is then calculated for the RFs using the procedure described in Section 2.3.

3. Results

To illustrate the method, we show its application on data from the terrestrial seismic station VSU. Figure 1a shows the raw data which consists of RFs computed from closely located events. In general, the data are noisy. Subplot (b) shows the distribution of singular values and its spectrum for the data. We see the general singular value repulsion behavior with a "bulk" noise region well separated away from the signal "spike." This noise bulk follows the limiting spectral distribution given by the MP law with extreme eigenvalues and their variance given by Equations 1 and 8. The red line shows the optimal threshold for singular value truncation when noise is modeled as an independent and identically distributed (i.i.d.) random matrix. Using the singular value above this threshold, we reconstruct the data by projecting it onto the corresponding eigenvector. Subplot (c) shows the reconstructed RF data showing clear coherent energy arrivals at ∼1, 5, 12, 14, and 23 s. We interpret these as the Ps phases of an intracrustal discontinuity (IC), the Moho (Ps) and a low-velocity zone, and the Moho PpPs and PsPs + PpSs phases, respectively. The reference timing for the Moho Ps phase here is taken from Knapmeyer-Endrun et al. (2014). In general, the method is applicable equally well to data sets covering a wider range of distances and back azimuths. The number of singular values above the threshold then increases

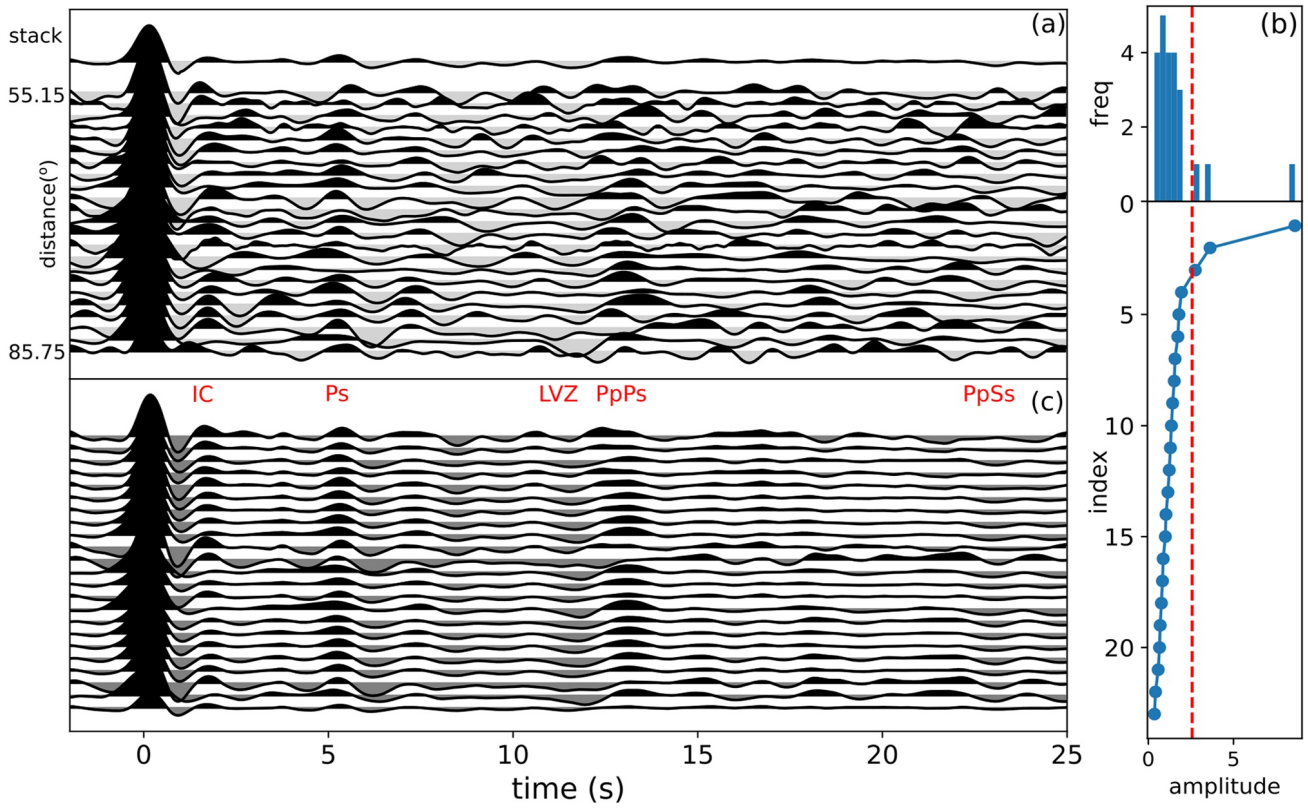

Figure 2. Same as Figure 1 but for epicentral distance range 55°–85° and back azimuth between 80° and 120°.

to accommodate the data variance. Figure 2 shows the reconstruction of RFs from similar back azimuths but a wider epicentral distance range (55°–85°). Here, the threshold increases to three to accommodate the move-out of various phases. Synthetic examples are provided in the Supporting Information (Figures S1 and S2 in Supporting Information S1).

Figure 3 shows the result of applying the phase identification methodology to our selected data from the InSight mission. Apart from the three primary phases at 2.4, 4.8, and 7.2 s previously identified in Knapmeyer-Endrun et al. (2021), the raw RF data (subplot (a)) does not seem to contain any consistent phases after the initial 8 s. From subplot (b), we see that the first principal component is sufficient to identify the main phase arrivals within the first 30 s of the RF waveforms. This is expected as all the events considered here have similar distances and back azimuths. The reconstructed RF waveforms are shown in subplot (c). In addition to the three primary phases, we report three new multiple phases at 15, 20, and 23 s. We interpret these as the P_2pPs, P_2pSs, and P_3pPs phases, where the sub-scripted numeral in the phase name denotes the generating interface. Note that the P_3pPs phase holds significant importance as it corroborates the existence of the much speculated third inter-crustal layer below the InSight landing site. These arrival timings are used to define a misfit window for the RFs which are then jointly inverted with the mean $v_{S_{,app}}$ profile. We initialized 72 chains of 1,000,000 iterations, each sampling the model space simultaneously and independently, with 500,000 iterations discarded as the burn-in phase. Outlier chains were removed, and the models were thinned to obtain a final ensemble of 100,000 models. The main results of the inversion are shown in Figure 4.

A three-layer model exhibits the highest probability density in the solution ensemble. Subplot (a) shows the posterior distribution of the v_S profiles as a function of depth, along with the probability for each interface depth. We see two well-defined mid-crustal interfaces at depths of 8 ± 1 and 21 ± 3 km, along with the crust-mantle transition at 43 ± 5 km. The resulting crustal models agree well with the three-layer models presented in Durán et al. (2022) and Knapmeyer-Endrun et al. (2021). The modeled $v_{S_{,app}}$ curves and the RFs follow the observed data closely and are shown in subplots (b) and (c), respectively. Due to the low SNR of the individual RF waveforms at longer periods, the $v_{S_{,app}}$ curves are limited to periods <13 s. This helps provide tight constraints on the observed

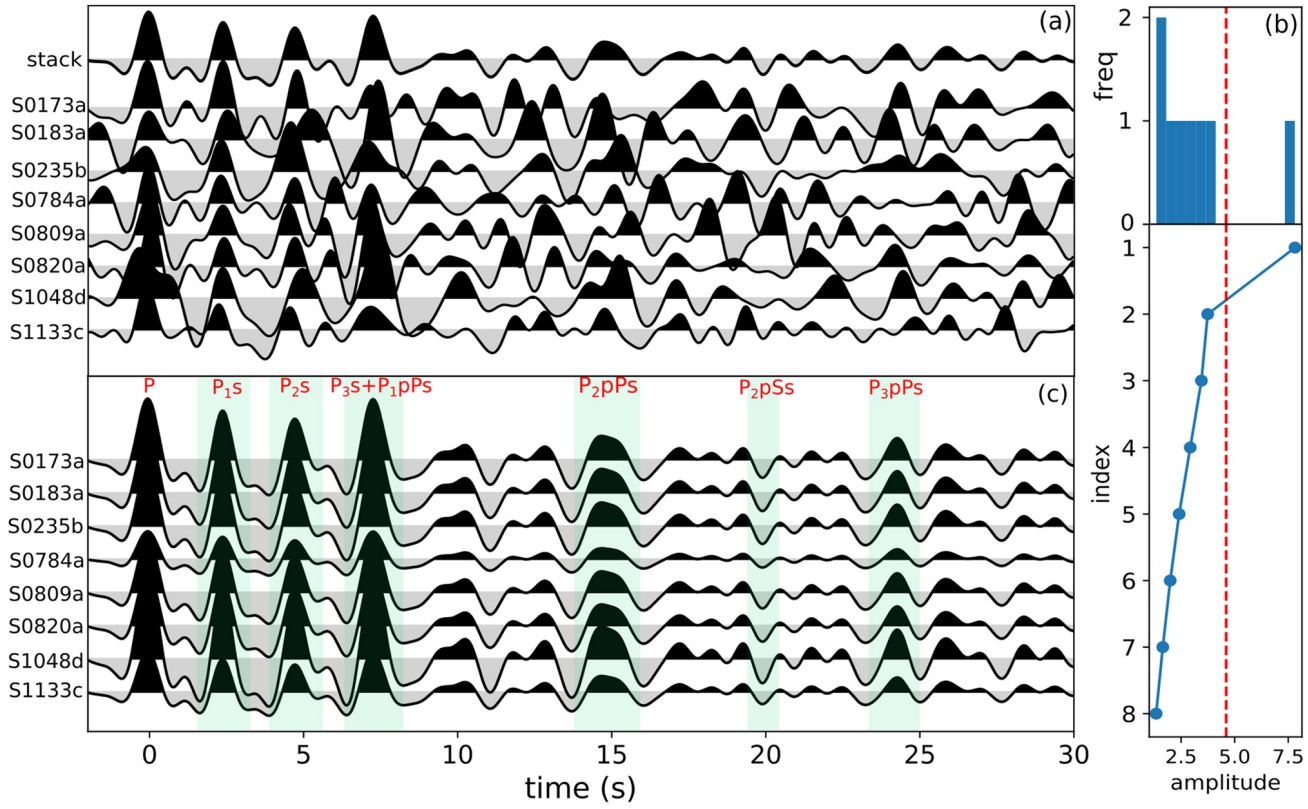

Figure 3. Same as Figure 1 but for Mars. The shaded regions show the denoted arrivals.

v_S value within the shallow part of the crust, but the uncertainty increases with depth where the v_S values and their increases are primarily controlled by the RF amplitudes. The estimated mean v_P/v_S ratio for the three layers is 1.82, 1.77, and 1.64, yielding an average value of ∼1.75 for the crust. A distinct negative arrival of unclear origin is seen at 11.5 s. Although we do not include this in our analysis to avoid over-interpretation, it could either be a Pp phase from the second interface or a low-velocity zone at a depth of ∼70–75 km. The P_1pSs would arrive earlier, between 8 and 10 s, ruling out this possibility. When combined with the observed gravity field using results from Wieczorek et al. (2022), our crustal thickness estimates predict a global average crustal thickness of 46–73 km, assuming a uniform density crust of 2,600 kgm^{-3} for Mars. If a higher crustal density is considered for the northern lowlands, the global average crustal thickness of Mars will lie in the range of 34–73 km.

4. Discussion

With just a handful of good quality, small magnitude, and closely located marsquakes, the analysis of the RF data from the Insight mission present us with many challenges. In this work, we attempt to use this close distance range to our advantage to uncover additional features in the data using concepts of random matrix theory and principal component analysis. For events from similar distances and back azimuths, considerably fewer principal components can reconstruct the main features present in the data. Additional components are needed as distance and back azimuth ranges increase. Using synthetics and real data, Zhang et al. (2019) demonstrated that just the first few principal components could effectively reconstruct all the data variance within events from varying back azimuths. Here, we used events with varying distances and similar back azimuths to establish an equivalent idea. A few points are, however, worth noting. Occasionally, data reconstruction with a few principal components can lead to an erroneous broadening of phases. Though it does not affect the detection of phases, it could sometimes lead to an unwanted merge of very close arrivals. We also find that the singular spectrum, and hence the resulting threshold, can show slight variations based on the data set's quality. For highly irregular RF waveforms, this could severely bias the threshold estimate to lower values. In this case, utilizing higher principal components for data reconstruction will likely result in individual waveform variations instead of emerging features like phase

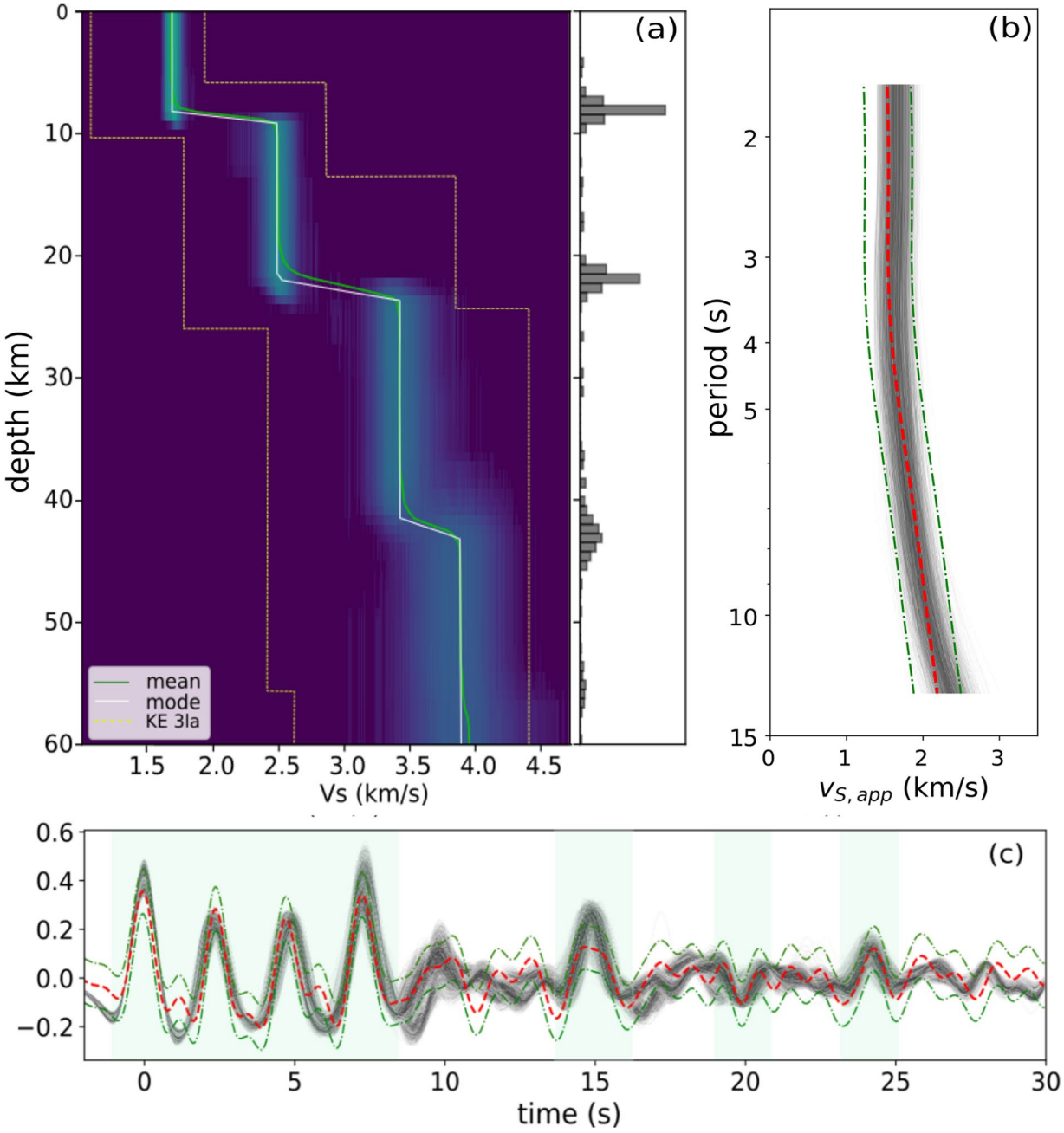

Figure 4. (a) Posterior density of resulting Vs profiles and with histograms for interface depth. KE 3la represents the 2σ bounds of the three-layer ensemble from Knapmeyer-Endrun et al. (2021). (b) Fit to the mean $v_{S,app}$ curve (c) Fit to the mean receiver function waveform. The red dashed lines denote the observed data and green dash-dotted lines represent the 2σ uncertainty.

move-out and back azimuth variations. The compact support of the random singular values can sometimes be disconnected, and therefore, choosing the threshold based only visually on the histograms can lead to errors. On the other hand, histogram bins might not always clearly reflect the transition gap from random to signal singular values. A full computation of the threshold is therefore required. The number of events is also an essential factor. As the size of the data set (m, n) increases, the fluctuations of the Tracy-Widom distribution decrease. Thus, the larger the data set, the higher the stability of the threshold. For a small data set, the assumption of the spiked covariance model can break down. Finally, the noise in RFs is not entirely random and generally has a finite covariance. A recent study by Donoho et al. (2020) generalizes the spiked covariance model to include correlated noise. Extending this analysis to include the correlated case is essential and will be the subject of a later study.

Various interpretations are available for the first two interfaces, ranging from a change in porosity to chemical composition. The low seismic velocity of the first layer has been attributed to a combination of high porosity (20%–30%) and low-density lithology of the region due to the presence of cements and aqueous alterations of minerals (Li et al., 2022b). With increasing depth, material compaction and viscous deformation of host rock can lead to the closure of pore spaces resulting in a transition zone between the porous and non-porous material (Gyalay et al., 2020). Fractured ejecta deposits from the Utopia basin, change in rock crystallinity, and the Borealis impact melt could also explain these crustal layering (Wieczorek et al., 2022). Recent studies on surface wave dispersion show an almost constant S wave velocity of ∼3.2 km/s in the top 5–30 km depth range for the crustal structure away from the InSight landing site (Kim et al., 2022). These values likely represent the average crustal structure in the Northern Hemisphere, indicating that the topmost low-velocity layer beneath the lander is plausibly a local feature.

5. Summary and Conclusion

The RF method has played an important role in the analysis of the Martian crustal structure using data from the InSight mission. In order to contribute to that effort, here we present a method to identify coherent phase arrivals in noisy RF waveforms by modeling data noise as samples from an independent and identically distributed random matrix and using this information to jointly invert the RFs with apparent velocity curves. With examples from terrestrial data, we first show how only a few singular values can help reconstruct coherent parts of the signals enabling the detection of phase arrivals in RF waveforms. The number of singular values needed for this depends on the range of the distance and back azimuths of the events in the data set, with often a single value being sufficient in the special case of closely located events. We then apply this method to a set of eight marsquakes detected by the InSight mission and evaluate the crustal structure below the landing site based on these data. Three new crustal phases were identified in the RF waveforms, which we interpret as P_2pPs, P_2pSs, and P_3pPs phases. A subsequent joint inversion of the RFs with the mean $v_{S,app}$ curve shows that the crust of Mars below the InSight landing site is composed of three distinct layers with increasing velocity. A crustal thickness of ∼43 km is estimated.

In conclusion, the results presented here agree well with previous work from Knapmeyer-Endrun et al. (2021). The identified P_3pPs phase suggests a strong preference for the three-layer model in their study. The inversion results presented here have further constrained the subsurface velocities at the InSight landing site. Our preferred interpretation of the observed crustal layering beneath InSight considers this a result of a series of transitions from sediments or pyroclastic deposits that experienced aqueous alterations to less porous Utopia ejecta and finally to the pre-existing crustal materials from early differentiation of Borealis impact melt (Wieczorek et al., 2022). A thicker crust, like one obtained from such a three-layer model, is also more compatible with the amount of heat-producing elements within the Martian crust estimated by spectroscopy observations and geodynamical modeling (Knapmeyer-Endrun et al., 2021; Taylor, 2013). A much lower bulk crustal density and significant enrichment in crustal heat-producing elements would otherwise be needed for a thinner crust (Knapmeyer-Endrun et al., 2021). However, it is unlikely that this three-layered formation is indicative of the global Martian crustal structure (Kim et al., 2022) and can be plausibly just a feature of the local geology in the vicinity of the InSight landing site.

Data Availability Statement

Seismic data for station VSU are publicly available and can be obtained from EIDA (http://eida.gfz-potsdam.de/webdc3/) using the event information provided in the Supporting Information. The InSight seismic data presented here (http://dx.doi.org/10.18715/SEIS.INSIGHT.XB_2016) are publicly available through the Planetary Data System (PDS) Geosciences node of the Incorporated Research Institutions for Seismology (IRIS) Data Management Center under network code XB (https://pds-geosciences.wustl.edu/missions/insight/seis.htm), and through the data center of Institut de Physique du Globe, Paris (http://www.seis-insight.eu).

Acknowledgments
R.J. acknowledges the funding provided by the IMPRS and the Emeritus group. The MPS MPG SEIS team acknowledges funding for development of the SEIS leveling system by the DLR German Space Agency. The authors acknowledge NASA, CNES, their partner agencies and Institutions (UKSA, SSO, DLR, JPL, IPGP-CNRS, ETHZ, IC, MPS-MPG) and the flight operations team at JPL, SISMOC, MSDS, IRIS-DMC, and PDS. This paper is InSight Contribution Number 188.

References

Ammon, C. J. (1991). The isolation of receiver effects from teleseismic *P* waveforms. *Bulletin of the Seismological Society of America*, *81*(6), 2504–2510. https://doi.org/10.1785/bssa0810062504

Baik, J., Arous, G. B., & Péché, S. (2005). Phase transition of the largest eigenvalue for nonnull complex sample covariance matrices. *Annals of Probability*, *33*(5), 1643–1697. https://doi.org/10.1214/009117905000000233

Banerdt, W. B., Smrekar, S. E., Banfield, D., Giardini, D., Golombek, M., Johnson, C. L., et al. (2020). Initial results from the InSight mission on Mars. *Nature Geoscience*, *13*(3), 183–189. https://doi.org/10.1038/s41561-020-0544-y

Benaych-Georges, F., & Nadakuditi, R. R. (2012). The singular values and vectors of low rank perturbations of large rectangular random matrices. *Journal of Multivariate Analysis*, *111*, 120–135. https://doi.org/10.1016/j.jmva.2012.04.019

Birch, F. (1961). The velocities of compressional waves in rocks to 10 kilobars, Part 2. *Journal of Geophysical Research*, *66*(7), 2199–2224. https://doi.org/10.1029/jz066i007p02199

Bodin, T., Sambridge, M., Tkalčić, H., Arroucau, P., Gallagher, K., & Rawlinson, N. (2012). Transdimensional inversion of receiver functions and surface wave dispersion. *Journal of Geophysical Research: Solid Earth*, *117*(B2). https://doi.org/10.1029/2011jb008560

Clinton, J. F., Ceylan, S., van Driel, M., Giardini, D., Stähler, S. C., Böse, M., et al. (2021). The Marsquake catalog from InSight, sols 0–478. *Physics of the Earth and Planetary Interiors*, *310*, 106595. https://doi.org/10.1016/j.pepi.2020.106595

Clinton, J. F., Giardini, D., Böse, M., Ceylan, S., van Driel, M., Euchner, F., et al. (2018). The Marsquake service: Securing daily analysis of SEIS data and building the Martian seismicity catalog for InSight. *Space Science Reviews*, *214*(8), 1–33. https://doi.org/10.1007/s11214-018-0567-5

Compaire, N., Margerin, L., Garcia, R. F., Pinot, B., Calvet, M., Orhand-Mainsant, G., et al. (2021). Autocorrelation of the ground vibrations recorded by the SEIS-InSight seismometer on Mars. *Journal of Geophysical Research: Planets*, *126*(4), e2020JE006498. https://doi.org/10.1029/2020je006498

Donoho, D. L., Gavish, M., & Romanov, E. (2020). ScreeNOT: Exact MSE-optimal singular value thresholding in correlated noise. arXiv preprint arXiv:2009.12297.

Dreiling, J., & Tilmann, F. (2019). BayHunter-McMC transdimensional Bayesian inversion of receiver functions and surface wave dispersion.

Drilleau, M., Samuel, H., Garcia, R. F., Rivoldini, A., Perrin, C., Michaut, C., et al. (2022). Marsquake locations and 1-D seismic models for Mars from insight data. *Earth and Space Science Open Archive*, *77*. https://doi.org/10.1002/essoar.10511074.2

Du, Z., & Foulger, G. (1999). The crustal structure beneath the northwest fjords, Iceland, from receiver functions and surface waves. *Geophysical Journal International*, *139*(2), 419–432. https://doi.org/10.1046/j.1365-246x.1999.00945.x

Durán, C., Khan, A., Ceylan, S., Zenhäusern, G., Stähler, S., Clinton, J., & Giardini, D. (2022). Seismology on Mars: An analysis of direct, reflected, and converted seismic body waves with implications for interior structure. *Physics of the Earth and Planetary Interiors*, *325*, 106851. https://doi.org/10.1016/j.pepi.2022.106851

Gagnepain-Beyneix, J., Lognonné, P., Chenet, H., Lombardi, D., & Spohn, T. (2006). A seismic model of the lunar mantle and constraints on temperature and mineralogy. *Physics of the Earth and Planetary Interiors*, *159*(3–4), 140–166. https://doi.org/10.1016/j.pepi.2006.05.009

Gavish, M., & Donoho, D. L. (2014). The optimal hard threshold for singular values is $4/\sqrt{3}$. *IEEE Transactions on Information Theory*, *60*(8), 5040–5053. https://doi.org/10.1109/tit.2014.2323359

Giardini, D., Lognonné, P., Banerdt, W. B., Pike, W. T., Christensen, U., Ceylan, S., et al. (2020). The seismicity of Mars. *Nature Geoscience*, *13*(3), 205–212.

Gyalay, S., Nimmo, F., Plesa, A.-C., & Wieczorek, M. (2020). Constraints on thermal history of Mars from depth of pore closure below insight. *Geophysical Research Letters*, *47*(16), e2020GL088653. https://doi.org/10.1029/2020GL088653

Hannemann, K., Krüger, F., Dahm, T., & Lange, D. (2017). Structure of the oceanic lithosphere and upper mantle north of the Gloria fault in the eastern mid-Atlantic by receiver function analysis. *Journal of Geophysical Research*, *122*(10), 7927–7950. https://doi.org/10.1002/2016JB013582

InSight Mars SEIS Data Service. (2019). SEIS raw data, InSight mission. IPGP, JPL, CNES, ETHZ, ICL, MPS, ISAE-Supaero, LPG, MFSC.

InSight Marsquake Service. (2022). Mars seismic catalog, InSight mission; v10 2022-04-01. ETHZ, IPGP, JPL, ICL, Univ. Bristol. https://doi.org/10.12686/a16

Johnstone, I. M. (2001). On the distribution of the largest eigenvalue in principal components analysis. *Annals of Statistics*, *29*(2), 295–327. https://doi.org/10.1214/aos/1009210544

Joshi, R., Knapmeyer-Endrun, B., Mosegaard, K., Igel, H., & Christensen, U. R. (2021). Joint inversion of receiver functions and apparent incidence angles for sparse seismic data. *Earth and Space Science*, *8*(10), e2021EA001733. https://doi.org/10.1029/2021EA001733

Julia, J., Ammon, C. J., Herrmann, R., & Correig, A. M. (2000). Joint inversion of receiver function and surface wave dispersion observations. *Geophysical Journal International*, *143*(1), 99–112. https://doi.org/10.1046/j.1365-246x.2000.00217.x

Khan, A., Ceylan, S., van Driel, M., Giardini, D., Lognonné, P., Samuel, H., et al. (2021). Upper mantle structure of Mars from insight seismic data. *Science*, *373*(6553), 434–438. https://doi.org/10.1126/science.abf2966

Kim, D., Banerdt, W. B., Ceylan, S., Giardini, D., Lekić, V., Lognonné, P., et al. (2022). Surface waves and crustal structure on Mars. *Science*, *378*(6618), 417–421. https://doi.org/10.1126/science.abq7157

Kim, D., Lekić, V., Irving, J. C. E., Schmerr, N., Knapmeyer-Endrun, B., Joshi, R., et al. (2021). Improving constraints on planetary interiors with PPs receiver functions. *Journal of Geophysical Research: Planets*, *126*(11), e2021JE006983. https://doi.org/10.1029/2021JE006983

Knapmeyer-Endrun, B., Ceylan, S., & van Driel, M. (2018). Crustal *S* wave velocity from apparent incidence angles: A case study in preparation for InSight. *Space Science Reviews*, *214*(5), 83. https://doi.org/10.1007/s11214-018-0510-9

Knapmeyer-Endrun, B., Krüger, F., & Group, T. P. W. (2014). Moho depth across the Trans-European Suture Zone from *P* and *S* receiver functions. *Geophysical Journal International*, *197*(2), 1048–1075. https://doi.org/10.1093/gji/ggu035

Knapmeyer-Endrun, B., Panning, M. P., Bissig, F., Joshi, R., Khan, A., Kim, D., et al. (2021). Thickness and structure of the Martian crust from InSight seismic data. *Science*, *373*(6553), 438–443. https://doi.org/10.1126/science.abf8966

Li, J., Beghein, C., Davis, P., Wieczorek, M. A., McLennan, S. M., Kim, D., et al. (2022b). Crustal structure constraints from the detection of the SsPp phase on Mars. *Earth and Space Science*, e2022EA002416. https://doi.org/10.1029/2022EA002416

Li, J., Beghein, C., Wookey, J., Davis, P., Lognonné, P., Schimmel, M., et al. (2022a). Evidence for crustal seismic anisotropy at the InSight lander site. *Earth and Planetary Science Letters*, *593*, 117654. https://doi.org/10.1016/j.epsl.2022.117654

Lognonné, P., Banerdt, W. B., Giardini, D., Pike, W., Christensen, U., Laudet, P., et al. (2019). SEIS: InSight's seismic experiment for internal structure of Mars. *Space Science Reviews*, *215*(1), 12.

Lognonné, P., Banerdt, W. B., Pike, W., Giardini, D., Christensen, U., Garcia, R. F., et al. (2020). Constraints on the shallow elastic and anelastic structure of Mars from insight seismic data. *Nature Geoscience*, *13*(3), 213–220.

Lognonné, P., Gagnepain-Beyneix, J., & Chenet, H. (2003). A new seismic model of the Moon: Implications for structure, thermal evolution, and formation of the Moon. *Earth and Planetary Science Letters*, *211*(1–2), 27–44. https://doi.org/10.1016/s0012-821x(03)00172-9

Marchenko, V. A., & Pastur, L. A. (1967). Distribution of eigenvalues for some sets of random matrices. *Matematicheskii Sbornik*, *114*(4), 507–536.

Schimmel, M., Stutzmann, E., Lognonné, P., Compaire, N., Davis, P., Drilleau, M., et al. (2021). Seismic noise autocorrelations on Mars. *Earth and Space Science*, *8*(6), e2021EA001755. https://doi.org/10.1029/2021ea001755

Shibutani, T., Sambridge, M., & Kennett, B. (1996). Genetic algorithm inversion for receiver functions with application to crust and uppermost mantle structure beneath eastern Australia. *Geophysical Research Letters*, *23*(14), 1829–1832. https://doi.org/10.1029/96GL01671

Svenningsen, L., & Jacobsen, B. (2007). Absolute *S* velocity estimation from receiver functions. *Geophysical Journal International*, *170*(3), 1089–1094. https://doi.org/10.1111/j.1365-246x.2006.03505.x

Taylor, G. J. (2013). The bulk composition of Mars. *Geochemistry*, *73*(4), 401–420. https://doi.org/10.1016/j.chemer.2013.09.006

Tracy, C. A., & Widom, H. (1996). On orthogonal and symplectic matrix ensembles. *Communications in Mathematical Physics*, *177*(3), 727–754. https://doi.org/10.1007/bf02099545

Vinnik, L., Chenet, H., Gagnepain-Beyneix, J., & Lognonne, P. (2001). First seismic receiver functions on the Moon. *Geophysical Research Letters*, *28*(15), 3031–3034. https://doi.org/10.1029/2001gl012859

Wiechert, E. (1907). *Über Erdbebenwellen. I. Theoretisches über die Ausbreitung der Erdbebenwellen. Nachrichten von der Gesellschaft der Wissenschaften zu Göttingen* (pp. 415–429). Mathematisch-Physikalische Klasse.

Wieczorek, M. A., Broquet, A., McLennan, S. M., Rivoldini, A., Golombek, M., Antonangeli, D., et al. (2022). InSight constraints on the global character of the Martian crust. *Journal of Geophysical Research: Planets*, *127*(5), e2022JE007298. https://doi.org/10.1029/2022je007298

Zhang, J., Chen, L., & Wang, X. (2019). Crustal structure study based on principal component analysis of receiver functions. *Science China Earth Sciences*, *62*(7), 1110–1124. https://doi.org/10.1007/s11430-018-9341-9

References From the Supporting Information

Ceylan, S., van Driel, M., Euchner, F., Khan, A., Clinton, J., Krischer, L., et al. (2017). From initial models of seismicity, structure, and noise to synthetic seismograms for Mars. *Space Science Reviews*, *211*(1–4), 595–610. https://doi.org/10.1007/s11214-017-0380-6

Chapter 5

Discussion and Outlook

With the first successful deployment of a broad-band seismometer on the surface of another terrestrial planet, NASA's InSight mission has enabled the in-situ investigation of the Martian interior. As the ancient crust of Mars holds clues to its evolution and formation, investigation of its thickness and structure have been one of the primary goals of the mission. The RF method has played an important role in the analysis of the Martian crustal structure using the InSight seismic data. This thesis presents some of the methods that were developed and applied in order to contribute to this endeavour.

Chapter 2 outlines a single-station technique that can be applied to study the crustal structure using sparse seismic data, as would be expected on a planet with highly uncertain seismicity levels. It describes the general RF technique, the limitations imposed by non-uniqueness on inversion results, and how these can be used to derive absolute S-wave velocities of the subsurface using P-wave polarization as a constraint. Further, an alternative method for calculating probability densities from the NA ensemble along with determining the optimal model among several others using AIC is also presented. Application to synthetic waveforms show promising results, in both single and multiple event cases. As expected, the uncertainty of the model parameters is observed to decrease with an increase in the size of the dataset.

Examples of application to terrestrial data from stations BFO and SUW show that the joint inversion of RFs and $v_{S,app}$ curves is suitable for use in diverse geological settings and Moho depths. As $v_{S,app}$ curves can be directly calculated from the RF data, reliance on other observable data can be avoided. This becomes especially important in extra-terrestrial setting where the seismic data might not contain certain observables like surface waves. On Mars, the lack of surface wave data limited the information that could be derived from their analysis. As absolute v_S values are highly influenced by the $v_{S,app}$ curve in the presented method, these need careful estimation. While the lack of measurements at shorter periods can lead to high uncertainty in regolith layer thickness, missing values at longer periods can increase uncertainty in the depths and velocities of deeper layers and upper mantle. Moreover, fractures and stress can lead to material anisotropy which can affect the inversion results. In this work the effects of anisotropy have been neglected. The model selection using AIC works well if the least misfit model is a good representative of

the entire ensemble. Strong deviations within the family can bias the preferred model. Moreover, AIC can often chose a more complex model when the sample-size is small. In this case, AICc is used instead, but the exact cut-off for the transition can be blurred for different data types. A more optimal approach to model selection is preferable.

Chapter 3 shows a first glance at the Martian seismic data from the InSight mission. Three low-frequency marsquakes with clearest P-wave onsets and polarizations have been analysed primarily using RF analysis. Three consistent phase arrivals at 2.4, 4.8 and 7.2 s are seen across all the events which make the data equally compatible with either a two-layer or a three-layer model. The additional constraints from noise and coda auto-correlations show energy maxima consistent with the first two interfaces, but show no clear indication of the third interface. The lack of events from a wider range of distances and the high noise levels in the later parts of the waveforms prevent identification of later arrivals, making an unambiguous choice difficult. Although spectroscopic observations of heat-producing elements, geodynamical, and moment of inertia studies favour the three-layer model, none could completely exclude the two layer model. This uncertainty also increases the range of mean global crustal thickness values that are compatible with the data.

Chapter 4 assumes the RF data to be a fixed-rank perturbation of random noise and attempts to separate the coherent signals from this noise using the generalized Marchenko-Pastur law. Once separated, the filtered waveforms are used to identify multiply-reflected phase arrivals. For small distance ranges, only a few and often a single principal component (PC) can suffice. This is also the case for the data from the InSight mission. As most of the events in our dataset are located in the general region of Cerberus Fossae, a single PC has been utilized to identify phases. The basic assumption in this method is that the noise in RF data is i.i.d. random. This, however, is not always the case. Correlations can exist within the data noise. Therefore, extending the analysis to a more general case of correlated noise could lead to better results. Another crucial assumption is that the location estimates and their uncertainties are precise. Given a single station, this can be difficult, although MQS has verified the high precision of its location algorithms through orbiter-imaged impacts. SVD is highly dependent on the data quality; hence differences may arise when used on data from different RF computation techniques. The number of events is also an essential factor. As the size of the dataset increases, the fluctuations of the Tracy-Widom distribution decrease. Thus, the larger the dataset, the higher the stability of the threshold. When the PC below the threshold is within the fluctuation regime of the largest noise eigenvalue, the assumption of the spiked covariance matrix can break down.

Finally, a transdimensional inversion method is adopted for a more robust model selection procedure. The optimal number of layers required by the data is assessed by calculating absolute model probabilities rather than AIC values to avoid data over-fitting or under-fitting. However, the full waveform is not inverted for, and only time windows containing the identified phases are used to form the misfit function. Although this avoids fitting noise, it could result in models with lower complexity than the entire RF waveform required. More minor discontinuities can be overlooked. A Gaussian correlation law is assumed for the data noise in the inversion algorithm. Although this is close to reality for

RF waveforms, a full covariance matrix can lead to better results. More data is needed to estimate such a covariance matrix reasonably, which can be difficult when only sparse data are available.

The peculiarities of the seismic data from the InSight mission also need careful analysis. Various signals of aseismic origin contaminate the data at different frequency ranges. Strong environmental injections also influence the recorded ground motion. The superposition of all these with the various seismic phases arriving at the station makes it difficult to identify them. More than 90% events fall in the HF category and cannot be used to calculate RFs as these do not interact with the crust-mantle boundary like teleseismic events.

The method presented in this thesis can nevertheless be improved using various strategies. The RF forward computation used here does not allow for dipping interfaces which could better model complex crusts. Including anisotropy analysis in the study can help avoid picking the wrong phase arrivals. Another improvement would be to use full RF waveforms and a data covariance matrix in the inversion process. This could improve the resolution of the retrieved v_S profiles.

Some uncertainty bounds could be attributed to the threshold value for PCA. The fluctuations of the Tracy-Widom distribution could be calculated for the dataset size, which hints at the stability of the threshold. With more surface wave data, the RFs could also be jointly available with their group and phase velocity dispersion curves. This can help provide more independent constraints on the absolute velocities, especially in the upper-mantle region. Rayleigh wave ellipticity measurements could also be used in conjunction with the RF waveforms for constraining velocities and discontinuities in the shallow crust. However, more data are required for such analysis. The work presented here can also be adapted and improved for planned future extra-terrestrial seismic missions like NASA's Dragonfly and Farside.

Chapter 6

Conclusion

Before NASA's InSight mission, constraints on Martian crust were primarily based on geodetic, gravity and topography data, geochemical analysis of Martian meteorites, and thermal evolution models. Their lack of sensitivity to absolute values resulted in high uncertainty in measurements. With over three years of continuous seismic monitoring of Mars, the InSight mission has provided valuable data on the planet's interior structure. The methods presented in this thesis have been applied to the InSight seismic data to evaluate the crustal thickness and layering below the landing site, along with the uncertainty estimates. Lognonné et al. (2020) provide the first constraints on the crustal structure using the methods developed in this thesis. Using RF and a $v_{S,_{app}}$ profile computed from a single marsquake (S0173a), they show the evidence of crustal layering on Mars with the first low-velocity layer extending down to a depth of ~ 10 km.

Chapter 3 of this thesis further investigates this layered crustal structure using three marsquakes and concludes the existence of two layers and possibly another third layer below the landing site. Assuming a two-layer crust, the crust-mantle boundary is located at 20 ± 5 km depth. In contrast, in the three-layer case, the crust-mantle boundary is located at a depth of 39 ± 8 km with another inter-crustal interface at ~ 20 km. Both models show a mid-crustal interface at ~ 10 km. This dubiety resulted from the interference of the directly converted phase from the third interface with the reverberation from the uppermost layer. Chapter 4 attempts to resolve this ambiguity using a random matrix theory approach. By extracting random noise from the RF data, it was possible to identify the reverberation from a deeper third layer. Inversion results suggest a strong preference for the three-layer model with a crust-mantle boundary at 43 ± 4 km depth, consistent with other studies using different approaches.

The interpretation of this layered crustal structure on Mars can be based on various arguments ranging from compositional to porosity changes. One possible interpretation from Wieczorek et al. (2022) suggests that the first layer could result from either heavily fractured extrusive lava flows or thick pyroclastic deposits that might have undergone aqueous alteration, which accounts for its low v_S value. The second layer below this could result from impact-ejecta sediments from the Utopia basin with much lower porosity indicating an abrupt increase in v_S. Finally, the last layer could represent the transition to

the initial crust formed from the differentiation of the material from the Borealis impact melt. It should be noted that this three-layer stratigraphy is not representative of the global Martian crust and is more plausibly a result of the local geology in the vicinity of the InSight landing site. A recent surface wave dispersion analysis does not show such a layered structure of the Martian crust. However, the last interface showing the transition to the ancient crust could also be present in the northern lowlands.

The range of possible crustal densities estimated for these models, estimated to lie between 2800-3100 kg/m^3, is substantially less than that predicted by surface materials at $\sim$ 3300 kg/m^3 (Baratoux et al., 2014). This lower bulk density can be explained by the presence of high porosity materials, presence of fluids, and fractures filled by low-density cements or a combination of these. Using the three-layer crust to model the cooling and differentiation history suggests that the crust of Mars is $\sim$ 13 times enriched in radioactive heat-producing elements compared to the primitive mantle. This is greater than that estimated by the surface measurements, indicating that most heat-producing elements are sequestered into the crust. These results can further be utilized to investigate dynamical mantle models for understanding the present and past Martian evolution, the origins of its crustal dichotomy and the mysteries surrounding crustal magnetism.

Appendix A

Supporting Information for Chapter 2

Earth and Space Science

Supporting Information for

Joint inversion of receiver functions and apparent incidence angles for sparse seismic data

Rakshit Joshi[1,4], Brigitte Knapmeyer-Endrun[2] , Klaus Mosegaard[3] , Heiner Igel[4] , Ulrich R. Christensen[1]

[1]Max-Planck-Institute for Solar System Research, Göttingen, Germany
[2]Bensberg Observatory, University of Cologne, Cologne, Germany
[3]Niels Bohr Institute, University of Copenhagen, Copenhagen, Denmark
[4]Ludwig-Maximilians-University, Munich, Germany

Contents of this file

Introduction

This document provides information on the search criteria needed to retrieve the terrestrial seismic data used in the manuscript along with the ray parameter used for RF calculation. The details of the source distances and models used to create the synthetic waveform have been tabulated additionally.

Terrestrial data for seismic stations BFO and SUW are publicly available and can be obtained from EIDA : http://www.orfeus-eu.org/data/eida/

Synthetic data was created using Instaseis (https://instaseis.net/). The interior models used in the manuscript are publicly available and can be obtained from : http://instaseis.ethz.ch/marssynthetics/

Station code	Network code	Latitude (°N)	Longitude (°E)
BFO	GR	48.330	8.30
SUW	PL	54.0125	23.1808

Table S1. Station information for seismic stations BFO and SUW

Event	Time	Ray parameter
3-SEP-2007	16:14:53	5.35
6-JUL-2008	09:08:21	5.31
6-JUN-2009	20:33:28	7.66
15-JAN-2009	17:49:39	5.32
24-NOV-2008	09:02:58	5.68
29-OCT-2009	17:44:31	7.78

Table S2. Event information for station BFO

Event	Time	Ray parameter
8-FEB-2008	09:38:14	6.38
30-SEP-2009	10:16:09	5.17
7-OCT-2009	21:41:13	4.57
30-MAR-2010	01:02:53	6.26
10-SEP-2008	13:08:14	6.35
2-OCT-2007	18:00:06	6.01

Table S3. Event information for station SUW

Model	Distance used (°)
C30VH_AKSNL	70
C30VL_AKSNL	40
C80VL_AKSNL	90, 80, 70, 60, 50, 40

Table S4. Source distance and models used for creating synthetic waveforms

Appendix B

Supporting Information for Chapter 3

Science
AAAS

Supplementary Materials for

Thickness and structure of the Martian crust from InSight seismic data

Brigitte Knapmeyer-Endrun[1]*, Mark P. Panning[2], Felix Bissig[3], Rakshit Joshi[4], Amir Khan[3,5], Doyeon Kim[6], Vedran Lekić[6], Benoit Tauzin[7,8], Saikiran Tharimena[2,9], Matthieu Plasman[10],Nicolas Compaire[11], Raphael F. Garcia[11], Ludovic Margerin[12], Martin Schimmel[13], Éléonore Stutzmann[10], Nicholas Schmerr[6,] E. Bozdağ[14], Ana-Catalina Plesa[15], Mark A. Wieczorek[16], Adrien Broquet[17],[16], Daniele Antonangeli[18], Scott M. McLennan[19], Henri Samuel[10], Chloé Michaut[7,20], Lu Pan[21], Suzanne E. Smrekar[2],Catherine L. Johnson[22,23],Nienke Brinkman[3], Anna Mittelholz[3], Attilio Rivoldini[24], Paul M. Davis[25], Philippe Lognonné[10,20], Baptiste Pinot[11], John-Robert Scholz[4], Simon Stähler[3], Martin Knapmeyer[15], Martin van Driel[3], Domenico Giardini[3], W. Bruce Banerdt[2]

[1] Bensberg Observatory, University of Cologne, Vinzenz-Pallotti-Str. 26, 51429 Bergisch Gladbach, Germany.

[2] Jet Propulsion Laboratory, California Institute of Technology; 4800 Oak Grove Dr., M/S 183-301, Pasadena, CA 91109, USA.

[3] Institute of Geophysics, ETH Zurich, Sonneggstr. 5, 8092 Zürich, Switzerland.

[4] Max Planck Institute for Solar System Research, Justus-von-Liebig-Weg 3, 37077 Göttingen, Germany.

[5] Physik-Institut, University of Zurich, Zurich, Switzerland.

[6] University of Maryland, College Park, Department of Geology, 8000 Regents Dr., College Park, MD, 20782-4211, USA.

[7] Université de Lyon, Ecole Normale Supérieure de Lyon, Université Claude Bernard Lyon 1, CNRS, Laboratoire de Géologie de Lyon : Terre, Planètes, Environnement, 69622 Villeurbanne, France.

[8] Research School of Earth Sciences, The Australian National University, Canberra, Australian Capital Territory 0200, Australia.

[9] now at University of Vienna, Althanstrasse 14, 1090 Vienna, Austria.

[10] Université de Paris, Institut de Physique du Globe de Paris, CNRS, 1 rue Jussieu, F-75005 Paris, France.

[11] Institut Supérieur de l'Aéronautique et de l'Espace SUPAERO, 10 Avenue Edouard Belin, 31400 Toulouse, France.

[12] Institut de Recherche en Astrophysique et Planétologie, Université Toulouse III Paul Sabatier, CNRS, CNES, 14 Av. E. Belin, 31400, Toulouse, France.

[13] Geosciences Barcelona - CSIC, Barcelona, Spain.

[14] Colorado School of Mines, Department of Geophysics, 1500 Illinois Street, Golden, CO 80401, USA.

[15] Institute of Planetary Research, German Aerospace Center (DLR), 12489 Berlin, Germany.

[16] Université Côte d'Azur, Observatoire de la Côte d'Azur, CNRS, Laboratoire Lagrange, France.

[17] Lunar and Planetary Laboratory, University of Arizona, Tucson, AZ 85721, USA.

[18] Sorbonne Université, Muséum National d'Histoire Naturelle, UMR CNRS 7590, Institut de Minéralogie, de Physique des Matériaux et de Cosmochimie, IMPMC, 75005 Paris, France.

[19] Department of Geosciences, Stony Brook University, Stony Brook, NY, 11794-2100, USA.

[20] Institut Universitaire de France.

[21] University of Copenhagen, GLOBE Institute, Center for Star and Planet Formation, Copenhagen, Denmark.

[22] Department of Earth, Ocean and Atmospheric Sciences, University of British Columbia, Vancouver, BC, V6T 1Z4, Canada.

[23] Planetary Science Institute, Tucson, 1700 East Fort Lowell, Suite 106, Tucson, AZ 85719-2395, USA.

[24] Royal Observatory of Belgium, Brussels, Belgium.

[25] Department of Earth, Planetary, and Space Sciences, University of California Los Angeles, CA90095, USA.

Correspondence to: bknapmey@uni-koeln.de

This PDF file includes:

Materials and Methods

S1. Receiver functions

The P-to-S receiver function (RF) method is based on the assumption that the P-component of a teleseismic P-wave recording approximates the source and distant path effects in the three-component seismogram. The P-component is obtained by removal of the instrument response, and transfer of the recorded seismograms into the ray coordinate system. Then, deconvolution of the P- from the SV-component of the P-wave and its coda results in the impulse response of the subsurface for transmitted S-waves, the so-called receiver function (*17*). On Earth, this is a standard method for determining and mapping crustal and upper mantle structure (*33-35*). The S-to-P RF method is based on the same principle, but uses P-precursors to the S-wave. It has the additional benefit that, while direct S-to-P conversions arrive before the S-onset, all multiply converted and reflected phases arrive after it. S-to-P receiver functions have previously been applied to extract crustal structure from the Apollo lunar data (*36,37*). Fig. S1 shows seismograms of two events for which precursors to the S-wave onset can tentatively be identified on the vertical component before any further processing. The timing of the initial precursor is consistent with the phase observed in S-to-P receiver functions (see sections S1.1, S1.3, and S1.4).

P-to-S RFs were calculated by seven groups using nine different algorithms and parameter settings for the rotation and deconvolution steps. This allows assessing the influence of a specific processing method on the resulting receiver function waveform. The different algorithms are described briefly below and summarized in Tab. S1. In contrast to the previous analysis of two events for shallow crustal layering *(18)*, RFs are calculated in the LQT ray coordinate system here instead of the ZRT system. While this involves an additional rotation around the P-wave incidence angle that needs to be determined from the data first, it has the advantage of better separating P- and SV-energy on the L- and Q-component, respectively, and thus, by removing energy from multiple P-wave reflections, providing a cleaner P-to-S RF. The P-wave recording of event S0173a contained a prominent glitch on all three components, and a deglitching method was first applied to remove this glitch (*18,38*). All P-to-S receiver functions are plotted overlaid on each other in Fig. 1A, and on the same scale but offset for clarity in Fig. S2. While the general shape of the different RFs and the timing of the prominent arrivals within the first 8 seconds is generally consistent between different methods, the frequency content and the amplitude of the arrivals varies, with higher frequencies contained in the RFs resulting from processing methods A1, A2, B1, C2, D, E1 and E2 compared to B2, C1, F and G. Accordingly, we chose one set of high-frequency and one set of low-frequency RFs as exemplary data sets representing the range of RFs for the inversions (section S3), to investigate both the effect of differences in RF processing and in inversion method on the resulting models. S-to-P RFs were calculated by a subset of three groups. The methods used are also detailed below and summarized in Tab. S1.

S1.1 Method A: (Vedran Lekic, Doyeon Kim)

We computed P-to-S and S-to-P RFs of two Mars events, S0173a and S0235b using transdimensional hierarchical Bayesian deconvolution (THBD, *39*). Instead of a single deconvolved timeseries, our method yields an ensemble of RFs for each event, whose features appear in proportion to their likelihood. We carried out one million iterations of the THBD, discarding the first half as burn-in, and saving every 1000th sample to the ensemble. A window between 8 to 9 seconds in duration, starting at the P- or S-arrival, was applied to remove later

arriving phases and pre-event noise while minimizing abrupt waveform truncation (dashed line, Fig. S3). We then estimated the up-going P and SV energy using a free surface transform matrix (*40*), using published back azimuths of 91° and 74° for S0173a and S0235b (*21*), respectively, and performing a grid-search on values of V_P, V_P/V_S, and ray parameter that minimize the correlation between the P and SV waveforms within 2 and 5 seconds of the P- and S arrival, respectively. To maximize the signal-to-noise ratio of the RFs, we also estimated two noise parameters that characterize the decay and oscillation rates of the noise correlation function derived from pre-event data. All of the parameters for processing the RFs are shown in Fig. S4 (see Fig. 1A for the suite of RFs computed by different methods).

S1.2 Method B: (Benoit Tauzin)

P-to-S RFs were computed for events S0173a, S0183a, S0235b and S0325a. Broadband records in the UVW system were deconvolved from the VBB instrumental response, synchronized, and rotated to the vertical-north-east (ZNE) system using information from the response file on May 23, 2019 (components azimuth and dip, poles and zeros). The information from MQS about the arrival times of the P-wave was then used to find the teleseismic P-wave coda on the records, and to normalize the traces with respect to the amplitude of the P-wave on the Z component. The onset time of the P-wave was measured by band-pass filtering (4th order Butterworth, forward and reverse) records within the 0.1-0.9 Hz frequency-band and picking the onsets on the Z component. The records are further analyzed to find the azimuths of arrival and polarizations of the P-waves in the vertical plane through principal component analysis, for component rotation from ZNE to PSvSh. The aligned and normalized waveforms were trimmed over a 5 s-long window after the onset of the P-wave. Covariance matrices were obtained (i) from the N and E components, for rotation from ZNE to vertical-radial-transverse (ZRT) directions, and (ii) from Z and R components for rotation from ZRT to the PSvSh system. Estimates for the best azimuth and polarization direction for the P-wave were obtained from the eigenvector direction minimizing the energy on the T and Sv components. The RFs were obtained from two methods, water-level deconvolution (*41*) and iterative time-domain deconvolution (*42*). The source was trimmed within -10 to +25 s from the P-wave onset, and tapered using a Tukey window. A low-pass Gaussian filter with parameter a = 3.0 rad/s was used in both cases. See Fig. S5 for the final RFs.

S1.3 Method C: (Felix Bissig, Amir Khan)

In order to compute P-to-S and S-to-P RFs for the events S0173a, S0183a, and S0235b, we first detrended and tapered waveforms in the ZNE-system and subsequently filter them by means of a Butterworth bandpass filter of 2nd order with corner periods at 2 and 10 sec or 1 and 8 sec, respectively. The former is referred to as “low-frequency”, the latter as “high-frequency” RFs, respectively. Seismograms were rotated to the ZRT-system on the basis of back-azimuth estimates provided by the MQS. Rotation to the LQT-system to further separate P- and SV-waves was achieved via a principal-component analysis approach, minimizing the energy on the R-/Z-component ±30 sec around the estimated P-/S-wave for P-to-S and S-to-P RFs, respectively. P- and S-wave arrival times were provided by MQS. For computing RFs, we utilized the iterative time-domain deconvolution (*42*), which requires appropriate estimates of the source- and response-signals. We therefore cut the L-/Q-components to [-20, +50 sec] around the picked P-wave for P-to-S RFs and to [-150, +50 sec] and [-100, +30 sec] around the S-wave for S-to-P RFs, respectively, and tapered them using a Hanning-window. Different source- and

response-windows were tested, but their influence on the final RF was found to be small. The so-obtained RFs were filtered between periods of 2 sec and 10 sec or 1 and 8 sec for low- and high-frequency RFs, respectively. See Fig. S6 for the final RFs.

S1.4 Method D: (Brigitte Knapmeyer-Endrun)

Data of events S0173a, S0183a, and S0235b were response corrected, rotated to the ZNE system and filtered by a Butterworth zero-phase bandpass of third order with corner periods at 0.1 and 0.8 Hz in the case of S0173a and S0235b and 0.3 and 0.8 Hz in the case of S0183a. Data were rotated to the ZRT system using the back-azimuth estimates by MQS, i.e. 91°, 74° and 73°, respectively. For further rotation to the LQT-system, the incidence angles were determined by polarization analysis via diagonalizing the coherence matrix of the P-wave onset. RFs were calculated by creating a time-domain Wiener filter that transforms the P-wavetrain on the P component into a band-limited spike (*43*,*44*). The three-component seismogram traces were then folded with the spiking filter to obtain the RFs. Various window lengths for the P-wave train, damping factors, and spike positions within the window were tested. The parameters actually used are deconvolution window length of 40 s for S0173a, 28 s for S0183a and 33 s for S0235b, with the spike position at the centroid of the signal (i.e., at 18.4 s, 11.5 s, and 14.4 s), and a damping factor of 0.1 for S0173a, 0.5 for S0235b and 1 for S0183a. Resulting P-to-S RFs, together with results for two additional, more noisy events, are shown in Fig. S7A. For these two events, S0407a and S0325a, only a distance estimate, but no azimuth was available from MQS. Thus, for determining the azimuths, a set of radial RFs were calculated after rotating the horizontal components of the waveform in 10° steps and compared to the radial RFs for the other three events, with special attention to the three arrivals within the first 8 s. The comparison pointed to a likely azimuth of 110±10° for S0325a and 90±10° for S0407a. The corresponding RFs still tend to have a lower signal-to-noise ratio than those of the three previous events, though, and stacking all five events only leads to small changes in the average waveform compared to the stack of only the three best events.

S-to-P RFs were computed in a similar fashion to P-to-S RFs for events S0235b, S0173a and S0325a. Results show a clear peak at 2.9 s, regardless of whether only data of S0235b and S0173a or all three events are stacked, and hints of later arrivals that are however not consistent between all three events (Fig. S7B).

S1.5 Method E: (Saikiran Tharimena)

The data for events S0173a, S0183a, and S0235b were corrected for the instrument response in the UVW system, and the resulting velocity seismograms were trimmed to 10 min before and 15 min after the P-wave arrival time as reported by MQS. For the S0173a event, deglitched data were also corrected for the instrument response. Data were rotated to the ZNE system and then to the ZRT system using back-azimuths of 91°, 73°, and 74° respectively, as reported by MQS. Furthermore, the waveforms were rotated to the LQT system, which separates P- and SV- energy on the L- and Q- components respectively. The incidence angles for rotation to the LQT system were estimated by principal component analysis where P-wave energy, around the estimated P-wave arrival, was minimized on the SV component. A second order Butterworth, zero-phase bandpass filter was applied with corners at 1 and 10s. The time axis of the resulting waveforms was centered on the P-wave arrival.

P-to-S receiver functions were calculated using the iterative time-domain deconvolution (ITD, *42*) and extended-time multi-taper deconvolution (EMTD, *45*) methods. For the ITD

method, the waveform in a time window 30s before and after the P-wave arrival on the L-component was chosen as source function and a Gaussian filter parameter of 5 rad/s was used. For the EMTD method, the source waveform was chosen on the L-component by manually selecting a window around the visible P-wave arrival. Deconvolution was then performed using a 50s window, a time-bandwidth product of 3 that translates to a frequency bandwidth of permissible spectral leakage of 0.2 Hz, and 4 tapers (*46*). For both methods, the source function was deconvolved from the SV component. Different time windows for the source function were tested and found to produce similar results.

S1.6 Method F: (Matthieu Plasman)

Data of events S0173a, S0183a and S0235b were detrended, response corrected and first rotated to the geographical system (ZNE). We then applied a Butterworth band-pass filter between 0.1 and 0.8 Hz for S0235b and S0173a and between 0.3 and 0.8Hz for S0183a and a symmetric taper using a Hanning-window. We next rotated data to the ZRT system using the back-azimuth estimated by MQS, i.e. 91°, 74° and 73°, respectively. We then finally rotated to the LQT system using the same incident angles computed in method D (18° for S0183a, 24.5° for S0235b and 29.5° for S0173a). RFs were computed from an iterative time-domain deconvolution on a 95 s time window (15s before P and 80s after) with a Gaussian width of 2.5s (*42*). The quality of the computed Q-RF is defined by how well it reproduces the initial Q signal when convolved with the source signal on the L-component. The recovered RFs reproduce 73.3%, 76.7% and 76.9% of the Q-component, respectively, for S0173a, S0183a and S0235b.

S1.7 Method G (Paul Davis):

Receiver functions were generated from 20 sample-per-second UVW deglitched data (*38*) taken 3 sec before the P arrival and 30 sec after for events S0173a, S0235b, S0183a, S0105a, S0325a, S0395a, S0421b. The data were corrected for the instrument response, filtered with a causal, 4-pole, bandpass, Butterworth filter between 0.25 and 0.8 Hz, and rotated, as in Method F to the LQT system using surface velocities of Vp=3.5 km/s and Vs=1.95 km/s. The receiver function analysis used Chuck Ammon's water level code, with water level 0.1 (*41*,*47*). The three events with known azimuths and ray parameter values (S0173a, S023b, S0183a) were used to construct a summed reference receiver function, R_{ref} (Fig. S8). We then tested all 28 deglitched event RFs for cross-correlation with R_{ref}, finding the maximum correlation by varying their unknown azimuths between 0 and 360 degrees in 10-degree steps, and setting the ray parameter inversely proportional to distance (determined by P-S times). Events with a cross-correlation greater than 0.5 were retained and are shown in Fig. S9. The 4 extra events, so found, are S0105a, S0325a, S0395a, and S0421b.

S2. Autocorrelations

S2.1 Method A (Nicolas Compaire, Ludovic Margerin, Raphael F. Garcia,)

To compute the autocorrelation functions (ACF) of the ambient noise recorded by SEIS, we based our approach on the workflow of Bensen et al. (*48*), but with two important differences. First, we compute the ACF by LMST (Local Mean Solar Time) hour, and not by day as it is the case in Bensen et al. *(47*). This allows us to check the stability of the reconstructed Green's functions over the duration of a SOL (martian day). Second, we apply a modified version of the pre-processing of De Plaen et al. (*49*) which has been tested in single-station configurations. The only difference lies in the special attention given to the effect of the spectral normalization on the

waveforms of the ACF. Similar to De Plaen et al. (*49*) and Ito and Shiomi (*50*), we do not apply any spectral whitening. This choice can result in a reconstruction of the Green's function of lesser quality because the required equipartition of energy is not ensured. Nevertheless, it prevents us from adding pre-processing artefacts to the ACF waveforms. Moreover, it has been shown by various studies (*51*,*52*) that the equipartition of energy is only required to perfectly retrieve the Green's function. The various phase arrivals can be reconstructed without this prerequisite, which is the primary goal of this study.

Each trace of one LMST hour duration is band-passed and cut into windows of 60 seconds duration with 70% overlap. One-bit normalization is applied to these windows in order to remove the effect of transient signals (*48*). The normalized autocorrelations were computed in the spectral domain and then linearly stacked in time domain to improve the Signal-to-Noise Ratio (SNR). The resulting stacked function is the ACF computed for a particular LMST hour and a particular SOL.

In order to compute the ACF on the scattered part of the seismic event recordings (e.g. *52*,*53*), we applied the same processing. When a clear S-phase is visible, we used it as the beginning of the coda time window of interest, otherwise the whole duration of the seismic event is used. Obviously, no subdivision in LMST hours was applied in that case. The event nomenclature refers to the catalogue of the MarsQuake Service (MQS) *(54*,*23*).

After the computation of the ACFs, we performed a SNR analysis over the correlation lag-time using the definition given in Clarke el al. (*55*). This SNR is defined as the ratio of the envelope of the stack to the variance over the realizations (the various SOLs for the ACF computed on ambient noise and the various events for the ACF computed on the events). This SNR is a good indicator of the reliability of the phase arrivals.

Our analysis validates energy arrivals in the ACF when the amplitude of the waveforms are large, the SNR is high and the same energy arrival is retrieved for different types of data (background noise and events). With such criteria in mind, Fig. S10A suggests that four arrivals are visible in the various datasets (at 5.6 s, 10.6 s, 12.6 s and 21 s) on the vertical ACF. Fig. S10B suggests several arrivals in the North ACF at 11.9 s, 14.4 s, 16.5 s and 22.4 s. Fig. S10C suggests arrivals in the East ACF at 9.0 s, 12.4 s and 14.5 s. A conservative estimate of the error bar of these arrival times is 1 s. Only the frequency range of 1-3 Hz, which is dominated by a broad amplification around 2.4 Hz, is considered for the noise auto-correlations because only in this frequency range, during nighttime, high SNR values are observed (*23*). The ACFs of the 2.4Hz events, High Frequency events (HF) and Very High Frequency events (VF) are also computed between 1 Hz and 3 Hz because it is in this frequency band that these events have the major part of their energy.

S2.2 Method B (Martin Schimmel, Eleonore Stutzmann)

In the following analysis, the main data pre-processing steps are correction to ground velocity, data segmentation and selection, and frequency band-pass filtering. These are common processing steps to prepare the data for the computation of autocorrelations. Often, these steps are expanded by amplitude normalization, such as by one-bit normalization and/or spectral whitening, to reduce bias due to outlying signals. Here, we do not make use of any amplitude normalization processing steps and focus our analysis on the vertical component VBB data at 20 samples-per-second (Sol 178-410).

Our data segmentation and selection *(56)* deviates from what is commonly used. In this step, we basically determine the seismic root-mean-square (RMS) amplitude variability with time. The measured RMS variability is then used to build a mask to select data segments without abrupt changes in the RMS amplitude. Data irregularities such as glitches and donks have an elevated RMS variability and are therefore excluded from further processing. Here, we use this data segmentation and selection step to build a smaller subsidiary dataset with a size of about 30% of the total data volume. The selected dataset contains only recordings with the lowest RMS amplitude variability. This processing step is justified since InSight seismic data contains many aseismic transient signals inherent to the difficult acquisition conditions *(18,57*).

Further pre-processing consists only in filtering the data to the desired frequency bands and to attenuate the strongest lander modes and tick noise through three band rejection filters. The autocorrelations are computed using the Phase Cross-Correlation (PCC; *58*). This method is based on analytic signal theory and finds the coherent signals through their instantaneous phase coherence as a function of lag time. The approach is amplitude unbiased. PCC has proven to be efficient in various seismic monitoring and imaging studies, including ambient noise autocorrelation research (*59-62*; among others). It works in analogy to the classical correlation and can also be employed in a computationally efficient manner to process large data volumes (*63*).

The computed autocorrelograms are then stacked both linearly and employing time-frequency phase weighted stacking (tf-PWS; *64,65*) for comparison. tf-PWS can further attenuate incoherent signals because it uses the instantaneous phase coherence.

Fig. S11 shows an autocorrelogram section for three-sol long, non-overlapping time windows. Negative amplitudes are in blue. The considered frequency band is 1.2-8.9 Hz and the three-sol binned autocorrelograms are stacked using tf-PWS. The figure shows three lag time windows to improve the visibility of signals through amplitude normalization in each of the lag time windows. The blue arrows mark signals which coincide with the expected P-to-P wave reflections (Fig. 3 D,E) for the proposed discontinuities. Similarly, the green arrows point to P-to-S or S-to-P reflection conversions from the same discontinuities. Fig. S11 presents these signals as stable features over the considered time span. Also note that the 6.14 s signal has a higher frequency content than the other signals. Further, this figure reveals the presence of other signals which have not yet been identified.

The total data stacks using the tf-PWS are shown with red lines in Fig. S12 for different frequency bands. Black traces are tf-PWSs using 10% of the available PCC autocorrelations and are shown to visualize amplitude variability. The frequency bands of the top three and lower-most panel are 1.5-3.0 Hz, 2.4-4.8 Hz, 3.6-7.2 Hz, and 1.2-8.9 Hz. The fourth panel contains the three total data tf-PWS stacks from the top three panels. The blue line in the lower-most panel shows the linear stack of all PCCs for comparison. The 6.14 s signal becomes visible only at the higher frequencies while the 10.46 s signal is coherent for the lower frequencies. The polarities are negative as expected for an impedance increase *(56)*. Linear and tf-PWS stacks both consistently show both signals.

S2.3 Method C (Doyeon Kim, Vedran Lekic, Nicholas Schmerr)

Similar to SEIS data from Mars where we only have seismic measurements from a single station, such single station driven constraints produced from both RF and autocorrelation function on Earth have shown to be consistent (*20*). To verify our RFs and their structural signals from the Martian subsurface, we use continuous seismic recordings of ambient noise (e.g., Fig.

S13) as well as high-frequency (HF) events on Mars (e.g., Fig. S14A-B) and compute autocorrelation functions (ACFs) to approximate the impulse response at InSight's seismometer. First, we take 6 months (between April and September, 2019) of deglitched continuous data (*38*) recorded by the very broadband (VBB) sensor. The instrument response is removed from the data to obtain velocity recordings and the three SEIS-VBB components are rotated to the ZNE coordinate frame. An example of the amplitude measurements from ambient noise waveforms is shown in Fig. S13. The ambient noise recording on Mars shows a clear contrast between the time-frequency character of daytime and nighttime signals (Fig. S13; *18*). This first order difference reflects the bimodal noise regime on Mars, with the current interpretation being that it is associated with the atmospheric boundary layer activity related to the transition from nighttime laminar flow to daytime turbulent flow (*18*). Data is segmented by a 30-min window and further separated into two groups using a Gaussian mixture model. The two groups represent signals from high vs. low amplitude noise regimes (e.g., day vs. night portions of the data).

Data from the two groups (Fig. S13D) are processed in the following manner. We apply a bandpass filter to the waveforms between 0.05-3.5 Hz. To suppress nonstationary noise, we normalize the data using a weighting function (*48*) that computes running absolute median amplitudes with a 300 s sliding window. We further apply spectral whitening (with a whitening width of 0.1 Hz) prior to autocorrelation in order to obtain stable autocorrelation functions in the lower frequencies. The power spectral density (PSD) of the noise records shows a relatively larger spectral amplitude below 1 Hz so an adaptive weighting function was used to address this bias toward lower frequencies in the records (*66*). The autocorrelation is computed in the spectral domain for each 30-min data segment using a 70% overlap between successive segments. Phase-weighted stacking is then performed on the autocorrelations, after which they are bandpass filtered between 1.5–3 Hz (e.g., Fig. S14C). To minimize the effect of 1 Hz instrument tick artifact and its overtones (e.g., Fig. S13C and S13E), a notching comb filter is applied to the processing flow. Source effects in the ACFs are suppressed by applying a cosine taper at lag-times <1.8 s. ACFs for the high-noise (daytime) and low-noise (nighttime) regimes are shown in Fig. S14C, in blue and red, respectively.

In addition to ambient noise, we perform autocorrelations on P- coda signals from 48 HF events (Fig. S14B lists HF events used). For each event, we used a standard algorithm of STA/LTA triggering on the corresponding Hilbert envelope averaged across components (Fig. S14A) to pick the P- and S-arrivals. Then, the P-arrival times are refined using an implementation of MCCC *(67)*, and used to precisely align the vertical component waveforms (Fig. S14B). Only the P-coda portion of the vertical component waveforms (Fig. S14A-B yellow vertical lines) is used for computing P-coda ACFs, and we maintain most of the steps from the ambient noise processing described above. These include minimization of the 1 Hz tick artifact, spectral whitening, post-filtering 1.5–3 Hz, and cosine tapering. The P-coda signal start time, relative to each P arrival, is taken to be the average across events of the times when the component-average envelope reaches its maximum value, prior to the arrival of the S wave. The P-coda signals used in the ACF construction have a duration of 148.7s, which corresponds to the shortest P-coda length amongst the HF events (e.g., Fig. S14A). Comparison with predicted arrival times from representative models produced by the RFs (e.g., Fig. 2) shows that many of these arrivals can be

explained by P-wave reflections from interfaces within the crust (P_1P, P_2P, P_3P and P_2P_2 in Fig. 3).

S3. RF inversion

S3.1 Method A (Felix Bissig, Amir Khan, Domenico Giardini)

Inversion method A follows Bissig et al. *(68)* in parametrizing the crust, modeling of RFs, and inversion strategy. A visualization of the model parametrization is given in Fig. S15. We invert for the seismic structure, i.e., density, S-wave, and P-wave velocity, from the surface to 100 km depth. Within the crust, we adopt a staircase-like structure, where the depth and magnitude of discrete S-wave velocity jumps across crustal discontinuities are free parameters in the inversion. At greater depth, we employ linear gradients in velocity from the Moho to 100 km depth and from there to 400 km, respectively. To allow for variations in mantle structure, the S-wave velocity at 100 km is a free parameter. Elastic properties are fixed to the seismic reference model TAYAK (*69*) below 400 km. We assume constant ratios of density- and P-to-S-wave velocity, i.e., ρ/Vs and Vp/Vs, respectively, from the surface to 100 km depth and invert for them. The quantity of model parameters depends on the number of crustal layers used (Tab. S3). Here we explore 2-, 3-, 4-, 6-, and 8-layer models.

For a given 1-D seismic model and event, we compute waveform synthetics via the reflectivity method (*70*). We vary epicentral distance for each of the three events separately, but use only one source depth value for all events in order to reduce computational costs by a factor of three. These four location parameters are treated as unknowns in order to achieve a greater variation in P-wave incidence angle. The moment tensor is set to that of an explosion and back-azimuth estimates are provided by Giardini et al. (*21*). Anelasticity is included through shear- and bulk-attenuation quality factors, which are held constant to their respective values in model TAYAK. Processing of synthetic and real waveforms are equivalent (cf. section S1.3), except that 1) the orientation of the LQ-axes is equal to that of real data, and 2) arrival times of P- and S-waves are computed via ray tracing (*71*).

The probabilistic solution to the inverse problem, $\boldsymbol{d} = g(\boldsymbol{m})$, where $\boldsymbol{d}$ are the observed data, $\boldsymbol{m}$ the model parameter vector, and g the forward operator mapping from model to data space, is expressed by (e.g., *72,73*):

$$\sigma(\boldsymbol{m}) \propto h(\boldsymbol{m})\mathcal{L}(\boldsymbol{d},\boldsymbol{m})$$

where $h(\boldsymbol{m})$ is the prior probability distribution of model parameters (cf. Tab. S3), $\mathcal{L}(\boldsymbol{d},\boldsymbol{m})$ is the likelihood-function quantifying the misfit between synthetic and observed data, and $\sigma(\boldsymbol{m})$ is the posterior distribution. We consider low- and high-frequency Ps RFs (processing method C) of events S0235b, S0173a, and S0183a in the inversion and discriminate between distinct time windows, *i*, in computing the likelihood-function for a given event, *e*:

$$\mathcal{L}_{e,i}(\boldsymbol{d}_e,\boldsymbol{m}) = exp(-\Phi_{e,i}(\boldsymbol{d}_e,\boldsymbol{m}))$$

where $\Phi_{e,i}(\boldsymbol{d}_e,\boldsymbol{m})$ is the L2-norm misfit between synthetic, $\boldsymbol{d}_e^{syn}$, and observed RF amplitudes, $\boldsymbol{d}_e^{obs}$, scaled by an uncertainty estimate, σ_e, and weighting factor, χ_e, for that particular event and window:

$$\Phi_{e,i}(\boldsymbol{d}_e, \boldsymbol{m}) = \chi_e\left(\frac{1}{2N\sigma_e^2}\sum_{j}^{N} || \boldsymbol{d}_{e,j}^{obs} - \boldsymbol{d}_{e,j}^{syn} ||^2\right)$$

We use four windows in total per event, one for the P-wave at time zero and three for the positive arrivals within the first 10 seconds. The windows are defined separately for each event and are shown in Fig. S16 and S17. Uncertainty is set to 50% of the mean absolute Ps RF amplitude within 0–10 sec. We opted for this rather conservative value to allow for an extended exploration of the model space. The weighting factor χ_e is set to 2/3 for S0235b and to 1/6 for S0173a and S0183a, respectively, reflecting the higher confidence in the Ps RF from event S0235b. The conjunction of the likelihood-functions for each event and window results in the total likelihood-function:

$$\mathcal{L}(d, m) = \prod_{e,i} \mathcal{L}_{e,i}(\boldsymbol{d}_e, \boldsymbol{m})$$

We sample the posterior distribution by means of the cascaded Metropolis-Hastings algorithm (*74*). At iteration n, a model, $\boldsymbol{m}^n$, is proposed and retained only if the following criterion is true for each event and window:

$$\frac{\mathcal{L}_{e,i}(\boldsymbol{d}_e, \boldsymbol{m}^n)}{\mathcal{L}_{e,i}(\boldsymbol{d}_e, \boldsymbol{m}^{n-1})} > \alpha$$

with α being a random number between 0 and 1.

We invert Ps RFs for S0235b, S0173a, and S0183a jointly in ten separate inversions that differ in the number of crustal layers and corner-frequencies of RFs. For each inversion, we ran 32 chains in parallel, each starting at a different initial model and subsequently sampling ~12,000 – 25,000 models of which every 10th was retained for further analysis. Overall, this results in ~40,000-80,000 collected models per inversion.

Inversion results are presented in blue color in Figs S18 and S19. All parametrizations are capable of fitting the timing of Ps RFs for events S0235b and S0173a, while a slight phase-shift is apparent in S0183a. Amplitudes are more difficult to model, in particular because observed Ps RFs of the different events disagree on the relative amplitudes of peaks and hence velocity-contrasts across discontinuities. However, we emphasize the large uncertainties associated with amplitudes, as evident for S0173a where differently deglitched data sets result in distinct amplitudes (Fig. S6). Parametrizations with more layers tend to produce gradient-like discontinuities that result in overall diminished RF amplitudes. From the model ensembles (Fig. S18A and S19A) and the discontinuity depth distributions (Fig S18B-G and S19B-G), we observe three discontinuities at depths 8±2 km, 20±5 km, and 39±8 km.

S3.2 Method B (Rakshit Joshi, Brigitte Knapmeyer-Endrun)

Here we have employed a modified version of the Neighbourhood Algorithm (NA) (*75,76*) for the simultaneous inversion of the three receiver functions computed from events S0173a, S0183a and S0235b *(77)*. The forward calculation of receiver functions is based on the code of Shibutani et al. *(78)* that uses a simple reflectivity matrix approach to provide the P-to-S response of a layer stack. The resulting synthetic vertical and radial RFs are convolved with the measured vertical RF to consider source complexity. An additional step of coordinate rotation and re-scaling is performed to transform the RF components into the ray coordinate system. Tests with synthetic seismograms for Mars models have shown that this allows obtaining results

comparable to full Instaseis synthetics based on an AxiSEM data base *(79)* with a greatly reduced computation time *(80)*. Density was not used as an independent parameter during the inversion, but calculated from P-wave velocity values using Birch's law *(81)*. In addition to the layer thickness and the S-wave velocity within the layer and the half-space, the V_p/V_s ratios of all the layers and half-space were also included as model parameters (Tab. S4). The two parameters that control the NA need to be tuned depending on the problem and the style of sampling needed. For an explorative search that is robust against local minima, we perform 2000 iterations in each inversion run with 200 models produced at each iteration and 200 cells re-sampled at each iteration, resulting in an ensemble of 400,000 models per run. Furthermore, each inversion was repeated several times with a different starting random seed value to test the stability of the results.

We invert the RF waveforms generated by processing methods C (Section S1.3), considering both low- and high-frequency P-to-S RFs. For each of these data sets, we tested the data against models with increasing degree of complexity. Starting with 2 layers with constant velocities over a half space, we subsequently increased the complexity to include cases with 3, 4, 6 and 8 layers. The L2 norm misfit was then used to compare observations to synthetic RFs using the same misfit function as described in Section S3.1. The uncertainty level along with the weighting factor and the time windows for misfit calculation for each event were also left unchanged in order to minimize any processing differences between the two inversion methods. From the resulting ensemble, we first retained every 5th model which down-sampled our ensemble to 80000 models. In order to reduce the bias in NA sampling, we then compared the distance of each model to the best fitting model within this subset using multi-dimensional mapping, and binned these models into 50 bins according to this distance. Finally, we selected 100 models from each bin, giving us a total of 5000 models. The results of the inversion are shown in yellow color in Figs S18 and S19, indicating that the data can be explained either by two discontinuities at depths 8±2 km and 20±5 km, or with an additional discontinuity at 39±8 km.

S4. Comparison with waveform modeling for source inversion (Nienke Brinkman, Simon Stähler, Domenico Giardini)

The first effort on fitting waveforms of observed marsquakes was done by Brinkman et al *(81)* in the context of seismic source inversion. This study was performed to find optimal source mechanisms of three high-SNR marsquakes (S0173a, S0183a, S0235a), and tested different crustal models. Considering P- and S-wave phases, the proposed two-layer model of this study provided well-matching waveform fits, specifically for the coda of the P-waves on the radial component and S-wave precursors, interpreted here as a S-to-P conversion at an interface in 24 km depth. Crustal models where the Moho was located deeper did generally not result in stable source results. For S0235b, we illustrate this agreement in Fig. S20 by showing waveform fits for two different crustal models.

S5. Global crustal thickness from gravity, topography, and seismic constraints (Mark Wieczorek, Adrien Broquet)

Our global crustal thickness modeling employs standard methods that have been applied previously to the terrestrial planets and Moon using spacecraft data *(83)*. In particular, the observed gravity field is assumed to be the result of surface relief, relief along the crust-mantle interface, and hydrostatic density interfaces in the mantle and core. The crust has a constant density in our models, with the sole exception of the low-density polar ice cap deposits. We

make use of 13 *a priori* density profiles of the mantle and core *(25)* that span the range of plausible pre-landing Martian compositional models and core radii. In addition to these reference models, we also include two additional reference density profiles based on the Martian bulk composition model of Yoshizaki and McDonough *(84)*.

For each reference interior model, the global crustal thickness model was computed as follows. First, the gravitational attraction of the surface was computed using finite-amplitude techniques *(85)*. Second, the gravitational attraction of the low-density polar caps was accounted for using densities of 1250 and 1300 kg m^{-3} for the north and south polar caps, respectively, along with the polar cap thickness model of Broquet et al. *(86)*. Third, the gravitational attraction of hydrostatic relief in the mantle and core beneath the lithosphere was computed using the method described in Wieczorek et al. *(25)*. Fourth, for an assumed average crustal thickness, and using the uppermost mantle density of the reference interior model, we inverted for the relief along the crust-mantle interface that satisfies the observed gravity field. Finally, the average crustal thickness was adjusted iteratively in order to obtain the desired value at the InSight landing site.

We made use of the MarsTopo2600 spherical harmonic shape model of Mars *(87)* and the GMM-3 gravity field model *(88)*. Spherical harmonic degrees were considered up to degree 90, and a downward continuation filter was employed that has a value of 0.5 at degree 50. For each reference interior model, we tested all bulk crustal densities that were greater or equal to 2550 kg m^{-3}, which is a reasonable lower bound taken from Goossens et al. *(10)*. It was found that as the crustal density increases, the minimum crustal thickness of the model decreases. The maximum permissible crustal density is thus obtained when the minimum crustal thickness reaches zero, which always occurred within the Isidis impact basin. Tests showed that the inclusion of a constant thickness layer at the surface with reduced densities (from meters to kilometers thick) had only an extremely minor impact on the results presented here. Further tests that made use of lower crustal densities in the southern highlands than in the northern lowlands *(26)* showed that the maximum permissible crustal densities were unchanged with respect to our constant density model. Fig. S21 shows a representative global crustal thickness model for one set of model parameters: Other models are, to first order, simply scaled versions of this model.

The two parameters that have the largest impact on the global crustal thickness model are the difference in density between the upper mantle and crust, and the seismic thickness of the crust at the InSight landing site. The average thickness of the crust for each model is plotted as a function of the crust-mantle density contrast in Fig. S22 for various assumed crustal thicknesses at the InSight landing site (text annotation) and reference interior models (legend). For a given InSight crustal thickness, the average thickness of the crust is seen to decrease with increasing density contrast, and this dependence is only weakly sensitive to the specific reference interior model that was used. Nevertheless, the reference interior model fixes the density of the upper mantle (which ranges from 3352 to 3492 kg m^{-3}), and this affects the permissible values of the crustal density and crust-mantle density contrast. The minimum density contrast for each curve corresponds to the maximum crustal density, and also corresponds to that model where the minimum crustal thickness is zero.

The average crustal thickness is plotted in Fig. S23 as a function of crustal density, for assumed thicknesses at the InSight landing site of either 20 or 39 km, central values for the two-layer and three-layer seismic models, respectively. For the 20-km thick case, the range of allowable crustal densities is small (2550-2700 kg m^{-3}), and the average crustal thickness is well constrained to 28-31 km. In contrast, for the 39-km thick case, the range of allowable crustal

densities is larger (2550-3050 kg m-3), and the average crustal thickness varies from 47 to 59 km. When the uncertainties associated with the InSight seismic thicknesses are considered, the two-layer model predicts an average crustal thickness between 24 and 38 km with a maximum permissible crustal density of 2850 kg m^{-3}. For the three-layer seismic model, the average crustal thickness is predicted to lie between 39 and 72 km with a maximum permissible crustal density of 3100 kg m^{-3}.

S6. Implications for the heat-producing element budget and the thermo-chemical history of Mars (Chloé Michaut, Ana-Catalina Plesa, Henri Samuel, Scott McLennan)

The crustal thickness inferred from RFs and gravity data allows placing constraints on the composition of the crust and of the mantle both in terms of major and trace elements. Due to enriched HPE, crustal thickness is a key parameter in predicting present-day heat flux. The present-day crustal thickness is an essential anchor point for thermo-chemical evolution models that predict past mantle rheology and cooling rates.

S6.1 Constraints from 1D parameterized models considering bulk crust formation by melt extraction over time

To exploit the relationship between the present-day crustal thickness and the planet's history, we conducted an extensive exploration of the possible thermo-chemical histories of Mars using parameterized convection calculations to model the evolution of a Mars-like planet for 4.5 Gyr. This approach models the heat transfer and the chemical element partitioning within the main planetary envelopes: an adiabatic convecting iron alloy core overlaid by a silicate mantle convecting underneath an evolving, stagnant lithospheric lid. The latter includes a crust enriched in radioactive heat producing elements (HPE). Both the crustal and lithospheric thicknesses evolve as a result of the thermal history of the planet. The crust is assumed to progressively form via magmatic processes triggered by shallow mantle melting. Details of the model can be found in Samuel et al. (*27*) and references therein. The only difference is that we now use melting curves that are more appropriate for a Martian-like composition (*89*) instead of the solidus and liquidus derived for a peridotitic mantle (*90*) that are more appropriate for an Earth-like composition. We note that the solidus of Ruedas and Breuer (*89*) is similar to the solidus of Duncan et al. (*91*), and nearly identical for the relevant pressure, at which partial melting takes place (i.e., up to 8 GPa). While this parameterized modelling approach is computationally efficient, it accurately reproduces 1D structures obtained in curved geometries (*27,28,92,93*). We explored a wide range of Martian evolutions by randomly sampling the values for the main governing parameters within plausible bounds. The sampling space is composed of mantle rheological parameters (effective activation energy E^* and activation volume V^*, reference viscosity η_0), initial thermal state (core-mantle boundary temperature Tc_0 and temperature at the top of the convecting mantle Tm_0), and the crustal enrichment factor, Λ (*i.e.*, the ratio of HPE content in the enriched crust to that of the primitive mantle). We fixed the bulk HPE content corresponding to the values suggested in Wänke and Dreibus *(2*9) (i.e., U=16 ppm, Th=56 ppb, K=305 ppm). The explored bounds of the governing parameters are listed in Table S5. The values of other model parameters can be found in Tab. 1 in the supplementary material of Samuel et al. *(27*).

Fig. S24 displays the sampled input range of governing parameters and several resulting distributions that lead to a present-day average crustal thickness in the range 39-72 km, as proposed by the three-layer crust inferred by RF analysis and gravity-topography considerations.

The latter correspond either to present-day model output (e.g., surface heat flow) or input governing parameters. The crustal thickness requirement considered here does not strongly constrain mantle activation energy or volume (Fig. S24a,b), but favours 1-σ range mantle reference viscosity around $10^{21\pm0.5}$ Pa s (Fig. S24c), which is in line with pre-mission estimates (*6,27*). The initial mantle temperature is also not strongly constrained, but relatively cold values (1770±50 K) are favoured in a statistical sense (Fig. S24d). The lack of strong constraints on the mantle rheology and its initial thermal state essentially stems from the trade-offs between temperature and viscosity, which require additional independent constraints such as orbital data (*27*) and/or tighter ranges of inferred crustal thickness to resolve. The predicted present-day surface heat flux ranges between 20 and 25 mW/m^2 (Fig. S24e), which is consistent with pre-mission estimates (*6,27,69,94*) and corresponds roughly to the sampled (i.e., *prior*) range. The latter is considerably influenced by the assumed bulk HPE content (*92,942*). The most strongly constrained quantity is the crustal enrichment with a corresponding range of 5-24 and a 1-σ range Λ=15.5±3.5 (Fig. S24f). This range is consistent with recent estimates that rely on elastic thickness constraints (*28*) and with a crustal HPE content inferred at the surface by GRS data corresponding to a crustal enrichment of 8.7 to 10.6 for crustal densities between 2550 and 3100 kg m^{-3}. We note that these crustal enrichment factors have been calculated based on the Wänke and Dreibus (*29*) bulk abundance of heat producing elements. The compositional model of Taylor (*30*) has a similar bulk abundance of radioelements, and, hence, will lead to similar enrichment factors. Other compositional models such as Yoshizaki and McDonough (*84*) with a higher bulk abundance of radioelements would require in a higher crustal enrichment to match the same geodynamical and geological constraints.

Performing the same exercise for the two-layer, thinner crust end-member (24-38 km) yields more constrained matching histories corresponding to a smaller solution subset (Fig. S25). A thinner crust requires an even colder mantle, triggering smaller amounts of partial melt at shallow depth. This colder mantle state calls for a higher HPE content in the crust (at the expense of that of the underlying mantle), and/or an initially colder mantle. These two effects can be observed in Fig. S25d and Fig. S25f, respectively. The initial mantle temperature is therefore more strongly constrained than in the thick crustal end-member case to 1750±40 K for the 1-σ range, (see Fig. S25d). The crustal enrichment relative to the primitive mantle is constrained to values distinctly larger than 16 (24.9±3 for the 1-σ range, see Fig. S25f). The reference viscosity remains constrained to $10^{21.3\pm0.5}$ Pa s (Fig. S25c) as in the thick three-layer crustal end-member. The temperature and pressure dependence of viscosity are constrained to relatively smaller values than in the thick crustal end-member. However, due to the persisting trade-off between temperature and viscosity such constraints remain relatively weak (with the corresponding 1-σ ranges: V^*=3.3±2 cm^3/mol, and E^*= 260±114 kJ/mol, see Fig. S25a and Fig. S25b). Finally, due to the same bulk HPE content considered for the two-layer and the three-layer cases, the corresponding present-day surface heat flux compatible with the thin end-member case is 20-24 mW/m^2 (Fig. S25e), which is very similar to the range inferred for the thick crustal end-member (Fig. S24e).

S6.2 Constraints from 3D convection models and 1D parameterized models accounting for regional variations in crust thickness and looking for present-day mantle melting

The surface of Mars is on average very old (>3 to 3.5 Gyr), showing that volcanism and resurfacing by lava flows was mostly active early in the Martian history, and then became much sparser. Although recent lava flows have been observed, visible only in the Tharsis province (*95*,

96), thermal evolution models producing widespread melting in the Martian mantle at the present-day are unlikely. For a given crustal HPE concentration, the occurrence of mantle melting is dependent on the crustal structure since the thicker the crust, the higher the amount of heat sources at that location and the larger the temperature at depth. To exploit this relationship, we also conducted an extensive exploration of the possible thermal history of Mars using parameterized convection models accounting for two different hemispheres with different crustal properties (*28*) as well as 3D convection simulations accounting for lateral variations in crustal thicknesses (*6*). In contrast to the previous set of numerical experiments (Section S6.1), the crustal structure is set at the start of the simulations (t=0) to account for an alternative crustal formation that would result from the differentiation of a magma ocean. The model is let to evolve for 4.5 Gyr in both the parametrized models and 3D simulations, where we used the Wänke and Dreibus *(2*9) model for radioelement concentration for the bulk silicate Mars. We also note that the bulk of the Martian crust has been built during the first 500 to 700 Myr (*96*), therefore the present-day thermal state is not sensitive to the exact mechanism of crustal growth but rather to the final crustal thickness.

We used the model of Thiriet et al. *(2*8) to account for the two hemispheres and consider a uniform crustal density, thermal conductivity and enrichment factor, but two different average crustal thicknesses for the North and the South, which respectively cover 40% and 60% of the planet's surface. One difference with the model of Thiriet et al. *(2*8) is that here we parameterized the average crustal thickness in the South, D_S, based on that in the North, D_N, using $D_S = D_N + h(1+\rho_c/(\rho_m-\rho_c))$, where $\rho_m=3500$ kg m^{-3} is the mantle density, ρ_c the crustal density, and h=3.3 km (instead of 6 km), a value that is in good agreement with inversions of gravity and topography data presented in this manuscript (Section S5). Another difference is that we estimated *a posteriori* the lithosphere thickness below the Tharsis province accounting for a thicker crust, which we also parameterized from the results of gravity and topography data inversions using $D_T = D_N + h_T(1+\rho_c/(\rho_m-\rho_c))$, where h_T=4.45 km and D_T is the average crustal thickness below the Tharsis province. The temperature at the radius at the base of the crust below the Tharsis province, $T_C(R_{MT})$, is then calculated assuming a steady-state temperature profile in the crust below Tharsis from the Moho heat flux, Q_{Moho}, which we estimate from the heat flux at a radius $r=R_{MT}$ in the southern hemisphere: $T_C(R_{MT})=A_C(R_P^2-R_{MT}^2)/6k+R_{MT}^2(A_CR_{MT}/3-Q_{Moho})(1/R_P-1/R_{MT})/k+T_S$, where T_S is the surface temperature, $k=3$ W m^{-1} K^{-1} is the crust thermal conductivity and A_C the present-day crustal heat production. Transient effects due to the decay of heat producing elements that are neglected in this calculation would increase the temperature at the Moho below Tharsis. Although they are not negligible in a lithosphere that is several hundreds of kilometres thick (*97*), they are much more limited in a crust of several tens of kilometres thickness. The lithosphere thickness, H_L^T, below the Tharsis province is then found by interpolating the temperature profile starting from the temperature at Moho depth considering a constant heat flux equal to the Moho heat flux in the lithospheric mantle and up to the temperature characterizing the base of the lithosphere, T_L.

For each model, we checked whether melting would occur at the present-day:

- within a plume ascending from the core-mantle boundary and up to the base of the lithosphere below Tharsis, by comparing the temperature of the plume (*28)* to the solidus temperature at the pressure of the base of the lithosphere below Tharsis (contrary to Thiriet et al. *(28)* we do not consider that the plume penetrates through the lithosphere),

- within local, smaller-scale, upwellings below the South, as well as below the North, by comparing the solidus temperature at the pressure of the lithospheric base in the South, respectively North, to the mantle temperature.

We assume that the melt reaches the surface and is responsible for the recent volcanic activity in Tharsis.

We used the parameterization of the solidus temperature $T^{T}_{solidus}$ by Ruedas and Breuer (*89*) applying a correction for crustal extraction from the primitive mantle: $T_{solidus}=T^{T}_{solidus}+d_{crust}\Delta T_{sol}/D_{ref}$, where ΔT_{sol}=150K, d_{crust} is the average crust thickness and D_{ref} =190 km.

The results of the parameterized model described above are in good agreement with fully dynamical 3D simulations (Figs. S26, S27), where the locations at which partial melt is produced in the mantle have been estimated by comparing the local temperature to the solidus *(*6). In both 1D and 3D models, melting occurs only below Tharsis if the percentage of the bulk radioelement content in the crust is about 55% or higher (Figs. S26 and S27). This is the case if the average GRS-derived concentration in HPE is used for the bulk crust in the 3-layer (thick crust) model (Λ=12.2±2.0). On the contrary, for the 2-layer (thin crust) model, a GRS-derived concentration in HPE for the bulk crust amounts to about 30% of bulk radioelement content in the crust and would lead to widespread melting as shown in both Fig. S26 and Fig. S27. While melts may not reach the surface and remain intrusive today, such widespread melting areas would be difficult to reconcile with the geological history of Mars since evidence of recent eruptions is only present in localized areas. As shown in Fig. S26, successful models that consider a thin crust can be found if the crustal enrichment of radioelements is increased (Λ=19.6±2.4). Given the range of surface concentration in HPE derived from GRS measurements, this would imply, however, that the lower crust contains significant amounts of HPE, and, hence, was formed by a different mechanism than the basaltic surface layer.

S6.3 Combining all constraints together

Overall, the consistent results obtained independently by the complementary approaches described above indicate that the thin crustal end-member requires a large concentration of radioelements in the crust (Λ>15 and a consistent most probable value of 22), larger than GRS estimates (7.8-9.5 and 8.7-10.6; Table S6) *(31,98,117*), which would point towards the presence of a buried enriched component. Such a large concentration of radioelements in the crust may imply an upward segregation of heat producing and incompatible elements during the solidification of an initial magma ocean as is observed on the Moon, or secondary differentiation events for the crust, as for the continental crust on Earth. On the other hand, the thicker three-layer model appears to be consistent with a crustal enrichment compatible with estimates from GRS, as well as progressive crust formation triggered by shallow melting. The commonly accepted estimates from Wänke and Dreibus *(2*9) and Taylor (*30*), favor the thicker crustal end-member. In addition, considerations on crustal production via magma extraction (Section S6.1) favor a crustal enrichment factor Λ=5-22 and a 1-σ range of 16.2±4.2 (Fig. S24f), while constraints on the occurrence of present-day melting underneath Tharsis only (Section S6.2) suggest a crustal enrichment factor of Λ=9-18 with 1-σ range of 12.2±2.0, leading to a consistent overlapping interval of Λ=9-18 and a consistent most probable (1-σ) overlapping range Λ=12.0-14.2 for the crustal enrichment of Mars.

In both thin or thick end-member cases, the reasonable assumption of a bulk HPE content from commonly accepted estimates by Wänke and Dreibus *(2*9) and Taylor (*30*) implies a present-day surface heat flux range of 20-25 mW/m^2 (Figs. S24e and S25e), which is consistent with the average values of 22.5-23.6 mW/m^2 associated with the 3D models (Figs. S26 and S27).

S7. Do GRS HPE Abundances Reflect the Uppermost Igneous Martian Crust?

The Mars Odyssey GRS instrument interrogates the upper few decimeters of the Martian surface and the analytical signal is dominated by what is generally considered to be well-mixed regolith and in places, also by dust *(98,99)*. Use of GRS HPE data (K and Th measured abundances and U based on an assumed Th/U ratio of about 3.8) as a crustal composition model (Table S6) assumes the HPE abundances reflect the uppermost igneous crust and are not significantly affected by upward or downward secondary mobility on a scale significantly greater than the GRS interrogation depths. There have been suggestions that GRS data are influenced by secondary aqueous processes, resulting in enrichments in the surficial regolith relative to protolith igneous materials *(e.g. 99)*, in part to explain differences between compositions (including HPE) in Martian meteorites (SNC) and the GRS data. However, in situ measurements of a wide variety of Martian rocks and regolith by rovers suggest that potassium abundances are significantly enriched, on average, compared to SNC meteorites *(e.g. 13,31,100)*. In addition, analyses of the NWA7034 Martian meteorite breccia (and its multiple pairs) has greatly expanded the range of HPE concentrations observed in Martian crustal rocks, consistent with elevated crustal HPE compared to SNC meteorites *(e.g. 14,101)*. A consequence of these observations is that the SNC meteorites are now widely considered to be non-representative of the overall crust *(e.g. 100)*. Many workers have instead observed spatial correlations of the GRS data that mostly align with factors such as apparent crustal age and crustal terrane type *(102,103,104)* and have further noted the lack of geochemical fractionation between K and Th that might be expected during alteration processes *(104)*, consistent with the compositions being representative of their igneous protoliths. If correct, then the GRS HPE data would be representative at least to the average impact gardening and sedimentary erosion depths that produce the regolith. Accordingly, while the possibility that GRS data reflect secondary alteration processes, leading to significant enrichments in average HPE abundances at the near-surface, cannot be entirely discounted, currently it is not a favored model.

On the other hand, there is a possibility of a slight "dilution" effect in the near-surface HPE concentrations due to hydrogen (likely both free and structural water) enrichments and accumulation of Cl- and S-bearing components measured by GRS *(98,105)*, and perhaps a meteoritic component, within the Martian regolith. Enrichments of H-, S- and Cl-rich materials ultimately result from various outgassing processes that accumulate at the near surface. The overall effect would be to lower the levels of HPE compared to the ultimate igneous protoliths. Taking these "dilution" factors into account is basically the procedure that Taylor and McLennan *(31)* carried out in order to arrive at their estimates of crustal HPE (Table S6).

S8. Implications for magnetization (Catherine Johnson, Anna Mittelholz)

The InSight fluxgate magnetometer, IFG, is the first surface magnetometer on Mars *(106)*. Prior to the InSight landing, satellite vector field measurements, B_{orbit}, allowed global modelling of the crustal magnetic field at the surface, B_{surf}, by downward continuing models derived from orbital data *(107,108)*. B_{surf} is to proportional to the product of the magnetization and the thickness of the magnetized layer. Previous satellite-based models have typically assumed the

layer thickness to be a constant value globally of 40 km *(107,108)*, in the absence of seismically-constrained values for absolute crustal thickness or other constraints on the magnetized layer thickness. From IFG data, the local magnetic field strength at the surface, B_{surf} was found to be an order of magnitude larger than satellite-based models *(106)*. Combined with geological information on the maximum burial depth of the magnetized layer these new observations allowed the minimum magnetization strength required to explain the surface field to be estimated for different maximum depths of the magnetized layer *(106,109)*. In this study, we extend our earlier work *(106)* to also include bounds on the maximum depth of the magnetized layer derived from the seismic data. We use the approach of *(109)*, summarized and applied in *(106)*, to estimate the minimum magnetization that is compatible with the surface magnetic field strength measured at the InSight landing site *(106,109)* and is also constrained by the two estimates for crustal thickness. The two crustal thickness models also have implications for the minimum magnetization that is compatible with the surface magnetic field strength measured at the InSight landing site (*106,109*). Deep magnetization extending to the Moho but confined below the seismically-determined layer 1, would have an amplitude of 1.8 A/m and 3.3 A/m for the ~20-km and ~37-km crustal thicknesses respectively. This represents a case in which the first layer transition around 10 km is indicative of a change in mineralogy or deposition age leading to no substantial magnetization acquisition in the upper layer. If substantial magnetization is carried in the upper seismically-determined layer (but beneath the thin few-hundred-meter-thick veneer of Amazonian and younger Hesperian flows), compatible with a longer-lived dynamo (*110*), magnetizations are <1 A/m for either crustal thickness model (Fig. S28).

S9. Matching moment of inertia and tidal Love Number (Attilio Rivoldini)

Further constraints on the set of average crust thickness and density pairs inferred in this study can be obtained from the moment of inertia (MOI) and tidal Love number k_2 of Mars (i.e. *69*). The moment of inertia provides a direct constraint on the crust of interior structure models as it is highly depending on the mass of the crust and mantle. The Love number k_2 of Mars requires a large core (i.e., *111*) and can for this reason further reduce the set of crust models. To assess the effect of the geodesy data (*111,112*) on the crust we use the same mantle composition models employed in this study (section S5) together with two plausible mantle temperature end-members (*113)*.

Following Rivoldini et al. *(114)*, we construct global interior structure models that use the two end-member temperature profiles in the mantle and assume a convecting liquid iron-sulfur core. The thermoelastic properties of the mantle for the studied compositions are computed with PerpleX *(115)* using the thermodynamic database and formulation of Stixrude and Lithgow-Bertelloni *(116)*. The crustal density and thickness of each model are chosen according to the relation depicted in Fig. S23. For each interior structure model, the MOI is then calculated and only models that agree with the measured value *(111,112)* within its uncertainty (1σ) are retained. A further down-selection of compatible models is achieved by retaining only those that have a core radius large enough to agree with the tidal Love number k_2 *(111)*.

We find that geodesy data favours for all composition models but the Yoshizaki and McDonough (*84*) composition a thick crust and hot mantle temperature (Fig. S29). Among the used composition models, the Yoshizaki and McDonough (*84*) model has less iron and for this reason a different mass distribution in the mantle that results in a weaker constraint on the crust density and thickness for the hot mantle temperature but it is in favor of thicker crust if the mantle temperature is colder.

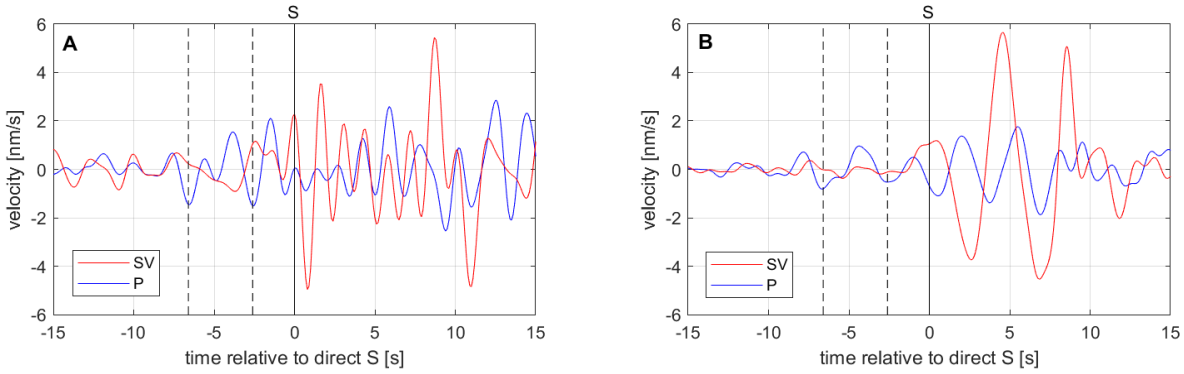

Fig. S1. S-onsets of events (A) S0173a and (B) S0235b, showing two precursory phases on the P-component. Data are band-pass filtered between 0.1 and 0.8 Hz and rotated in the P-SV coordinate system. Vertical solid black lines mark the S-onset, vertical dashed black lines the two precursors (with inverted sign, as expected for S-to-P conversions) at about 2.6 s and 6.6 s. Note that the definition of coordinate systems implies a change in sign between the radial component, as shown in Fig. S2, and the SV-component shown here. Phase picks are on the first local maximum rather than on the onsets here as those are easier to identify for the precursors.

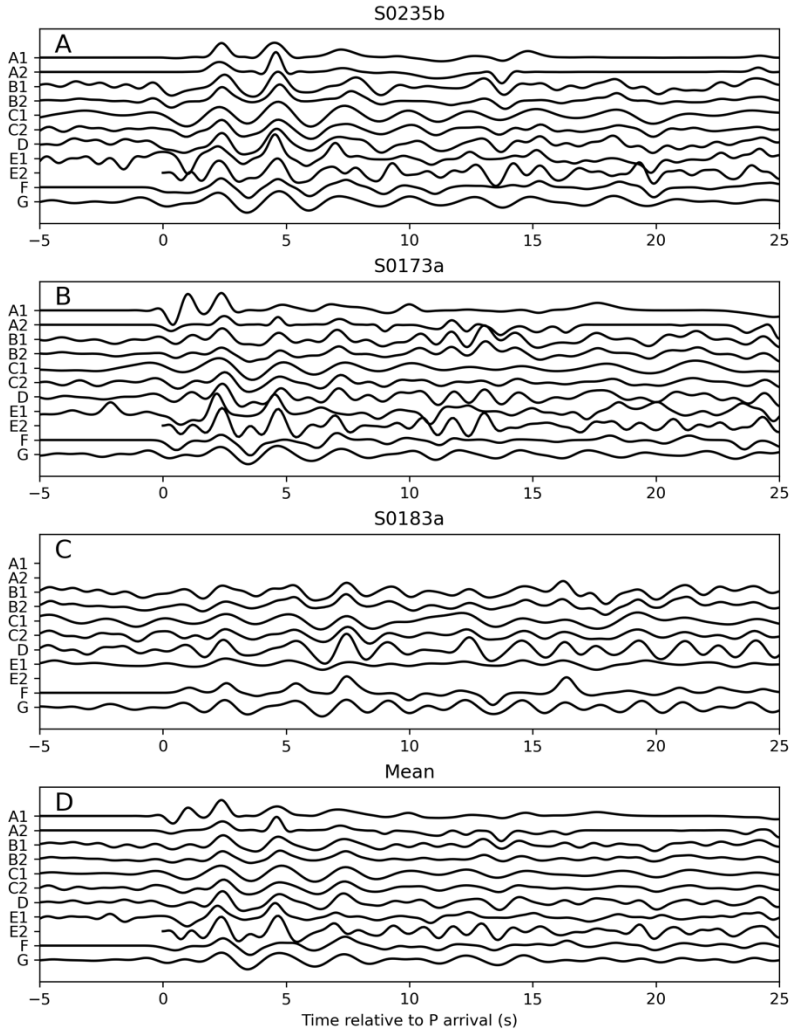

Fig. S2. All P-to-S receiver functions estimated by different groups plotted with identical amplitude scaling and offset for clarity. Data are shown separately for events S0235b (A), S0173a (B), S0183a (C) and the mean across all events calculated with the specific method (D). For clarity, data using a slightly higher frequency passband in method A (panels A2 and B2 in Fig. S4) are plotted as A1, while the remaining P-to-S receiver functions are plotted as A2.

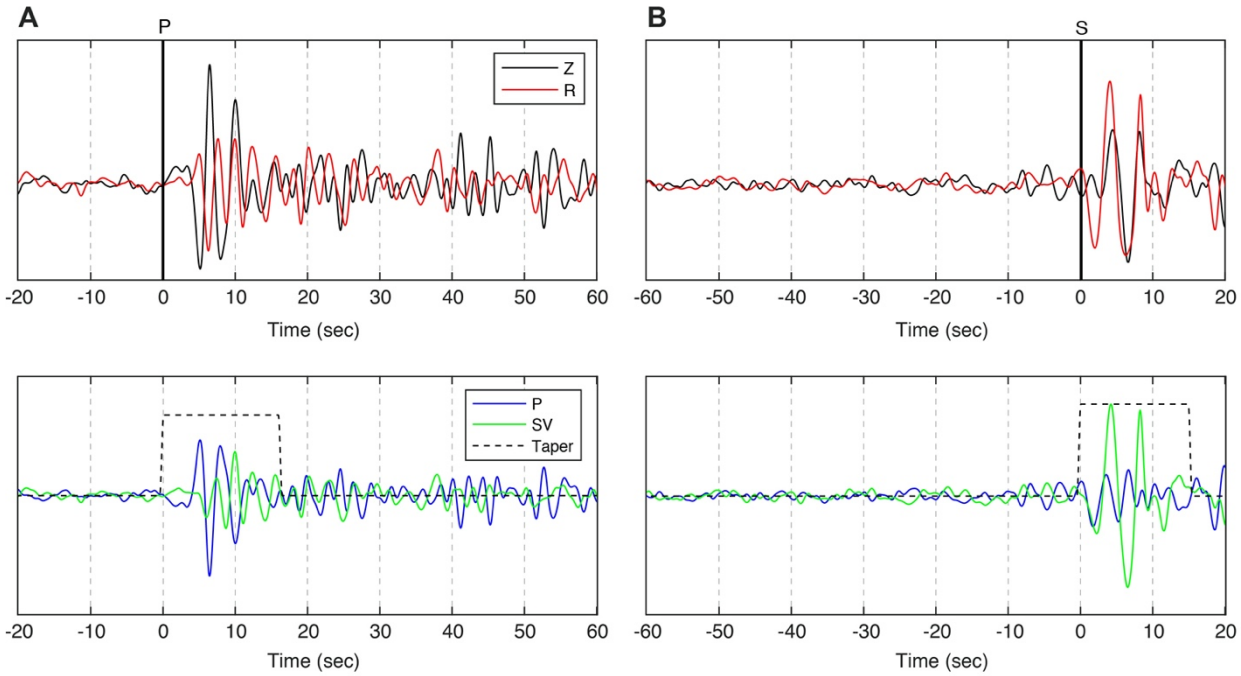

Fig. S3. Waveforms of event S0235b used in the (A) P-to-S and (B) S-to-P RF analysis. Waveforms plotted here are bandpass filtered 0.1-0.7 Hz and 0.05-0.7 for (A) and (B), respectively. We estimate the up-going P-SV waves (bottom) from the recorded Z-R waveforms (top) using the free surface transformation by minimizing the correlation between P- and S-energy at the time of the P or S arrival, computed in 8s-long windows starting at the P or S arrival.

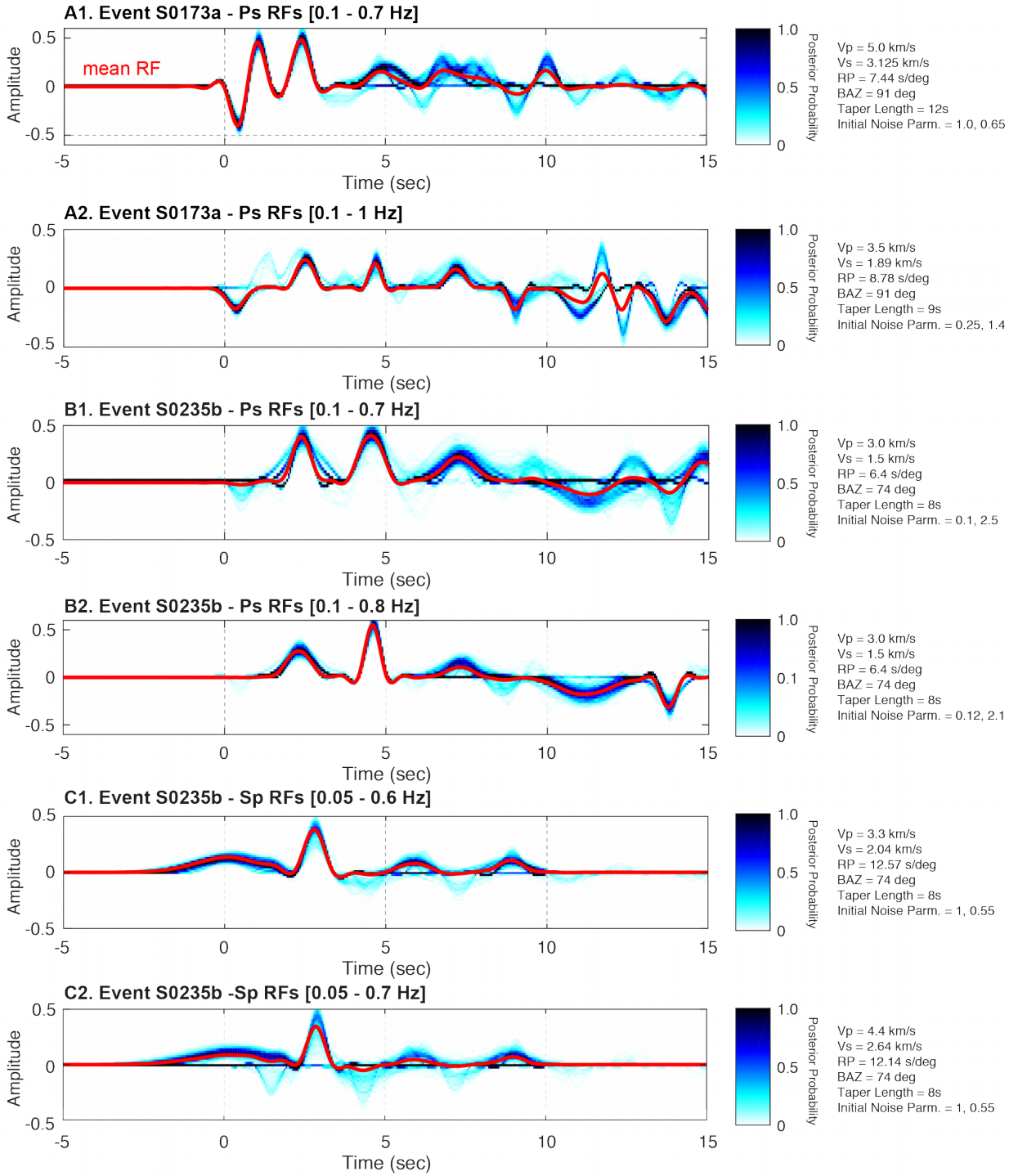

Fig. S4. Ensemble P-to-S and S-to-P RFs combining all of the models. For each event, one million iterations of the THBD were performed, discarding the first half as burn-in, and saving every 1000th sample to the ensemble. The average RF for each of the ensembles is shown in red. All of the parameters used to process the RFs (parameters associated with taper length, free surface transformation, and noise parameterization) are shown in the right-hand side of each ensemble solutions. NB: the acronyms for Vp, Vs, RP and BAZ refer to P-wave velocity, S-wave velocity, ray parameter, and back azimuth, respectively.

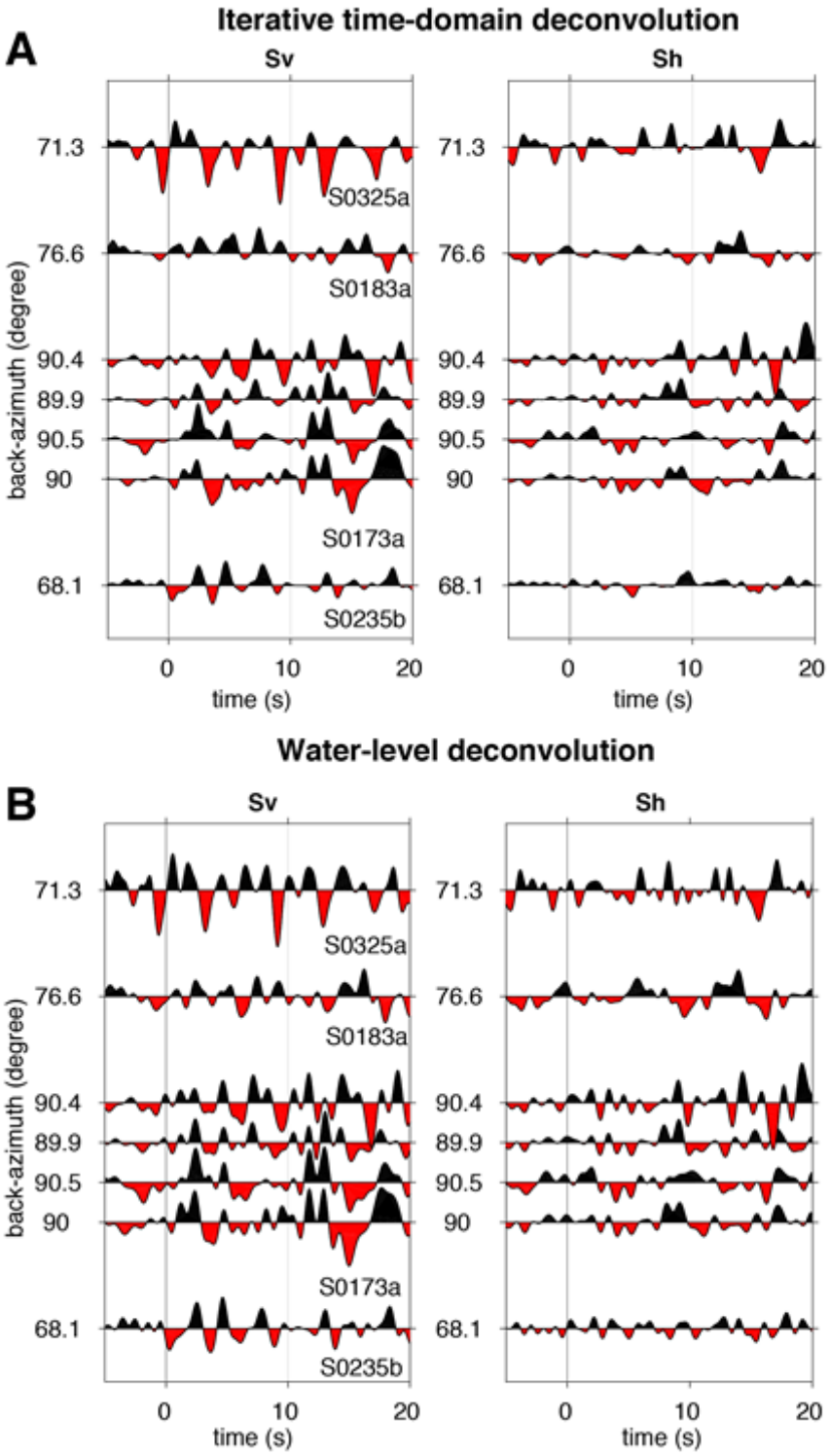

Fig. S5. RFs obtained from iterative time-domain (A) and water-level (B) deconvolutions as described in Methods B. Left and right panels show the Sv and Sh components for the four marsquakes, whose names are indicated at the bottom of the Sv traces. Estimated back-azimuths are indicated along the vertical axis. For S0173a, results of four different deglitching algorithms are shown *(38)*.

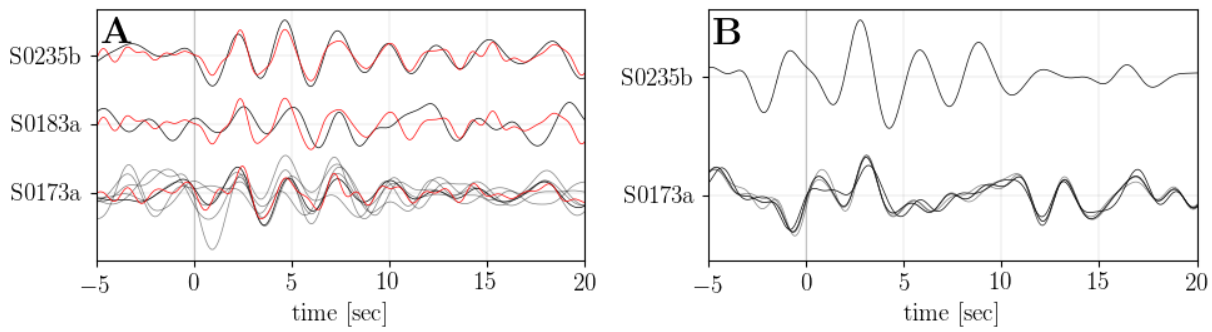

Fig. S6. P-to-S (A) and S-to-P RFs (B) for events S0173, S0183a, and S0235b using method C. RFs for event S0173a are based on waveforms deglitched by different groups (grey lines), whereas the RF based on the "final" deglitched data set and used for the inversion is depicted in black. The additional set of P-to-S RFs filtered at higher frequencies are shown in red.

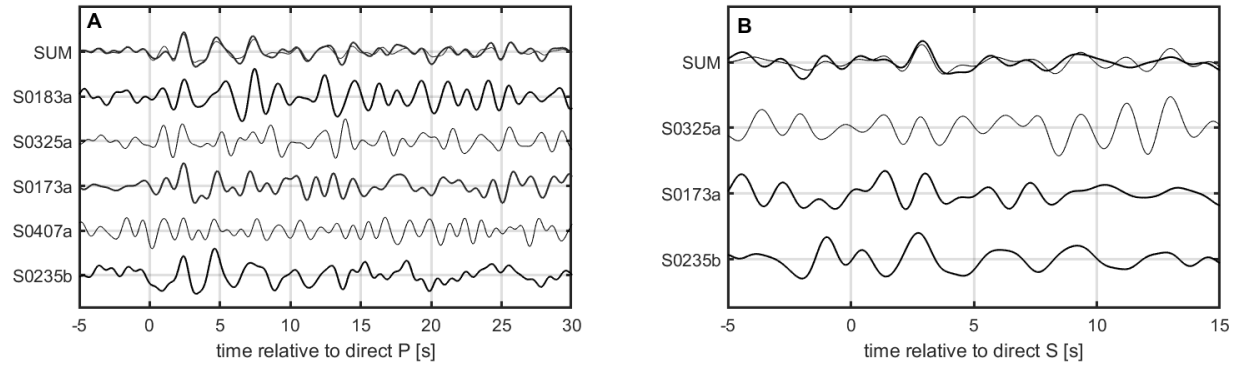

Fig. S7. P-to-S and S-to-P RFs using method D. (A) P-to-S RFs for events S0235b, S407a, S0173, S0325a and S0183a. Summed trace either contains only the three best events (S0235b, S0173a, S0183a; thick black line) or all five events (thin black line). (B) S-to-P RFs for events S0235b, S0173a and S0325a. Summed trace either contains only the two clearest traces (S0235b, S0173a; thick black line) or all three events (thin black line).

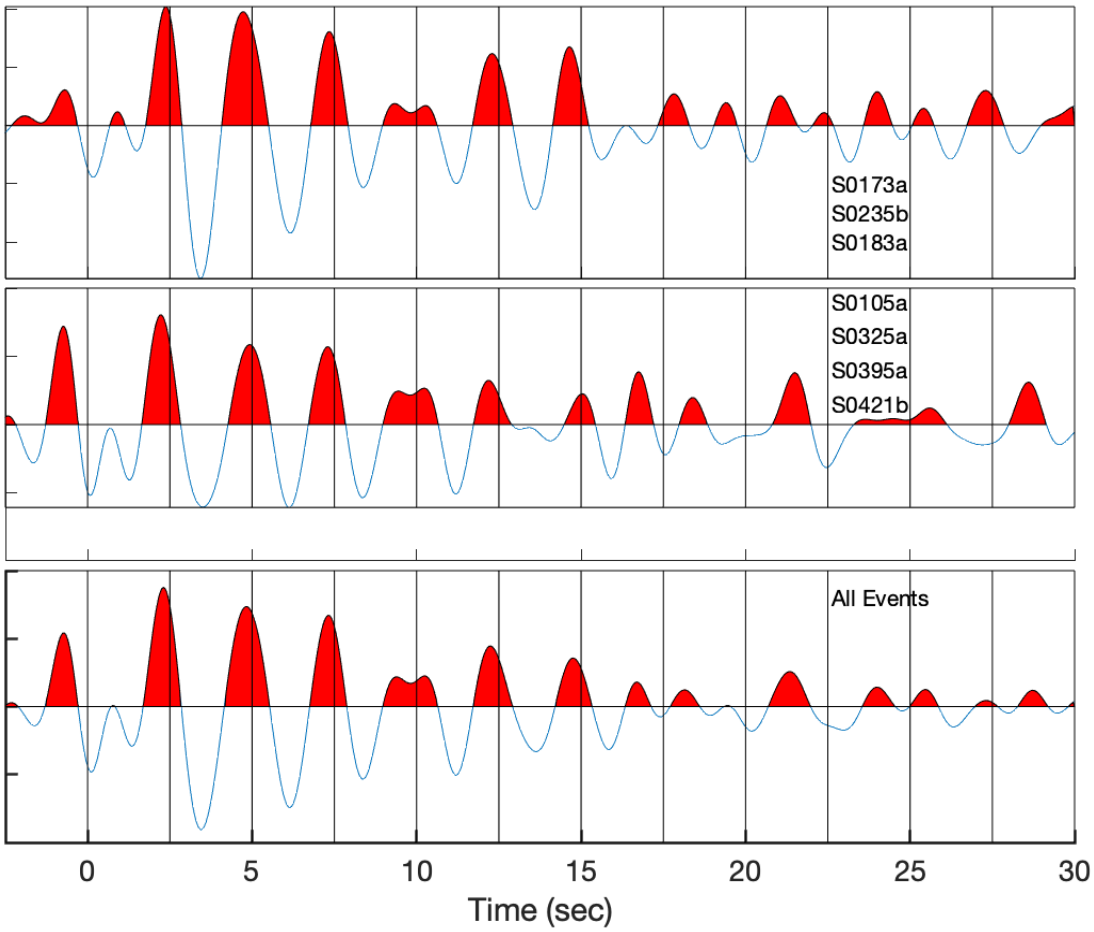

Fig. S8. Comparisons between stacks of receiver functions computed with method G. The top stack is R_{ref}. The events in the second stack were inverted for azimuth by comparing with R_{ref}. The third stack is for all events.

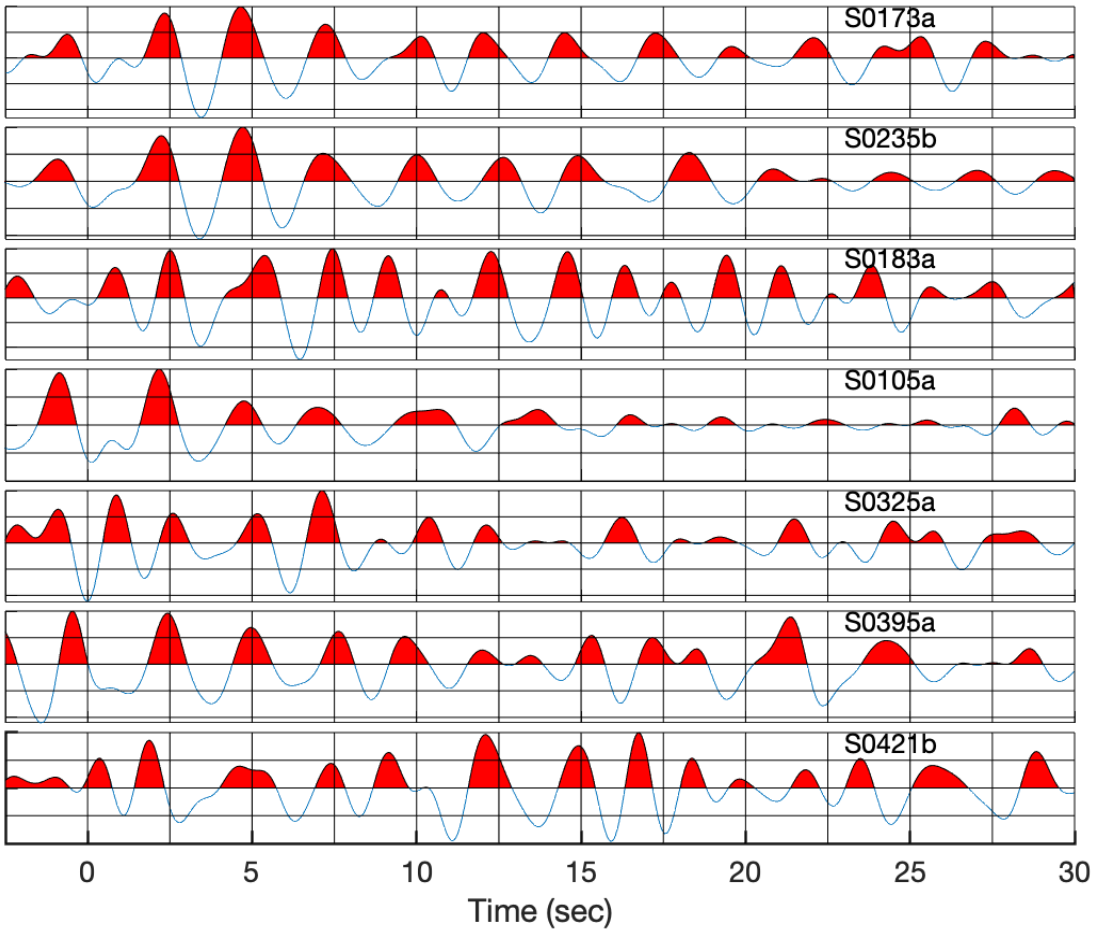

Fig. S9. Receiver functions for 7-deglitched events marked, using method G.

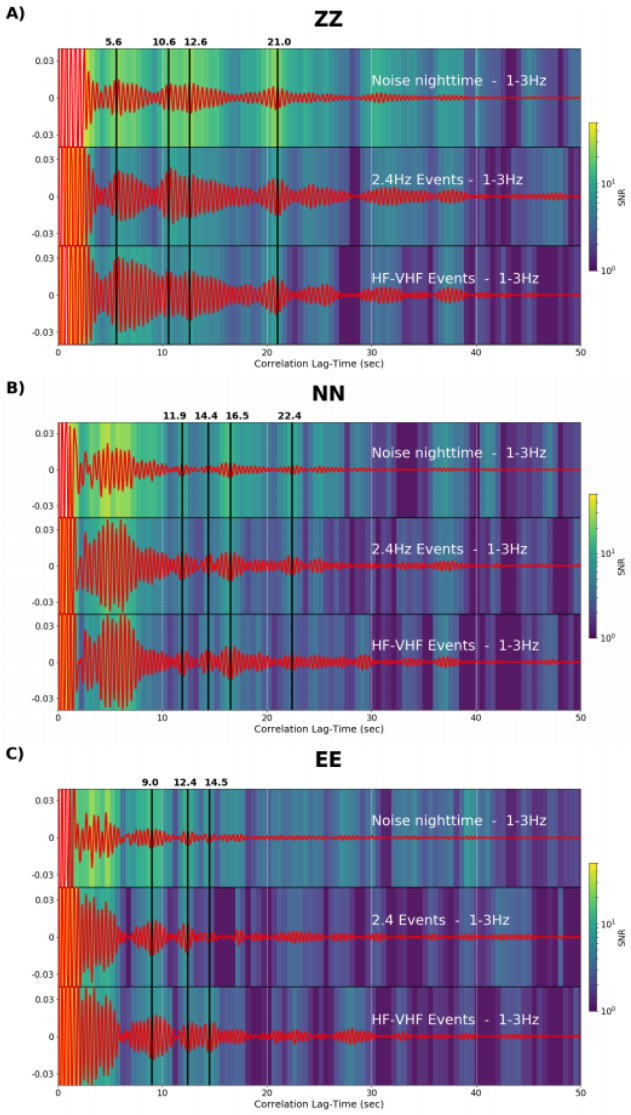

Fig. S10. Comparison of waveforms (in red) and SNR (color bar) of the ACFs for (A) the vertical (ZZ) component, (B) the North (NN) component and (C) the East (EE) component. From top to bottom: ACF computed on the ambient noise between 1 Hz and 3 Hz during nighttime (17:00 LMST to 23:00 LMST) (149 SOLs); ACF computed on 2.4 Hz events between 1 Hz and 3Hz (69 events); ACF computed on high frequency (HF) and very high frequency (VF) events between 1 Hz and 3 Hz (55 events). The colored background corresponds to the signal-to-noise ratio (SNR) in logarithmic scale. The various vertical black lines indicate potential energy arrivals corresponding to large amplitudes in the waveforms, and large SNR. (A) On the ZZ component we identify arrivals at 5.6 s, 10.6 s, 12.6 s and 21.0 s. (B) On the NN component we identify arrivals at 11.9 s, 14.4 s, 16.5 s and 22.4 s. (C) On the EE component we identify arrivals at 9.0 s, 12.4 s and 14.5 s.

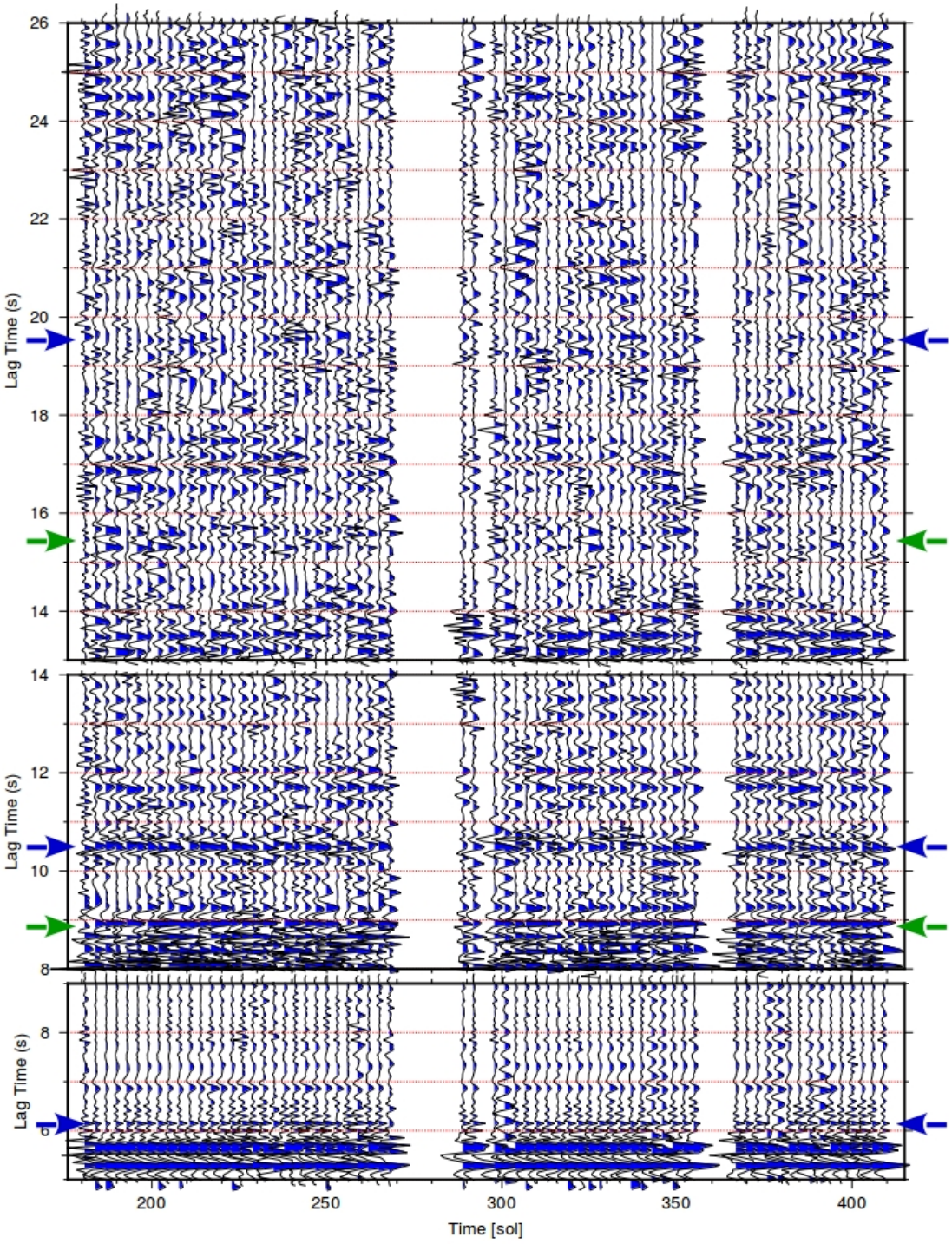

Fig. S11. Vertical-component noise autocorrelation stacks for sliding three-sol data windows. The frequency band is 1.2-8.9 Hz and data windows do not overlap. Shown are time-frequency phase weighted stacks of phase autocorrelations. Blue marks negative amplitudes. The blue and green arrows point to expected or observed P-wave reflections and converted P-to-S (and vice versa) reflections. The three lag-time windows have been used to improve the visibility through independent amplitude normalization.

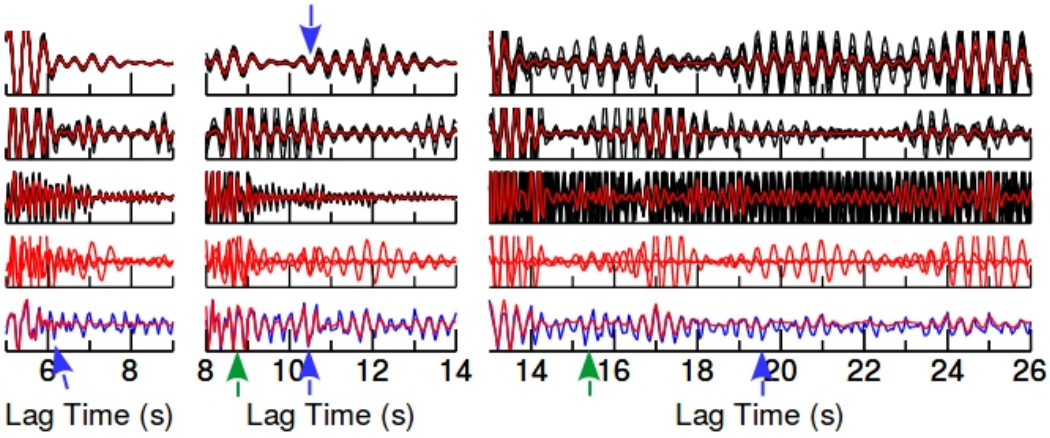

Fig. S12. Vertical-component noise autocorrelation stacks. The three lag-time windows correspond to those of Fig. S11 and have been chosen to improve signal visibility. Red and black traces show time-frequency phase weighted stacks of phase autocorrelations. Red and black mark the stacks for all data and subsidiary data sets of 10%, respectively. The first three panels are for 1.5-3.0 Hz, 2.4-4.8 Hz, and 3.6-7.2 Hz band-passed filtered noise. The fourth panel compares the stacks from the top three panels. The lowermost panel shows the linear stack (blue line) and phase weighted stack (red line) of phase autocorrelations in the frequency band 1.2-8.9 Hz. Arrows are the same as for Fig. S11.

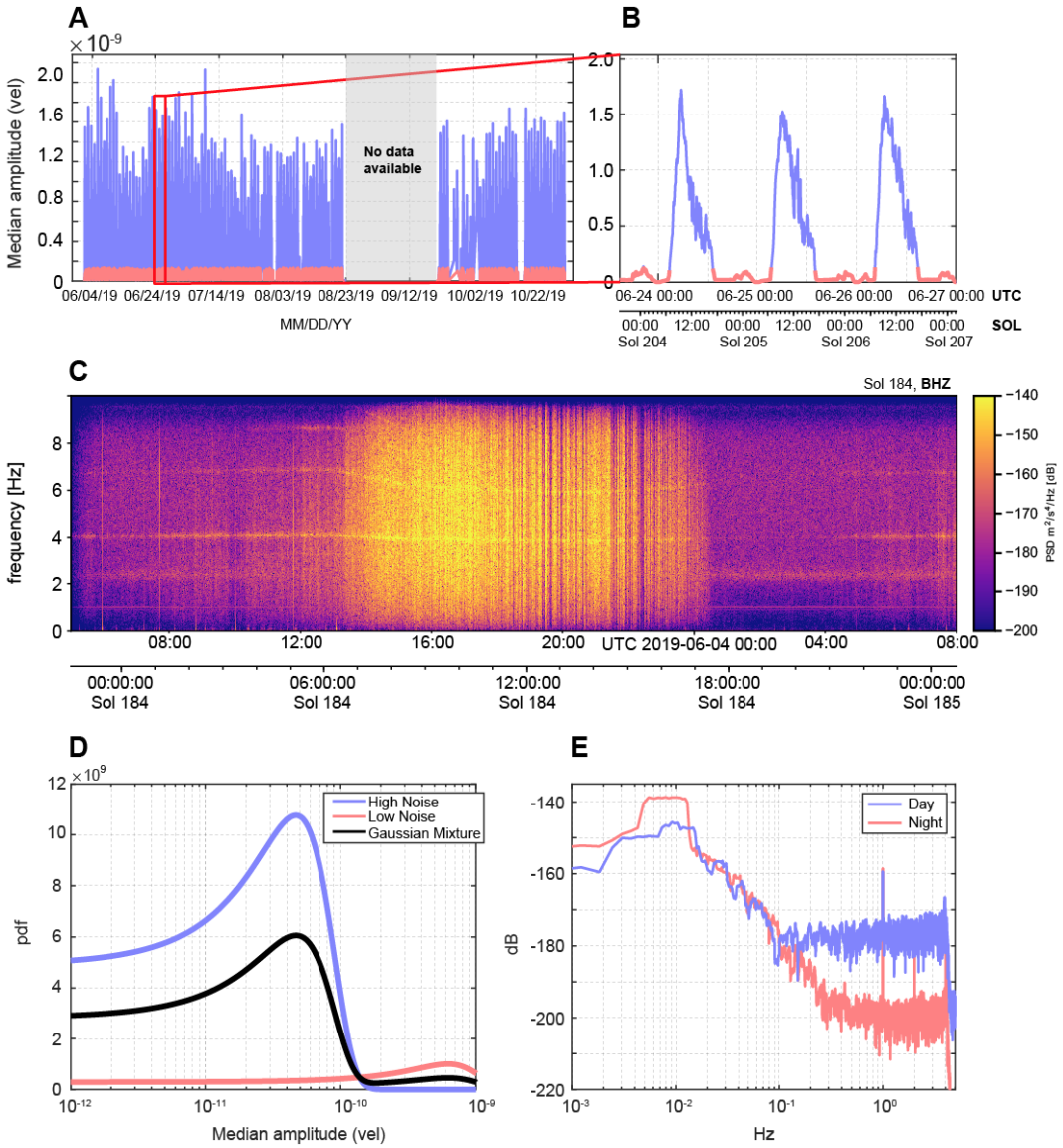

Fig. S13. Seismic noise recordings at Mars. (A) Median amplitude of 20 Hz broadband velocity recordings (VBB) during June-November, 2019. Blue and red lines indicate low and high noise level recordings modeled in (D). SEIS data in gray shaded box is not available due to solar conjunction. (B) Outset shows rise and fall of the amplitudes between three sols of recording (June 24-27, 2019). (C) Spectrogram of one sol of SEIS data recorded on the vertical component, showing a clear contrast between the nighttime and daytime signal. During the day, large signals are generated by windy conditions, while at night the signals approach the noise floor of the VBB. Several resonance modes are apparent, including tick noise at 1 Hz (with its overtones) and a potential structural resonance at 2.4 Hz. (D) PDF of a Gaussian mixture model with two components (high and low noise) used for distinguishing day vs. night portions of the data. (E) Average power spectral density of daytime (blue) and nighttime (red) signals. NB: the acronyms for MM/DD/YYYY, UTC, pdf, and PSD refer to month/day/year, universal time coordinated, probability density function, and power spectral density, respectively.

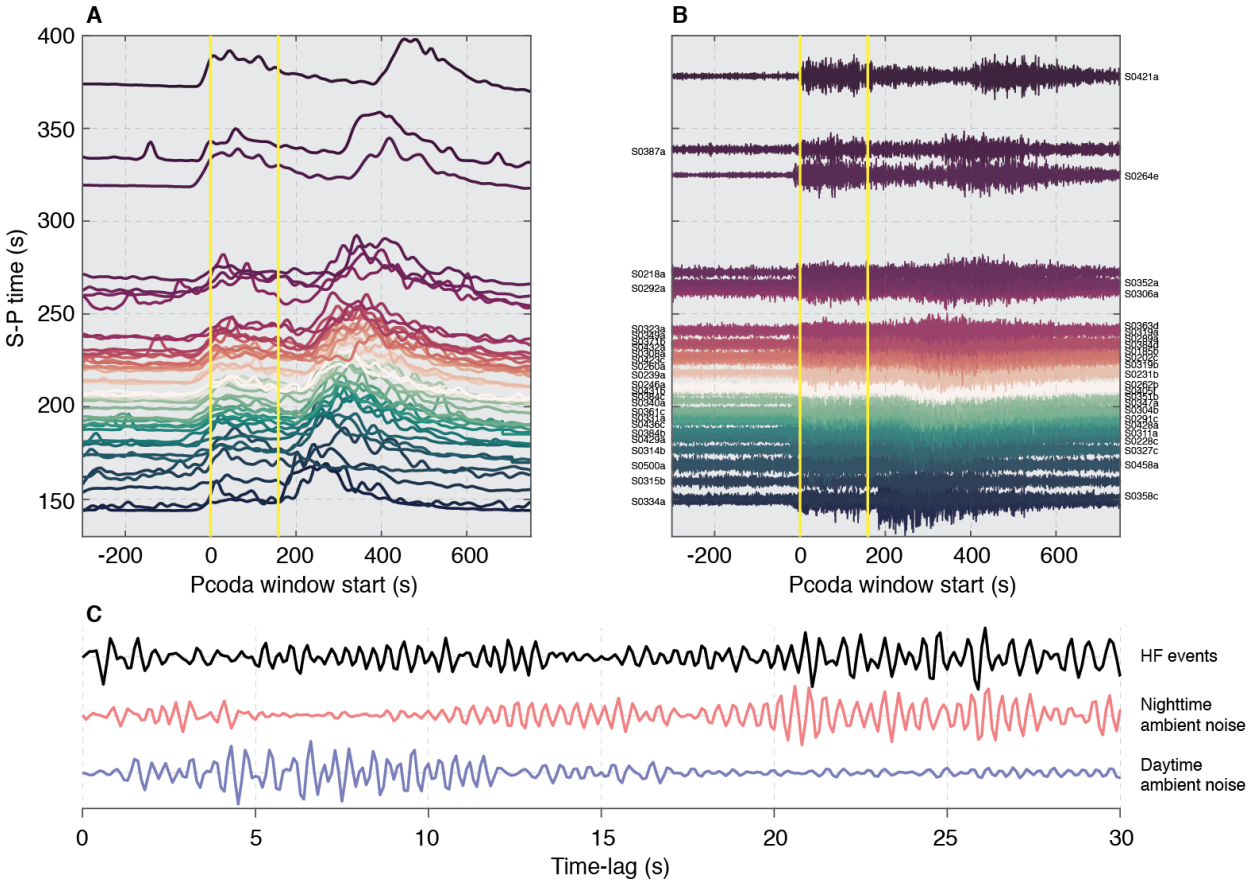

Fig. S14. HF event data, and comparison of the ACF stacks. (A) Average three-component envelopes aligned by P arrival from the 48 HF marsquakes analyzed, and the corresponding (B) vertical component waveforms. Yellow lines denote the P-coda analysis windows used in the correlation analysis. (C) Comparison of phase-weighted ACF stacks computed from day- and night-time continuous ambient noise recordings (blue and red, respectively) and P-coda energy from the HF events (black), post-filtered between 1.5-3.0 Hz.

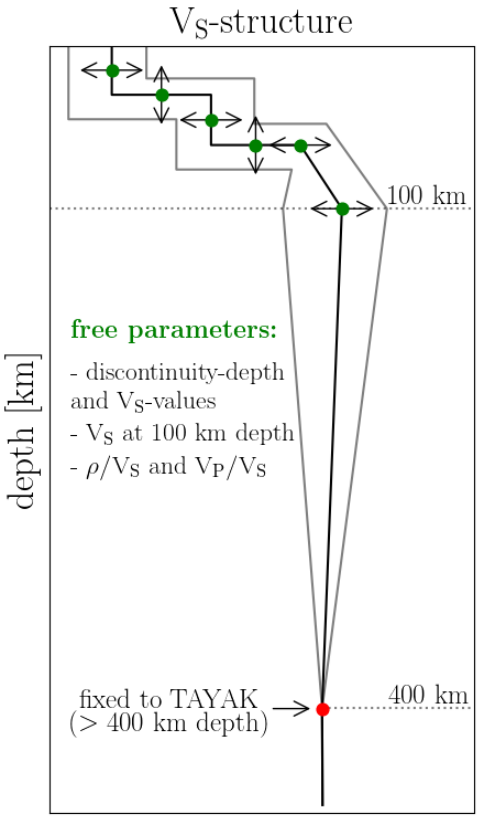

Fig. S15. Sketch of model parametrization (inversion method A). The black and grey lines indicate example-profiles of S-wave velocity ($\sqrt{Vs}$), while free parameters are visualized as green dots in contrast to fixed nodes in red. See text for further explanations.

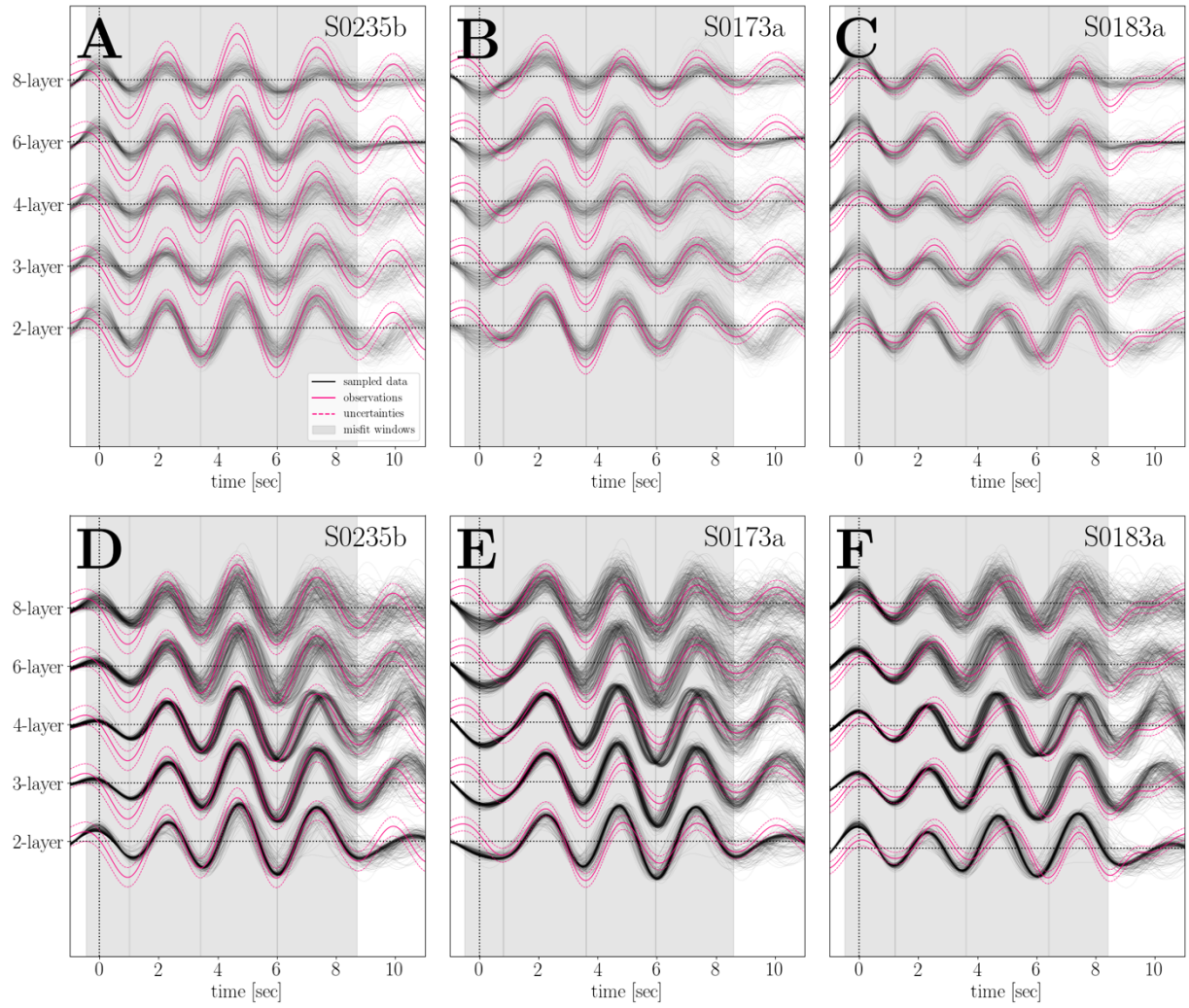

Fig. S16. Data fit resulting from joint inversions of S0235b (A, D), S0173a (B, E), and S0183a (C, F) low-frequency Ps RFs using inversion method A (top) and B (bottom), respectively. Inversions differ in the number of crustal layers included (vertical axis). Observed data and their uncertainty bounds are plotted in magenta as solid and dashed lines, respectively. Synthetics picked from the model samples are shown in grey. Grey shaded areas indicate time windows employed in misfit computation.

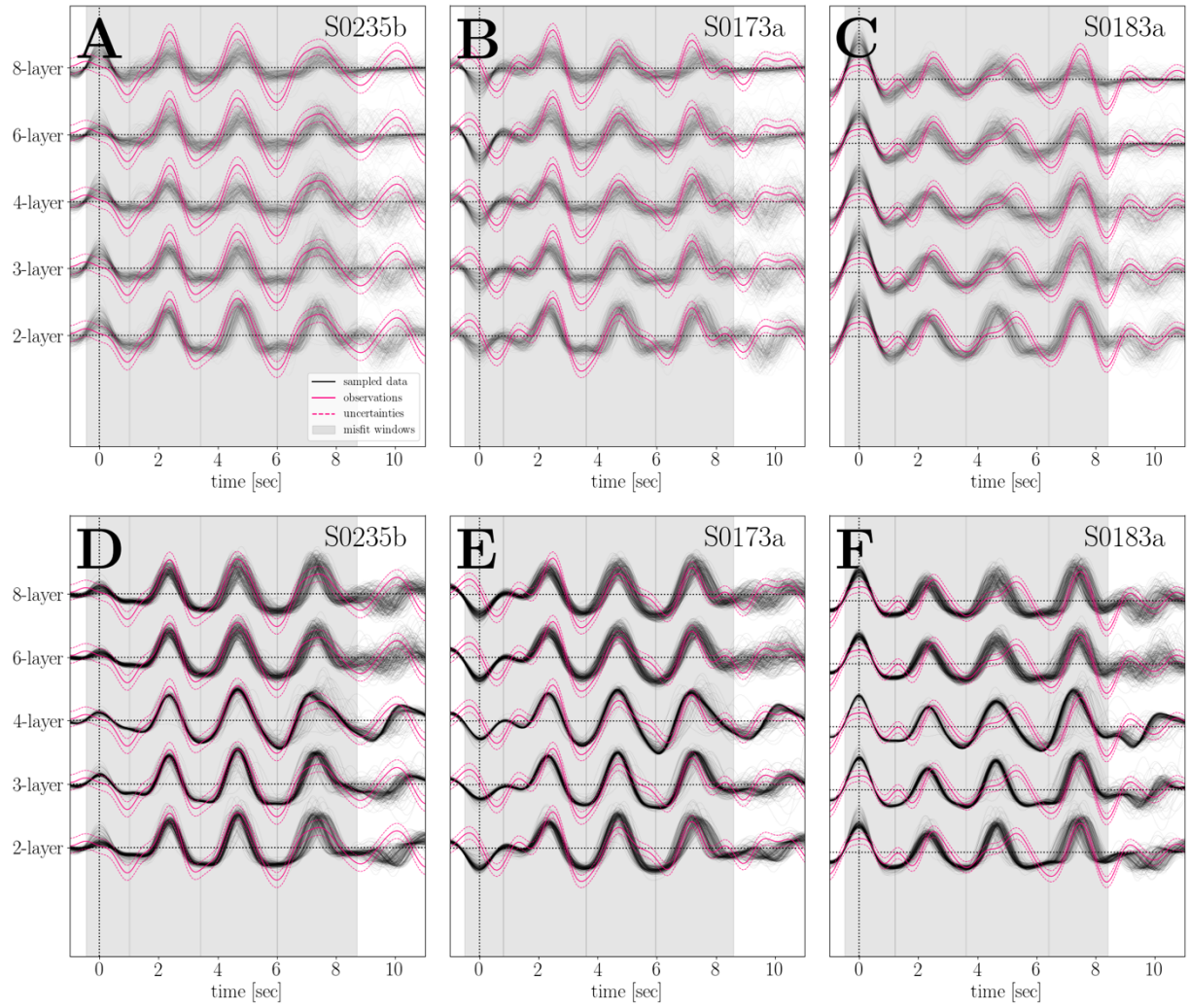

Figure S17: **Same as Figure S16, but for high-frequency Ps RFs.**

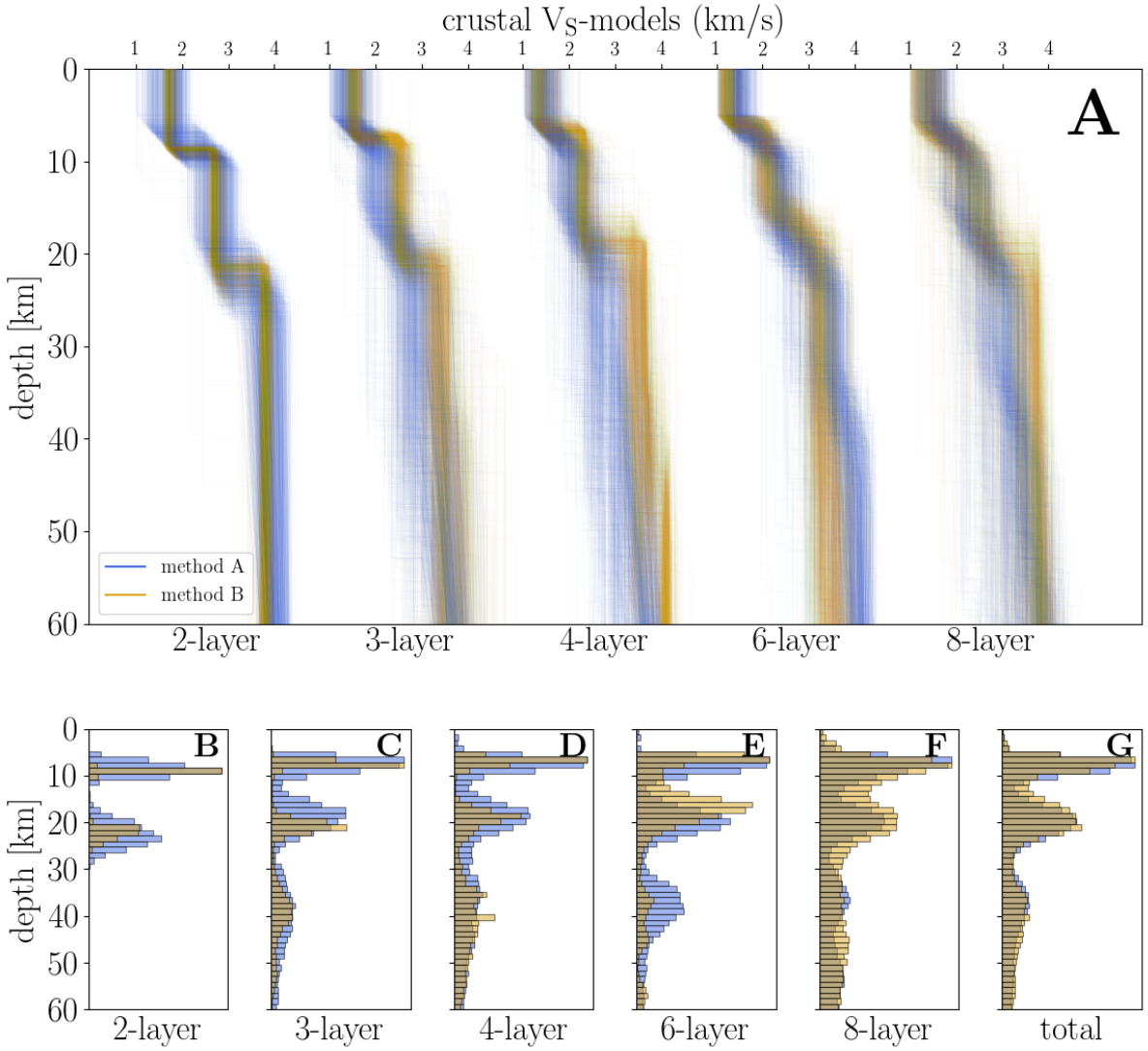

Fig. S18. A collection of S-wave velocity profiles (A) extracted from the model ensemble from low-frequency Ps RF inversions differing in number of crustal layers for inversion method A (blue) and B (orange), respectively, and corresponding discontinuity-depth histograms (B-G).

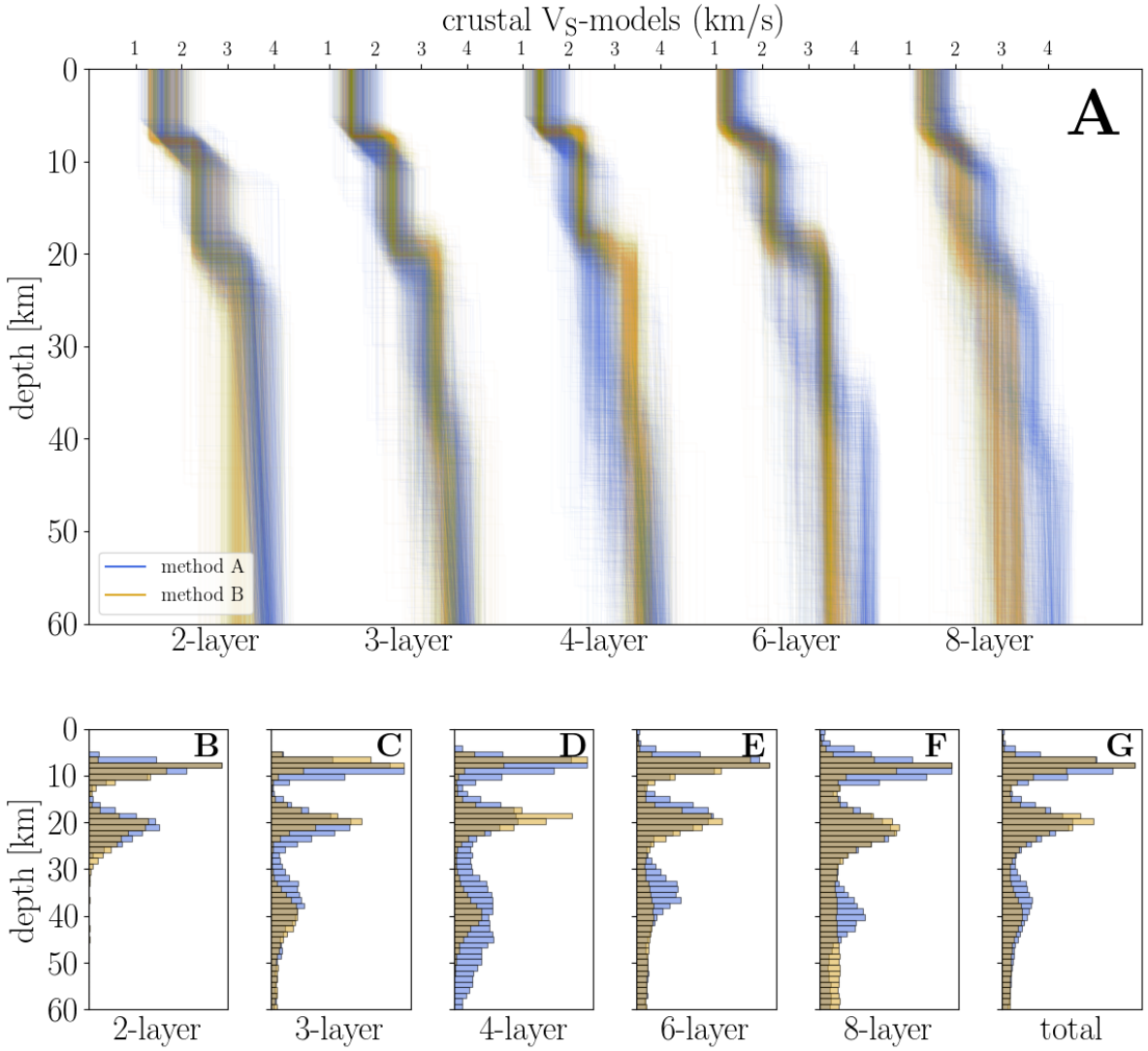

Fig. S19. Same Figure S18, but for high-frequency inversions

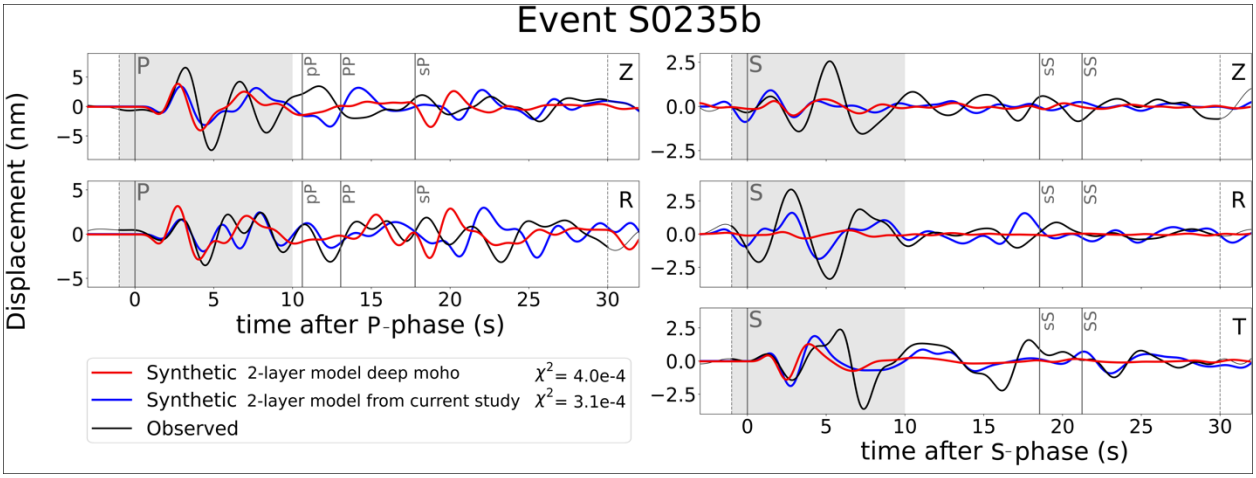

Fig. S20. Source inversion results for event S0235b (black lines show the recorded data) taken from Brinkman et al. (*82*) for 2 layer-models with the Moho at 80 km (red lines) and 24 km (blue lines). The latter model is equivalent to the 2-layer model of this study. The two left panels represent from top to bottom the vertical (Z) and radial (R) component of the P-waveform. The right three panels show from top to bottom the vertical (Z), radial (R) and transverse (T) component of the S-waveform. The dashed gray lines and area present the total length of the inversion window and higher weighted part of the inversion window, respectively. The solid gray vertical lines denote the first arriving P- and S-waves and later-arriving phases (pP, PP, sP, sS and SS) calculated using ray theory. The misfit value (χ^2) for each of the inversion is specified in the legend.

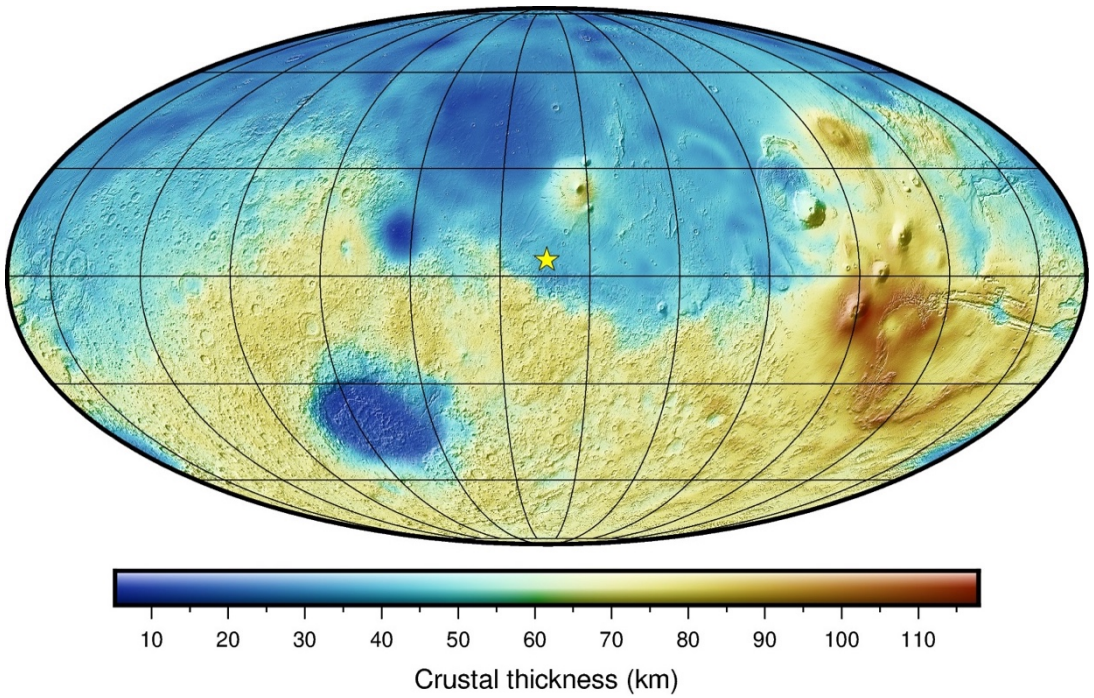

Fig. S21. A representative global crustal thickness model of Mars. This model uses the reference interior model of TAYAK (*26*), a crustal density of 2900 kg m^{-3}, and an assumed crustal thickness at the InSight landing site of 39 km. The average crustal thickness for this model is 56 km, the minimum thickness is 5 km (located in the Isidis impact basin), and the maximum thickness is 118 km (located in the Tharsis plateau). The yellow star denotes the location of the InSight landing site, grid lines are spaced every 30° of latitude and longitude, and the image is presented using a Mollweide projection with a central meridian of 135.6° E longitude.

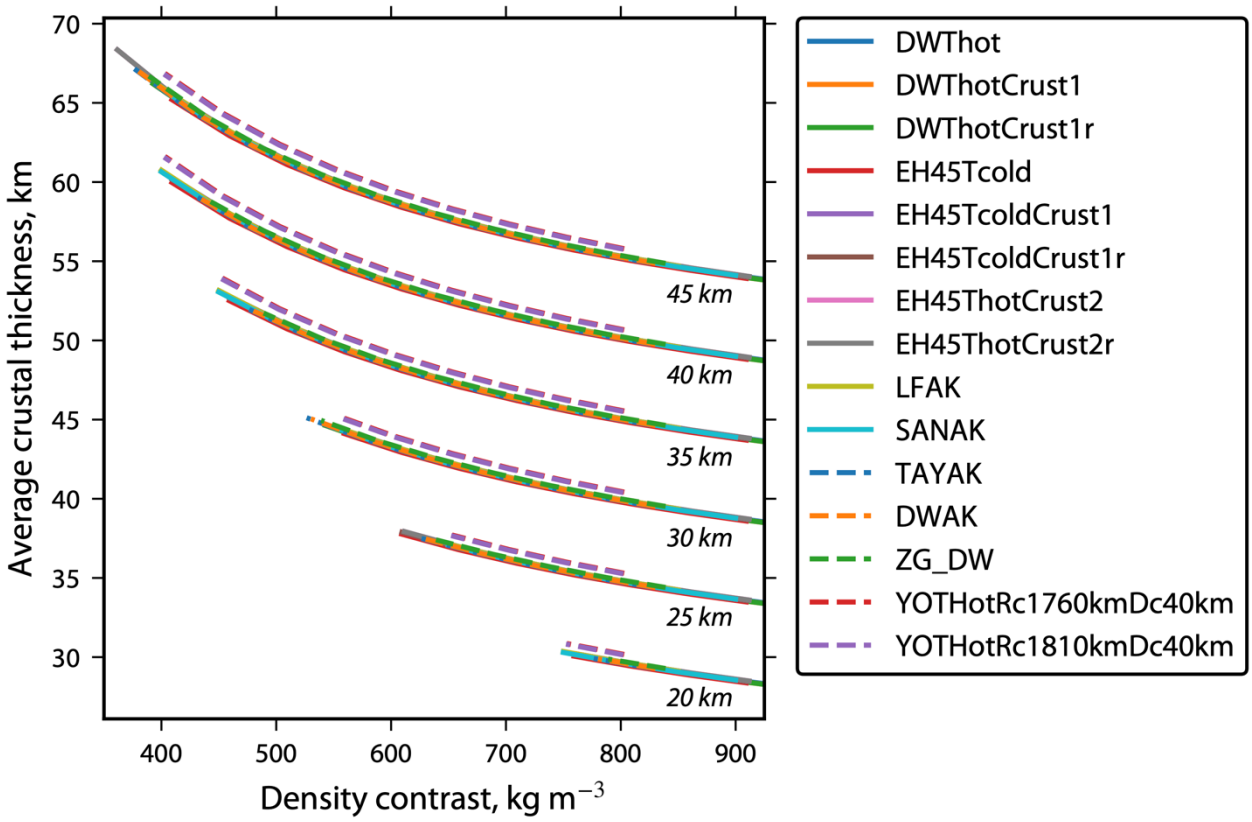

Fig. S22. Average thickness of the Martian crust as a function of the density contrast across the crust-mantle interface from inversions of global gravity and topography data. Each curve corresponds to a different reference interior model that specifies the density profile of the mantle and core (legend) and an assumed seismic thickness at the InSight landing site (text annotation). Shown are suites of models for InSight seismic thicknesses from 20 to 45 km. The minimum crustal density is assumed to be 2550 kg m^{-3}, and the maximum density is limited by the ability of the model to fit the observed seismic thickness and gravity field. The interior reference models are described in Smrekar et al. (*26*).

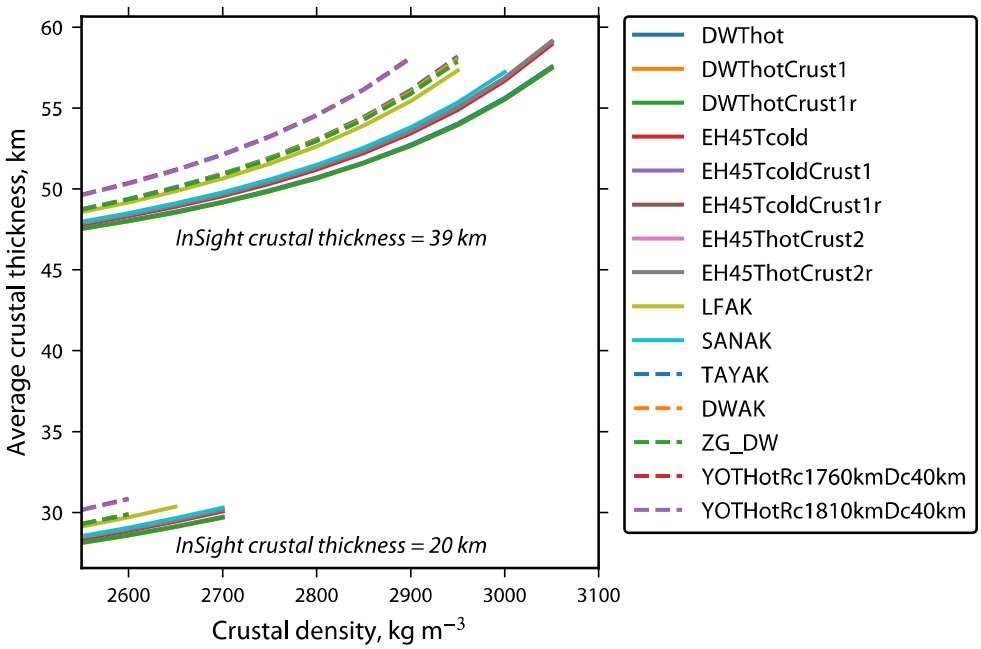

Fig. S23. Average thickness of the Martian crust as a function of crustal density from inversions of global gravity and topography data. Each curve corresponds to a different reference interior model that specifies the density profile of the mantle and core (legend). Shown are two suites of models that satisfy two possible seismic thicknesses at the InSight landing site of 20 and 39 km. The minimum crustal density is assumed to be 2550 kg m^{-3}, and the maximum density is limited by the ability of the model to fit the observed seismic thickness and gravity field. The interior reference models are described in Smrekar et al. *(26)*.

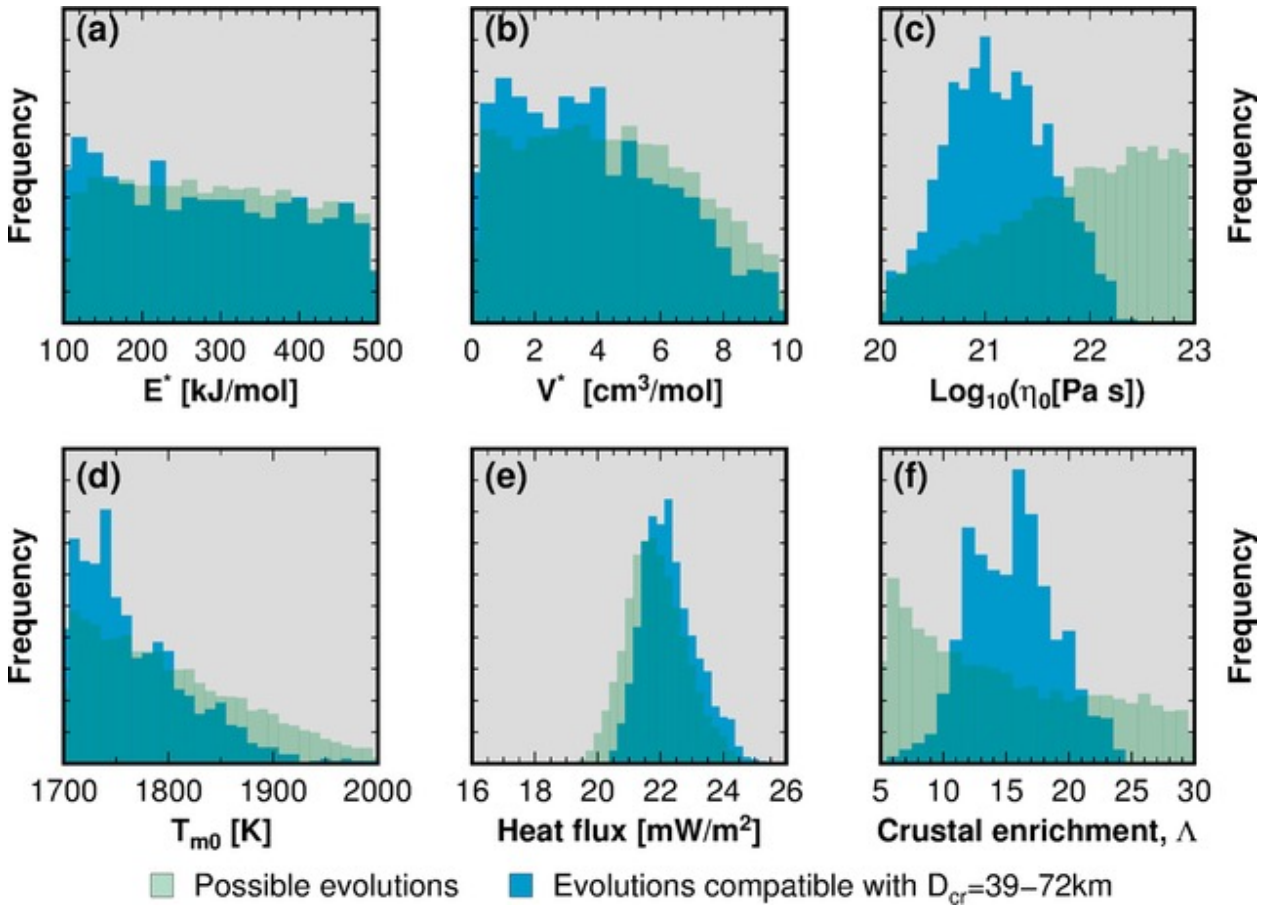

Fig. S24. Results of the parameterized convection modelling. Exploration of the parameter space for the thermo-chemical evolution of a Mars-like planet, showing the input governing parameters and output quantities associated with n=10^4 possible histories and a subset (n=10^3) of modelled histories that are compatible with a present-day crustal thickness ranging between 39 km and 72 km.

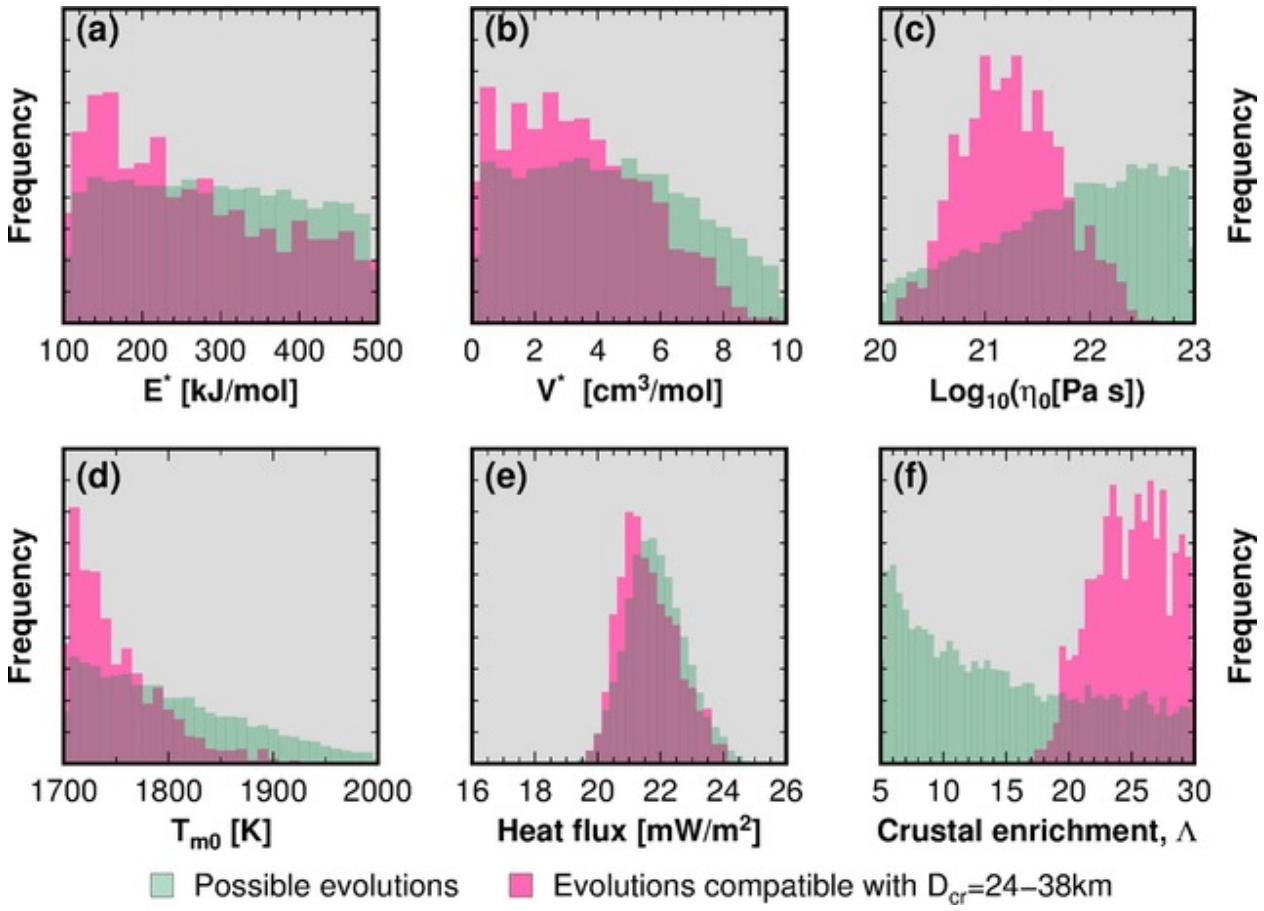

Fig. S25. Results of parameterized convection modelling. Exploration of the parameter space for the thermo-chemical evolution of a Mars-like planet, showing the input governing parameters and output quantities associated with $n=10^4$ possible histories and a subset ($n=10^3$) of modelled histories that are compatible with a present-day crustal thickness ranging between 24 km and 38 km.

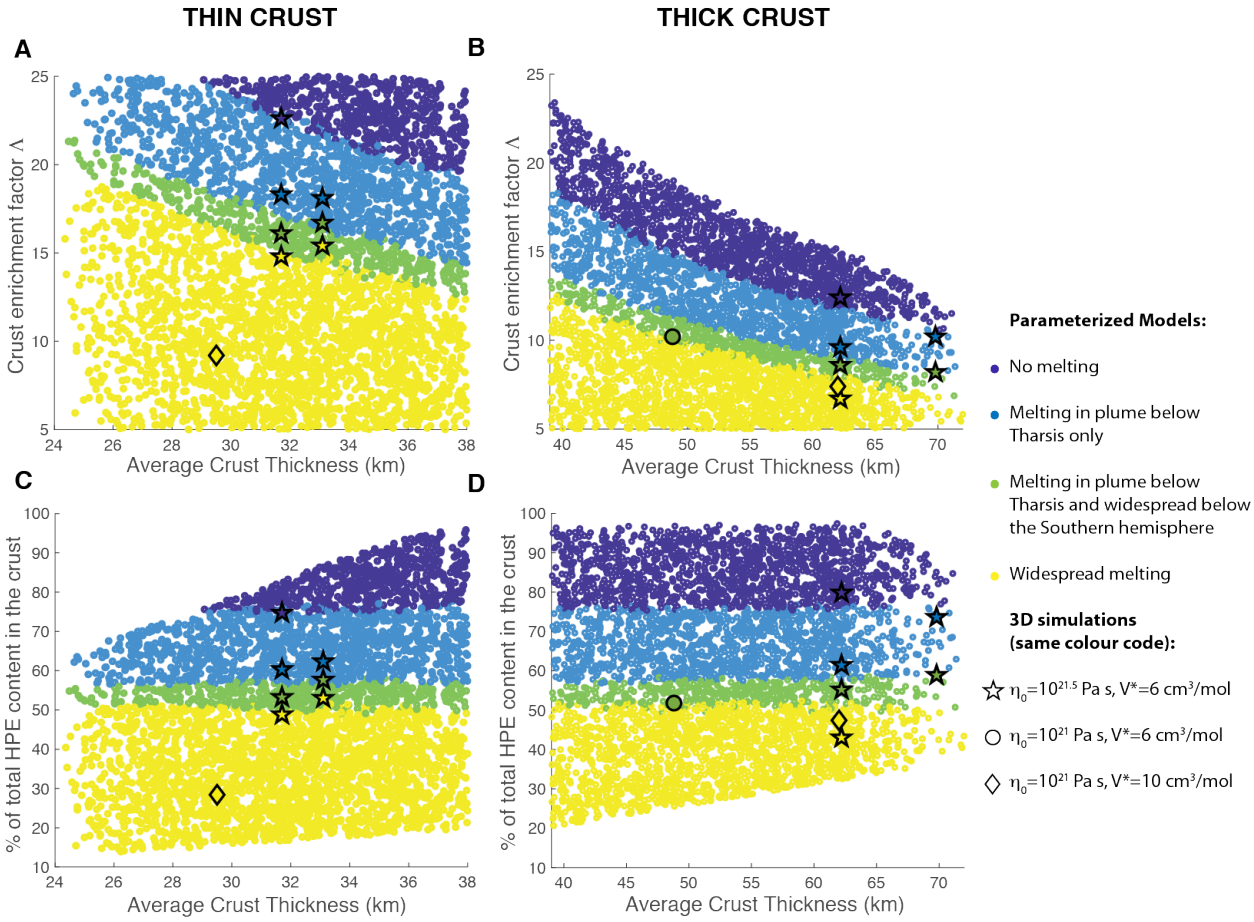

Fig. S26. Results of parameterized convection modelling accounting for different crustal structures in the geological provinces of Mars, testing for melting in a plume below Tharsis. 5000 models randomly sampled in terms of crustal density (2550-2850 kg m^{-3} in the thin crust case, 2550-3100 kg m^{-3} in the thick case), northern crustal thickness (16-28 km in the thin crust case, 28-55 km in the thick crust case), these a priori ranges being given by topography and gravity data inversion (Section S5). The crustal enrichment factor Λ is in the range 5-25. The rheology is fixed with a reference viscosity η_0=$10^{21.5}$ Pa s at T_0=1600 K and E*=300 kJ mol^{-1}, V*=*6* cm^3/mol. The initial mantle temperature is T_{m0}=1800 *K* and the core radius is R_C=1850 km. Results for 6 of the 3D simulations indicated on the graph are shown on Fig. S27.

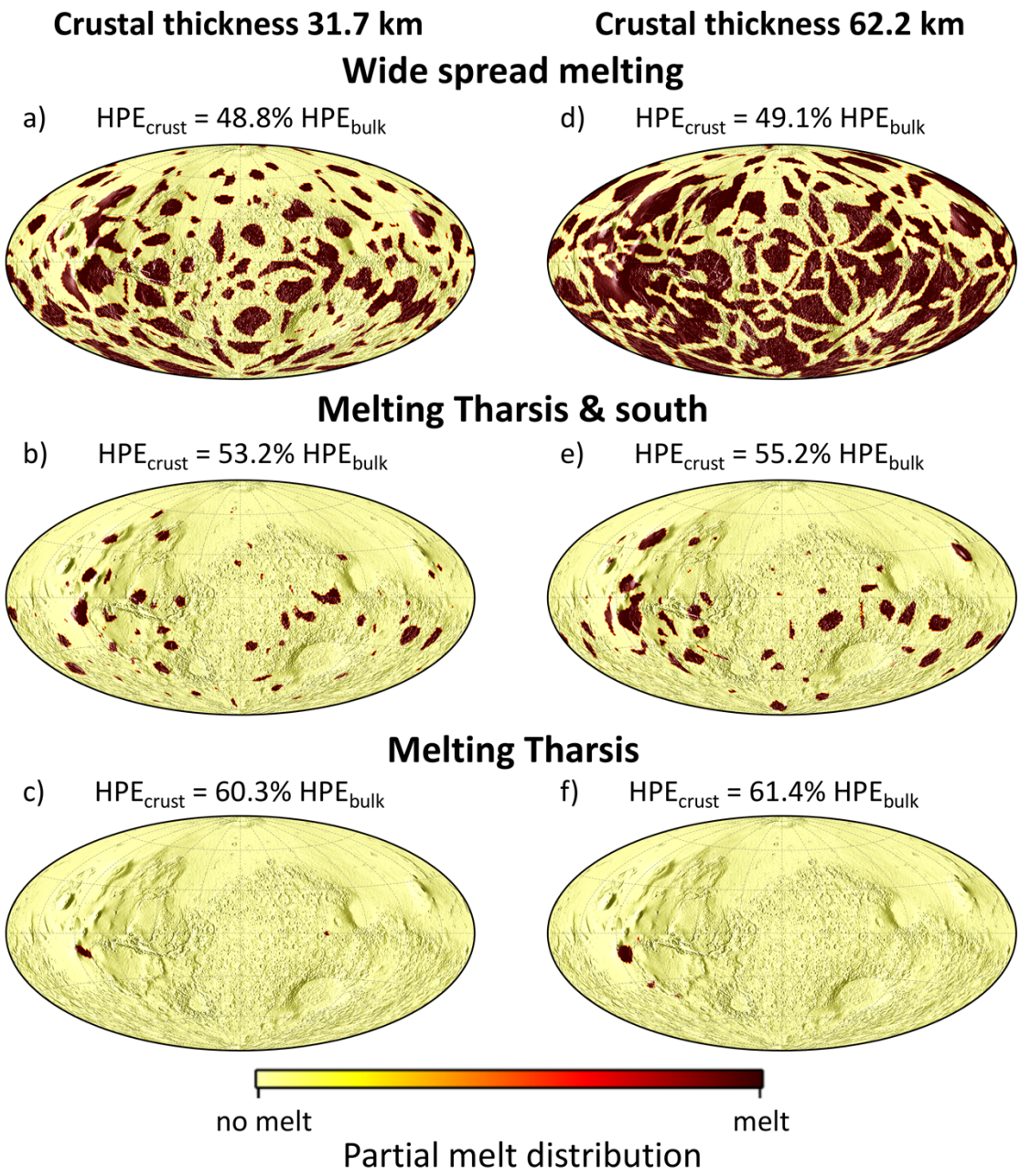

Fig. S27. Distribution of partial melt produced by mantle plumes in the interior of Mars at present day. The left column shows the models that employ a thin crust (31.7 km) and contain the following amounts of radioelements in the crust: a) 48.8%, b) 53.2%, and c) 60.3% of the total bulk content. The right column shows models with a thick crust (62.2 km) that contains: d) 49.1%, e) 55.2% and f) 61.4% of the total heat-producing element content. All models use the same parameters as the parametrized thermal evolution models in Fig. S26 and are indicated by star symbols on Fig. S26. The amount of melt reduces with increasing radioelement content in the crust, and the melt distribution becomes confined to smaller regions on the southern hemisphere and finally to Tharsis.

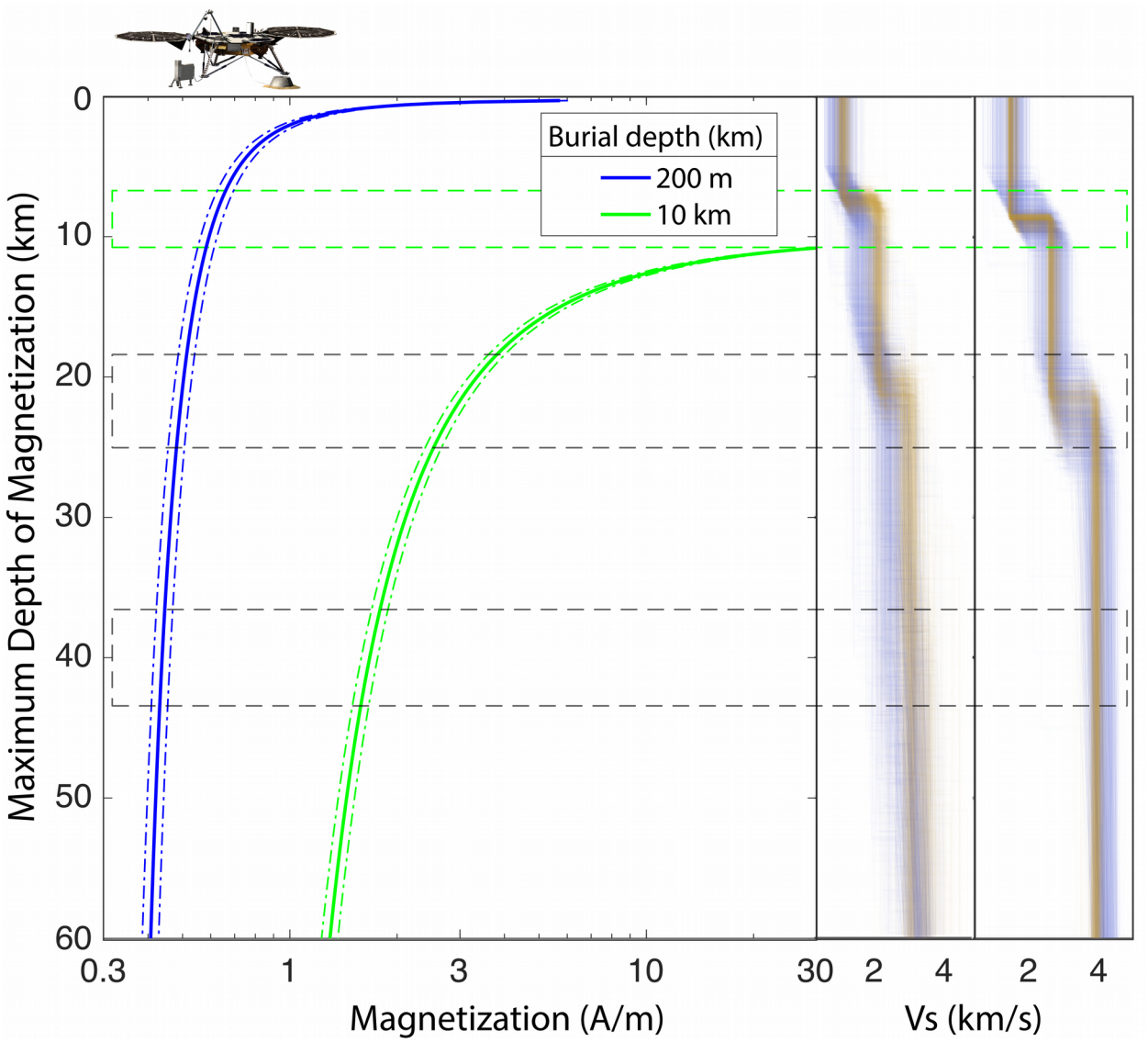

Fig. S28. Estimation of minimum magnetization. The minimum magnetization required from a surface field of 2013 nT and the upper and lower 99% confidence intervals on the surface field strength (*107*). Burial depth describes the depth extent of the unmagnetized layers above the top of the magnetized layer. For a burial depth of 200 m (blue), corresponding to burial beneath the young, Amazonian-Hesperian, near-surface lava flows (*107*) magnetizations are ~0.4 A/m if the entire underlying crust is magnetized. A burial depth of 10 km requires magnetizations larger than 1 A/m. The velocity profiles show the range of seismically-determined interface depths as in Fig. 2 of the main paper.

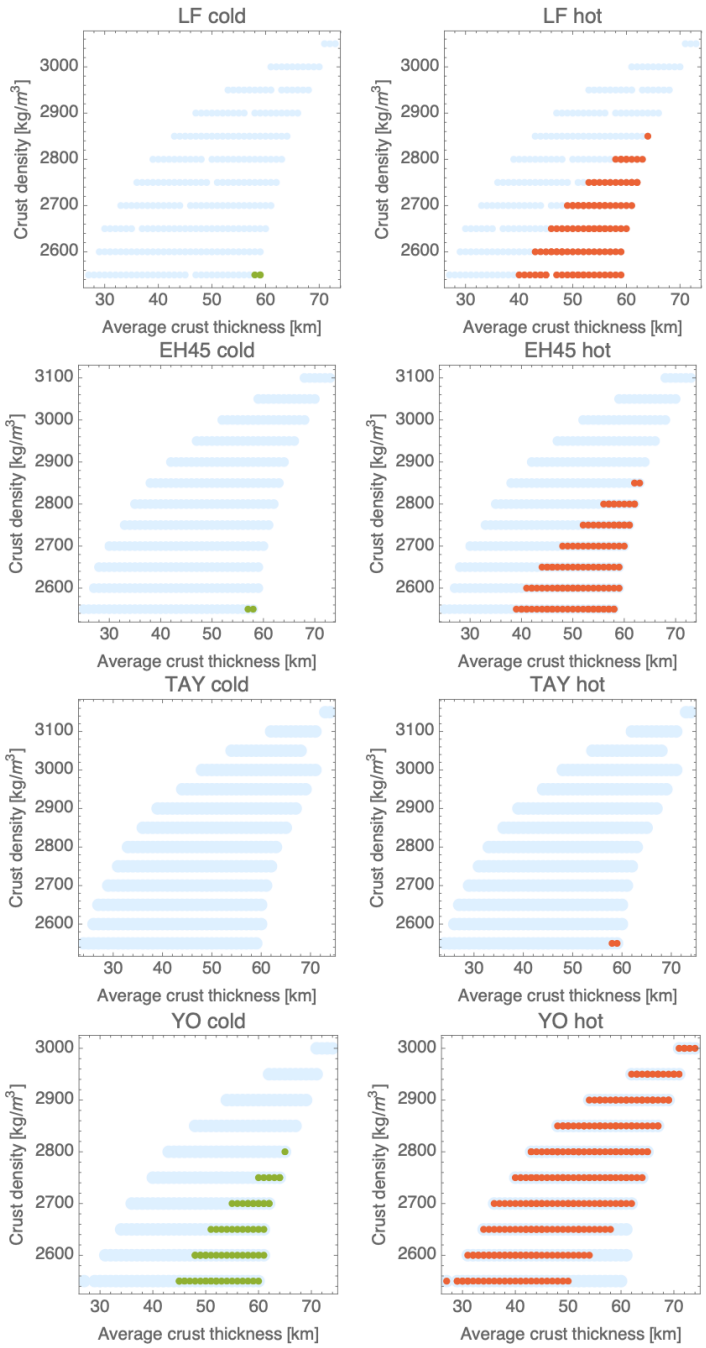

Fig. S29. Ability of crustal models to match moment of inertia and k_2. Each panel shows the average crust density and thickness pairs (blue dots) resulting from this study for different mantle composition and two mantle temperature end members (hot and cold). The colored dots represent the crust density and thickness pairs of interior structure models that agree with the moment of inertia of Mars and have a core large enough to agree with the tidal Love number k_2. Figures are labelled with the composition models discussed in section S5.

Method	RFs	Rotation angles	Deconvolution method	Length of source window for deconvolution	Filter band [Hz]
A	P-to-S and S-to-P	MQS backazimuths and free surface transfer matrix for incidence angles *(39)*	transdimensional hierarchical Bayesian *(39)*	8-9 s after P- or before S-arrival	event dependent: 0.1-1 or 0.1-0.8 for P-to-S, 0.05-0.7 for S-to-P
B	P-to-S	principal component analysis for both azimuth and incidence angle	water-level *(41)*	-10 to +25 s around P-wave onset	0.1-0.9
			iterative time-domain *(42)*		
C	P-to-S and S-to-P	MQS backazimuths and principal component analysis for incidence angles	iterative time-domain *(42)*	-20 to +50 s around the P-wave onset -150 to +50 s and -100 to +30 s around the S-wave onset	0.1-0.5 (low-frequency), 0.125-1 (high-frequency)
D	P-to-S and S-to-P	MQS backazimuths and principal component analysis for incidence angles	Wiener filter *(43,44)*	event dependent, between 28 and 40 s after P- or before S-arrival	event dependent: 0.1-0.8 or 0.3-0.8
E	P-to-S	MQS backazimuths and principal component analysis for incidence angles	iterative time domain *(42)*	30 s around P-wave onset	0.1-1
			extended-time multi-taper deconvolution *(45)*	50 s around P-wave onset	
F	P-to-S	MQS backazimuths and incidence angles from D	iterative time domain *(42)*	-15 to +80 s around the P-wave onset	event dependent: 0.1-0.8 or 0.3-0.8
G	P-to-S	MQS backazimuth and	water-level *(41,47)*	-3 to + 30 s around the P-wave onset	0.25-0.8

		incidence from ray parameter and assumed near-surface velocities			

Table S1. Summary of processing methods and parameters used by different groups to compute RFs.

Data set / lead team	SEIS sensors	Sol range	Number of events	Pre-processing	Comments
Continuous Noise Analysis / ISAE-IRAP	three components VBB-VEL channels	222 to 399	N.A.	Tick-noise and glitch removal	Deglitch by ISAE
HF events / ISAE-IRAP	three components VBB-VEL channels	N.A.	41	Tick-noise and glitch removal	Deglitch by ISAE / Event quality: B and C
VHF events / ISAE-IRAP	three components VBB-VEL channels	N.A.	14	Tick-noise and glitch removal	Deglitch by ISAE / Event quality: B and C
2.4Hz events / ISAE-IRAP	three components VBB-VEL channels	N.A.	69	Tick-noise and glitch removal	Deglitch by ISAE / Event quality: B and C
Continuous Noise Analysis / CSIC, IPGP	vertical component VBB-VEL channel	178 to 410	N.A.	Data selection based on RMS amplitude; band rejection filtering to remove lander modes and tick noise	PCC, linear and tf-PWS stacks
Continuous Noise Analysis / UMD	vertical components VBB-VEL channels	123 to 301	N.A.	Glitch removal: moving median or comb filter to remove tick noise	Consider day time vs. night time data
HF events / UMD	three components VBB-VEL channels	N.A.	48	moving median filter to remove tick noise	Event quality: B and C

Table S2. Summary of data sets and processing used by different groups to compute ACFs.

Description	Parameter	Quantity	Prior range
Crustal layer thickness (km)	δz	N_{lay}	0.1-50 km $\sum_i \delta z_i < 100\ km$
S-wave velocity of uppermost crustal layer (km/s)	V_S^0	1	1.0-4.0
S-wave velocity jump across crustal discontinuities (km/s)	δV_S	N_{lay}	0.0-1.5
S-wave velocity at 100 km depth (km/s)	V_S^{100}	1	4.0-4.5
Density- and P-to-S-wave velocity crustal ratios	ρ/V_S V_P/V_S	1 1	0.7-0.9 1.7-1.9
Source depth (km)	Z_{src}	1	40-100
Epicentral distance (°) [cf. Giardini et al., *21*]	Δ(S0235b) Δ(S0173a) Δ(S0183a)	1 1 1	25-30 25-30 40-60
total		$8 + 2 \cdot N_{lay}$	

Table S3. Overview of model parameters and the range of the uniformly distributed prior values for RF inversions described in section 3.1. N_{lay} denotes the number of crustal layers used in the crustal parametrization.

Parameter	Range
layer depth (km)	0-100
S-wave velocity (km/s)	1 - 5
V_P/V_S ratio	1.5 - 2.1

Table S4. Parameter range used in the inversion of RFs with method B (section S3.2). The same limits were used for all the layers in the respective model parameterization, and – for the velocity ranges – the half-space.

Parameter	Meaning	Range
E^*	Mantle effective activation energy	100-500 kJ/mol
V^*	Mantle effective activation volume	0-10 cm^3/mol
η_0	Mantle reference viscosity	10^{20}-10^{23} Pa s
Λ	Crustal HPE enrichment	5-30
Tm_0	Initial uppermost convecting mantle temperature	1700-2000 K
Tc_0	Initial CMB temperature	Tm_0 + [100-300] K

Table S5. **Ranges considered in the governing parameter space for the exploration of the thermo-chemical history of a Mars-like planet.** See text for further details.

	K (μg g^{-1})	Th (μg g^{-1})	U (μg g^{-1})	Λ	Reference
Martian crust					
Bulk crust	3,740	0.70	0.18	8.7 – 10.6	*31*
"GRS crust"	3,300	0.62	0.16*	7.8 – 9.5	*117*
2-layer crust	8,240 – 9,210	1.51 – 1.69	0.43 – 0.48	22	
3-layer crust	4,132 – 5,861	0.76 – 1.08	0.22 – 0.31	12 – 14	
Martian primitive mantle					
Wänke & Dreibus	305	0.056	0.016		*29*

*-assuming Th/U=3.8.

Table S6. Estimates of HPE concentrations in the Martian crust and primitive mantle. The conversion between the enrichment factors and concentrations of heat producing elements has been calculated assuming a bulk density of 3500 kg/m^3. For the crustal density the range of 2550-2850 kg m^{-3} and 2550-3100 kg m^{-3} has been used for the 2-layer and 3-layer crust, respectively.

Appendix C

Supporting Information for Chapter 4

Geophysical Research Letters

Supporting Information for

Joint inversion of receiver functions and apparent incidence angles to determine the crustal structure of Mars

Rakshit Joshi[1,5], Brigitte Knapmeyer-Endrun[2], Klaus Mosegaard[3], M. A. Wieczorek[4], Heiner Igel[5], Ulrich R. Christensen[1], Philippe Lognonné[6]

[1]Max-Planck-Institute for Solar System Research, Göttingen, Germany

[2]Bensberg Observatory, University of Cologne, Cologne, Germany

[3]Niels Bohr Institute, University of Copenhagen, Copenhagen, Denmark

[4]Université Côte d'Azur, Observatoire de la Côte d'Azur, CNRS, Laboratoire Lagrange, Nice, France

[5]Ludwig Maximilian University of Munich , Munich, Germany

[6]Université de Paris, Institut de Physique du Globe de Paris, CNRS, Paris, France

Introduction

This document provides information which includes the search criteria needed to retrieve the InSight and terrestrial seismic data used in the manuscript, 1D probability distributions for v_S, v_p/v_s ratio and noise parameters and synthetic examples. Terrestrial data for seismic stations VSU are publicly available and can be obtained from EIDA http://eida.gfz-potsdam.de/webdc3/

Contents of this file

Tables S1, S2, S3, S4
Figure S1, S2, S3, S4, S5

Event	Time	Lat. (°N)	Long. (°E)	Type	Quality	Filter Freq.
S0173a	2019-0523T02:19:33	3.45	164.48	LF	A	0.1-0.8
S0183a	2019-06-03T02:22:25	15.09	179.59	LF	B	0.1-0.8
S0235b	2019-07-26T12:19:16	11.59	163.79	BB	A	0.3-0.8
S0784a	2021-02-09T12:11:32	-	-	BB	B	0.3-0.8
S0809a	2021-03-07T11:09:26	5.40	165.55	LF	A	0.3-0.8
S0820a	2021-03-18T14:51:33	4.9	165.91	LF	A	0.3-0.8
S01048d	2021-11-07T22:04:04	-1.10	165.31	LF	A	0.12-0.8
S01133c	2022-02-03T08:08:25	3.89	165.89	BB	A	0.12-0.8

Table S1. Event information for InSight data

Station code	**Network code**	**Latitude (°N)**	**Longitude (°E)**
VSU	GE	58.462	26.7347

Table S2. Station information for seismic station VSU

Time (UTC)	Lat(°N)	Lon(°E)	Distance(°)	Dep(km)	Mag (M_w)
2010-12-23T14:00:32.033	53.13	171.16	65.0839	18	6.3
2006-10-01T09:06:02.032	46.47	153.24	66.5045	19	6.5
2006-09-30T17:50:23.005	46.35	153.17	66.5888	11	6.6
2009-01-15T17:49:39.007	46.86	155.15	66.7549	36	7.4
2008-05-25T19:28:20.090	52.23	176.16	66.8954	17	6.2
2006-11-16T06:20:20.077	46.36	154.47	66.9907	9	6
2007-01-13T04:23:21.016	46.24	154.52	67.1134	10	8.1
2010-07-18T05:56:44.091	52.88	-169.85	68.2012	14	6.6
2008-05-02T01:33:37.024	51.86	-177.53	68.2728	14	6.6
2006-08-26T23:46:18.052	51.38	-179.54	68.4368	35	5.7
2007-01-13T04:33:21.011	51.84	-176.28	68.4681	35	6
2006-08-26T23:40:39.047	51.33	-179.57	68.4806	35	5.7
2006-05-10T02:42:51.003	52.51	-169.26	68.6241	18	6.4
2006-07-08T20:40:00.098	51.21	-179.31	69.6377	22	6.6

Table S3. Event information for station VSU (small distance range case)

Time (UTC)	Lat(°N)	Lon(°E)	Distance(°)	Dep(km)	Mag (M_w)
2008-10-06T06:08:39.048	32.24	104.98	55.15	9	5.8
2006-05-11T17:22:51.096	23.31	94.31	59.73	30	5.6
2007-06-02T21:34:57.078	23.03	101.05	62.49	5	6.1
2007-07-30T22:42:05.063	19.31	95.61	62.70	14	5.6
2007-05-16T08:56:14.012	20.51	100.73	64.40	9	6.3
2010-03-30T16:54:46.073	13.67	92.83	65.99	34	6.7
2008-06-27T11:40:13.099	11.01	91.82	67.73	17	6.6
2008-06-28T12:54:46.036	10.85	91.71	67.81	15	6.1
2010-05-31T19:51:45.086	11.13	93.46	68.46	112	6.5
2010-06-12T19:26:50.046	7.88	91.94	70.47	35	7.5
2006-06-21T12:34:52.068	6.94	92.45	73.53	16	6.0
2007-10-04T12:40:31.013	2.54	92.9	75.54	35	6.2
2010-05-09T05:59:41.062	3.75	96.02	76.06	38	7.2
2006-08-11T20:54:14.037	2.4	96.35	77.39	22	6.2
2008-07-14T04:44:51.064	2.18	96.52	78.66	24	5.6
2010-04-06T22:15:01.058	2.38	97.05	79.16	31	7.8
2006-05-16T15:28:25.092	0.09	97.05	79.72	12	6.8
2009-09-30T10:16:09.025	-0.72	99.87	80.84	81	7.5
2009-08-16T07:38:21.070	-1.48	99.49	81.30	20	6.7
2007-09-20T08:31:14.049	-2	100.1	82.07	30	6.7
2008-02-25T21:02:18.042	-2.24	99.81	83.11	25	6.7
2009-10-01T01:52:27.033	-2.52	101.5	84.21	9	6.6
2008-05-18T12:17:23.034	-3.2	101.4	85.74	32	5.7

Table S4. Event information for station VSU (large distance range case)

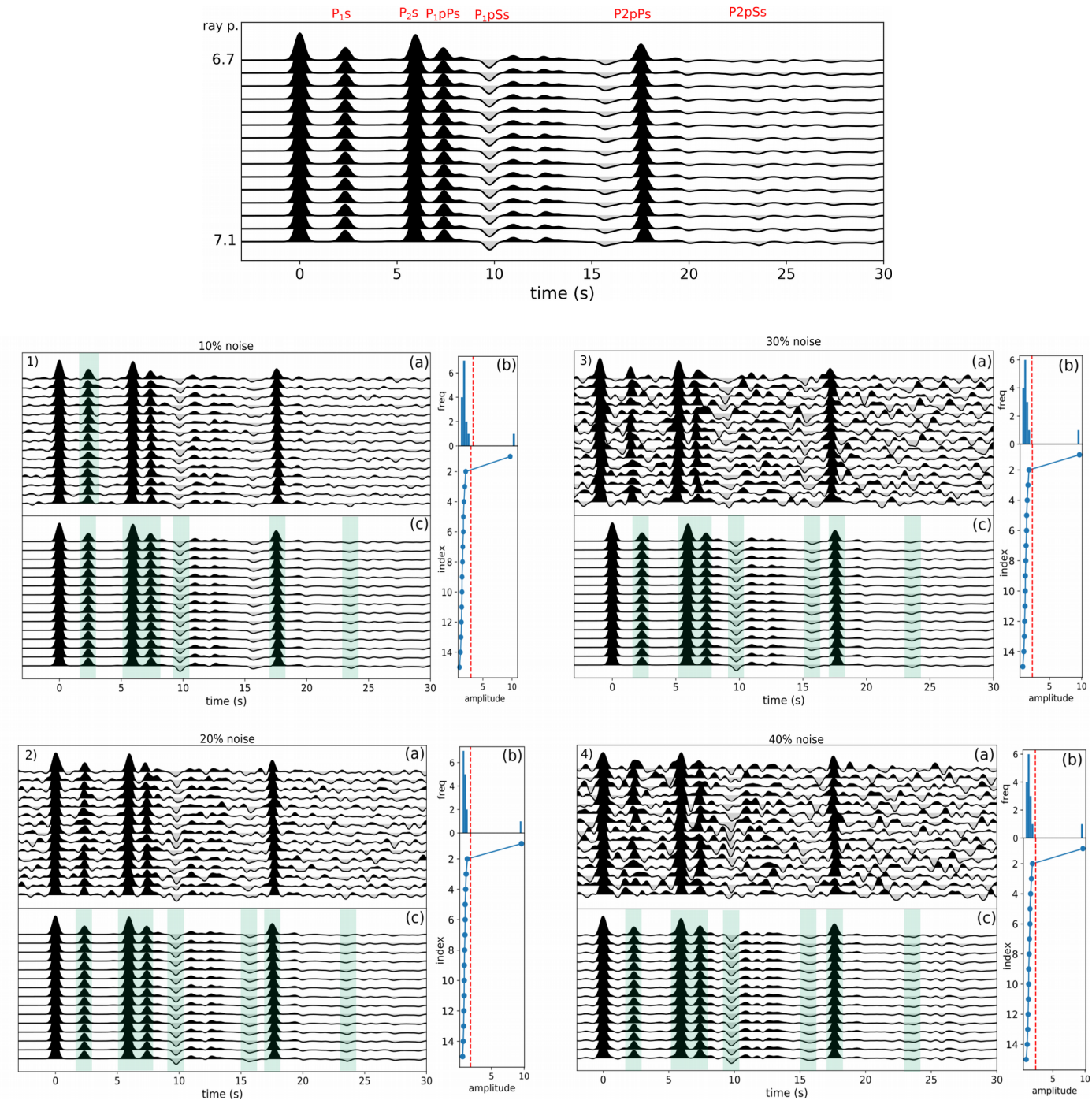

Figure S1. Synthetic example for small distance ranges: (top) original RFs computed from martian interior model C30VL_AKSNL (Ceylan et. al. (2017)) for ray parameters between 6.7 s/deg and 7.1 s/deg (bottom) (a) corruption of RFs by different noise levels. Noise was created using transverse component of terrestrial RFs and setting the maximum amplitude to the desired fraction of maximum amplitude of synthetic radial RFs (b) Singular values and their distribution (c) Reconstructed RFs

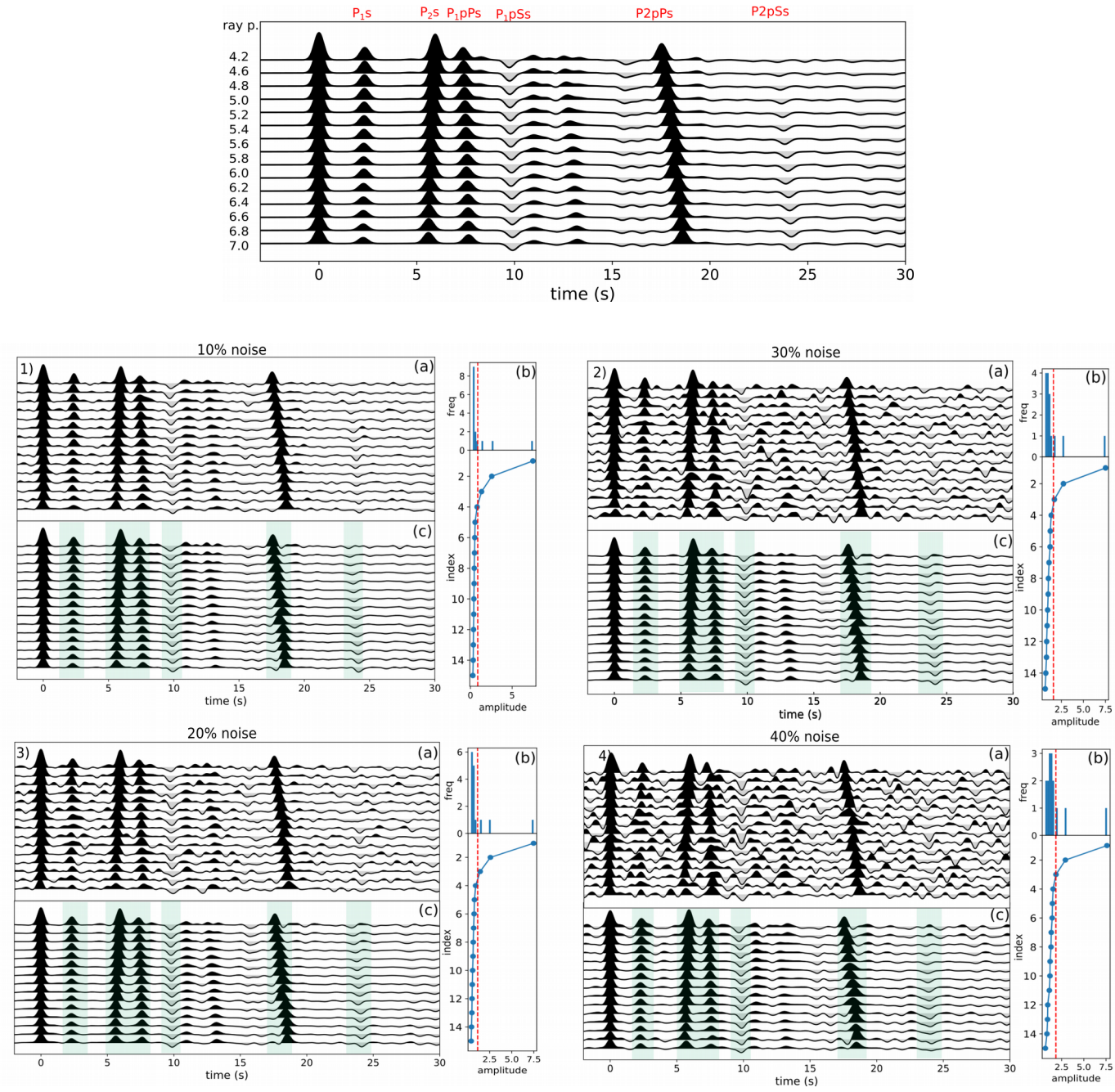

Figure S2. Synthetic example for large distance ranges: (top) original RFs computed from martian interior model C30VL_AKSNL (Ceylan et. al. (2017)) for ray parameters between 4.2 s/deg and 7.0 s/deg (bottom) (a) corruption of RFs by different noise levels. Noise was created using transverse component of terrestrial RFs and setting their maximum amplitude to the desired fraction of maximum amplitude of synthetic radial RFs (b) Singular values and their distribution (c) Reconstructed RFs

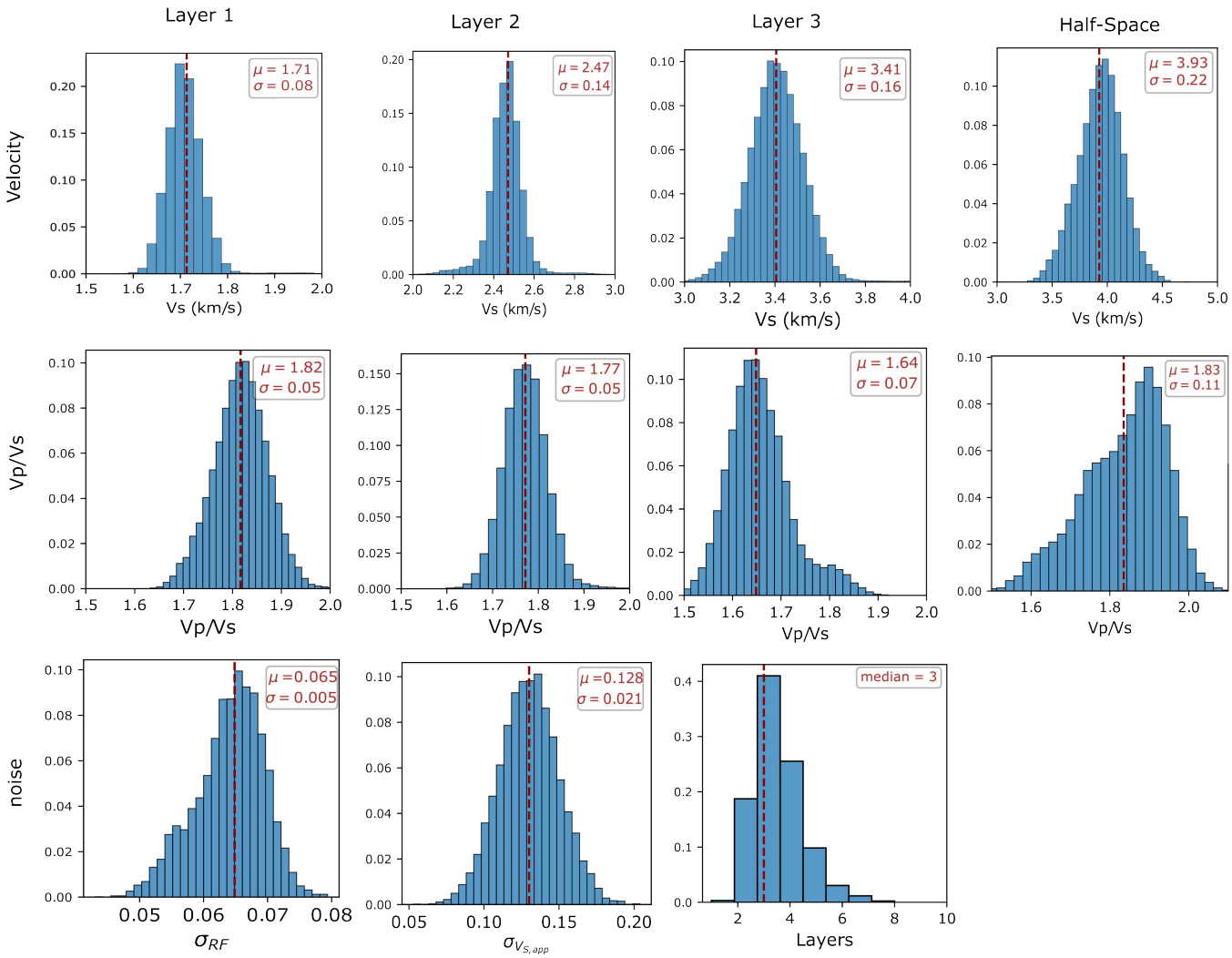

Figure S3. 1D distributions of model parameters

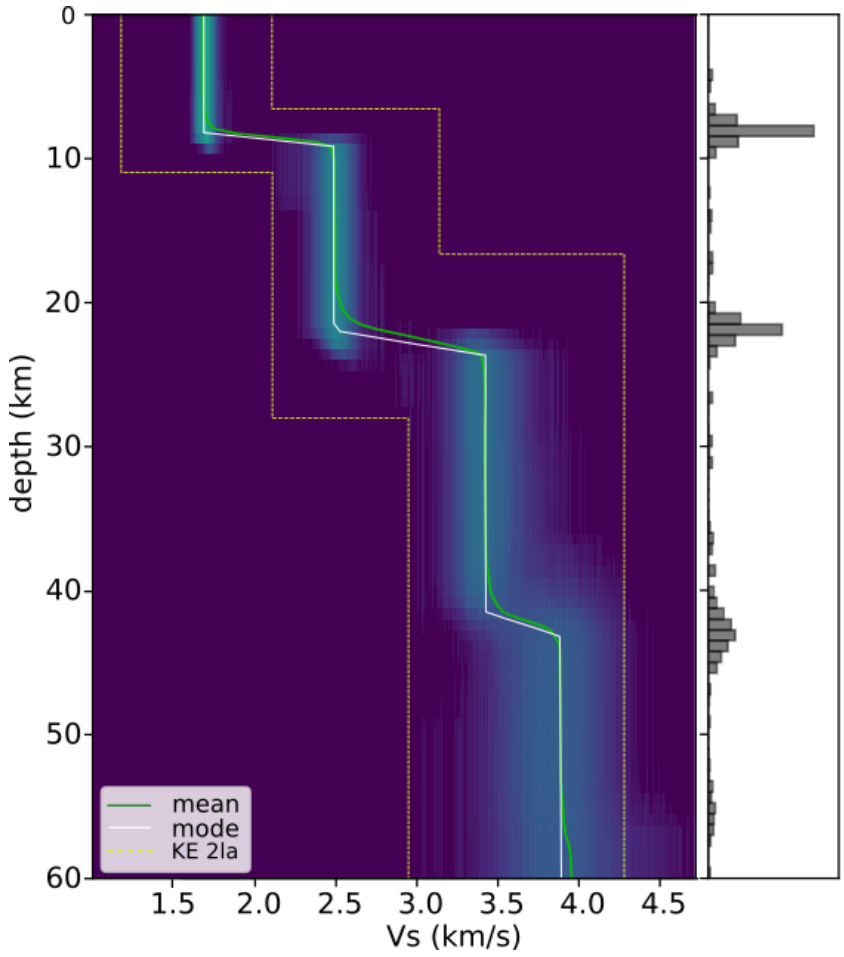

Figure S4. Posterior density of resulting Vs profiles and with histograms for interface depth. KE 2la represents the 2σ bounds of the two-layer ensemble from Knapmeyer-Endrun et al. (2021)

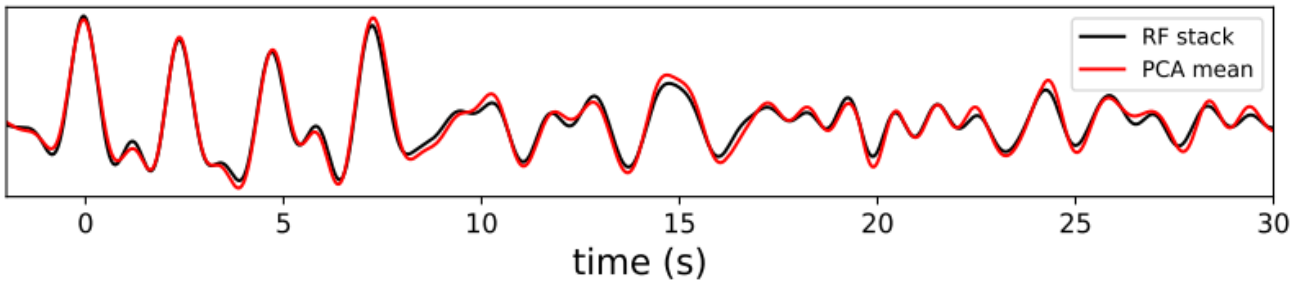

Figure S5. Comparison of the mean RF with the mean PCA filtered waveforms

Algorithm for PCA and optimal threshold truncation

1) Creation of the data matrix: If there are m waveforms with n time samples each, a data-matrix $\boldsymbol{Y}_{n\times m}$ can be formed as:

$$\boldsymbol{Y} = [y_1, y_2, \ldots, y_m] = \begin{bmatrix} y_{11} & \cdots & y_{1n} \\ \vdots & \ddots & \vdots \\ y_{n1} & \cdots & y_{nm} \end{bmatrix}$$

2) Calculation of the covariance matrix $\boldsymbol{M}$:
$\boldsymbol{M} = \frac{1}{m-1}\Sigma_{j=1}^{m}\boldsymbol{y_j}{\boldsymbol{y_j}}^T = \frac{1}{m-1}YY^T$

3) Eigenvalue decomposition of covariance matrix $\boldsymbol{M}$:

$$\boldsymbol{M} = \boldsymbol{U}\boldsymbol{\Lambda}\boldsymbol{U}^T = [u_1, u_2, \ldots, u_m] \begin{bmatrix} \lambda_{11} & \cdots & \lambda_{1n} \\ \vdots & \ddots & \vdots \\ \lambda_{n1} & \cdots & \lambda_{nm} \end{bmatrix} [u_1, u_2, \ldots, u_n]^T$$

Here, Λ represents the eigenvalues sorted in descending and arranged into a corresponding eigenvalue matrix $\Lambda = Diag\,[\lambda_1, \lambda_2, \ldots, \lambda_n]$, and $\boldsymbol{U}$ denotes the corresponding eigenvectors arranged into a matrix. The singular values of Y are the square roots of the eigenvalues, hence the singular value matrix $\Sigma = \sqrt{\Lambda}$ The eigenvectors $\boldsymbol{U} = [u_1, u_2, \ldots, u_m]$ are normalized to a unit magnitude and arranged into columns. This forms the right singular vector.

4) Calculation of left singular vector $\boldsymbol{V}$: The covariance matrix $\boldsymbol{M}$and the right singular vector $\boldsymbol{U}$ are then used to from $\boldsymbol{V} = \boldsymbol{M}\Sigma^T\boldsymbol{U}$. $\boldsymbol{V} = [v_1, v_2, \ldots, v_m]$ is normalized to unit magnitude and forms the left singular vector.
The data matrix $\boldsymbol{Y}$ can now be expanded as: $\boldsymbol{Y} = \boldsymbol{U}\boldsymbol{\Sigma}\boldsymbol{V}^T$

5) Estimation of noise level $\sigma(Y)$: We plug in the values of λ_{med} and μ_{MP} into Eq 8. Here, λ_{med} is the median of the square roots of eigenvalues (singular values of Y), and μ_{MP} is is approximated by integrating the singular value spectrum over the minimum and maximum values of the bulk.

6) Calculation of threshold $\tau_\star$: We first calculate the value of $\omega(\gamma)$: $\omega(\gamma) = 0.56\gamma^3 - 0.95\gamma^2 + 1.82\gamma + 1.43$. Here γ represents the matrix aspect ratio m/n. This value is then multiplied by λ_{med}. This gives the threshold: $\hat{\tau_\star} = \omega(\gamma) \cdot \lambda_{med}$

7) Data reconstruction using PCs above threshold: A new singular value matrix $\bar{\boldsymbol{\Sigma}}$ is formed by replacing all the singular values below the threshold by 0. The approximate data can then be calculated by: $X(\boldsymbol{Y}) = \boldsymbol{U}\bar{\boldsymbol{\Sigma}}\boldsymbol{V}^T$

References

Ceylan, S., van Driel, M., Euchner, F. *et al.* From Initial Models of Seismicity, Structure and Noise to Synthetic Seismograms for Mars. *Space Sci Rev* 211, 595–610 (2017). https://doi.org/10.1007/s11214-017-0380-6

Bibliography

K. Aki and P. G. Richards. *Quantitative seismology*. 2002.

K. M. Al-Yahya. Application of the partial Karuhen-Loève transform to suppress random noise in seismic sections 1. *Geophysical prospecting*, 39(1):77–93, 1991.

C. J. Ammon. The isolation of receiver effects from teleseismic P waveforms. *Bull. Seismol. Soc. Am*, 81(6):2504–2510, 1991.

C. J. Ammon, G. E. Randall, and G. Zandt. On the nonuniqueness of receiver function inversions. *Journal of Geophysical Research: Solid Earth*, 95(B10):15303–15318, 1990.

D. L. Anderson, W. Miller, G. Latham, Y. Nakamura, M. Toksöz, A. Dainty, F. Duennebier, A. R. Lazarewicz, R. Kovach, and T. Knight. Seismology on Mars. *Journal of Geophysical Research*, 82(28):4524–4546, 1977.

J. Andrews and A. Deuss. Detailed nature of the 660 km region of the mantle from global receiver function data. *Journal of Geophysical Research: Solid Earth*, 113(B6), 2008.

J. Baik, G. B. Arous, and S. Péché. Phase transition of the largest eigenvalue for non-null complex sample covariance matrices. *The Annals of Probability*, 33(5):1643–1697, 2005.

W. Banerdt, S. Smrekar, P. Lognonné, T. Spohn, S. Asmar, D. Banfield, L. Boschi, U. Christensen, V. Dehant, W. Folkner, et al. InSight: a discovery mission to explore the interior of Mars. In *44th Annual Lunar and Planetary Science Conference*, number 1719, page 1915, 2013.

D. Banfield, J. Rodriguez-Manfredi, C. Russell, K. Rowe, D. Leneman, H. Lai, P. Cruce, J. Means, C. Johnson, A. Mittelholz, et al. InSight auxiliary payload sensor suite (APSS). *Space Science Reviews*, 215(1):1–33, 2019.

D. Banfield, A. Spiga, C. Newman, F. Forget, M. Lemmon, R. Lorenz, N. Murdoch, D. Viudez-Moreiras, J. Pla-Garcia, R. F. Garcia, et al. The atmosphere of Mars as observed by InSight. *Nature Geoscience*, 13(3):190–198, 2020.

D. Baratoux, H. Samuel, C. Michaut, M. J. Toplis, M. Monnereau, M. Wieczorek, R. Garcia, and K. Kurita. Petrological constraints on the density of the Martian crust. *Journal of Geophysical Research: Planets*, 119(7):1707–1727, 2014.

N. Barlow. Mars: An introduction to its interior, surface and atmosphere. *Mars: An Introduction to its Interior*, 2014.

T. Bayes. LII. An essay towards solving a problem in the doctrine of chances. By the late Rev. Mr. Bayes, FRS communicated by Mr. Price, in a letter to John Canton, AMFR S. *Philosophical transactions of the Royal Society of London*, (53):370–418, 1763.

M. Bekara and M. Van der Baan. Local singular value decomposition for signal enhancement of seismic data. *Geophysics*, 72(2):V59–V65, 2007.

F. Benaych-Georges and R. R. Nadakuditi. The singular values and vectors of low rank perturbations of large rectangular random matrices. *Journal of Multivariate Analysis*, 111:120–135, 2012.

C. M. Bertka and Y. Fei. Mineralogy of the Martian interior up to core-mantle boundary pressures. *Journal of Geophysical Research: Solid Earth*, 102(B3):5251–5264, 1997.

C. M. Bertka and Y. Fei. Density profile of an SNC model Martian interior and the moment-of-inertia factor of Mars. *Earth and Planetary Science Letters*, 157(1-2):79–88, 1998a.

C. M. Bertka and Y. Fei. Implications of Mars Pathfinder data for the accretion history of the terrestrial planets. *Science*, 281(5384):1838–1840, 1998b.

I. Bianchi, J. Park, N. Piana Agostinetti, and V. Levin. Mapping seismic anisotropy using harmonic decomposition of receiver functions: An application to Northern Apennines, Italy. *Journal of Geophysical Research: Solid Earth*, 115(B12), 2010.

B. G. Bills and A. J. Ferrari. Mars topography harmonics and geophysical implications. *Journal of Geophysical Research: Solid Earth*, 83(B7):3497–3508, 1978.

T. Bodin, M. Sambridge, H. Tkalčić, P. Arroucau, K. Gallagher, and N. Rawlinson. Transdimensional inversion of receiver functions and surface wave dispersion. *Journal of Geophysical Research: Solid Earth*, 117(B2), 2012.

M. Böse, J. F. Clinton, S. Ceylan, F. Euchner, M. van Driel, A. Khan, D. Giardini, P. Lognonné, and W. B. Banerdt. A probabilistic framework for single-station location of seismicity on Earth and Mars. *Physics of the Earth and Planetary Interiors*, 262: 48–65, 2017.

M. Böse, D. Giardini, S. Stähler, S. Ceylan, J. F. Clinton, M. van Driel, A. Khan, F. Euchner, P. Lognonné, and W. B. Banerdt. Magnitude Scales for MarsquakesMagnitude Scales for Marsquakes. *Bulletin of the Seismological Society of America*, 108(5A):2764–2777, 2018.

N. Brinkman, S. C. Stähler, D. Giardini, C. Schmelzbach, A. Khan, A. Jacob, N. Fuji, C. Perrin, P. Lognonné, E. Beucler, et al. First focal mechanisms of marsquakes. *Journal of Geophysical Research: Planets*, 126(4):e2020JE006546, 2021.

S. Ceylan, J. F. Clinton, D. Giardini, M. Böse, C. Charalambous, M. van Driel, A. Horleston, T. Kawamura, A. Khan, G. Orhand-Mainsant, J.-R. Scholz, S. C. Stähler, F. Euchner, W. B. Banerdt, P. Lognonné, D. Banfield, E. Beucler, R. F. Garcia, S. Kedar, M. P. Panning, W. T. Pike, S. E. Smrekar, A. Spiga, N. L. Dahmen, K. Hurst, A. E. Stott, R. D. Lorenz, M. Schimmel, E. Stutzmann, J. ten Pierick, V. Conejero, C. Pardo, and C. Perrin. Companion guide to the marsquake catalog from InSight, Sols 0–478: Data content and non-seismic events. *Physics of the Earth and Planetary Interiors*, 310: 106597, 2021. ISSN 0031-9201. doi: https://doi.org/10.1016/j.pepi.2020.106597.

C. Chai, C. J. Ammon, M. Maceira, and R. B. Herrmann. Inverting interpolated receiver functions with surface wave dispersion and gravity: Application to the western US and adjacent Canada and Mexico. *Geophysical Research Letters*, 42(11):4359–4366, 2015.

S.-J. Chang, C.-E. Baag, and C. A. Langston. Joint analysis of teleseismic receiver functions and surface wave dispersion using the genetic algorithm. *Bulletin of the Seismological Society of America*, 94(2):691–704, 2004.

J. Chong, S. Ni, R. Chu, and P. Somerville. Joint Inversion of Body-Wave Receiver Function and Rayleigh-Wave Ellipticity. *Bulletin of the Seismological Society of America*, 106(2): 537–551, 2016.

J. Clinton, D. Giardini, M. Böse, S. Ceylan, M. van Driel, F. Euchner, R. F. Garcia, S. Kedar, A. Khan, S. C. Stähler, et al. The Marsquake service: Securing daily analysis of SEIS data and building the Martian seismicity catalogue for InSight. *Space Science Reviews*, 214(8):1–33, 2018.

J. F. Clinton, S. Ceylan, M. van Driel, D. Giardini, S. C. Stähler, M. Böse, C. Charalambous, N. L. Dahmen, A. Horleston, T. Kawamura, et al. The Marsquake catalogue from InSight, Sols 0–478. *Physics of the Earth and Planetary Interiors*, 310:106595, 2021.

N. L. Dahmen, J. F. Clinton, S. Ceylan, M. van Driel, D. Giardini, A. Khan, S. C. Stähler, M. Böse, C. Charalambous, A. Horleston, et al. Super high frequency events: A new class of events recorded by the InSight seismometers on Mars. *Journal of Geophysical Research: Planets*, 126(2):e2020JE006599, 2021a.

N. L. Dahmen, G. Zenhäusern, J. F. Clinton, D. Giardini, S. C. Stähler, S. Ceylan, C. Charalambous, M. van Driel, K. J. Hurst, S. Kedar, et al. Resonances and lander modes observed by InSight on Mars (1–9 Hz). *Bulletin of the Seismological Society of America*, 111(6):2924–2950, 2021b.

G. Dreibus and H. Wänke. Accretion of the Earth and the inner planets. *Geochemistry and Cosmochemistry*, pages 1–20, 1984.

Z. Du and G. Foulger. The crustal structure beneath the northwest fjords, Iceland, from receiver functions and surface waves. *Geophysical Journal International*, 139(2):419–432, 1999.

F. J. Dyson. A Brownian-motion model for the eigenvalues of a random matrix. *Journal of Mathematical Physics*, 3(6):1191–1198, 1962.

L. T. Elkins-Tanton, E. Parmentier, and P. Hess. Magma ocean fractional crystallization and cumulate overturn in terrestrial planets: Implications for Mars. *Meteoritics & Planetary Science*, 38(12):1753–1771, 2003.

R. W. England and J. Ebbing. Crustal structure of central Norway and Sweden from integrated modelling of teleseismic receiver functions and the gravity anomaly. *Geophysical Journal International*, 191(1):1–11, 2012.

V. Farra and L. Vinnik. Upper mantle stratification by P and S receiver functions. *Geophysical Journal International*, 141(3):699–712, 2000.

Y. Fei, J. Li, C. M. Bertka, and C. T. Prewitt. Structure type and bulk modulus of Fe3S, a new iron-sulfur compound. *American Mineralogist*, 85(11-12):1830–1833, 2000.

W. Folkner, C. Yoder, D. Yuan, E. Standish, and R. Preston. Interior structure and seasonal mass redistribution of Mars from radio tracking of Mars Pathfinder. *Science*, 278(5344):1749–1752, 1997.

W. M. Folkner, V. Dehant, S. Le Maistre, M. Yseboodt, A. Rivoldini, T. Van Hoolst, S. W. Asmar, and M. P. Golombek. The rotation and interior structure experiment on the InSight mission to Mars. *Space Science Reviews*, 214(5):1–16, 2018.

A. W. Frederiksen, H. Folsom, and G. Zandt. Neighbourhood inversion of teleseismic Ps conversions for anisotropy and layer dip. *Geophysical Journal International*, 155(1): 200–212, 2003.

S. L. M. Freire and T. J. Ulrych. Application of singular value decomposition to vertical seismic profiling. *Geophysics*, 53(6):778–785, 1988. doi: 10.1190/1.1442513.

J. Gagnepain-Beyneix, P. Lognonné, H. Chenet, D. Lombardi, and T. Spohn. A seismic model of the Lunar mantle and constraints on temperature and mineralogy. *Physics of the Earth and Planetary Interiors*, 159(3):140–166, 2006. ISSN 0031-9201. doi: https://doi.org/10.1016/j.pepi.2006.05.009.

W. H. Geissler, F. Sodoudi, and R. Kind. Thickness of the central and eastern European lithosphere as seen by S receiver functions. *Geophysical Journal International*, 181(2): 604–634, 2010.

D. Giardini, P. Lognonné, W. B. Banerdt, W. T. Pike, U. Christensen, S. Ceylan, J. F. Clinton, M. van Driel, S. C. Stähler, M. Böse, et al. The seismicity of Mars. *Nature Geoscience*, 13(3):205–212, 2020.

M. P. Golombek, W. B. Banerdt, K. L. Tanaka, and D. M. Tralli. A prediction of Mars seismicity from surface faulting. *Science*, 258(5084):979–981, 1992.

S. Goossens, T. J. Sabaka, A. Genova, E. Mazarico, J. B. Nicholas, and G. A. Neumann. Evidence for a low bulk crustal density for Mars from gravity and topography. *Geophysical research letters*, 44(15):7686–7694, 2017.

M. Grad, T. Tiira, and E. W. Group. The Moho depth map of the European Plate. *Geophysical journal international*, 176(1):279–292, 2009.

K. Hannemann, F. Krüger, T. Dahm, and D. Lange. Oceanic lithospheric S-wave velocities from the analysis of P-wave polarization at the ocean floor. *Geophysical Supplements to the Monthly Notices of the Royal Astronomical Society*, 207(3):1796–1817, 2016.

K. Hasselmann. A statistical analysis of the generation of microseisms. *Reviews of Geophysics*, 1(2):177–210, 1963.

M. Hobiger, M. Hallo, C. Schmelzbach, S. Stähler, D. Fäh, D. Giardini, M. Golombek, J. Clinton, N. Dahmen, G. Zenhäusern, et al. The shallow structure of Mars at the InSight landing site from inversion of ambient vibrations. *Nature communications*, 12 (1):1–13, 2021.

InSight Marsquake Service. Mars Seismic Catalogue, InSight Mission; V10 2022-04-01, 2022.

G. Jackson, I. Mason, and S. Greenhalgh. Principal component transforms of triaxial recordings by singular value decomposition. *Geophysics*, 56(4):528–533, 1991.

B. H. Jacobsen and L. Svenningsen. Enhanced uniqueness and linearity of receiver function inversion. *Bulletin of the Seismological Society of America*, 98(4):1756–1767, 2008.

I. F. Jones. *Applications of the Karhunen-Loeve transform in reflection seismology*. PhD thesis, University of British Columbia, 1985.

I. F. Jones and S. Levy. Signal-to-noise ratio enhancement in multichannel seismic data via the Karhunen-Loeve transform. *Geophysical prospecting*, 35(1):12–32, 1987.

J. Julià, J. Vila, and R. Macià. The receiver structure beneath the Ebro basin, Iberian Peninsula. *Bulletin of the Seismological Society of America*, 88(6):1538–1547, 1998.

J. Julia, C. Ammon, R. Herrmann, and A. M. Correig. Joint inversion of receiver function and surface wave dispersion observations. *Geophysical Journal International*, 143(1): 99–112, 2000.

W. M. Kaula. The moment of inertia of Mars. *Geophysical Research Letters*, 6(3):194–196, 1979.

A. Khan, M. van Driel, M. Böse, D. Giardini, S. Ceylan, J. Yan, J. Clinton, F. Euchner, P. Lognonné, N. Murdoch, et al. Single-station and single-event marsquake location and inversion for structure using synthetic Martian waveforms. *Physics of the Earth and Planetary Interiors*, 258:28–42, 2016.

A. Khan, C. Liebske, A. Rozel, A. Rivoldini, F. Nimmo, J. Connolly, A.-C. Plesa, and D. Giardini. A geophysical perspective on the bulk composition of Mars. *Journal of Geophysical Research: Planets*, 123(2):575–611, 2018.

K. Kieling, D. Roessler, and F. Krueger. Receiver function study in northern Sumatra and the Malaysian peninsula. *Journal of Seismology*, 15(2):235–259, 2011.

D. Kim, P. Davis, V. Lekić, R. Maguire, N. Compaire, M. Schimmel, E. Stutzmann, J. CE Irving, P. Lognonné, J.-R. Scholz, et al. Potential pitfalls in the analysis and structural interpretation of seismic data from the Mars InSight mission. *Bulletin of the Seismological Society of America*, 111(6):2982–3002, 2021.

R. Kind, G. Kosarev, and N. Petersen. Receiver functions at the stations of the German Regional Seismic Network (GRSN). *Geophysical Journal International*, 121(1):191–202, 1995.

R. Kind, X. Yuan, and P. Kumar. Seismic receiver functions and the lithosphere–asthenosphere boundary. *Tectonophysics*, 536:25–43, 2012.

T. Kleine, C. Münker, K. Mezger, and H. Palme. Rapid accretion and early core formation on asteroids and the terrestrial planets from Hf–W chronometry. *Nature*, 418(6901): 952–955, 2002.

M. Knapmeyer, J. Oberst, E. Hauber, M. Wählisch, C. Deuchler, and R. Wagner. Working models for spatial distribution and level of Mars' seismicity. *Journal of Geophysical Research: Planets*, 111(E11), 2006.

M. Knapmeyer, S. C. Stähler, I. Daubar, F. Forget, A. Spiga, T. Pierron, M. van Driel, D. Banfield, E. Hauber, M. Grott, et al. Seasonal seismic activity on Mars. *Earth and Planetary Science Letters*, 576:117171, 2021.

B. Knapmeyer-Endrun, F. Krüger, W. H. Geissler, P. W. Group, et al. Upper mantle structure across the Trans-European Suture Zone imaged by S-receiver functions. *Earth and Planetary Science Letters*, 458:429–441, 2017.

B. Knapmeyer-Endrun, S. Ceylan, and M. van Driel. Crustal S-wave velocity from apparent incidence angles: a case study in preparation for InSight. *Space Science Reviews*, 214 (5):1–40, 2018.

A. S. Konopliv, S. W. Asmar, W. M. Folkner, Ö. Karatekin, D. C. Nunes, S. E. Smrekar, C. F. Yoder, and M. T. Zuber. Mars high resolution gravity fields from MRO, Mars seasonal gravity, and other dynamical parameters. *Icarus*, 211(1):401–428, 2011.

A. S. Konopliv, R. S. Park, and W. M. Folkner. An improved JPL Mars gravity field and orientation from Mars orbiter and lander tracking data. *Icarus*, 274:253–260, 2016.

G. Kosarev, L. Makeyeva, and L. Vinnik. Inversion of teleseismic P-wave particle motions for crustal structure in Fennoscandia. *Physics of the Earth and planetary interiors*, 47: 11–24, 1987.

C. A. Langston. Structure under Mount Rainier, Washington, inferred from teleseismic body waves. *Journal of Geophysical Research: Solid Earth*, 84(B9):4749–4762, 1979.

J. F. Lawrence and P. M. Shearer. A global study of transition zone thickness using receiver functions. *Journal of Geophysical Research: Solid Earth*, 111(B6), 2006.

J. F. Lawrence, D. A. Wiens, A. A. Nyblade, S. Anandakrishnan, P. J. Shore, and D. Voigt. Crust and upper mantle structure of the Transantarctic Mountains and surrounding regions from receiver functions, surface waves, and gravity: implications for uplift models. *Geochemistry, Geophysics, Geosystems*, 7(10), 2006.

T. Lay and T. C. Wallace. *Modern global seismology*. Elsevier, 1995.

S. Le Maistre. *The rotation of Mars and Phobos from Earth-based radio-tracking observations of a lander*. PhD thesis, UCL-Université Catholique de Louvain, 2013.

D.-C. Lee and A. N. Halliday. Core formation on Mars and differentiated asteroids. *Nature*, 388(6645):854–857, 1997.

V. Levin and J. Park. Crustal anisotropy in the Ural Mountains foredeep from teleseismic receiver functions. *Geophysical Research Letters*, 24(11):1283–1286, 1997.

V. Levin and J. Park. P-SH conversions in layered media with hexagonally symmetric anisotropy: a cookbook. In *Geodynamics of Lithosphere & Earth's Mantle*, pages 669–697. Springer, 1998.

V. Levin, J. Park, M. Brandon, J. Lees, V. Peyton, E. Gordeev, and A. Ozerov. Crust and upper mantle of Kamchatka from teleseismic receiver functions. *Tectonophysics*, 358 (1-4):233–265, 2002.

X. Liu. Ground roll supression using the Karhunen-Loeve transform. *Geophysics*, 64(2): 564–566, 1999.

K. Lodders and B. Fegley Jr. An oxygen isotope model for the composition of Mars. *Icarus*, 126(2):373–394, 1997.

P. Lognonné, J. Gagnepain-Beyneix, and H. Chenet. A new seismic model of the Moon: implications for structure, thermal evolution and formation of the Moon. *Earth and Planetary Science Letters*, 211(1-2):27–44, 2003.

P. Lognonné, W. B. Banerdt, D. Giardini, W. T. Pike, U. Christensen, P. Laudet, S. De Raucourt, P. Zweifel, S. Calcutt, M. Bierwirth, et al. SEIS: InSight's seismic experiment for internal structure of Mars. *Space Science Reviews*, 215(1):1–170, 2019.

P. Lognonné, W. B. Banerdt, W. Pike, D. Giardini, U. Christensen, R. F. Garcia, T. Kawamura, S. Kedar, B. Knapmeyer-Endrun, L. Margerin, et al. Constraints on the shallow elastic and anelastic structure of Mars from InSight seismic data. *Nature Geoscience*, 13 (3):213–220, 2020.

P. Lowell. First photographs of the canals of Mars. *Proceedings of the Royal Society of London. Series A, Containing Papers of a Mathematical and Physical Character*, 77 (515):132–135, 1906.

P. C. Mahalanobis. On the generalized distance in statistics. National Institute of Science of India, 1936.

A. Malinverno. Parsimonious Bayesian Markov chain Monte Carlo inversion in a nonlinear geophysical problem. *Geophysical Journal International*, 151(3):675–688, 2002.

S. G. Mangino, G. Zandt, and C. J. Ammon. The receiver structure beneath Mina, Nevada. *Bulletin of the Seismological Society of America*, 83(2):542–560, 1993.

P. J. McGovern, S. C. Solomon, D. E. Smith, M. T. Zuber, M. Simons, M. A. Wieczorek, R. J. Phillips, G. A. Neumann, O. Aharonson, and J. W. Head. Localized gravity/topography admittance and correlation spectra on Mars: Implications for regional and global evolution. *Journal of Geophysical Research: Planets*, 107(E12):19–1, 2002.

P. J. McGovern, S. C. Solomon, D. E. Smith, M. T. Zuber, M. Simons, M. A. Wieczorek, R. J. Phillips, G. A. Neumann, O. Aharonson, and J. W. Head. Correction to "Localized gravity/topography admittance and correlation spectra on Mars: Implications for regional and global evolution". *Journal of Geophysical Research: Planets*, 109(E7), 2004.

D. McKenzie, D. N. Barnett, and D.-N. Yuan. The relationship between Martian gravity and topography. *Earth and Planetary Science Letters*, 195(1-2):1–16, 2002.

W. Menke. The resolving power of cross-borehole tomography. *Geophysical Research Letters*, 11(2):105–108, 1984.

D. Mimoun, N. Murdoch, P. Lognonné, K. Hurst, W. T. Pike, J. Hurley, T. Nébut, and W. B. Banerdt. The noise model of the SEIS seismometer of the InSight mission to Mars. *Space Science Reviews*, 211(1):383–428, 2017.

K. Mosegaard and A. Tarantola. Monte Carlo sampling of solutions to inverse problems. *Journal of Geophysical Research: Solid Earth*, 100(B7):12431–12447, 1995.

G. Neumann, M. Zuber, M. A. Wieczorek, P. McGovern, F. G. Lemoine, and D. Smith. Crustal structure of Mars from gravity and topography. *Journal of Geophysical Research: Planets*, 109(E8), 2004.

F. Nimmo. Constraining the crustal thickness on Mercury from viscous topographic relaxation. *Geophysical research letters*, 29(5):7–1, 2002.

T. J. Owens, S. R. Taylor, and G. Zandt. Crustal structure at regional seismic test network stations determined from inversion of broadband teleseismic P waveforms. *Bulletin of the Seismological Society of America*, 77(2):631–662, 1987.

A. A. Ozacar, H. Gilbert, and G. Zandt. Upper mantle discontinuity structure beneath East Anatolian Plateau (Turkey) from receiver functions. *Earth and Planetary Science Letters*, 269(3-4):427–435, 2008.

S. Özalaybey, M. K. Savage, A. F. Sheehan, J. N. Louie, and J. N. Brune. Shear-wave velocity structure in the northern Basin and Range province from the combined analysis of receiver functions and surface waves. *Bulletin of the Seismological Society of America*, 87(1):183–199, 1997.

M. P. Panning, É. Beucler, M. Drilleau, A. Mocquet, P. Lognonné, and W. B. Banerdt. Verifying single-station seismic approaches using Earth-based data: Preparation for data return from the InSight mission to Mars. *Icarus*, 248:230–242, 2015.

J. Park and V. Levin. Receiver functions from multiple-taper spectral correlation estimates. *Bulletin of the Seismological Society of America*, 90(6):1507–1520, 2000.

S. Park and M. Ishii. Near-surface compressional and shear wave speeds constrained by body-wave polarization analysis. *Geophysical Journal International*, 213(3):1559–1571, 2018.

M. Pauer and D. Breuer. Constraints on the maximum crustal density from gravity–topography modeling: Applications to the southern highlands of Mars. *Earth and Planetary Science Letters*, 276(3-4):253–261, 2008.

G. B. M. Pedersen. Chaotic Terrain (Mars). In *Encyclopedia of Planetary Landforms*, pages 1–6. Springer New York New York, NY, 2014.

K. A. Pesce. *Comparison of receiver function deconvolution techniques*. PhD thesis, Massachusetts Institute of Technology, 2010.

R. J. Phillips and R. E. Grimm. Martian seismicity. In *Lunar and Planetary Science Conference*, volume 22, 1991.

R. A. Phinney. Structure of the Earth's crust from spectral behavior of long-period body waves. *Journal of Geophysical Research*, 69(14):2997–3017, 1964.

A.-C. Plesa, M. Grott, N. Tosi, D. Breuer, T. Spohn, and M. Wieczorek. How large are present-day heat flux variations across the surface of Mars? *Journal of Geophysical Research: Planets*, 121(12):2386–2403, 2016.

J. Rhie and B. Romanowicz. A study of the relation between ocean storms and the Earth's hum. *Geochemistry, Geophysics, Geosystems*, 7(10), 2006.

G. P. Roberts, B. Matthews, C. Bristow, L. Guerrieri, and J. Vetterlein. Possible evidence of paleomarsquakes from fallen boulder populations, Cerberus Fossae, Mars. *Journal of Geophysical Research: Planets*, 117(E2), 2012.

C. A. Robinson. The crustal dichotomy of Mars. *Earth, Moon, and Planets*, 69(3):249–269, 1995.

M. Sambridge. Geophysical inversion with a neighbourhood algorithm—I. Searching a parameter space. *Geophysical journal international*, 138(2):479–494, 1999.

C. Sanloup, A. Jambon, and P. Gillet. A simple chondritic model of Mars. *Physics of the Earth and Planetary Interiors*, 112(1-2):43–54, 1999.

B. Savage and P. G. Silver. Evidence for a compositional boundary within the lithospheric mantle beneath the Kalahari craton from S receiver functions. *Earth and Planetary Science Letters*, 272(3-4):600–609, 2008.

M. K. Savage. Lower crustal anisotropy or dipping boundaries? Effects on receiver functions and a case study in New Zealand. *Journal of Geophysical Research: Solid Earth*, 103 (B7):15069–15087, 1998.

C. Schiffer, R. Stephenson, G. N. Oakey, and B. H. Jacobsen. The crustal structure of Ellesmere Island, Arctic Canada—teleseismic mapping across a remote intraplate orogenic belt. *Geophysical Journal International*, 204(3):1579–1600, 2016.

C. Schiffer, T. Eken, S. Rondenay, and T. Taymaz. Localized crustal deformation along the central North Anatolian Fault Zone revealed by joint inversion of P-receiver functions and P-wave polarizations. *Geophysical Journal International*, 217(1):682–702, 2019.

C. Schiffer, A. L. Peace, S. Jess, and S. Rondenay. The crustal structure in the Northwest Atlantic region from receiver function inversion – Implications for basin dynamics and magmatism. *Tectonophysics*, 825:229235, 2022. ISSN 0040-1951. doi: https://doi.org/10.1016/j.tecto.2022.229235.

J.-R. Scholz, R. Widmer-Schnidrig, P. Davis, P. Lognonné, B. Pinot, R. F. Garcia, K. Hurst, L. Pou, F. Nimmo, S. Barkaoui, et al. Detection, analysis, and removal of glitches from InSight's seismic data from Mars. *Earth and Space Science*, 7(11): e2020EA001317, 2020.

V. Schulte-Pelkum and K. H. Mahan. A method for mapping crustal deformation and anisotropy with receiver functions and first results from USArray. *Earth and Planetary Science Letters*, 402:221–233, 2014.

A. F. Sheehan, G. A. Abers, C. H. Jones, and A. L. Lerner-Lam. Crustal thickness variations across the Colorado Rocky Mountains from teleseismic receiver functions. *Journal of Geophysical Research: Solid Earth*, 100(B10):20391–20404, 1995.

T. Shibutani, M. Sambridge, and B. Kennett. Genetic algorithm inversion for receiver functions with application to crust and uppermost mantle structure beneath eastern Australia. *Geophysical Research Letters*, 23(14):1829–1832, 1996.

D. E. Smith, M. T. Zuber, H. V. Frey, J. B. Garvin, J. W. Head, D. O. Muhleman, G. H. Pettengill, R. J. Phillips, S. C. Solomon, H. J. Zwally, et al. Mars Orbiter Laser Altimeter: Experiment summary after the first year of global mapping of Mars. *Journal of Geophysical Research: Planets*, 106(E10):23689–23722, 2001.

F. Sohl and T. Spohn. The interior structure of Mars: Implications from SNC meteorites. *Journal of Geophysical Research: Planets*, 102(E1):1613–1635, 1997.

T. Spohn, M. H. Acuña, D. Breuer, M. Golombek, R. Greeley, A. Halliday, E. Hauber, R. Jaumann, and F. Sohl. Geophysical constraints on the evolution of Mars. *Chronology and evolution of Mars*, pages 231–262, 2001.

T. Spohn, M. Grott, S. Smrekar, J. Knollenberg, T. Hudson, C. Krause, N. Müller, J. Jänchen, A. Börner, T. Wippermann, et al. The heat flow and physical properties package (HP3) for the InSight mission. *Space Science Reviews*, 214(5):1–33, 2018.

T. Spohn, T. L. Hudson, L. Witte, T. Wippermann, L. Wisniewski, B. Kedziora, C. Vrettos, R. D. Lorenz, M. Golombek, R. Lichtenheldt, M. Grott, J. Knollenberg, C. Krause, C. Fantinati, S. Nagihara, and J. Grygorczuk. The InSight-HP3 mole on Mars: Lessons learned from attempts to penetrate to depth in the Martian soil. *Advances in Space Research*, 69(8):3140–3163, 2022. ISSN 0273-1177. doi: https://doi.org/10.1016/j.asr.2022.02.009.

K. Stammler. SeismicHandler—programmable multichannel data handler for interactive and automatic processing of seismological analyses. *Computers & geosciences*, 19(2): 135–140, 1993.

É. Stutzmann, M. Schimmel, P. Lognonné, A. Horleston, S. Ceylan, M. van Driel, S. Stahler, B. Banerdt, M. Calvet, C. Charalambous, et al. The polarization of ambient noise on Mars. *Journal of Geophysical Research: Planets*, 126(1):e2020JE006545, 2021.

Y. A. Surkov and R. Kremnev. Mars-96 mission: Mars exploration with the use of penetrators. *Planetary and space science*, 46(11-12):1689–1696, 1998.

L. Svenningsen and B. Jacobsen. Absolute S-velocity estimation from receiver functions. *Geophysical Journal International*, 170(3):1089–1094, 2007.

T. Tanimoto, J. Um, K. Nishida, and N. Kobayashi. Earth's continuous oscillations observed on seismically quiet days. *Geophysical Research Letters*, 25(10):1553–1556, 1998.

A. Tarantola and B. Valette. Generalized nonlinear inverse problems solved using the least squares criterion. *Reviews of Geophysics*, 20(2):219–232, 1982.

F. W. Taylor. The scientific exploration of Mars. *The Scientific Exploration of Mars*, 2009.

G. J. Taylor, J. Stopar, W. V. Boynton, S. Karunatillake, J. M. Keller, J. Brückner, H. Wänke, G. Dreibus, K. E. Kerry, R. C. Reedy, et al. Variations in K/Th on Mars. *Journal of Geophysical Research: Planets*, 111(E3), 2006.

S. R. Taylor and S. McLennan. *Planetary crusts: their composition, origin and evolution*, volume 10. Cambridge University Press, 2009.

N. Teanby. Predicted detection rates of regional-scale meteorite impacts on Mars with the InSight short-period seismometer. *Icarus*, 256:49–62, 2015.

A. N. Tikhonov and V. Y. Arsenin. Methods of solution of ill-posed problems, 1979.

C. A. Tracy and H. Widom. On orthogonal and symplectic matrix ensembles. *Communications in Mathematical Physics*, 177(3):727–754, 1996.

A. Trebi-Ollennu, W. Kim, K. Ali, O. Khan, C. Sorice, P. Bailey, J. Umland, R. Bonitz, C. Ciarleglio, J. Knight, et al. InSight Mars lander robotics instrument deployment system. *Space Science Reviews*, 214(5):1–18, 2018.

D. L. Turcotte, R. Shcherbakov, B. D. Malamud, and A. B. Kucinskas. Is the Martian crust also the Martian elastic lithosphere? *Journal of Geophysical Research: Planets*, 107(E11):1–1, 2002.

M. van Driel, S. Ceylan, J. F. Clinton, D. Giardini, A. Horleston, L. Margerin, S. C. Stähler, M. Böse, C. Charalambous, T. Kawamura, et al. High-frequency seismic events on Mars observed by InSight. *Journal of Geophysical Research: Planets*, 126(2):e2020JE006670, 2021.

J. Vaucher, D. Baratoux, M. Toplis, P. Pinet, N. Mangold, and K. Kurita. The morphologies of volcanic landforms at Central Elysium Planitia: Evidence for recent and fluid lavas on Mars. *Icarus*, 200(1):39–51, 2009.

J. Vergne, G. Wittlinger, Q. Hui, P. Tapponnier, G. Poupinet, J. Mei, G. Herquel, and A. Paul. Seismic evidence for stepwise thickening of the crust across the NE Tibetan plateau. *Earth and Planetary Science Letters*, 203(1):25–33, 2002.

L. Vinnik. Detection of waves converted from P to SV in the mantle. *Physics of the Earth and planetary interiors*, 15(1):39–45, 1977.

L. Vinnik, H. Chenet, J. Gagnepain-Beyneix, and P. Lognonne. First seismic receiver functions on the Moon. *Geophysical Research Letters*, 28(15):3031–3034, 2001.

L. P. Vinnik, C. Reigber, I. M. Aleshin, G. L. Kosarev, M. K. Kaban, S. I. Oreshin, and S. W. Roecker. Receiver function tomography of the central Tien Shan. *Earth and Planetary Science Letters*, 225(1-2):131–146, 2004.

H. Wänke and G. Dreibus. Chemistry and accretion history of Mars. *Philosophical Transactions of the Royal Society of London. Series A: Physical and Engineering Sciences*, 349(1690):285–293, 1994.

E. Wiechert and K. Zoeppritz. Über Erdbebenwellen. *Nachrichten von der Gesellschaft der Wissenschaften zu Göttingen, Mathematisch-Physikalische Klasse*, 1907:415–549, 1907.

M. A. Wieczorek and R. J. Phillips. The structure and compensation of the lunar highland crust. *Journal of Geophysical Research: Planets*, 102(E5):10933–10943, 1997.

M. A. Wieczorek and R. J. Phillips. Potential anomalies on a sphere: Applications to the thickness of the lunar crust. *Journal of Geophysical Research: Planets*, 103(E1): 1715–1724, 1998.

M. A. Wieczorek and M. T. Zuber. Thickness of the Martian crust: Improved constraints from geoid-to-topography ratios. *Journal of Geophysical Research: Planets*, 109(E1), 2004.

M. A. Wieczorek, A. Broquet, S. M. McLennan, A. Rivoldini, M. Golombek, D. Antonangeli, C. Beghein, D. Giardini, T. Gudkova, S. Gyalay, et al. InSight constraints on the global character of the Martian crust. *Journal of Geophysical Research: Planets*, page e2022JE007298, 2022.

M. Wilde-Piorko, M. Grad, and T. W. Group. Crustal structure variation from the Precambrian to Palaeozoic platforms in Europe imaged by the inversion of teleseismic receiver functions—project TOR. *Geophysical Journal International*, 150(1):261–270, 2002.

X. Yuan, R. Kind, X. Li, and R. Wang. The S receiver functions: synthetics and data example. *Geophysical Journal International*, 165(2):555–564, 2006.

L.-S. Zhao, M. K. Sen, P. Stoffa, and C. Frohlich. Application of very fast simulated annealing to the determination of the crustal structure beneath Tibet. *Geophysical Journal International*, 125(2):355–370, 1996.

L. Zhu and H. Kanamori. Moho depth variation in southern California from teleseismic receiver functions. *Journal of Geophysical Research: Solid Earth*, 105(B2):2969–2980, 2000.

M. T. Zuber, S. C. Solomon, R. J. Phillips, D. E. Smith, G. L. Tyler, O. Aharonson, G. Balmino, W. B. Banerdt, J. W. Head, C. L. Johnson, et al. Internal structure and early thermal evolution of Mars from Mars Global Surveyor topography and gravity. *science*, 287(5459):1788–1793, 2000.

Acknowledgements

First, I would like to express my gratitude to Brigitte for allowing me to be a part of the InSight Science Team and work on this beautiful project. Despite her busy schedule and the large spatial distance between us, she made time to provide detailed comments and suggestions on my work. I am incredibly grateful to Uli for the constant support and valuable advice throughout this time. His profound knowledge, dynamic way of leading the department, considerate availability, and understanding have been exemplary. I am deeply indebted to Heiner for introducing me to the world of seismology and for his constant mentoring over the past six years. His encouragement and assistance at every stage of this project were instrumental in completing this successfully. I am profoundly grateful to Klaus for providing his excellent mathematical insights into the subject, without which it would not have been possible to make it this far. Conversations with him have always been effortless and enlightening.

I would also like to express my gratitude to the Planetary Dynamics group. Even with a lot of dynamo jargon, the meetings were always fun and very insightful. Thank you for being so patient and tolerant. I felt a sense of belonging even though I was the only seismologist around. I am also extremely grateful to the InSight Science Team - the meetings, presentations, and discussions have helped me immensely. I would like to especially acknowledge Savas, Raphael, and Martin for all their help at various times. I am also thankful to Sonja for her support and availability and to the International Max-Planck Research School for providing me with a platform to perform original research. And, of course, to all the staff at MPS that always helped in every situation, even in the middle of the night.

I want to express my deepest gratitude to all my friends who made this journey fun and enjoyable. Surviving Göttingen without you all would have been tough, especially during the Covid times. I miss the evenings we spent together with food, beer, music, and lots of fun. A special thanks to Bianca for beautifully supporting me through all this, putting up with me hooked to my PC for hours on end, and driving me around the whole country from time to time. My most profound appreciation to Einav for not letting me quit when I was at the lowest point. And most importantly, none of this could have happened without my family. Thank you for believing in me and supporting all my dreams all these years. I would not have been here without you. I always have you in my heart.